LARGE-SCALE ROUGHNESS EFFECT ON FREE-SURFACE AND BULK FLOW CHARACTERISTICS IN OPEN-CHANNEL FLOWS

by

Ceyda Polatel

An Abstract

Of a thesis submitted in partial fulfillment of the
requirements for the Doctor of Philosophy degree
in Civil and Environmental Engineering in
the Graduate College of
The University of Iowa

July 2006

Thesis Supervisors: Adjunct Associate Professor Marian Muste
Professor Virendra C. Patel

ABSTRACT

Our ability to accurately predict the flow rate in open-channel flows using only the free-surface characteristics is currently limited by the capabilities of the measurement instruments and lack of adequate mathematical models to describe the free-surface velocity for the variety of situations encountered in field conditions. This dissertation is concerned with the description of open-channel flow over large-scale roughness and determination of bulk flow parameters in view of implementing non-contact, remote discharge estimation techniques. In general, flow discharge estimation requires information about flow depth, velocity distribution over the depth, bed topography, and roughness. Discharge estimation based on a pointwise velocity measurement at the free-surface requires to relate this velocity with the depth-averaged velocity using additional characteristics embedded in the signature of the bed geometry on the free-surface. These problems are addressed through experimental and numerical studies.

Experiments were performed in a hydraulic flume with varying flow depth and bed roughness. Rectangular ribs and two-dimensional dune-shaped obstacles were placed on the flume bottom to simulate different bed roughness conditions. Laser Doppler Velocimetry (LDV) measurements were made to obtain the vertical velocity profiles at various locations. Large-Scale Particle Image Velocimetry (LSPIV) measurements were made to determine the velocity distribution at the free-surface. Large-Eddy Simulation (LES) with “rigid-lid” approximation for the free-surface was used to numerically simulate the flow over rib and dune geometries.

The measured and calculated velocity fields were used to determine a representative spatially-averaged velocity profile over the roughness wavelength. A two-layer, power-law model was then used to compare the flow over different roughness conditions and to establish an indexing parameter that links free-surface velocity to the bulk flow velocity. The experimental and numerical results presented here provide valuable insights into the flow structures at the free-surface and near-surface turbulence. The study therefore contributes to identification of velocity distribution laws over large-scale roughness, and facilitates remote discharge measurements in open-channel flows.

Abstract Approved: _____
Thesis Supervisor

_____
Title and Department

_____
Date

_____
Thesis Supervisor

_____
Title and Department

_____
Date

LARGE-SCALE ROUGHNESS EFFECT ON FREE-SURFACE AND BULK FLOW CHARACTERISTICS IN OPEN-CHANNEL FLOWS

by

Ceyda Polatel

A thesis submitted in partial fulfillment of the
requirements for the Doctor of Philosophy degree
in Civil and Environmental Engineering in
the Graduate College of
The University of Iowa

July 2006

Thesis Supervisors: Adjunct Associate Professor Marian Muste
Professor Virendra C. Patel

Graduate College
The University of Iowa
Iowa City, Iowa

CERTIFICATE OF APPROVAL

_____

PH.D. THESIS

_____

This is to certify that the Ph.D. thesis of

Ceyda Polatel

has been approved by the Examining Committee for the thesis requirement for the Doctor of Philosophy degree in Civil and Environmental Engineering at the July 2006 graduation.

Thesis Committee: _____
Marian Muste, Thesis Supervisor

_____
Virendra C. Patel, Thesis Supervisor

_____
Robert Ettema

_____
Ching-Long Lin

_____
George Constantinescu

ACKNOWLEDGEMENTS

Many people contributed to this work and made it possible. My heartfelt gratitude must first go to my advisors V. C. Patel and Marian Muste for their support, guidance, and patience during my studies at the University of Iowa. I am particularly thankful for their careful review and insightful comments through my study.

I was fortunate to participate in many collaborative efforts with researchers throughout my doctoral studies. I am grateful to Ram Balachandar for showing me the nuances of experimental studies and his enthusiastic work with me on LDV. I learnt the basics of PIV from Beom-Soo Hyun and Kwonkyu Yu during the early stages of my research. I thank Wolfgang Rodi and Thorsten Stoesser for providing the LES code and for being a constant resource during the last two years of my research. I am grateful to Thorsten for his dedicated work with me on LES. Acknowledgement is also made to the IFH for the computing time used for the simulations.

Zhongwei Li and Joerg Schoene have been members of my research group, and contributed to experimental part of the thesis. I especially thank Youngsung Kim for his valuable help towards the preparation of this thesis. I thank IIHR Model Annex crew and computer administrators for their helps and Judy Holland and Laura Myers for helping with numerous practical matters.

I would like to thank my co-workers in South Florida Water Management District Juan Gonzalez, Zhiming Chen, Claudia Manriquez, and Asif Mohamed for their support and friendship.

More than a lab to study, IIHR has been home to me during my PhD study. I am grateful all the members of IIHR who made the lab a wonderful environment to work in. I thank the graduate student of IIHR from the Middle East Technical University and friends all over the world along with Surajeet Gosh, Nobuaki Sakamoto, Berna Uckac, Eva Munoz, Clemens Braun, and Zafer Yildirim for always being there to listen and encourage me. I especially thank Manivannan Kandasamy for being the best friend of all times and always showing me how to see the bright side of things.

I thank my family, Sahika Polatel, Ayda Polatel, Taylan Polatel, Cafer Yilmaz, Fatma Yildirim, and Deniz Yildirim, for their constant support and encouragement. My special thanks go to my mother, Cezminur Polatel, and my late father, Sukru Polatel, who instilled in me the love of knowledge.

Financial support for this work was provided by USGS- National Institutes of Water Resources. The numerical study in the Institute for Hydromechanics, Karlsruhe University was partially supported by Anne Cleary International Research Fellowship.

ABSTRACT

Our ability to accurately predict the flow rate in open-channel flows using only the free-surface characteristics is currently limited by the capabilities of the measurement instruments and lack of adequate mathematical models to describe the free-surface velocity for the variety of situations encountered in field conditions. This dissertation is concerned with the description of open-channel flow over large-scale roughness and determination of bulk flow parameters in view of implementing non-contact, remote discharge estimation techniques. In general, flow discharge estimation requires information about flow depth, velocity distribution over the depth, bed topography, and roughness. Discharge estimation based on a pointwise velocity measurement at the free-surface requires to relate this velocity with the depth-averaged velocity using additional characteristics embedded in the signature of the bed geometry on the free-surface. These problems are addressed through experimental and numerical studies.

Experiments were performed in a hydraulic flume with varying flow depth and bed roughness. Rectangular ribs and two-dimensional dune-shaped obstacles were placed on the flume bottom to simulate different bed roughness conditions. Laser Doppler Velocimetry (LDV) measurements were made to obtain the vertical velocity profiles at various locations. Large-Scale Particle Image Velocimetry (LSPIV) measurements were made to determine the velocity distribution at the free-surface. Large-Eddy Simulation (LES) with "rigid-lid" approximation for the free-surface was used to numerically simulate the flow over rib and dune geometries.

The measured and calculated velocity fields were used to determine a representative spatially-averaged velocity profile over the roughness wavelength. A two-layer, power-law model was then used to compare the flow over different roughness conditions and to establish an indexing parameter that links free-surface velocity to the bulk flow velocity. The experimental and numerical results presented here provide valuable insights into the flow structures at the free-surface and near-surface turbulence. The study therefore contributes to identification of velocity distribution laws over large-scale roughness, and facilitates remote discharge measurements in open-channel flows.

TABLE OF CONTENTS

LIST OF TABLES

LIST OF FIGURES

LIST OF SYMBOLS

Roman Symbols

$< \cdot >$	double averaged velocity
a, m	power-law fit coefficients
a_b, m_b	power-law fit coefficients at the extent of the inner layer
c	velocity of surface waves
D	diameter
d	diameter
Fr	Froude number
g	gravitational acceleration
h	flow depth
h/k	roughness submergence ratio
h_x, h_y, h	dimension of computational domain in x-, y- and z- directions, respectively
k	roughness height
k_s	equivalent sand grain roughness
k_s+	roughness Reynolds number
k_x	roughness dimension in x-direction
Re	Reynolds number
u_*	shear velocity
u', v', w'	perturbation velocity
U, V, W	time-averaged velocity components
$u, v, w,$	instantaneous velocity components

U_0	time-averaged free-surface velocity
u_0	instantaneous free-surface velocity
U_{Bulk}	double- and depth-averaged flow velocity
u_i	velocity components
$u'u'$, $v'v'$, $w'w'$	root-mean-square turbulence intensities
$u'w'$	Reynolds shear stress
z_0	location of virtual origin above channel bed
z_b	extent of the inner layer

Greek Symbols

ΔU^+	roughness function
κ	Karman's constant
λ	roughness wavelength
ν	kinematic viscosity
ρ	fluid density
ω	vorticity

Abbreviations

2D	two-dimensional
3D	three-dimensional
DNS	Direct Numerical Simulation
FS	Free-surface
IVR	Index-velocity rating
LDV	Laser Doppler Velocimetry
LES	Large-Eddy Simulation

LSPIV	Large-Scale Particle Image Velocimetry
OCF	Open-channel flow
PIV	Particle Image Velocimetry
RANS	Reynolds-Averaged Navier-Stokes
rms	root-mean-square
SGS	Subgrid Scale
SIP	Strongly Implicit Procedure

CHAPTER 1
INTRODUCTION

1.1 Motivation

Velocity and appearance of the free-surface in an open-channel flow provide valuable information for assessing the bulk flow characteristics. Moreover, the free-surface carries the signature of the bed roughness and flow regime while it affects the turbulent flow structures and bed forms. Establishing a relationship between the state of the free-surface and vertical velocity profile would immediately assist the non-contact discharge measurement methods currently being developed by various instrument manufacturers and water resources management agencies.

This research originated from the need to provide scientific support for remote discharge estimation methods that attempt to use free-surface velocity as an indicator for the bulk flow velocity. The study is expected to facilitate remote discharge measurements by free-surface velocity indexing through the analysis of the turbulent open channel flows with special emphasis on the free-surface and its relationship with the depth-averaged velocity under various flow and roughness conditions.

The primary research question that this study seeks to answer is -

How free-surface texture and velocity distribution are affected by flow regime and bed roughness conditions, and how they can be related to the depth-averaged velocity?

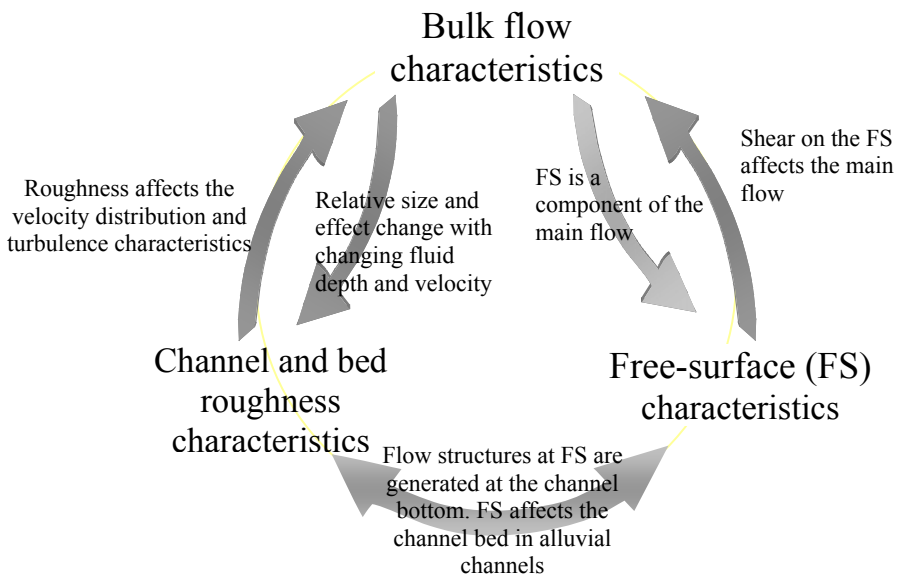

Figure 1.1 Free-surface (FS) flow characteristics can be divided into three categories: main flow, channel geometry (and roughness) and free-surface region.

Throughout this study, the free-surface region of the flow field receives special attention. The analysis of instantaneous, time-, space- and double-averaged properties is divided into three groups as free-surface effect, roughness effect, and main flow characteristics as illustrated in Figure 1.1.

For a given cross-section of an open-channel, flow discharge can be estimated by integrating the streamwise velocity distribution over the cross-sectional area. As an integral property of the velocity field, the flow discharge is related to the velocity at any point in the field. However, the relation between the free-surface and the flow discharge goes beyond the contribution of the free-surface velocity in depth-averaging. Free-surface characteristics and discharge are interrelated by the hydraulic characteristics of the flow as illustrated in Figure 1.2. As the flow changes from laminar to turbulent, or from subcritical to supercritical, free-surface waviness and turbulent structures vary

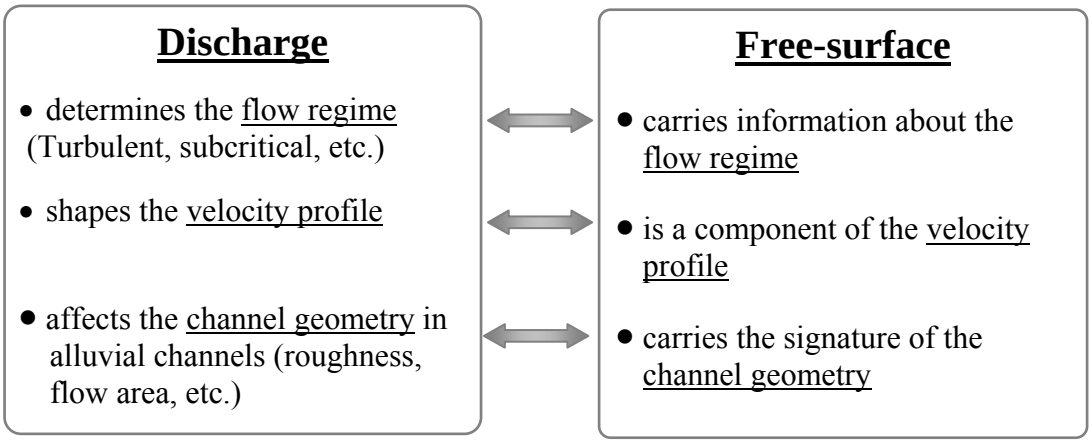

Figure 1.2 Relationship between free-surface velocity and discharge.

dramatically (Nakayama, 2000). In the case of alluvial channels, where the channel boundaries are deformable, flow area, bed forms generation and their effect on the flow changes with flow discharge (Yalin, 1992; Rantz & others, 1982a, 1982b). The change in these parameters further affects the free-surface characteristics (Nezu & Nakagawa, 1993; Bennett & Best, 1995; Pan & Banerjee, 1995; Yue *et al.* 2005a).

There is no analytical expression for the vertical velocity distribution for turbulent open-channel flows. Hence, empirical equations based on experimental observations are widely used for flow rate estimation (e.g., Manning's equation, Chezy equation). These relationships have been established under the assumptions of steady, uniform flows over small-scale, distributed roughness. At the flow measurement sites where the underlying assumption of steady, uniform flow is not satisfied, the application of these empirical equations yields inaccurate estimates of the flow rates.

Conventionally, flow rating curves using the relationship between the discharge and the flow depth (or stage) have been used for discharge monitoring purposes. Usually, rating curves are obtained at channel cross-sections where uniform flow conditions are

satisfied. At locations where such conditions can not be achieved, this relationship deviates from the assumed one-to-one relationship, and the flow rate estimation produces erroneous results.

Index-velocity rating (IVR) has gained popularity in the last few decades as an alternative discharge estimation method at stations where other methods are not appropriate. This method relates the "index velocity" (the velocity at a single point or along a line) to the depth-averaged velocity in the channel. With the advent of non-contact remote discharge methods, use of free-surface velocity as the index velocity has advantages in the aspects of convenience in finding its location and magnitude (Cheng *et al.,* 2002).

This research facilitates remote discharge measurements through investigation of the factors affecting the free-surface appearance and velocity. The study seeks an answer to the research question stated above through a set of physical and numerical experiments, in which a range of flow and geometrical characteristics are considered.

1.2 Background

Despite the long history of research on free-surface flow over rough bed, a holistic approach to the problem, considering the whole flow field from the channel bottom to the free-surface, is relatively new. The following review of the concept is divided into three sections: flow over rough beds, free-surface region and velocity indexing.

1.2.1 Flow over Rough Beds

While it is very important to have both conceptual understanding and quantitative description of turbulent flows, their random nature makes a deterministic solution of

equations of motion unattainable. Given their engineering importance and also their complexity, turbulent flows on rough surfaces have been extensively studied in the past, as indicated by reviews of Raupach *et al.* (1991), Patel (1998), Nikora *et al.* (2001), and Jimenez (2004). The mean velocity profiles in channels over rough beds differ considerably from the profile over a smooth bed since the bottom drag is significantly larger when roughness elements are present. Despite extensive studies on the subject, definitive functional relationships between the roughness geometry and the effect of roughness on the mean flow are still not established.

As Jimenez (2004) summarizes, sufficiently large roughness modifies the whole flow. Although most of the turbulent energy is generated close to the wall, large roughness affects the turbulence structure throughout the flow depth. Most studies of near-wall turbulent flow postulate a universal velocity profile in which there exists an overlap region where the mean streamwise velocity component varies logarithmically with the normal distance form the wall. The conventional expression for the velocity distribution is given as (e.g., Nezu & Nakagawa, 1993)

$$U^+ = \frac{1}{\kappa}\ln z^+ + A - \Delta U^+ \tag{1.1}$$

in which the shift due to roughness, roughness function, is usually expressed as

$$\Delta U^+ = \frac{1}{\kappa}\ln k_s^+ + B \tag{1.2}$$

where A is the constant for a smooth surface, (+) indicates normalization with the shear velocity, u_*, and the kinematic viscosity, ν. B is a constant depending on the roughness characteristics, k_s is the equivalent sand roughness, and ΔU^+ is called the roughness function. Coordinates and sign convention used in the above equations and throughout

the study is shown in Figure 1.3. The instantaneous velocity vector is decomposed into its components as

$$u = U + u', v = V + v', w = W + w' \tag{1.3}$$

where U, V, and W are the time averages of u, v, and w, respectively, and the fluctuating part of the velocity components are represented by u', v', and w'.

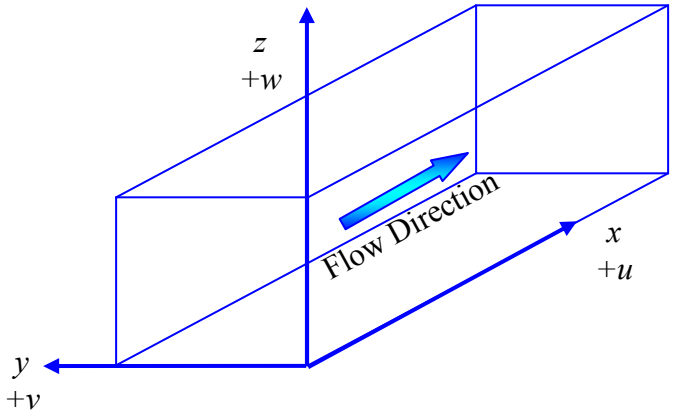

Figure 1.3 Coordinates and sign convention used in the study.

In accordance with Eq. (1.1), the velocity profile over a rough surface has a semi-logarithmic region with the same slope (1/κ) as that on a smooth surface. Although the profile over a rough surface is shifted from the smooth surface by a constant, ΔU^+, velocity profile for rough boundary flows is not completely defined because the relation between the roughness geometry and the roughness function is full of controversy.

While the semi-log model is well established in the literature, dimensional analysis indicates the possibility of two main models, namely, power law and log law.

For complete similarity, the velocity gradient in the overlap region is independent of both the inner and outer length scales, and the scaling of the velocity profile can be shown to be logarithmic (Tennekes & Lumley, 1972). For incomplete similarity, the velocity gradient depends on one or both length scales, and the scaling of the velocity profile has been shown to be a power law (Barenblatt, 1993; Barenblatt & Prostokishin, 1993)

$$u^+ = a\left(z^+\right)^m \tag{1.4}$$

where *a* and *m* are the power law fit coefficients. Barenblatt *et al.* (1997) define these parameters for smooth pipe and boundary layer flow as:

$$a = \frac{1}{\sqrt{3}}\ln \mathrm{Re} + \frac{5}{2} \text{ and } m = \frac{3}{3}\ln \mathrm{Re} \tag{1.5}$$

Typical values of these coefficients for open-channel flows are summarized and discussed in various studies (Nezu & Nakagawa, 1993; Kotey *et al.,* 2003).

Kotey *et al.* (2003) provide an assessment of the ability of power laws to describe the mean velocity profile in the overlap regions of a zero pressure gradient boundary layer over a rough surface. Analogous to the use of a roughness function they suggest a modification to the power law velocity profile to account for the roughness effect in the overlap region as

$$u^+ = \frac{a}{E}\left(z^+\right)^{m+\xi} \tag{1.6}$$

where E and ξ are roughness parameters and *a* and *m* are the smooth-wall coefficients of Eq. (1.5). For the test cases of their experimental study they obtained a range of ξ = 0.148 - 0.130 and E = 3.27 –5.41. They claim Eq. (1.6) reflects the roughness effect better than the traditionally used roughness shift parameter of ΔU^+, and concluded that the power

law effectively describes the mean velocity profile over both smooth and rough boundaries better than log law.

Besides the discussion of which law describes the overlap layer better, it should be kept in mind that existence of such a layer is established only in simple flows, such as pipe and two-dimensional boundary layer flows. An overlap region occurs only at high Reynolds numbers, and as White (1991) states it may not be seen in complex flow conditions, such as separation or high adverse pressure gradients, at all. Thus, in large-scale roughness flows with low submergence ratio (h/k, where h is flow depth, and k is roughness height) such a region may not exist.

Considering the findings of Krogstad (1991) and Djenidi *et al.* (1999), it is possible that the large-scale organized motions in the outer layer of the flow may not be universal, i.e., each boundary condition leaves its own signature on the structure of the outer layer. The effect of wall roughness on the turbulent flow characteristics increases with the increase of the roughness size (k). For flow over large-scale roughness with size of the same order of the flow depth (h), it is expected that the flow structures and velocity distribution are highly dependent on the roughness geometry.

1.2.1.1 Turbulent Flow Structures

Turbulent structures play an important role in heat and momentum transfer, sediment transport, and dispersion of contaminants. Identification of coherent vortical structures is not only useful for understanding turbulent motion, but crucial in the development of viable turbulence models for complex flows.

Fulgosi (2003) defines a coherent structure as a connected, large-scale turbulent fluid mass with a phase-correlated vorticity throughout its spatial extent. The separation

between coherent and non-coherent motion is of crucial importance to obtain a better understanding of the transport processes. In fact, on a smooth-wall turbulent boundary layer, streamwise coherent structures have been linked to ejections and sweeps, which are responsible for moving slow-moving fluid into the outer layer and bringing high-momentum fluid into the wall region, respectively. These events generate the major part of the drag and are well correlated with heat and mass transfer fluxes (Lam & Banerjee, 1992). The key issue is to define a suitable criterion that identifies boundaries, topology, and dynamics in the spatial and temporal extent of these structures.

There are several ways to describe and quantify the turbulent structures. High vorticity magnitude, $|\vec{\omega}|$, is a possible candidate for vortex identification in free-shear flows. However, the vortex contours can be extremely complex, and the structures that are visible in plots of vorticity depend largely on the choice of a low level threshold (McIlwain & Pollard, 2002). Besides, in the presence of a boundary the mean-shear creates a residual vorticity, which is uncorrelated with the vorticity caused by the coherent motions.

A more efficient way to identify vortical structures is the λ_2-method of Jeong & Hussain (1995) in which the negative λ_2, the second largest eigenvalue of the tensor $S_{ik}S_{kj}+\Omega_{ik}\Omega_{kj}$, is employed to capture vortex core. Here S_{ij} and Ω_{ij} are the symmetric and antisymmetric parts of the deformation rate tensor $\frac{\partial u_i}{\partial x_j}$, i.e., $S_{ij}=\frac{1}{2}\left(\frac{\partial u_i}{\partial x_j}+\frac{\partial u_j}{\partial x_i}\right)$ and $\Omega_{ij}=\frac{1}{2}\left(\frac{\partial u_i}{\partial x_i}+\frac{\partial u_j}{\partial x_j}\right)$.

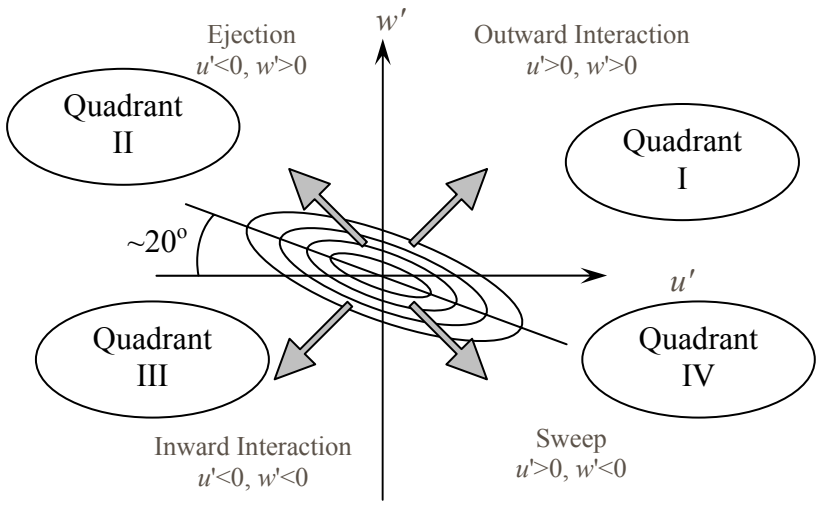

Figure 1.4 Schematic of quadrants of events.

Another commonly used method is the so-called Quadrant Analysis which is used to analyze the generation mechanisms of the turbulent structures. If the fluctuations in horizontal (u) and vertical (w) velocity are decomposed into their deviations from the mean, they can be sorted into four quadrants as shown in Figure 1.4. An event is defined as a structure in the flow field which occurs as a sequence of velocity fluctuations in one of the quadrants of the (u', w') plane. The events are classified according to quadrant of u'-w' plane that they happen and named as 'Outward Interactions', 'Ejections', 'Inward Interactions' and 'Sweeps', representing Quadrant 1,2,3, and 4, respectively.

Turbulent flow structures observed on the free-surface, such as boils, require similar analysis. The quadrant analysis may also be used to isolate the contributions to the Reynolds shear stress from the sweeps, ejections, inward and outward interactions. For example, contributions from the i^{th} quadrant of the $u' - w'$ plane, are

$$(-u'w')_i = \frac{1}{T}\int_o^T -u'w'S_i dt \qquad i = 1, 2, 3, \text{ and } 4 \tag{1.7}$$

where S_i is the quadrant sorting function. The intermittency factor Q_i is defined as the ratio of the total residence time T_i of u' in the quadrant i to the total measuring time T. It is an integral measure for the relative importance of the structure defined by the i^{th} quadrant and given as:

$$Q_i = T_i / T \tag{1.8}$$

In the present study, quadrant analysis based on conditional sampling suggested by Lu & Willmarth (1973) is used to detect turbulent structures and events. Similar analysis can be made on the u'- v' fluctuations at the free-surface.

1.2.1.2 Roughness Effect and Characterization

In hydraulic engineering, nearly all practical flows are considered hydraulically rough, i.e. the roughness is large enough to destroy the viscous layer (k^+>80). As discussed in the previous section, the roughness causes a shift in the velocity profile in semi log plot. However, the effect of large-scale roughness may go beyond this shift, and change the outer, so-called wake layer. Large-scale roughness has been reported to have major effect on the time- and space- averaged properties as well as the instantaneous flow field (Yalin, 1992; Krogstad & Antonia, 1999; Nakayama, 2000; Nezu & Nakagawa, 1993).

Traditionally Nikuradse's sand roughness is used to classify the roughness type. However, Bandyopadhyay (1987) argues that the concept of equivalent sand roughness, k_s, as "devoid of any physical significance and problematic determination". This point is especially valid for large-scale roughness. Despite these concerns, effect of isolated

large-scale roughness on mean velocity profile is often chosen as the classification criterion (Krogstad & Antonia, 1994; Djenidi *et al.,* 1999) for large roughness.

Chow (1959) summarizes the basic flow characteristics of different roughness types. The classification is based on the assumption that the loss of energy in turbulent flow over a rough surface is due largely to the formation of wakes behind each roughness element. The intensity of such vorticity sources in the direction of flow will determine the turbulence characteristics with roughness wavelength, λ, playing a major role. For rib roughness, for example, the ratio of λ, to the roughness height, k, is widely used as the classification parameter. Taking λ/k as the criteria, roughness is categorized into three categories as k-, transitional, and d- type roughness (Figure 1.5). Despite the small differences in the assumed limits of these categories, the following roughness characterization is commonly accepted.

$\lambda/k > 4$ k-type

$\lambda/k < 2$ d-type

$2 < \lambda/k < 4$ transition

Instantaneous and time-averaged properties of turbulent flow over d-type roughness have been reported to be very similar to those of flow over a smooth wall (Wood & Antonia, 1975; Bandyopadhyay, 1987). For this reason, this type of roughness is not considered in this study. Instead, the study is focused on flow over distributed, k-type roughness, where the effect of individual roughness elements can be observed in the time-averaged and instantaneous flow properties.

The turbulence over large-scale, k-type roughness is dominated by the influence of the separation zone and vorticity generated along the boundary shear layer, where high

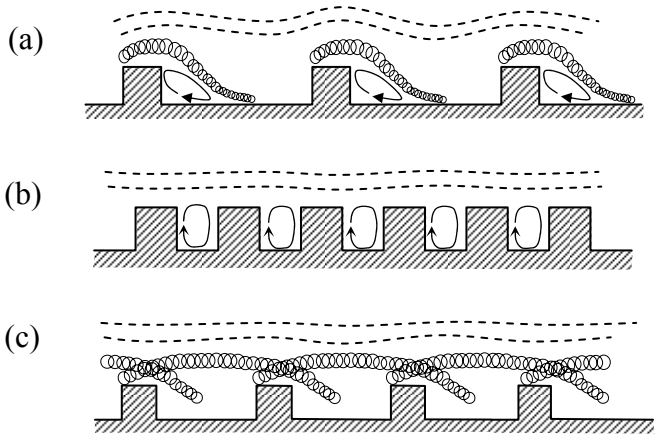

Figure 1.5 Types of rough-surface flows: (a) k-type; (b) d-type; (c) transitional (Chow, 1959).

Reynolds stresses are present. The generation, transport and dissipation of the coherent structures are highly dependent on the roughness geometry. For k-type roughness, it is possible to identify the effects of individual roughness elements on the turbulent structures. Due to the strong relationship, a unique signature of each roughness condition on the turbulent structures is expected.

Figure 1.6 shows the main features of the flow over k-type rib roughness, where mean flow detaches from the roughness element, and reattaches ahead the next roughness element. An internal boundary layer develops from the reattachment point. It is reported that the existence of reattachment point plays an important role in the generation of the macro turbulence structures and the time-averaged properties of velocity field of flow over rough surfaces (Yalin, 1992; Nezu & Nakagawa, 1993; Nakayama, 2000; Maddux, 2002). Earlier experimental studies on flow over ribs and dunes are summarized in Table 1.1 and Table 1.2, respectively. The geometries of the roughness considered in the present study were decided by the review of the studies given in these tables.

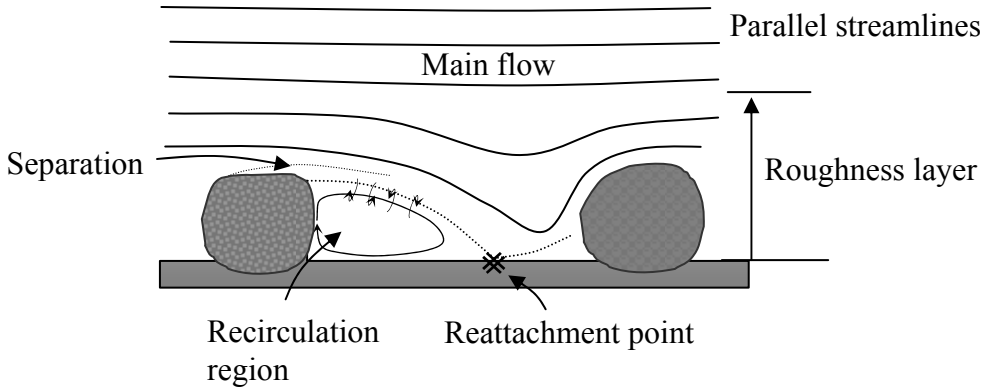

Figure 1.6 Schematic of flow over k-type roughness.

Most of the approaches for describing roughness effect on the time-averaged velocity profile are along Nikuradse's approach of equivalent sand-grain roughness, k_s, and roughness function, ΔU^+. As mentioned previously, for large-scale roughness, such as ribs and dunes, this function may not be sufficient to describe the complete effect of the roughness, but still gives an important insight to physics of the flow. Earlier research on wavy walls (Cui, 2000; Yue *et al.*, 2003; Nakagawa & Hanratty, 2001, 2003) report the existence of roughness function, ΔU^+, which can be observed as a shift in the wavelength-averaged velocity profile, normalized by wavelength-averaged u_* plotted in logarithmic format. This shifted velocity profile has the same slope as the profile on a smooth wall. Numerical and experimental studies show that, for roughness with an order of magnitude smaller than the flow depth, periodic roughness types such as dunes and waves can be regarded as distributed roughness (Lyn, 1993; Yoon & Patel, 1996; Cui, 2000).

Observations on the flow over large roughness have pointed out the difficulties in locating the origin of the velocity profile, which complicates the application of ΔU^+ for roughness characterization. Moreover, studies of Krogstad & Antonia (1999) showed that even for the roughness types creating the same ΔU^+, the turbulence characteristics can vary significantly. Considering the findings of Djenidi *et al.* (1999) and Krogstad (1991), it is possible that the large-scale organized motion in the outer part of the flow may not be universal, i.e. each boundary roughness leaves its own signature on the structure of the outer layer.

In this study, in parallel to the free-surface response to the large-scale roughness, the velocity profiles and turbulence characteristics are investigated for both the limitations and capabilities of conventional roughness characterization methods to explain flow over large-scale roughness.

1.2.1.3 Two-Layer Velocity Profile

Turbulent flow over roughness adjusts itself according to changes in the flow area, flow separations, and reattachment. In the small-scale, flow throughout the whole wavelength of the roughness is expected to not repeat at any two locations. However, for various application purposes, a functional description of the velocity profile describing the average flow field is needed.

The double- (time- and space-) averaged velocity and Reynolds stress profiles for flow over large-scale roughness show a two-layer structure (Smith & McLean, 1977; Nelson *et al*., 1993; Fedele & Garcia, 2000; Maddux, 2002) as illustrated in Figure 1.7. The layer where the effect of individual roughness elements can be observed is called the inner layer. The layer further away from the bed where the effect of individual roughness

elements is washed out is called the outer layer. Inner and outer layers of the double-averaged velocity profile are joined at a matching level, z_b. Several investigations have concentrated on the characterization of the mean flow and turbulence structure in these two layers. However, there is no consensus on the velocity distribution laws (Fedele & Garcia, 2000; Nikora *et al*., 2004).

There is agreement in the literature that, in the outer layer, the averaged velocity profile has a conventional logarithmic region based on shear velocity, u_*, location of virtual origin, z_0, and roughness height, k. In the inner layer the velocity profiles do not follow a general trend. Before McLean *et al.* (1999) raised concerns on its validity, it was believed that the inner layer also follows the log law evaluated with a different shear velocity. Various models for the vertical distribution of the double-averaged streamwise velocity in the inner layer have been proposed. Nikora *et al*. (2004) groups these models in: (1) constant, (2) exponential, and (3) linear velocity distributions. For roughness types investigated in the present study, both the logarithmic and linear profiles for the inner layer have been earlier suggested by Nelson *et al*. (1993) and Maddux (2002), respectively. In this study a power law model is preferred over log law model for reasons explained in Appendix A.

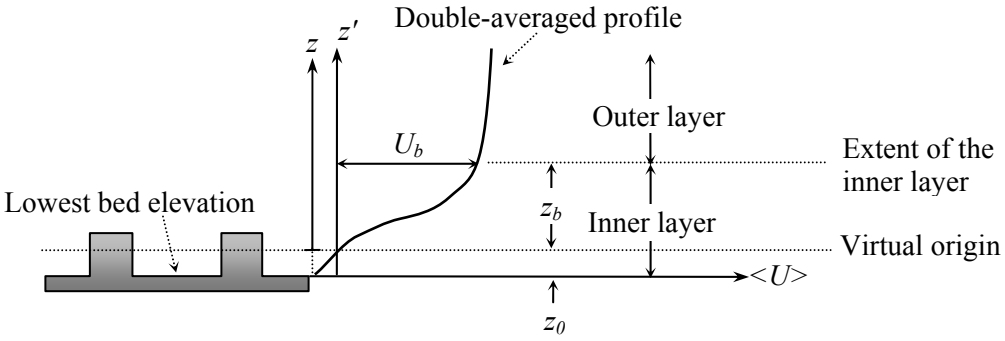

Figure 1.7 Schematic of the double-averaged flow over large-scale roughness.

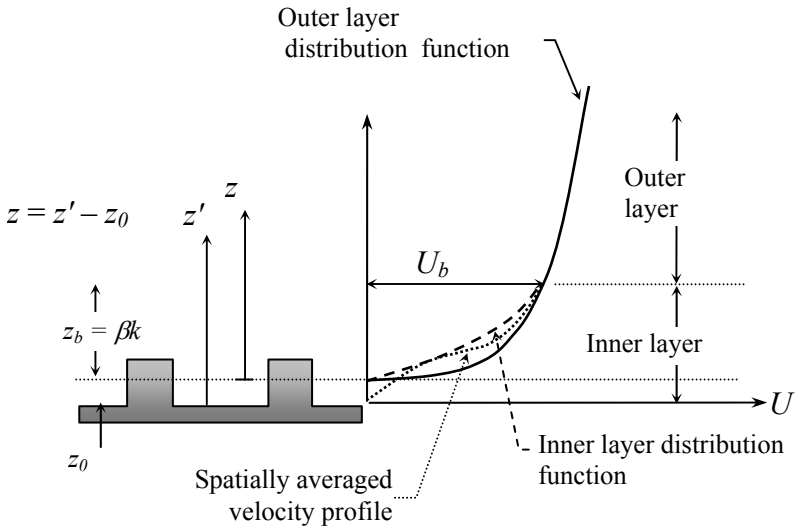

Figure 1.8 Schematic of composite profile over large-scale roughness.

At the edge of the inner layer, where $z = z_b$, the velocity, U_b, satisfies the distribution functions from both inner and outer layers. In the outer layer, where $z > z_b$, *the* velocity distribution can be defined by

$$\frac{U}{u_*} = a\left(\frac{z}{h}\right)^m \tag{1.9}$$

where the coefficients a and m are found from the least square fit to experimental data, and h, the flow depth, is used as the normalization parameter since it is the characteristics length of the outer layer.

From the relationship of m and Re given in Eq. 1.5, power-law fit will approach to a linear function (m=1) with decreasing Re. The characteristic length and velocity in the definition of Re should be chosen carefully, before starting to seek power law parameters in the inner layer. In the inner layer where $z < z_b$,

$$\frac{U}{u_*} = a_b\left(\frac{z}{h}\right)^{m_b} \tag{1.10}$$

where a_b and m_b are the power law parameters found from the least square fit to the *spatially averaged* velocity distribution in the inner layer.

To compare z_b values for different roughness conditions, a non-dimensionalized boundary point, β, can be defined as (See Figure 1.8)

$$\beta = \frac{z_b}{k} \tag{1.11}$$

The variation of β with flow and roughness conditions will be discussed in Chapter 5.

Another important feature of the velocity profile over large-scale roughness is the location of the origin over the channel bed. Formally, the virtual origin (or theoretical

wall) is defined as the location from which the vertical distances in distribution functions (e.g. log law or power law) are measured, or where the average velocity is zero.

The location of virtual origin over the channel bed is a measure of the interaction between the mean flow and the roughness. There is no theoretical method to find the virtual origin for any roughness type; it is known to be a function of roughness Reynolds number, k_s+ (Yalin, 1992; Nezu & Nakagawa, 1993). It is also expected to be located close to the roughness crest for d-type roughness and close to the channel bottom for k-type roughness. The relationship between z_0 and ΔU^+ has been reported in earlier studies (Perry *et al.*, 1969; Cui *et al.*, 2003; Fedele & Garcia, 2000; Nakagawa *et al.,* 2003, Nakagawa & Hanratty, 2003).

A schematic representation of velocity profiles over the channel bottom and the virtual origin are shown in Figure 1.8. A proper definition of the virtual origin will minimize errors arising from the assumption of self-similarity in the roughness layer, and makes it possible to apply roughness function for flow over large-scale roughness. An improper positioning of the virtual origin causes a larger angular deviation in the semi-log velocity profile of the flow over roughness. The significance accurately locating the virtual origin and the mathematical description of error in the velocity distribution function caused by not doing so will be discussed in Chapters 4 and 5. The logarithmic law of velocity distribution above the virtual origin is

$$\frac{u}{u_*} = \frac{1}{\kappa}\ln\left(\frac{u_*}{\nu}\left(z' - z_0\right)\right) + A - \Delta U^+ \qquad (1.12)$$

where z' is the vertical distance from the channel bottom, and z_0 is the location of the virtual origin above the channel bottom. It is clear that an error in the location of z_0 will cause an error in the slope of the velocity profile in semi-log scale.

A geometrical average of the roughness height, as in atmospheric boundary layer studies, or the intercept of the logarithmic velocity distribution function (mostly from k_s in hydraulics applications) are commonly used methods to locate the virtual origin. In this study the application of various methods to locate the virtual origin are discussed and applied in Chapters 4 and 5.

The present study uses a two-prong approach whereby detailed LDV experiments and LES are used to investigate the structural properties of the double-averaged velocity profile over large-scale roughness. Experiments are used to validate LES, which in turn provide high-resolution data. LES results are subsequently analyzed to find the location of the virtual origin and the extent of the inner layer using concepts and formulations of previous studies reviewed above.

1.2.2 Free-Surface

Many issues related to mean and turbulence characteristics in the vicinity of the free-surface of open-channel flows remain unresolved. Of particular importance herein is the nature and characteristics of structures formed at the free-surface, their relationship with channel bathymetry, and velocity distribution laws over the channel depth for a variety of conditions. Investigation of these topics is a great challenge for experimental and numerical simulations. It is difficult to make measurements of velocity and turbulence at or near the free-surface and it is still not feasible today to carry out direct numerical simulations of flows at moderate to high Reynolds numbers.

A great deal of effort has been made recently towards the understanding of free-surface turbulence (Nakayama, 2000; Buffin-Belanger, Roy & Kirkbride, 2000; Kurose & Komori, 2001). It has been pointed out that turbulence structure is affected by the

presence of a free-surface and turbulent energy redistribution changes within a surface-influenced layer. Recent investigations show that there are interactions between the free-surface turbulent structures and flow physics underlying the channel turbulence. The complexity of these interactions has been demonstrated by numerical simulations (e.g., Shi *et al.*, 2000) and experimental studies (Tamburrino & Gulliver, 1994; Yue *et al.*, 2005b).

Predictive models of the scalar transport across the free-surface have been considered by several investigations (Banerjee, 1992; Nagaosa & Handler, 2003). Dankwerts (1951), for example, assumed that fluid elements on the free-surface are replaced at random with fluid elements from below. His considerations have been termed surface renewal models and have been applied in attempts to estimate turbulent heat and mass fluxes. The surface renewal approximation predicts that the heat and mass transfer coefficient is proportional to the inverse square of the time scale of coherent vortices near the surface.

The laboratory experiments by Komori e*t al.* (1989) and Rashidi (1997) presumed that large-scale coherent vortices generated in the near-wall region advect toward the free-surface and become surface renewal eddies. Their measurements of the surface renewal and near-wall bursting frequencies reveal that 70% to 90% of bursting eddies produced in the near-wall turbulence move toward the subsurface region without annihilation. Moog & Jirka (1995) have studied the 'macro-roughness effect' on the turbulent energy dissipation rate near the free-surface. They have related a gas transfer coefficient with the turbulent dissipation rate near the surface, and evaluated the macro-

roughness enhancement over a rough bed. They conclude that macro-roughness may have an important role on the coherent structures in open-channel flow.

Rashidi (1997) carried out flow visualization experiments using a hydrogen-bubble technique and found that hairpin-like coherent vortices include surface patches as they interact with the free-surface. Rashidi asserted that the interaction of near-wall coherent vortices with the free-surface is a direct cause of the formation of surface patches and the enhancement of turbulent heat and mass transfer at the free-surface. Best (2005) observed significant interactions of large-scale vortices, whose origin is in the near-wall region, with the free-surface. While these flow visualizations have provided evidence of the interaction of the near-wall turbulence with the free-surface, the details of the generation mechanics of the surface renewal events are not completely resolved.

Large-scale vortical (macroturbulence) structures are reported to advect through the entire water depth, and affect the sediment transport in alluvial channels. Best (2005) links the origin of these structures to shear layer development in the lee of the dune. Nezu & Nakagawa (2003) associated flow separation with the form of these coherent flow structures and their eruption on the free-surface. The bursting motions generated in the wall region moves toward the free-surface and form a boil there. Jackson (1976) described the features of boil vortices from field observation in rivers, and concluded that roughness and sediment may modify the intensity of the bursting, but do not alter the basic burst cycle. It is very likely that the coherent structures and their statistical properties in flow over large-scale roughness bed are different from those over a smooth bed or small sized roughness (such as sand grains).

There are many studies in the literature reporting how bed roughness changes the macroturbulence structures at the free-surface (Nakagawa *et al.,* 1975; Nezu & Nakagawa, 1993). Nezu & Nakagawa (1993) classified boils into three groups depending on different mechanism of generation. They report that *boils of the first kind* appear behind dunes, large-scale ripples and man-made backward-facing steps in the river bottom. Thus, their location is confined to fixed zones. However, the occurrence of the boils is intermittent and somewhat random in time. They are the result of fluctuation of the reattachment point. Therefore, they do not appear in flows over a smooth rigid bed. *Boils of the second kind* are associated with cellular secondary currents, and they occur in wide, straight rivers, generating boil streets aligned with the flow. They are reported to be intermittent in time and do not appear on smooth flat channels. *Boils of the third kind* are associated with the bursting motions. They have been observed at low Reynolds numbers. Since bursting motions occur randomly in space and time, occurrence of this kind of boils is random.

Bursts are characterized by an ejection of fluid with low streamwise momentum from the wall region, i.e. $-u'w'$ is negative and w is large and positive. As illustrated in Figure 1.9, smooth wall, roughness, and secondary effects, such as sidewalls and wind, can also cause large vortical structures at the free-surface. The combined effects of these three generation mechanisms shape the texture of the free-surface. While boils of the third kind are generated regardless of the shape of the riverbed, boils of the first and second kinds are thought to be caused by sand waves in the streamwise and spanwise directions, respectively. Because boils of the third kind usually occur less frequently in

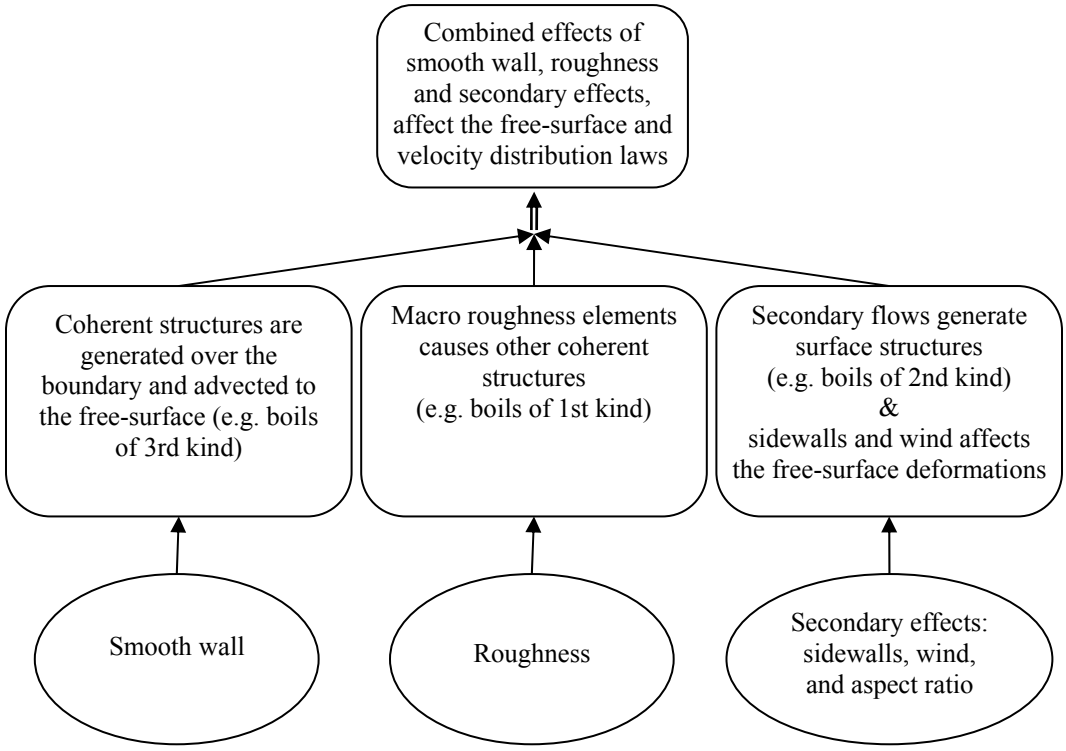

Figure 1.9 Schematic description of generation of free-surface structures.

high *Re* flows such as rivers, boils associated with dune type sand waves are expected to be boils of the first kind, caused mainly by kolk vortices.

1.2.3 Velocity Indexing

The idea behind remote discharge measurements in channels and rivers is to remotely obtain channel bathymetry and velocity distribution information, and subsequently integrate them according to the physics of the open-channel flow (see Figure 1.10). For this purpose, it is crucial to have a unique and accurate relationship between the velocity distribution and flow conditions, i.e., channel geometry, secondary currents, and wind effect. Extensive studies have been reported in the literature dealing

with estimating the velocity distribution by using a pointwise measured velocity for a given bed configuration (Rantz *et al.* 1982b; Fujita *et al.* 1998; Chen & Chiu 2002; Cheng *et al.* 2004). The concept of relating depth-averaged velocity to a single, pointwise velocity measurement is called indexing. This method has become important with development and use of new measurement technologies that use one point velocity measurement to characterize velocity distribution over the depth.

Even though the method is newly developed, the index velocity method has been investigated for its applicability to field conditions by Church *et al.* (1999), Haeni (2000), and Simpson *et al.* (2000). Currently, there are relatively high-accuracy instruments for remote measurement of stream cross-sections. Consequently, most of the uncertainties in discharge estimation are induced by inaccuracies in the mean velocity estimation (Muste *et al.,* 2001). The parameters involved in velocity indexing have been individually measured by using particle-image velocimetry, lasers, radar, and acoustics in related applications (Melcher, *et al.*, 1999). Hydro21 (Cheng *et al.*, 2001) proof-of-concept tests in field conditions have illustrated that remotely sensed bathymetry (based on ground penetrating radar), combined with free-surface velocity measurements (based on microwave radar), have the potential to yield non-contact river discharge estimates (Cheng *et al.*, 2001).

Studies taking different velocities (e.g., maximum velocity, free-surface velocities, or combination of velocities at certain fractions of water depth) as indexing velocity exist in the literature (Rantz *et al.*, 1982b; Chiu & Tung, 2002). Use of free-surface velocity as indexing velocity has advantages in the aspects of convenience in finding location and magnitude of the free-surface velocity and aptness to non-contact

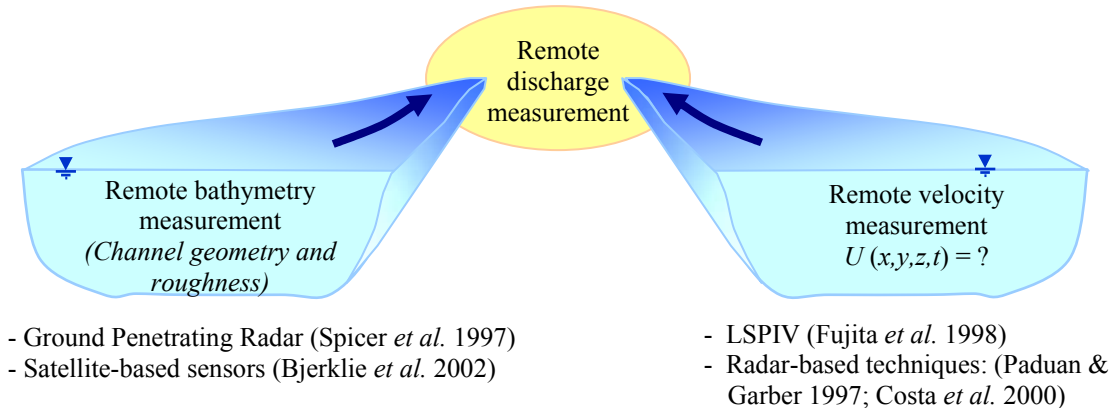

Figure 1.10 Two components of the remote discharge measurement.

measurements (Bjerklie *et al.* 2002; Cheng *et al.* 2004). Due to the limitations of the measurement techniques, the free-surface velocity could not be measured in the past. However, as given in a review by Costa *et al.* (2002), recently developed methods such as radars and image velocimetry methods make it possible to measure free-surface velocity, and subsequently determine the discharge.

A functional relationship, relating point velocity measurement to depth-averaged velocity, is needed to estimate channel or river discharge. By taking free-surface velocity as the indexing velocity, the velocity index, α, can be defined as

$$\text{Velocity Index } (\alpha) = \frac{\text{Depth-averaged velocity } (U_{Bulk})}{\text{Free-surface velocity } (U_0)} \tag{1.13}$$

The magnitude of α can be taken as constant for a given river cross-section (Cheng *et al.,* 2001), and can be found mathematically for a known distribution function. However, the classical velocity distribution functions (e.g., log law and power law) usually stem from semi-empirical relationships derived for boundary-layer flows, and there is substantial experimental evidence showing that they may be inaccurate at or near the free-surface.

The state of the free-surface in open channel flows has a unique relationship with the velocity distribution and other flow conditions (Muste *et al.* 2001). If this relationship can be identified, a direct discharge measurement is made possible by only one velocity measurement at the free-surface. With this perspective, the search for non-contact discharge measurement takes the direction of seeking the relationship between the free-surface velocity, U_0, and depth-averaged velocity, U_{Bulk}.

Dypvik & Lohrmann (2003) discuss validity of index velocity method as an internationally accepted method for discharge calculation, and agree on the potential in this method as a basis for remote discharge measurement techniques. Costa, *et al.* (2000) concludes that after conducting proof-of-concept experiment "with further refinements, it is thought that open-channel flow can be measured reliably by non-contact methods", they report that mean velocity is 0.85 $<U_0>$ ($\alpha = 0.85$). This value of velocity index, α, will be refined in the current research.

The objective of the present research is to obtain velocity indices, α, for channel flows over various bed roughness and flow conditions (e.g. Froude number and aspect ratio) to help answer the research question given in Section 1.1. For this purpose, a set of experiments was planned, in which the effects of aspect ratio and bed characteristics could be investigated. In accordance with the motivation of non-contact measurements, both free-surface velocities and velocity distributions were measured remotely in the laboratory. To measure the free-surface velocity Large Scale Particle Image Velocimetry (LSPIV) method was selected since it is the most suitable technique available. To obtain the velocity distribution, Laser Doppler Velocimetry (LDV) method was used due to its non-intrusivity, accuracy, and directional sensitivity.

1.3 Research Objectives and Thesis Overview

Improved understanding of the roughness effect on the free-surface is necessary to further our understanding of physical processes that occur in free-surface flows. The goal of this dissertation is to investigate roughness effect on the free-surface and the bulk properties of open-channel flows.

The research attempts to answer the following questions:

- How dunes and ribs affect the mean velocity field?
    - Can dunes and ribs be treated by classical roughness theories?
    - How the macro turbulence structures caused by dunes and ribs affect the velocity distribution and free-surface appearance?
    - How available velocity distribution functions can be applied to the large-scale roughness flows?
    - How can the roughness characteristic lengths and scaling parameters be defined for large-scale roughness?
- Can we use water surface velocity as an index velocity for computing river discharge?
    - What is the relationship between surface velocity and depth averaged mean velocity?
- How the bed roughness, Reynolds number, secondary flows, and aspect ratio affect the surface deformations?
    - Can we remotely capture these deformations?
    - Can we quantify them?
    - How these deformations are related to surface velocity?

Chapter 2 begins with a discussion of the experimental method, and current challenges and practices in free-surface measurements. The method used in the LDV and LSPIV experiments is described. Chapter 3 describes the numerical model used in the simulations, and the benefits gained by employing LES. Chapter 4 presents the methods followed for data reduction and calculation of important parameters. The discussion of the results across the flow cases is presented in Chapter 5. Chapter 6 summarizes the contributions of this work and provides recommendations for future directions.

Table 1.1 Summary of experimental studies on flow over rib roughness.

References	**Roughness Type**	**Technique**	**Meas. at**	α_k	***h/k* or δ/k**	**Measured Quantity**	**Reference velocity**	**Re k^+**	**Scaling parameter**	λ_s	λ_k
Perry *et al.*, (1969)	Train of ribs at the lower boundary	BL Wind Tunnel	Above the crest	1	δ/k 3-24	u	U_∞=20.42 –32.31 m/s	k^+= 250 - 2500	u_*, ε, k	2	2
Wood &Antonia (1975)	Train of ribs at the lower boundary	PSP Wind tunnel	Four stations	1	δ/k=16	u, v, w	u_*	$Re_\theta \approx 3200$ k^+=60	U_∞, θ, u_*, k, δ	2	2
Bandyo-padhyay (1987)	Train of ribs at the lower boundary	BL Wind Tunnel	At various locations	1.05 2.55		Drag, u	U_∞, u_*	Re_θ= 670~760 k^+=4	U_∞, u_* ,δ^*, θ, ε	2.1, 5.1	2.1, 5.1
Liou and Kao (1988)	Two single roughness elements at the lower and upper wall	LDV and Num Water channel	23 stations u/s and d/s of roughness elements.	-	k/h = 0.13-0.33 w/k = 1-10	u, w	U_{Bulk}	Re_D=2.0x10^3 - 7.6x10^4	U_∞, k, h	-	-
Liou, Chang, & Hwang (1990)	Two pairs of roughness elements at the lower and upper wall	LDV and Num Water channel	Various stations at the groove and one at the crests	0.5-0.02	k/h = 0.133 w/k =1	u, w	U_{Bulk}	Re_D=1.2x10^4 to 1.2x10^5	U_∞, k, h	1-100	1-100
Liou, Wu & Chang (1993)	Two trains of ribs, one at the lower and the other at the upper wall	LDV Water channel	At x/k= -0.5, 2, 7	0.2	h/k = 7.5	u, v	U_{Bulk}	Re_D=3.3x10^4	U_∞, k, h	10	10
Okamoto *et al.*, (1993)	Train of ribs at the lower boundary,	Wind Tunnel	One above ribs and 13 on the groove	1-8.5		u (T, T_w, T_∞)	U_∞=16	$U_\infty k/\nu$= 1.0x10^4	U_∞, δ	2 - 17	2-17

Table 1.1 Continued

References	**Roughness Type**	**Technique**	**Meas. at**	α_k	***h/k* or δ/k**	**Measured Quantity**	**Reference velocity**	**Re k^+**	**Scaling parameter**	λ_s	λ_k
Mochizu-ki, *et al.* (1996)	Train of ribs at the lower boundary	Hot wire BL	Over the crest	1		*u, w, u′, w′*	u_0=3-12 m/s	Re_θ=1300 - 5000	U_∞, δ	2	2
Djenidi, *et al.*, (1999)	Train of ribs at the lower boundary	LIF and LDV Water tunnel	Several points over the cavity and crest	1	δ/k = 7 to 9	*u, v, w* Flow visualize-tion	u_* (0.011 ~ 0.024)	900 ~ 2300 (θ) k^+=124 at (Re_θ = 2300)	u_*, δ, U_∞ (U_∞-*U*)/u∗	2	2
Islam *et al.*, (2002)	Train of 4 mm ribs at the upper wall	PIV Water Channel	Center, downstream and upstream of the rib	0.2, 0.1	*h/k* = 6, 10	*u, v*, κ, L_R	U_{Bulk}	1400 - 50000	L_R/k	10, 20	10, 20
Becker *et al.* (2002)	Single roughness element	LDV	Several points around the roughness element	-		*U, w*	u_*, u_0	180 < Re_k < 740 k^+= 5.5 - 21	δ, θ, U_∞	-	-

LIF : Laser Induced Fluorescence

BL: Developing boundary layer

U_{Bulk} : Bulk velocity

h : Flow depth

L_R : Reattachment length

δ : Boundary layer thickness

$\alpha_k=2k/\lambda$

k : roughness height

PSP : Pitot static probe and a Pressure Gauge

U_∞: Free stream velocity

U_c: Centerline velocity

D : Hydraulic depth

λ : Wavelength

θ : Momentum thickness

λ_k : Vertical roughness density = λ/k (=2/α_k)

λ_s : Horizontal roughness density = λ/s (s=1 for dunes)

Table 1.2 Summary of experimental studies on flow over fixed dunes.

References	**Roughness Type**	**Technique**	**Meas. at**	α_k	***h* (m)**	**Measured Quantity**	**Reference velocity (m/s)**	**Re**	**Scaling parameter**	λ_s	λ_k
Raudkivi (1966)	Smooth dunes	Const temp. anemometry	Above and between the crests	0.17	0.126	*u, w, u′, v′,* pressure, shear stress	U_{Bulk} = 0.299	0.05/ν	-	1	11.765
Rifai & Smith (1971)	Smooth dunes		Above and between the crests	0.2	0.2796	*u*, *u*', pressure	U_{Bulk} = 0.576	0.06/ν	-	1	10.000
Shen *et al.* (1990)	Smooth dunes		Above and between the crests	0.3	0.221-0.323	*u*, pressure, shear stress	U_{Bulk} =0.147-0.534	0.032/ν-0.172/ν	-	1	6.667
Nelson, McLean, Wolfe (1993)	Smooth dunes	LDV	Several cross sections	0.49 - 1.5	0.04, 0.02	*u, w, u′w′*	U_{Bulk} =0.1, 0.25	0.100/ν - 0.052/ν	-	1	4.082-0.727
McLean, Wolfe, Nelson (1999)	Smooth dunes	Acoustic Profiler	Several cross sections	0.39-2.75	0.04 0.04 0.04	*u*	U_{Bulk}= 0.20-0.54	0.008/ν-0.027/ν	*Q, k*	1	5.128 -0.727
Mierlo & Ruiter (1988)	Smooth dunes	LDV	Several cross sections	0.32 0.44	0.08 0.08	*u*	U_{Bulk} = 0.44 0.55	0.352/ν 0.440/ν	-	1	6.349 4.515
Smith & Ettema (1995)	Smooth dunes	LDV	Several cross sections	0.30-0.44	0.17-0.23	*u, w, u′, w′*	U_{Bulk} = 0.33-0.48	0.077/ν, 0.086/ν	U_{Bulk}	1	16.16-23.52
Best (2005b)	Smooth dunes	PIV and field observations	Several locations	0.13	0.133	*u, w, u′, w′*	U_{Bulk} = 0.44 (at crest)	0.041/*v* (at crest)	U_{max}	1	15.75

CHAPTER 2
EXPERIMENTS

This chapter describes the laboratory experiments conducted to investigate the effect of roughness on the free-surface and the bulk flow characteristics in open-channel flows. To investigate the physics of the flow over dunes and ribs, detailed experiments and visualization of the turbulent structures were conducted.

The experiments entailed a series of flows covering a Reynolds number range of 1,000 to 50,000, aspect ratios of 6 to 24, and two “macro” roughness geometries, namely, ribs and two-dimensional dunes. Motivated by non-contact measurements, free-surface velocities and velocity distributions were measured remotely in the laboratory. Free-surface velocity distribution was measured using Large-Scale Particle Image Velocimetry (LSPIV), the only technique available for this purpose. Laser Doppler Velocimetry (LDV) was selected to measure the velocity profiles, due to its non-intrusive nature and accuracy.

Flow depths were selected such that the aspect ratio (AR) was larger than 5 in order to attain two-dimensional open-channel flow. Three different flow depths, namely, 6, 8, and 10 cm were obtained for each roughness case. For flow over smooth, flat bed, flow depth of 2.5 cm was also tested for different free-surface velocities to investigate the effects of Reynolds number and Froude number on the velocity distribution in shallow open-channel flow.

Three rib configurations and one representative dune geometry were used to simulate large-scale roughness. Flow measurements over a smooth bed were also conducted to obtain data.

2.1 Experimental Set-Up

2.1.1 Flume

The experiments were conducted in the 10 m long, 0.61 m wide and 0.5 m deep, glass sided, recirculating tilting flume (see Figure 2.1) of IIHR. The water is recirculated by a 7.5-horsepower variable speed, pump located beneath the flume. The flow is returned to the headbox of the flume via pipes.

To damp large scale turbulence and secondary currents, the entrance flow is conditioned by means of a honeycomb flow straightener, consisting of a stack of wiremesh, and a floating wood grid placed just downstream of the straightener. The water depth was adjusted using the control at the downstream end of the flume. The flume is supported by pivot and a jack so that the bed slope can be adjusted without interrupting the flow. Precisely leveled steel rails for the instrument carriage mounted atop the flume walls provide the reference frame for elevation relative to a plane tilted at the flume slope. The slope of the bed was measured by means of a dial gauge at the downstream end of the flume.

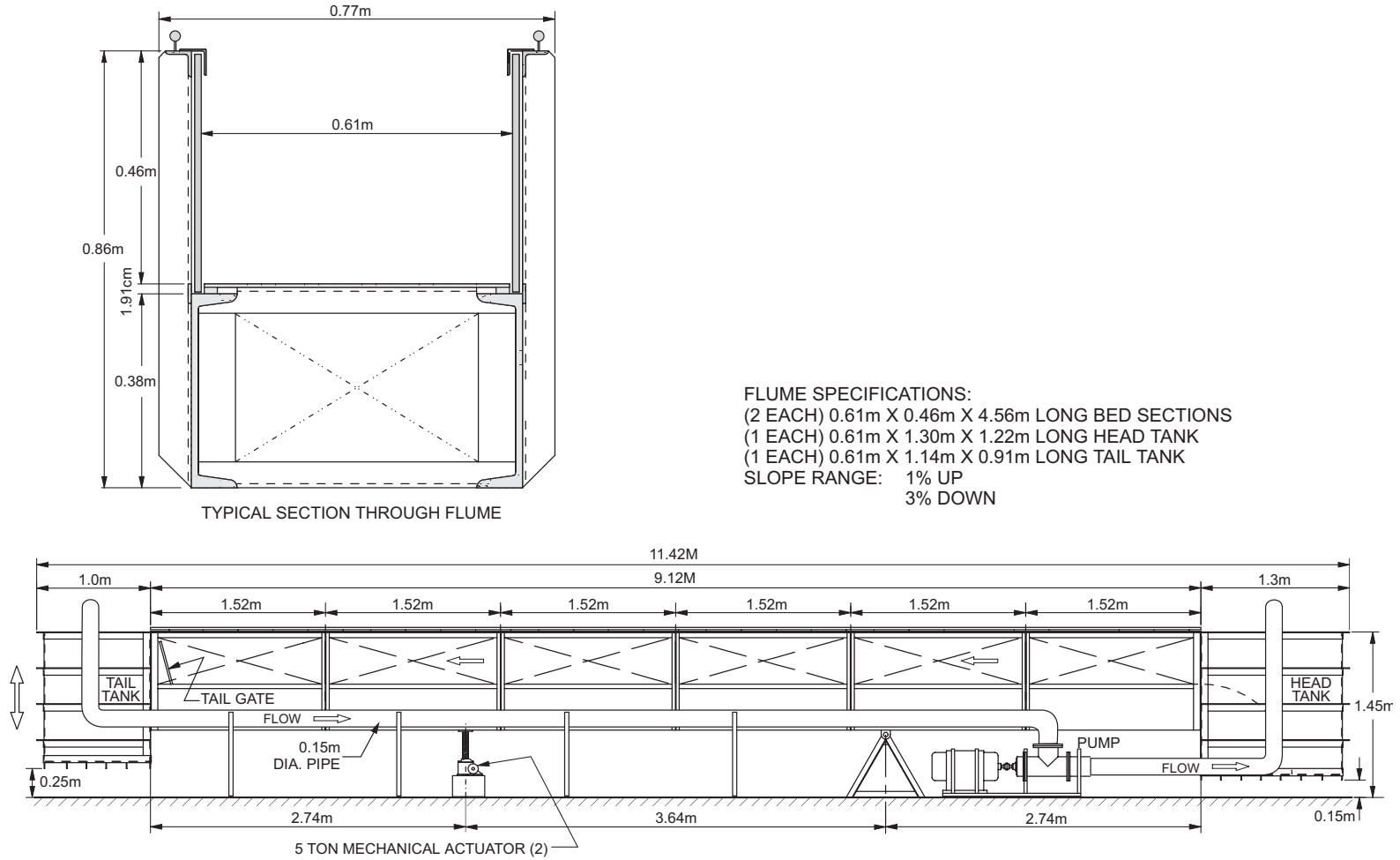

Figure 2.1 Open channel flume used in experiments.

2.1.2 Roughness Geometry

This study deals with two kinds of *k*-type roughness: two-dimensional, fixed dunes and ribs (also called square cavities or longitudinal bars). Dunes are very common bed-form structures in natural channels; they also form in engineered canals and pipelines. Rib roughness can be considered to represent two-dimensional gravels with square cross-section. The roughness geometries were selected by the help of earlier research listed in Tables 1.1 and 1.2. As mentioned in Chapter 1, d-type roughness is not considered, because it is reported to behave similar to the smooth wall and does not show the effect of individual roughness elements.

For flow over rib roughness, three different λ/k ratios were selected, namely, 4.5, 9, and 18. Square rib elements of 1 cm x 1 cm cross-section and 61 cm length in the spanwise direction were used. Three LDV measurement locations were selected; two at the top of two consecutive ribs, and one in between. Figure 2.2.a shows the cross-sectional view of the ribs and the LDV measurement locations, L1, L2 and L3.

As Bennett (1995 & 1997) reports, dunes most often form as a continuous train, and show remarkable similarity in wavelength and height. The presence of dunes on the bed significantly increases flow resistance, and their presence and growth play a major role in velocity distribution. As this study focuses on the velocity distribution and turbulence properties (and is not concerned with sediment transport and dune formation), dunes with fixed geometry were selected for the tests.

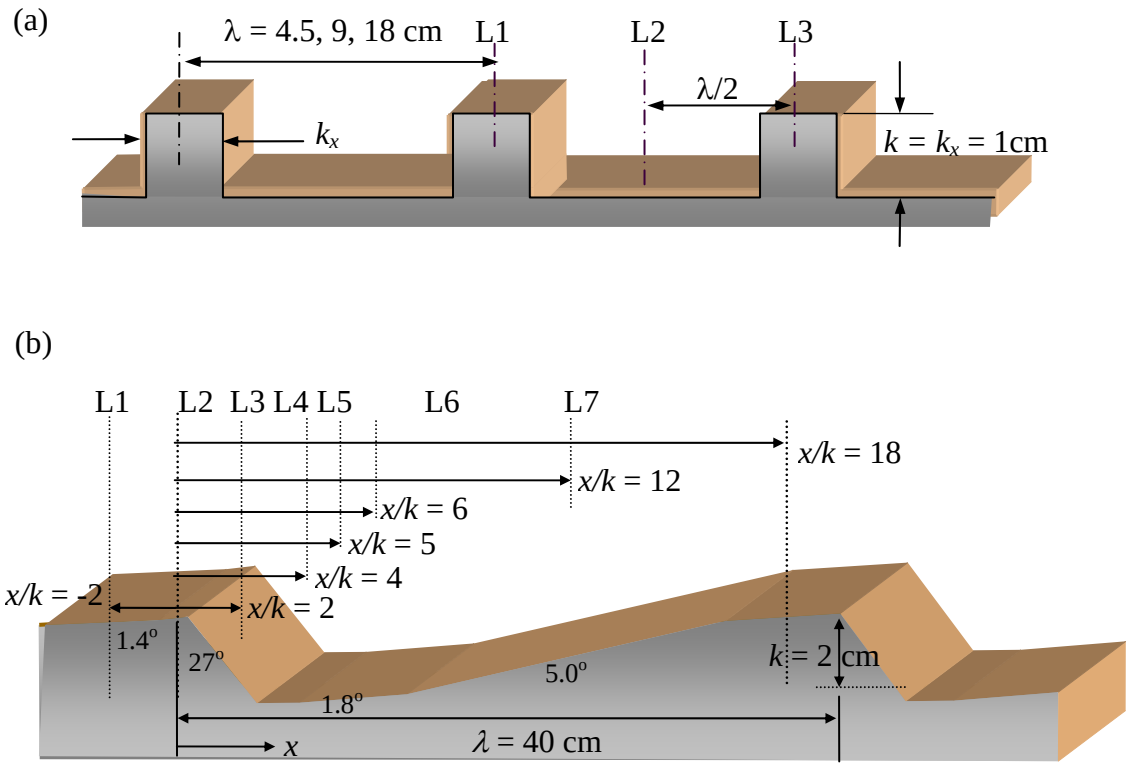

Figure 2.2 Roughness geometries for (a) ribs, and (b) two-dimensional dunes.

A train of 22 dunes of geometry shown in Figure 2.2.b was used. Dune geometry is identical with that used by van Mierlo & Ruiter (1988) and other previous studies to allow direct comparison. Seven LDV measurement locations were selected as indicated in Figure 2.2.b. LSPIV measurements were made over the whole dune wavelength (L1 – L7). For cases with roughened dunes, a wiremesh made of 1 mm – diameter wire with 5 mm openings was placed over the surface of the dunes. Another roughened dune type was obtained by gluing a layer of sand particles of 1.65 to 2 mm diameter over the dune surface.

2.2 Flow Conditions

The experiments were divided into three sets: as flow over (a) smooth flat bed, (b) rib roughness, and (c) two-dimensional dunes. The free-surface velocity was maintained at around 0.5 m/s.

2.2.1 Flow over Smooth Flat Bed

Measurements of the velocity and turbulence characteristics of the flow over a smooth, flat bed were used to provide reference for the flows over rough walls. The smooth bed experiments are divided into two groups: shallow open-channel flow (OCF) over a range of velocities, and OCF with a constant velocity over a range of flow depths. The hydraulic conditions for these cases are summarized in Table 2.1 and Table 2.2. The Froude and Reynolds numbers reported in the tables are based on flow depth, h, and bulk flow velocity, U_{Bulk}. AR stands for the aspect ratio (the ratio of channel width, h_y, to flow depth, h). S_0 represents the channel slope, and U_0 is the free-surface velocity.

Flow cases S01, S02, S03, and S04 were planned to investigate the effect of surface velocity on the flow characteristics. By using the upstream and downstream controls, the flow depth was fixed at 2.5 cm, while the free-surface velocity was changed. In the second series of smooth bed flows, the depth ranged from 6 cm to 10 cm. The flow conditions for cases with flow depth higher than 6 cm are given in Table 2.2. The analysis of the cases with flow depths higher than 10 cm showed strong 3D effects, and therefore omitted from the present analysis.

Table 2.1 Conditions for shallow flow over flat bed.

Code	*h (m)*	U_0 *(m/s)*	U_{Bulk} *(m/s)*	*Fr*	*Re*	*AR*	u_* *(m/s)*	S_0
S01	0.025	0.044	0.029	0.06	718.4	24.38	0.0050	2.81E-4
S02	0.025	0.106	0.085	0.17	2119.8	24.38	0.0073	6.81E-4
S03	0.025	0.205	0.173	0.35	4322.4	24.38	0.0100	4.32E-3
S04	0.025	0.384	0.336	0.68	8389.5	24.38	0.0174	8.58E-3

Table 2.2 Flow conditions for flat bed experiments with varying flow depth.

Code	*h (m)*	U_{LDV}	U_0 *(m/s)*	U_{Bulk} *(m/s)*	*Fr*	*Re*	*AR*	u_* *(m/s)*	S_0
S06	0.06	0.506	0.490	0.445	0.50	26700	10.16	0.0213	3.83E-04
S08	0.08	0.504	0.489	0.449	0.51	35920	7.62	0.0229	1.70E-04
S10	0.10	0.496	0.485	0.455	0.46	45500	6.10	0.0247	1.70E-04

2.2.2 Flow over Ribs

The conditions for the experiment of flow over ribs with wavelength (λ) of 4.5 cm, 9 cm, and 18 cm are summarized in Table 2.3, Table 2.4, and Table 2.5, respectively. The locations of the verticals where LDV measurements were taken are shown in Figure 2.2.a.

Table 2.3 Conditions for flow over rib roughness with λ = 0.045 m. Velocities, depths, shear velocities are reported for location L1 (roughness crest).

Code	*h (m)*	λ *(m)*	U_{LDV} *(m/s)*	U_0 *(m/s)*	U_{Bulk} *(m/s)*	*Fr*	*Re*	*AR*	u_* *(m/s)*	S_0
R01	0.055	0.045	0.474	0.46	0.370	0.50	20350	11.08	0.053	3.48E-3
R02	0.075	0.045	0.505	0.49	0.396	0.46	29723	8.13	0.051	3.27E-3
R03	0.095	0.045	0.503	0.49	0.406	0.42	38526	6.42	0.049	-

Table 2.4 Conditions for flow over rib roughness with λ = 0.09 m. Velocities, depths, shear velocities are reported for location L1 (roughness crest).

Code	*h (m)*	λ *(m)*	U_{LDV}	U_0 *(m/s)*	U_{Bulk} *(m/s)*	*Fr*	*Re*	*AR*	u_* *(m/s)*	S_0
R04	0.055	0.09	0.350	0.34	0.289	0.39	15915	11.08	0.050	2.49E-03
R05	0.075	0.09	0.447	0.43	0.376	0.44	28200	8.13	0.055	2.55E-03
R06	0.095	0.09	0.514	0.49	0.440	0.46	41800	6.42	0.059	2.61E-03

Table 2.5 Conditions for flow over rib roughness with λ = 0.18 m. Velocities, depths, shear velocities are reported for location L1 (roughness crest).

Code	*h (m)*	λ *(m)*	U_{LDV} *(m/s)*	U_0 *(m/s)*	U_{Bulk} *(m/s)*	*Fr*	*Re*	*AR*	u_* *(m/s)*
R07	0.055	0.18	0.359	0.35	0.307	0.42	16896	11.08	0.047
R08	0.075	0.18	0.434	0.42	0.364	0.42	27321	8.13	0.053
R09	0.095	0.18	0.512	0.49	0.434	0.45	41273	6.42	0.054

2.2.3 Flow over Dunes

The conditions for the test series with dunes are presented in Table 2.6 and Table 2.7. The locations of the verticals where the LDV measurements were obtained are shown in Figure 2.2.b. For the highest flow depth two additional experiment sets were conducted whereby dunes were further roughened with micro-roughness elements, namely, sand particles and a wire mesh.

Table 2.6 Conditions for flow over dunes. Values reported for location L1 (roughness crest).

Code	*h (m)*	U_{LDV} *(m/s)*	U_0 *(m/s)*	U_{Bulk} *(m/s)*	*Fr*	*Re*	*AR*	u_* *(m/s)*
D01	0.06	0.418	0.41	0.369	0.48	22140	10.2	0.0339
D02	0.08	0.467	0.44	0.394	0.44	31520	7.6	0.0323
D03	0.10	0.477	0.475	0.425	0.43	42500	6.1	0.0299

Table 2.7 Conditions for flows over dunes with superimposed sand particles and wiremesh. Values reported for location L1 (roughness crest).

Code	***h (m)***	U_{LDV} ***(m/s)***	U_0 ***(m/s)***	U_{Bulk} ***(m/s)***	***Fr***	***Re***	***AR***	u_* ***(m/s)***
Sand	0.10	0.505	0.48	0.436	0.44	43600	6.1	0.040
WM	0.10	0.525	0.515	0.466	0.47	46600	6.1	0.036

2.3 Experimental Procedures

The main objective of the experiments is to obtain detailed velocity profiles for representative locations over the roughness elements, including the velocity at the free-surface. Velocities throughout the water column, including the free-surface were obtained by combining LDV and LSPIV in an arrangement illustrated in Figure 2.3. LDV measures velocities in the column of water (in a vertical), while LSPIV measures free-surface velocities. It is worth noting that that there is no alternative instrument to measure free-surface velocity. The two non-intrusive measurement techniques are able to document instantaneous and mean flow characteristics at the free-surface and in the water column with high temporal and spatial resolutions. The details of LSPIV experiments and free-surface visualizations will be discussed in the next sections.

The experiments were conducted according to the following protocol:

1. Set up of the flow conditions. Uniform flow was obtained iteratively for the targeted depth and velocity. Starting from rough settings for S_0, h and U_0, the channel slope was adjusted by changing the height of the downstream pivot of the flume. The flow depth was adjusted by adding or removing water from the channel, and surface velocity was controlled by decreasing or increasing the circulating-pump setting.

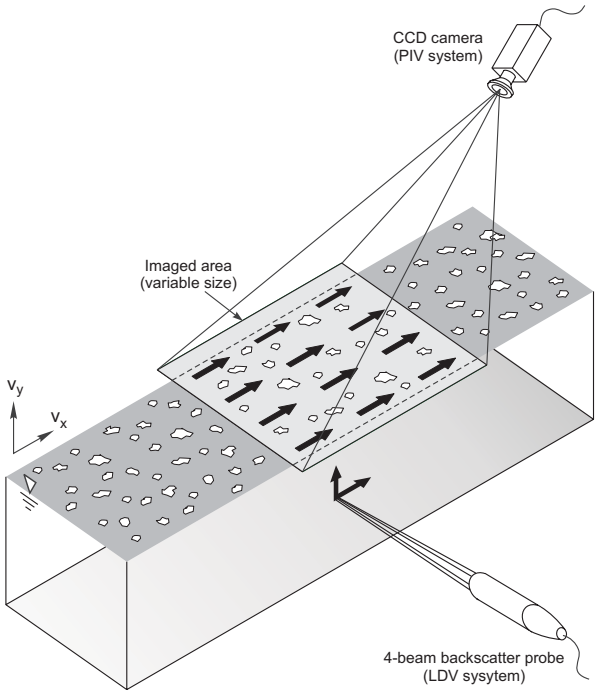

Figure 2.3. Experimental arrangement for LDV and LSPIV.

2. LDV measurements. After the uniform flow conditions were achieved, water was seeded with Titanium Oxide particles until the optimum data rate for the LDV system was attained. For flow over roughness, LDV measurements above the crest of two consecutive roughness elements were obtained to check the flow uniformity. The purpose of the LDV measurements was to obtain mean flow and turbulence characteristic over the flow depth.
3. Surface texture recordings. Recordings of the free-surface appearance were made with a CCD digital video camera placed above the channel. The purpose of these measurements was to capture the free-surface texture concurrently with the

velocity information to identify the effect of roughness and aspect ratio on the free-surface characteristics.

4. LSPIV measurements. The free-surface of the flow was seeded with styropor (which has smaller density than the water) particles. Flow surface was illuminated from the sides with halogen lamps. Recordings were taken using a digital video camera fixed above the channel. The purpose of these measurements was to obtain the flow distribution and velocity magnitude at the free-surface.

2.3.1 LSPIV

LSPIV is an extension of conventional PIV for free-surface velocity measurements over large areas (Fujita *et al.*, 1998). While the image- and data-processing algorithms are similar to those used in conventional PIV, adjustments are required for seeding, illumination and recording, and pre-processing of the recorded images.

2.3.1.1 Seeding

Free-surface measurements are the focus of this research. The free-surface movement captured by the imaging devices is possible through the addition of illumination and small particles conveyed by the free-surface. Therefore, the capability of the tracing particles to follow the movement of the free-surface is critical.

There are several possible sources of errors in seeding the free-surface flow. One major error source in the experiments is caused by seeding due to the fact that particles floating on the free-surface are entrained by the drag force acting on their submerged volumes (hence, they will accurately follow the flow when their submergence is large), and that polystyrene particles develop electrostatic forces that produce additional particle movement until they form stable clusters.

Other potential sources can be induced by the steps involved in the conduct of LSPIV measurements, image processing, and post-processing. Overall, the velocity estimated by LSPIV, U_{LSPIV}, can be written as:

$$\left\{\begin{array}{c}\text{Measured velocity} \\ (U_{LSPIV})\end{array}\right\} = \left\{\begin{array}{c}\text{Actual free-surface velocity, } U_0\end{array}\right\} + \left\{\begin{array}{c}\text{Effect of other forces on seeding particles, } \varepsilon_F\end{array}\right\} + \left\{\begin{array}{c}\text{Measurement and data reduction errors, } \varepsilon_M\end{array}\right\}$$

$$U_{LSPIV} = U_0 + \varepsilon_F + \varepsilon_M \qquad (2.1)$$

The error caused by seeding material not exactly following the flow creates a bias error. The seeding material used in LSPIV experiments for tracing the free-surface was Styropor® expandable polystyrene (by BASF) with a bulk density of 12.5 kg/m^3 and diameters in the 2 to 3 mm range. For the error analysis two other seeding materials, paper confetti and black polypropylene beads were also tested. The analysis of effect of seeding material on the LSPIV measurements, and the uncertainty analysis are presented in Appendix B. Figure 2.4.a is a sample recording obtained in the flume to measure the free-surface velocity using LSPIV method with white polystyrene particles.

"Seeding" might occur naturally in rivers as a result of large-scale turbulent structures (boils) breaking up at the free-surface, debris transported during high flows, and foam patches traveling with the flow. The later "natural" seeding is shown in Figure 2.4.b, where an year-round phenomenon observed on Iowa River free-surface, downstream of the Burlington spillway in Iowa City is shown. The spillway entrains air into the flow loaded with decomposed organic matter continuously producing foam on the free-surface. This natural occurrence creates patches of foam on the free-surface that are much alike the seeding used in LSPIV experiments of the present study.

(a)

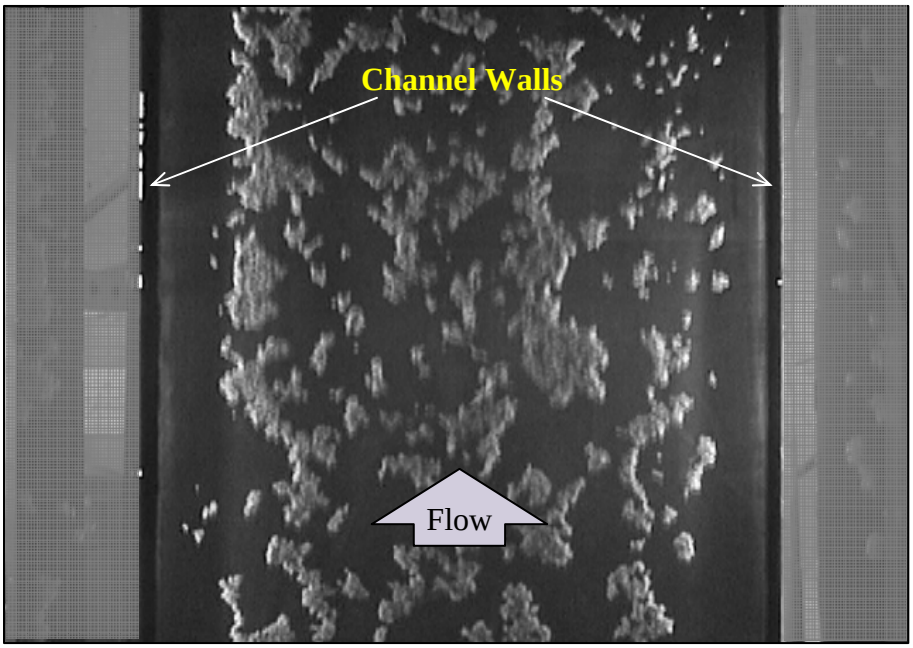

(b)

Figure 2.4 Photographs of the free surface of (a) LSPIV experiments with seeding material, and (b) Iowa River in February 2004 showing lathering surfactants.

2.3.1.2 Illumination and Recording

A digital camera (Sony DCR-TRV320) was used for recording the free-surface flow. Two quartz-halogen photographic lamps with diffusers were used to illuminate the test area. As shown in Figure 2.5, the transparent walls of the channel were covered with black boards to create a 2 cm longitudinal opening on the sides of the channel in the vicinity of the water surface plane. Proceeding in this way, only the water surface was illuminated and high contrast was obtained. The camera was positioned perpendicular to the flow at a distance of 1.5 m from the free-surface. The images covered an area of roughly 1 m by 0.7 m (see Figure 2.4.a). A grid overlaid near the free-surface was used to scale the images from camera to real-world coordinates. Examination of the grid recordings revealed that the images were not distorted by the camera optics so that there was no need for image reconstruction due to perspective or optical distortion.

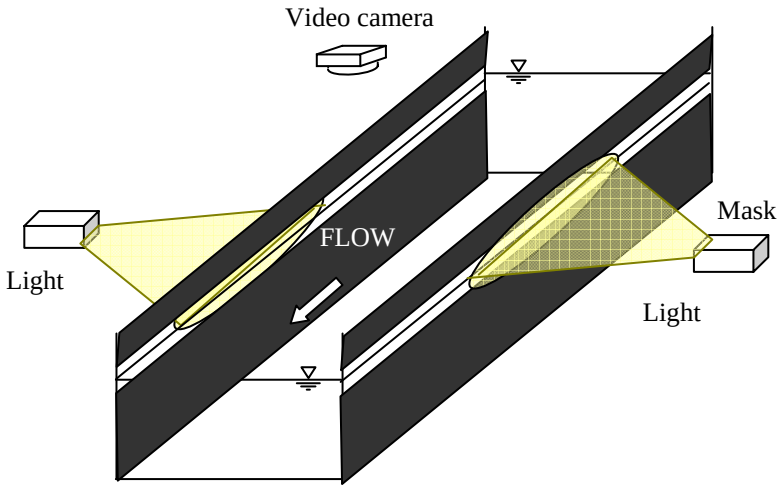

Figure 2.5 LSPIV system.

2.3.1.3 Image Processing

The image processing algorithm EdPIV® developed by Gui & Merzkirch (2000) was employed to obtain the velocity vectors. EdPIV uses single-exposed multiple frames, as opposed to the multi-exposure single frame procedure, where several exposures can superpose on the same frame (Raffel, 1997). This approach is a straightforward application of PIV concepts to video-based recording systems that successively record single image processing video frames. The image processing algorithm belongs to the so-called pattern matching approach that performs correlation on the gray-level values contained in small regions of the imaged area, called interrogation areas. EdPIV processing procedures also entail image correction, boundary mask, background removing, error detection, and error correction options.

Figure 2.6 illustrates an image pair of two successive video frames separated by a time interval, *dt*. The interrogation area (IA) in the figure is selected by considering the size of the foam pattern tracing the flow. The search area (SA) defines the area that is searched for possible displacements in the image pair. The arrow from point a_{ij} to point b_{ij} represents the identified displacement.

The correlation algorithm includes several PIV evaluation techniques, such as central difference interrogation, continuous window shifting, and image pattern correction. In essence, the algorithm finds the correlation between the image pattern enclosed in the interrogation area centered on a point a_{ij} in the image recorded at time *t*, and the IA centered at point b_{ij} in the image recorded at time $t+dt$, as illustrated in Figure 2.6. The correlation coefficient $R(a_{ij}, b_{ij})$ is a similarity index for the groups of pixels

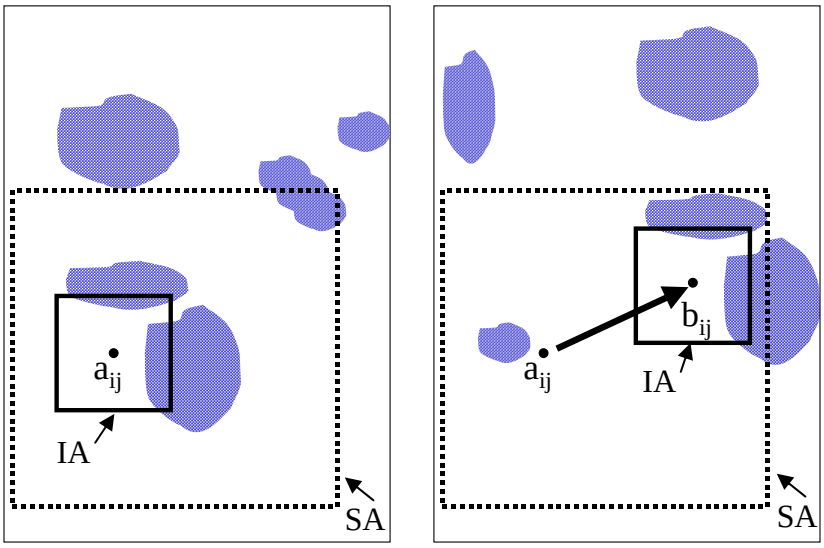

Figure 2.6. Sketch illustration of the algorithm used to identify the flow tracer displacement used in LSPIV.

contained in the two compared IAs. Correlation coefficients for a given a_{ij} are only computed for points b_{ij} within a search area defined around the point a_{ij}.

The size and the shape of the SA are chosen on the basis of a priori knowledge of the flow field, such as the direction and magnitude of the mean flow in order to reduce the computational time. The most probable displacement of the fluid from point a_{ij} during the period *dt* corresponds to the maximum correlation coefficient $R(a_{ij}, b_{ij})$. A parabolic interpolation is used to determine the displacement with sub-pixel accuracy. Fujita *et al.* (1998) show that particle-image displacements of about 0.2 pixels can be captured using this parabolic fitting when displacement gradients are relatively small.

When several successive frames are available, as it is in the present cases (1,000 to 2,000), the most probable displacement is assessed using the maximum average coefficient of correlation computed over the complete sequence of images. Velocity

vectors are derived from these displacements by dividing them by *dt*, the time between successive frames. The final vector field density is dependent on the choice of selection of the pitch step, which defines the computational grid for the analyzed imaged area. Given the statistical approach used to determine the displacements and the imperfections of the recorded images, it is possible to obtain spurious velocity vectors. Numerous post-processing routines are available to detect such vectors (see Raffel *et al.*, 1998). In the present case, post-processing consisted simply of interpolating linearly the missing grid points along current lines.

2.3.2 LDV

LDV was used to measure the velocities in the water column. LDV measurements were conducted with a two-component fiber optic LDV system of conventional design. A schematic of the LDV setup is shown in Figure 2.7. Principles of operation of the instrument and post processing have been documented in detail by the earlier publications, and will not be repeated herein (Hyun *et al.*, 2003b; Liou *et al.*, 1993; Nezu & Rodi, 1986). A two-component, two-color, fiberoptic-based LDV system (TSI 900-3) was used in the experiments. The system comprises of L-70-2 two-watt Argon-Ion Laser, the two-component fiberoptic Colorburst™ transmitting optics, Colorlink™ receiving optics, IFA 655 signal processor (burst correlator), and FIND™ interfacing and data analysis software. Two instantaneous velocity components (streamwise and vertical) were measured with the LDV system. At each measurement point, 15,000 samples were collected, and the standard TSI software was used to determine the mean and turbulence statistics.

(a)

(b)

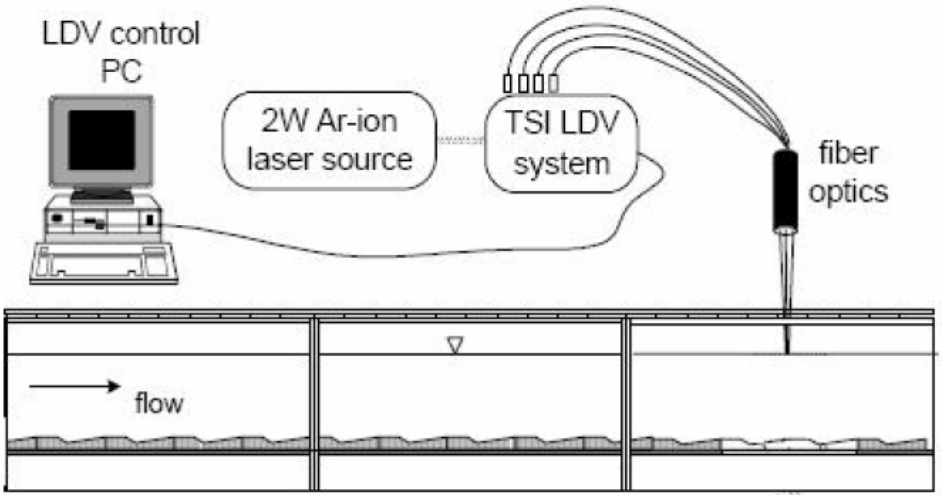

Figure 2.7 (a) Photograph, and (b) schematic of the LDV setup (Hyun *et al.*, 2003b).

2.4 Characterization of Free-Surface Texture

The purpose of the free-surface texture measurements was to quantitatively and qualitatively characterize the free-surface appearance. It was expected that by

characterizing the free-surface texture, additional information related to the effect of roughness and aspect ratio on the free-surface could be obtained.

One major difficulty in these experiments was to select an appropriate viewing angle of the free-surface, as changes in camera position and illumination conditions dramatically change the appearance of the free-surface recordings.

Figure 2.8, Figure 2.10, and Figure 2.12 illustrate the changes of surface texture with illumination setting. The illumination condition and position of the camera are presented in the accompanying figures in Figure 2.9, Figure 2.11, and Figure 2.13, respectively. It can be observed that by changing the orientation of the lights different sized structures are emphasized. Figure 2.8 shows a sample free-surface recording obtained under illumination conditions given in Figure 2.9. Figure 2.10 shows the state of the free-surface, illuminated from the sides of the channel through a 1-cm slit at the black masks covering the channel walls. The images are zoomed at the central part of the channel. As it is seen from the figure, a more stressed waviness is observed for larger depths.

Even though Figure 2.8 and Figure 2.10 give valuable information about the surface structures, a different view of the free-surface is selected to obtain a quantitative description of the surface waviness. The illumination conditions of Figure 2.12 were selected to be applied to the other flow cases for comparison purposes. Obtained video recordings of the free-surface waves are further analyzed in Chapters 4 and 5 in order to convert these qualitative observations into quantitative characterizations.

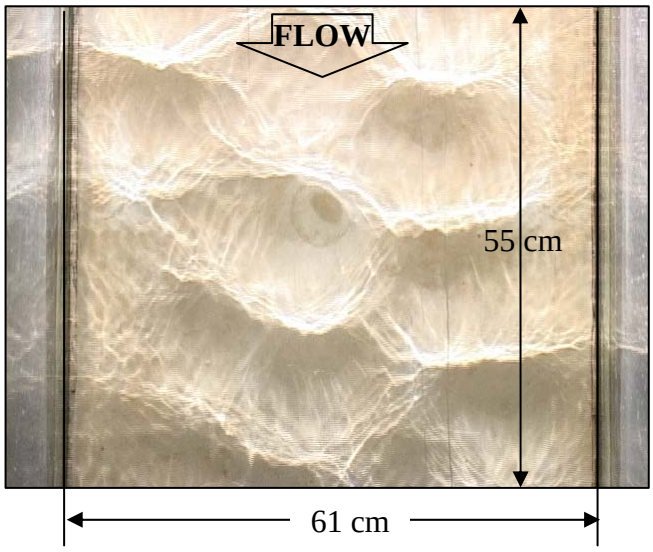

Figure 2.8 Free-surface texture for flow over smooth flat bed with flow depth of 8 cm with illumination from upstream and downstream. Camera is looking straight down.

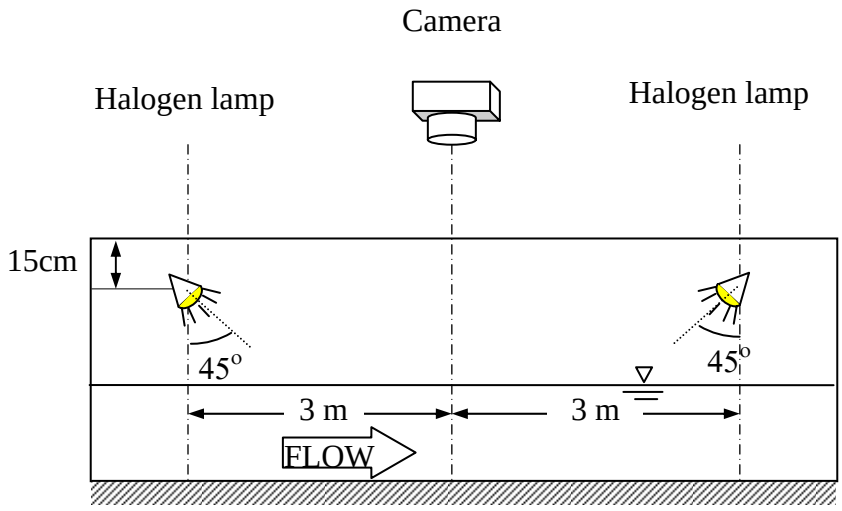

Figure 2.9 Illumination setting used during the recording of image in Figure 2.8.

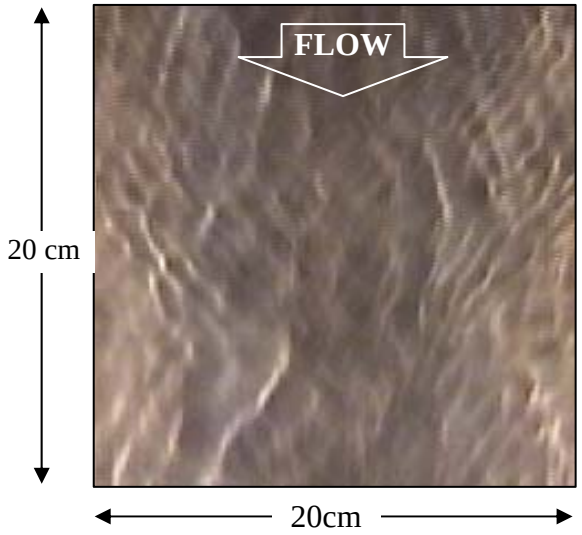

Figure 2.10 Free-surface texture for over smooth flat bed with flow depth of 8 cm with illumination from sides of the channel. Camera is looking straight down.

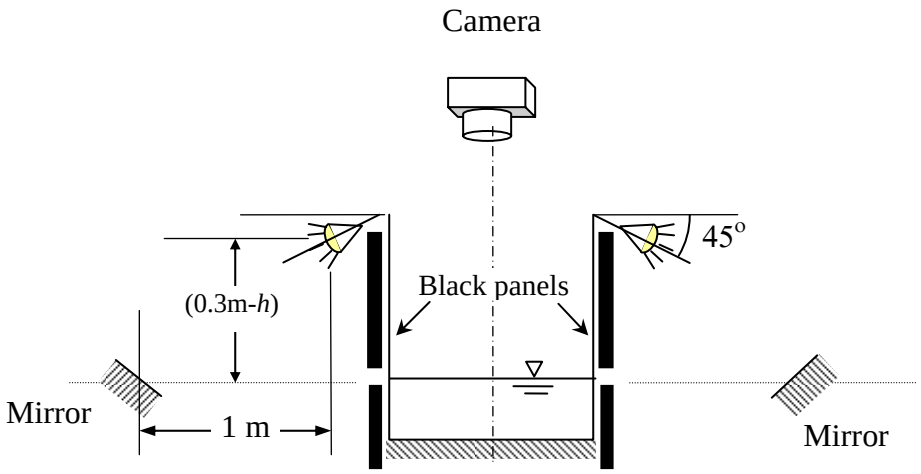

Figure 2.11 Illumination setting used during the recording of image in Figure 2.10.

Figure 2.12 Free-surface texture for flow over smooth flat bed with flow depth of 8 cm with illumination from upstream. Camera was placed downstream of the channel with 30^{o}-angle from horizontal.

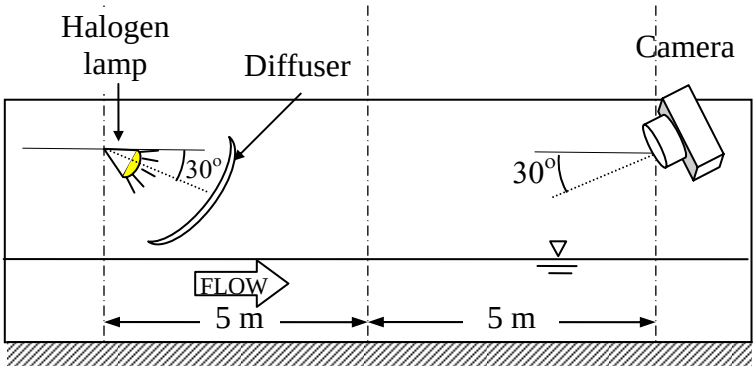

Figure 2.13 Illumination setting used during the recording of image in Figure 2.12.

CHAPTER 3
LARGE-EDDY SIMULATIONS

3.1 Description of the Code

The LES code MGLET originally developed at the Institute for Fluid Mechanics at Technical University of Munich (Tremblay & Friedrich, 2001) was used to perform the Large Eddy Simulations. The code was provided by the Institute for Hydromechanics of the University of Karlsruhe for this study. The code solves the filtered Navier-Stokes equations discretized with the finite volume method, and is based on a staggered Cartesian grid. Convective and diffusive fluxes are approximated with central differences of second-order accuracy and time advancement is achieved by a second-order, explicit Adams-Bashford scheme. The Poisson equation for coupling the pressure to the velocity field is solved iteratively with the Strongly Implicit Procedure (SIP) of Stone (1968). The subgrid-scale stresses appearing in the filtered Navier-Stokes equations are computed using the dynamic approach of Germano *et al.* (1991). The no-slip boundary condition is applied on the surface of the dune and the ribs, and the immersed boundary method is employed. This method is a combination of applying body forces in order to block the cells that are fully inside the dune geometry, and a Lagrangian interpolation scheme of third order accuracy, which is used for the cells that are intersected by the roughness surface to maintain the no-slip condition. Further details of the LES model can be found in Manhart *et al.* (2001), and Tremblay & Friedrich (2001).

3.2 Turbulence Model

Large-eddy simulation employs a spatial filter to separate the small scales from the large scales. The large eddies are explicitly calculated, while the effect of the smaller eddies are modelled. The application of this filter (denoted by an overbar) to the incompressible Navier-Stokes and continuity equations results in

$$\frac{\partial \overline{u}_i}{\partial t} + \frac{\partial \overline{u_i u_j}}{\partial x_j} = -\frac{1}{\rho}\frac{\partial \overline{p}}{\partial x_i} + \nu \frac{\partial^2 \overline{u}_i}{\partial x_j \partial x_j}, \qquad \frac{\partial \overline{u}_i}{\partial x_i} = 0 \tag{3.1}$$

where $\overline{u}_i$ denotes the filtered velocity field, $\overline{p}$ is the filtered pressure, and Einstein summation notation is used (Pope, 2000). The filtered product of the velocities $\overline{u_i u_j}$ appearing in the advection term creates a closure problem for the equations because the unfiltered velocity field u_i is unknown. Bringing this term to the right-hand side and rearranging, LES equations are obtained as

$$\frac{\partial \overline{u}_i}{\partial t} + \frac{\partial \overline{u}_i \overline{u}_j}{\partial x_j} = -\frac{1}{\rho}\frac{\partial \overline{p}}{\partial x_i} + \nu \frac{\partial^2 \overline{u}_i}{\partial x_j \partial x_j} - \frac{\partial \tau_{ij}}{\partial x_j} \tag{3.2}$$

where the effect of the small scales appears through a subgrid scale (SGS) stress term, $\tau_{ij} = \overline{u_i u_j} - \overline{u}_i \overline{u}_j$. This term must be parameterized as a function of the filtered velocity $\overline{u}_i$ to close the equations. A popular SGS modelling was proposed by Smagorinsky (1963), which is in the form of

$$\tau_{ij} = -2\nu_T \overline{S}_{ij} + \frac{1}{3}\tau_{kk}\delta_{ij} \tag{3.3}$$

where $\overline{S}_{ij}$ is the filtered strain rate and ν_T is the eddy viscosity, which is defined as $\nu_T = C_s \Delta^2 \left|\overline{S}\right|$, where Δ is the filter width. Germano *et al.* (1991) proposed a method to adjust the constant C_s in time and space. The subfilter-scale motions are responsible for energy dissipation, and it is crucial that the subfilter-scale stress representation perform

well so that the resolved quantities are predicted accurately. SGS modelling has been the subject of extensive studies in turbulence research. The difficulty in formulating a closure model for LES is that modelling of the unresolved motions must be based only on knowledge of the resolved motions. There has been much success using subfilter-scale models for LES in numerous laboratory and real-scale problems, and improvements in model performance can be expected due to increased computing speed (which allows finer grid resolution). The performance of dynamic models over a rough wall has been studied earlier by Cui (2000), Yue *et al.* (2003), Chow (2004) and Stoesser *et al. (*2005).

3.3 Description of the Simulated Flow

Open channel flow and flow in closed channels have very similar flow and turbulence characteristics except the region very close to the free surface (Nakayama & Yokojima, 2001). An open-channel flow can be regarded half of a closed channel taking the symmetry line as the free-surface. Because of this the mean velocity profiles of open and closed channel flow are similar when plotted from channel wall to symmetry line. However, the profiles of the turbulence fluctuations differ close to the surface due to the damping of the fluctuations in the vertical direction at the surface into the fluctuation parallel to the free-surface. Another important difference is that in open channel hydraulics the driving force is the gravity and the channel slope, S_0. In a horizontal closed channel the driving mechanism is the pressure difference between inlet and outlet. Numerical simulations of the open-channel flows have taken advantage of these similarities by using a horizontal bed with a pressure difference as the driving force.

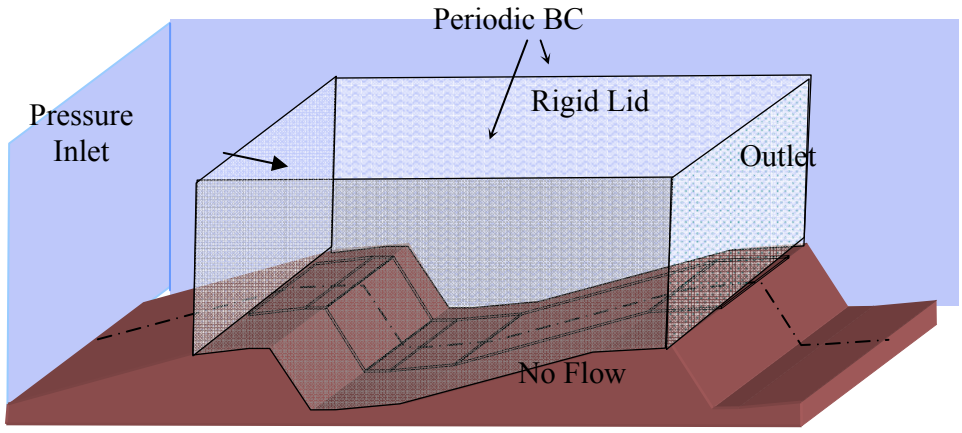

Figure 3.1 Boundary Conditions.

3.4 Boundary Conditions

The boundary conditions in open-channel flow simulations of the present study are shown in Figure 3.1. The water surface was represented by a symmetry condition that does not allow deformations in the vertical direction, and sets velocity gradients parallel to the surface to zero. By balancing the pressure gradient and the static pressure distribution, the influence of water waves at the surface was neglected. LES calculations of Patel & Lin (2004) and Yue *et al.* (2003) using a level set method to model the free surface deformation state that the waves on the free-surface have small effects on the flow except in the streamwise turbulence intensities. The upstream and downstream conditions were simulated as pressure inlet and outlet.

Periodic boundary conditions are used in order to overcome the difficulty of supplying time dependent boundary conditions at the inlet and outlet of the computational domain. To obtain periodic boundary condition for the pressure field the pressure is split

into the periodic and the non-periodic part, p_b, that varies linearly in x direction. The periodic part corresponds to the pressure distribution in the domain after subtracting the linear term that balances the friction losses ($f_x = -(1/\rho)(\partial p_b/\partial x)$) as driving force.

In wall bounded flows the boundary layer region has a strong influence on the whole flow field by producing turbulence and friction effects. This region scales with the viscous length which is small compared to outer flow scale. Thus resolution close to the wall needs to be higher than the outer flow if no further modeling is used. The shear stress or friction is then calculated as

$$\tau_w = \rho\nu\left(\frac{\partial u}{\partial z}\right)_{z=0} \tag{3.4}$$

This formula can only be used when a mesh size of same order of magnitude of the viscous length is used.

3.5 Computational Domain

For simulation of the flow over the dunes, the computational domain spanned one dune length, λ, in the streamwise, *1.5h*-*2h* in spanwise and *1h* in vertical directions as sketched in Figure 3.2. For rib roughness the domain length is taken as 2λ to 4λ due to the smaller roughness wavelength. The number of grid points was slightly different for each flow case. Typically, a grid consisted of 500 x 80 x 120 grid points in streamwise, spanwise, vertical directions, respectively. The grid spacing in terms of wall units were $\Delta x^+ \approx 30$ in streamwise direction, $\Delta y^+ \approx 45$ in spanwise direction and 5 for Δz^+ near the roughness surface. The grid configuration for the flow over dunes with 8 cm flow depth (D02), and 4.5 cm-wavelength ribs with flow depth of 8.5 cm (R02) are shown in Figure 3.3, and Figure 3.4.

The dimension of the computational domain in spanwise direction, h_y, has an affect on the generation and the size of coherent structures. To represent the turbulent structures of the open-channel flow accurately, h_y has to be larger than the flow depth; smaller length scale in spanwise direction introduces error (Fröhlich *et al.,* 2005). Computations with different grids sizes in Fröhlich *et al.* (2005) reveals this error to be from a minor importance compared to the sensitivity of near wall and spanwise resolution and reports that reducing the spanwise domain tend to "squeeze" only the largest scales.

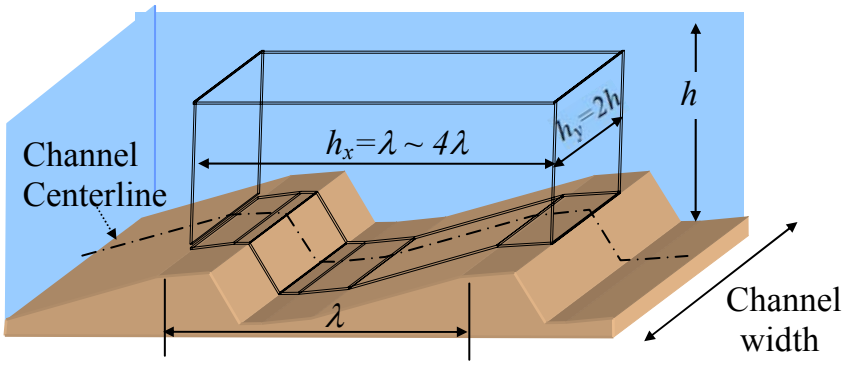

Figure 3.2 Computational domain for flow over dune cases.

(a)

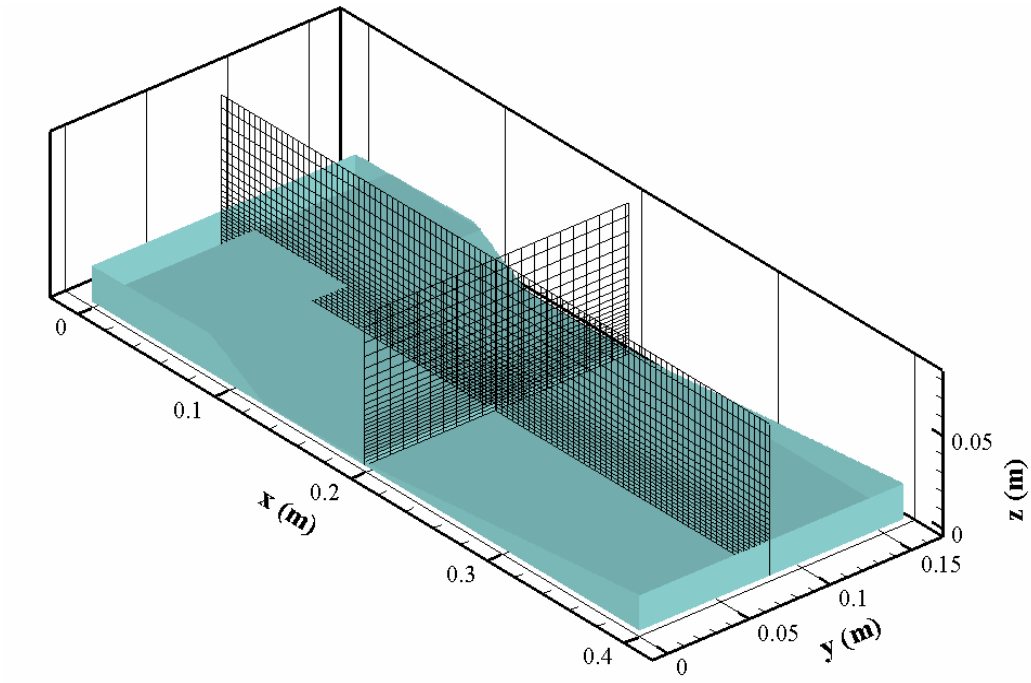

(b)

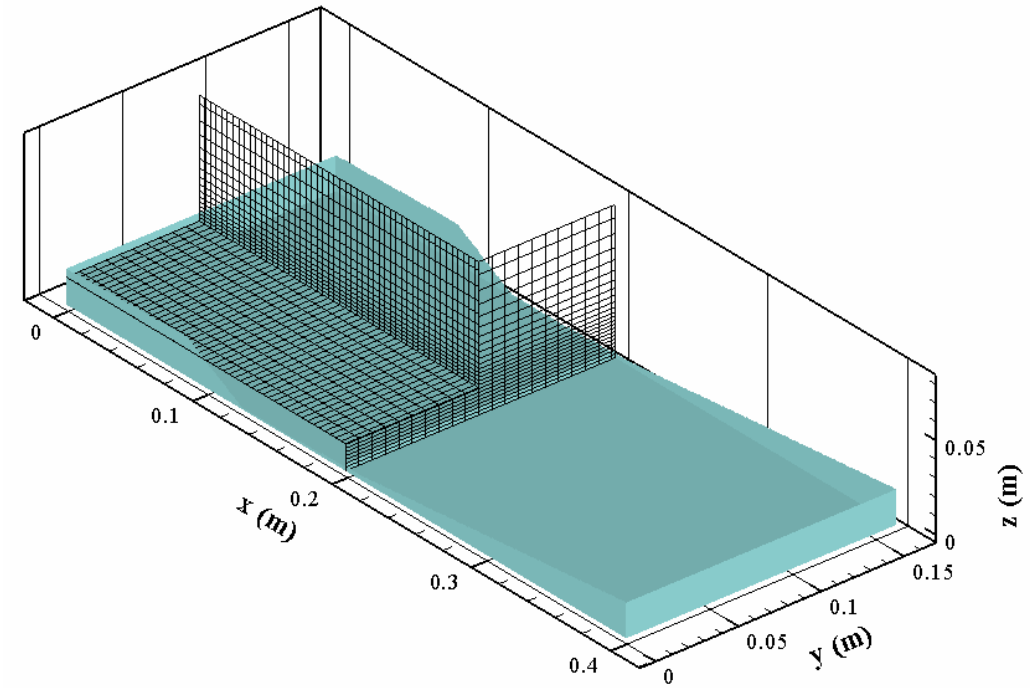

Figure 3.3 (a) Vertical and (b) cross-sectional view of the mesh used in simulations of flow over dunes with flow depth of 8 cm (D02). Every fourth line is plotted.

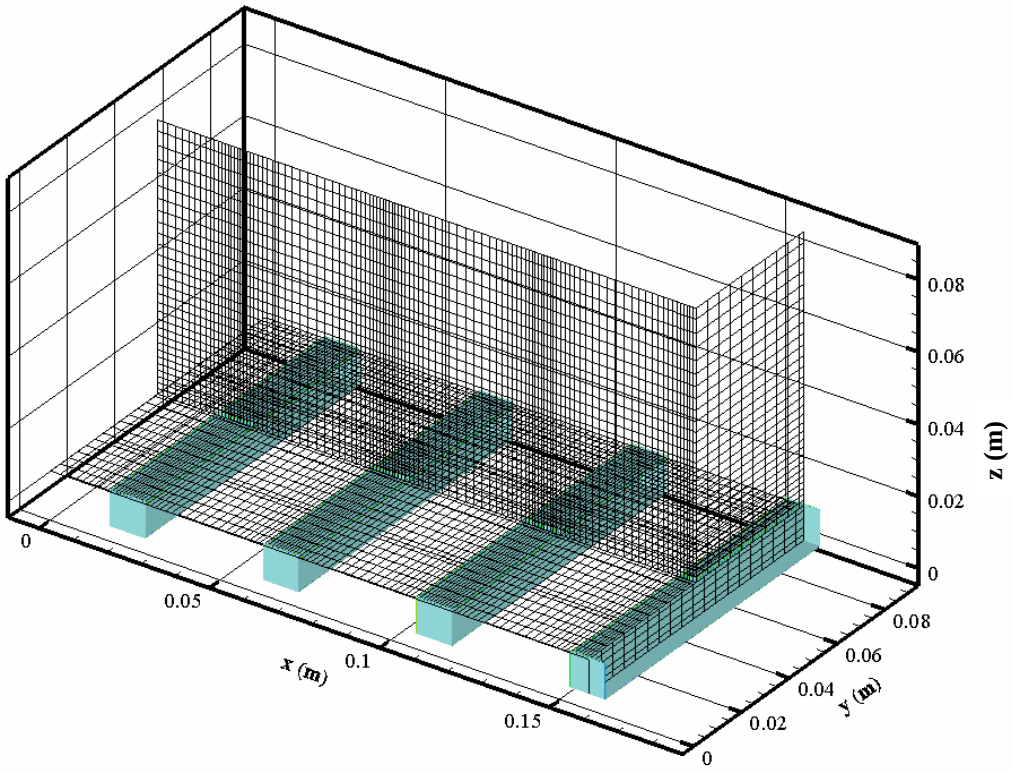

Figure 3.4 A cross-sectional view of the mesh used in simulations of flow over rib roughness with λ = 4.5 cm and h = 8.5 cm (R02). Every fourth line is plotted.

3.5.1 Roughness Geometries

The roughness geometries used in the simulations were identical to those used in the experiments. Rib roughness of 1 cm x 1 cm cross-section, spanning the computational domain was used (see Figure 3.5). Two roughness wavelengths of the ribs were selected to be 4.5 cm and 9 cm. To simulate the flow over two-dimensional dunes, the same geometry as in the experiments, 2 cm height and 40 cm wavelength, were used (Figure 3.6).

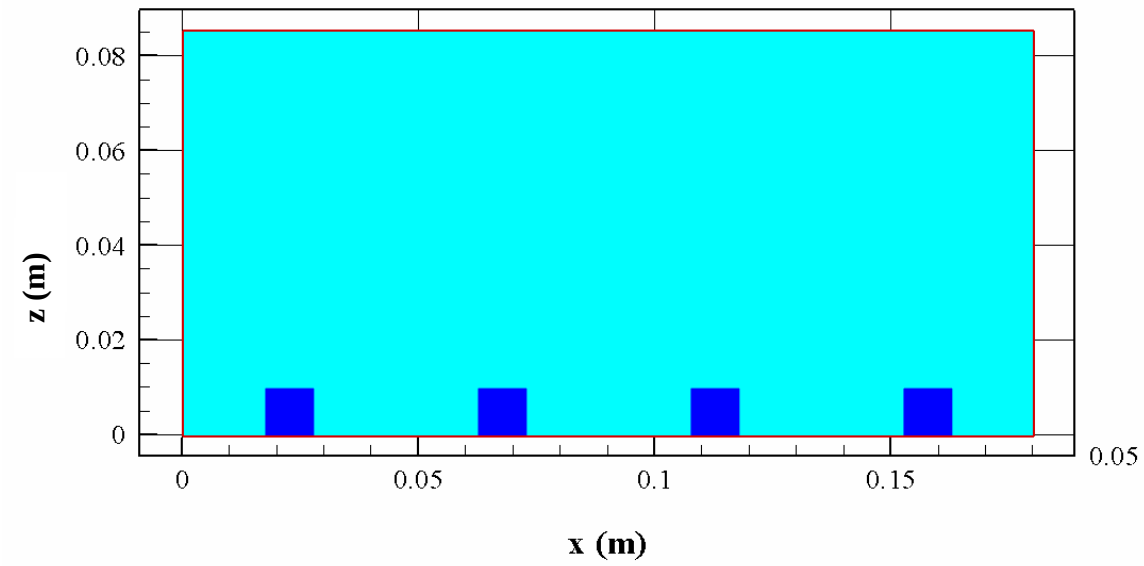

Figure 3.5 Roughness geometry and computational domain for flow over rib roughness with $\lambda = 4.5$ cm and $h = 8.5$ cm (R02).

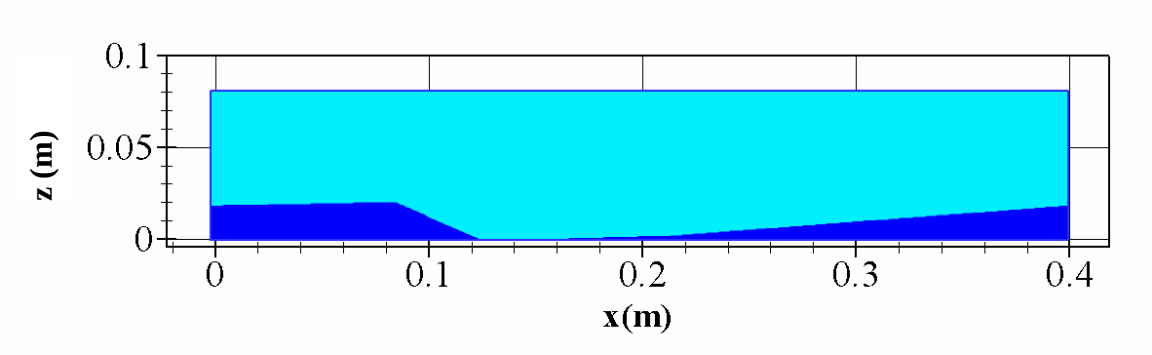

Figure 3.6 Roughness geometry and computational domain for flow over dunes with flow depth of 8 cm (D02).

3.6 Validation

In order to validate the results of the Large Eddy Simulations, streamwise components of the time averaged velocity are compared with the experimental data. Figure 3.7 shows the comparison of LES to the experimental data at the six measurement verticals. The length of the recirculation zone seems to be correctly calculated (see locations x/k = 6, x/k = 12) as well the developing boundary layer (location x/k = 12) although the length of recirculation seems slightly under predicted (see locations x/k = 4, x/k = 5). Comparison of turbulence intensities for streamwise velocity component is shown in Figure 3.8. The overall prediction of the mean velocity and turbulence intensities can be said to be satisfactory and in a very good agreement with the observed data.

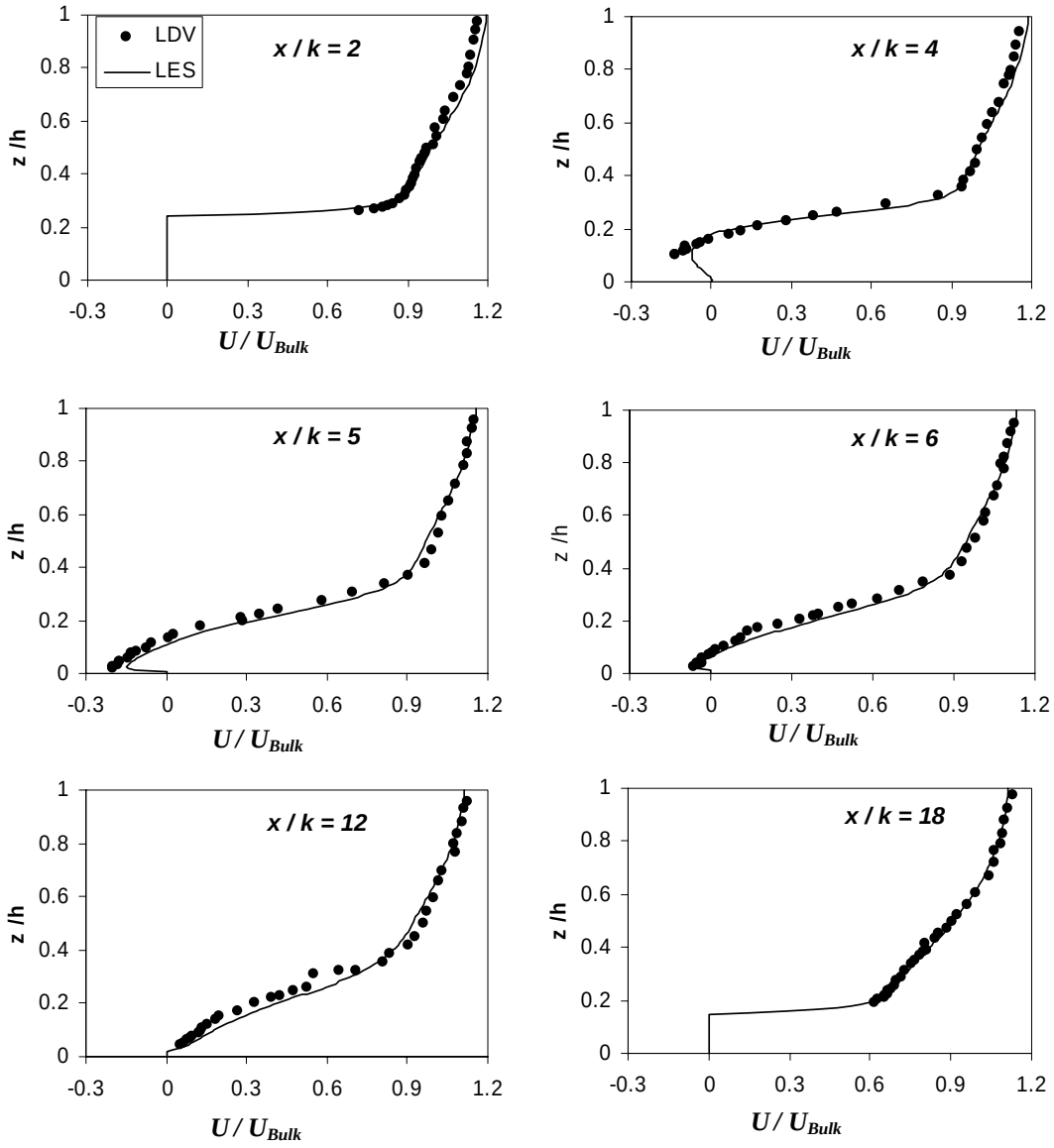

Figure 3.7 Comparison of time-averaged streamwise velocities for L1 –L6 for flow over dune with flow depth of 8 cm (D02).

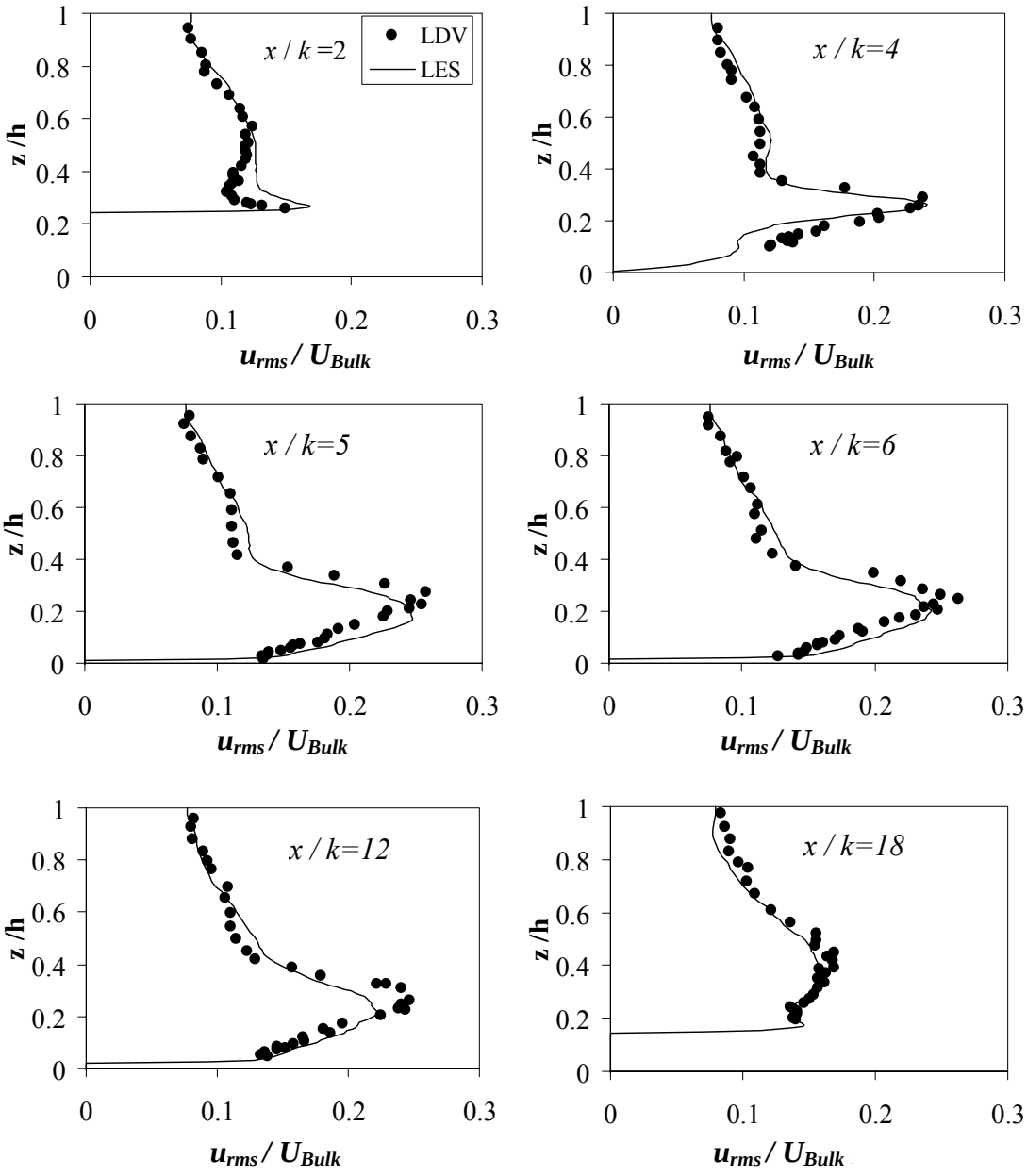

Figure 3.8 Comparison of time-averaged u_{rms} for L1 – L6 for flow over dune with flow depth of 8 cm (D02).

CHAPTER 4
METHODS OF DATA ANALYSIS

4.1 Introduction

This chapter presents the analysis procedures used for processing the experimental and numerical data obtained from methods described in Chapters 2 and 3. The main goal of the measurements, simulations and data analysis was to capture the characteristics of open-channel flows over *k*-type roughness illustrated in Figure 4.1.a and Figure 4.1.b. This roughness type is common in alluvial channel flows where the channel bed is covered by gravel or bed forms.

The analysis of the experimental and numerical results is aimed at describing both the detailed features of the flow over large-scale roughness (such as streamline pattern, flow acceleration, separation, flow reversal, deflection, shear zones) as well as integral flow parameters (e.g. index velocity) needed for various practical applications such as implementation of non-intrusive velocity and discharge measurement techniques in the field conditions.

Most of the reported quantities were obtained both experimentally and from numerical simulations. Some analyzed characteristics could only be investigated using one of the approaches because of the limitations of the technique (e.g. instantaneous pressure field is obtained only numerically). Time-averaged velocity and turbulence profiles were used to validate the numerical simulations so that the numerical results for the parameters and flow cases that could not be obtained experimentally may be considered with confidence.

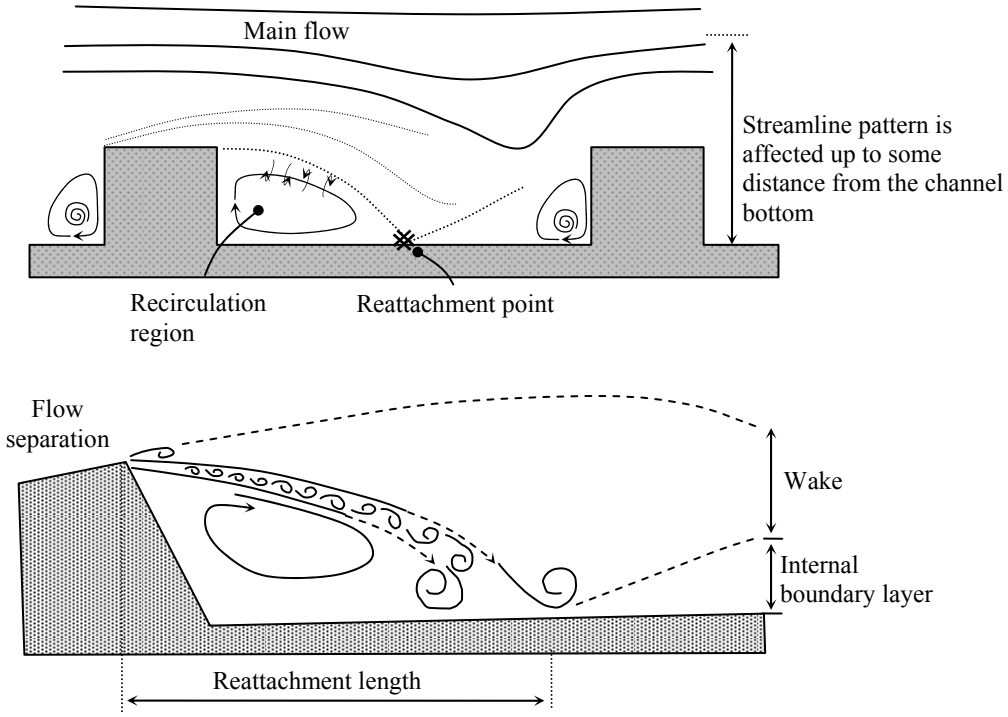

Figure 4.1 Schematic description of flow over k-type roughness (a) flow over ribs, (b) flow over dunes.

To cope with the complexity of the flow over large-scale roughness the analysis is grouped into four categories (see Figure 4.2) as

- Instantaneous flow field
- Time-averaged flow field
- Spatially-averaged flow field
- Bulk flow properties

Each of these four time- and/or space- resolved flow characteristics provides distinct insights on the flow structures and important practical information. The flow that we observe in the nature at any given time is what we call the *instantaneous flow field*. The turbulence structures, waves, transport of sediment and contaminant are directly

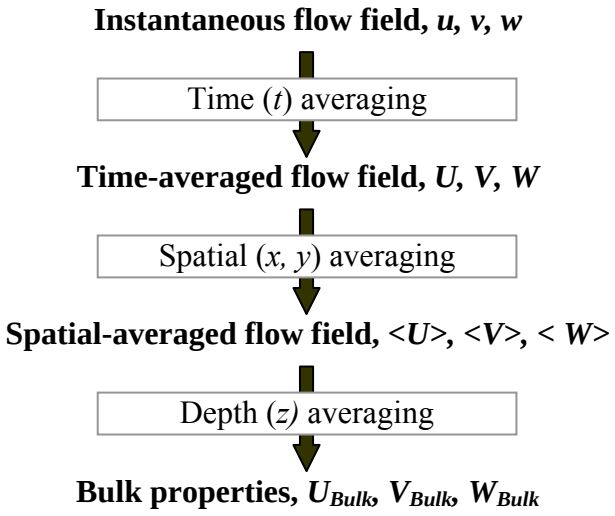

Figure 4.2 Flow field resolution of turbulent flows.

influenced by the instantaneous features of the flow. Commensurate with the nature of the flow, the measurement of instantaneous properties can be very challenging.

For most practical purposes, the flow features of interest are the time- and/or space-averaged properties. Time-averaged properties are the statistical means of the instantaneous properties in a period of time. Taking the spatial average of the time-averaged flow field in the horizontal plane (along *x*- and *y*- directions) yields the spatially-averaged flow field. By further averaging spatio-temporal flow characteristics over the flow depth, important bulk flow characteristics are obtained. The sequence of data analysis steps used in the present study is sketched in Figure 4.2

4.2 Instantaneous Flow Field

The observations on instantaneous flow field provide critical information on the flow physics. However, capturing three-dimensional instantaneous flow field in experiments is very challenging. In this study, experimentally validated LES results are therefore used to investigate the three-dimensional properties of the flow. Experimental

methods were used for the quadrant analysis and spectrum analysis for the surface waviness. Numerically obtained instantaneous streamlines for the flow over ribs with 9 cm wavelength and 8.5 cm flow depth (R05) are shown in Figure 4.3.a. It is observed that the streamlines lose their homogenous horizontal pattern close to the channel bed. The recirculation region downstream of the ribs and the reattachment point can be easily detected from the instantaneous streamlines in the figure. Similar observations can be made for the flow over a dune with a flow depth of 8 cm (D02) shown in Figure 4.3.b. The streamlines of the instantaneous flow field for other flow cases are presented and discussed in Chapter 5.

Figure 4.4 shows the instantaneous streamwise velocity profile, u(z), in the middle of the groove at four, equally-spaced locations along the channel width. Due to turbulent nature of the flow, the instantaneous velocity distribution at the same distance from the entrance of the computational domain varies dramatically. It can be noted from the figure that the variation in the magnitude of the instantaneous velocity components in the outer layer of the flow can be in the order of magnitude of the velocity itself. For the sample shown in Figure 4.4, the instantaneous streamwise velocity component, u, for $z \sim 0.056$ m changes from 0.57 m/s to 1.26 m/s within the span of the computational domain, hy. In uniform flows, these variations are expected to cancel each other over a period of time.

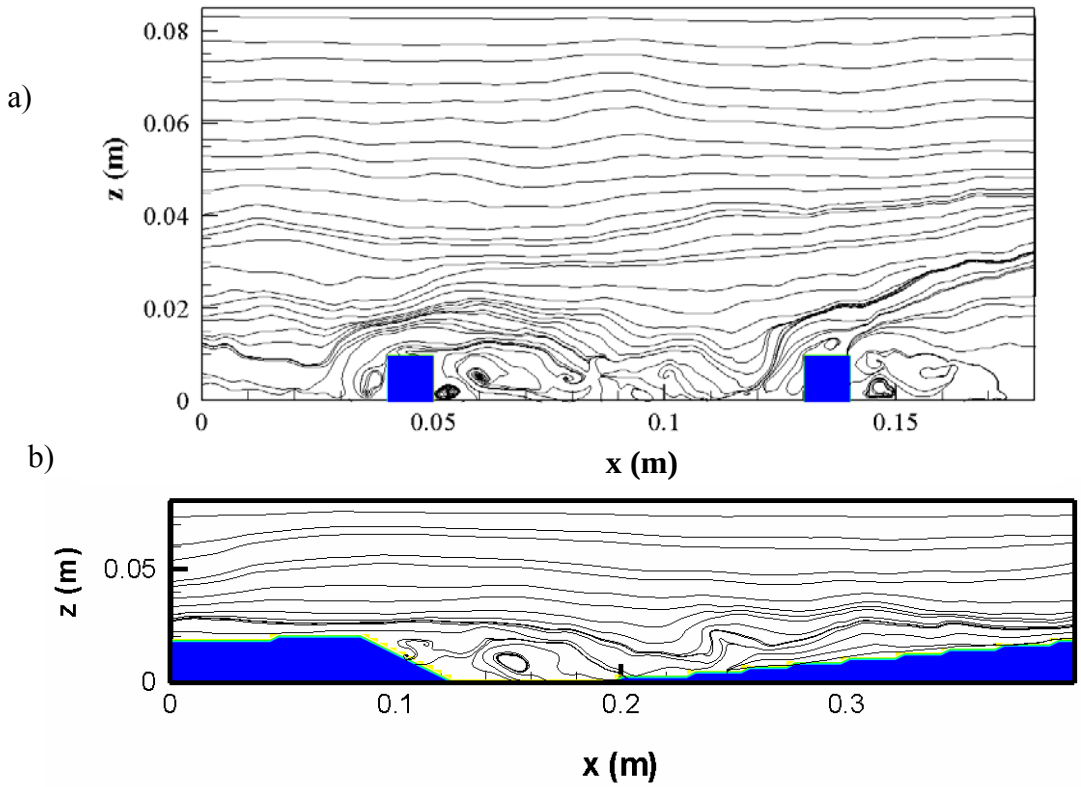

Figure 4.3 Streamlines for the instantaneous flow field over (a) ribs with 9 cm wavelength and 8.5 cm flow depth (R05) and (b) dunes with 8 cm flow depth (D02).

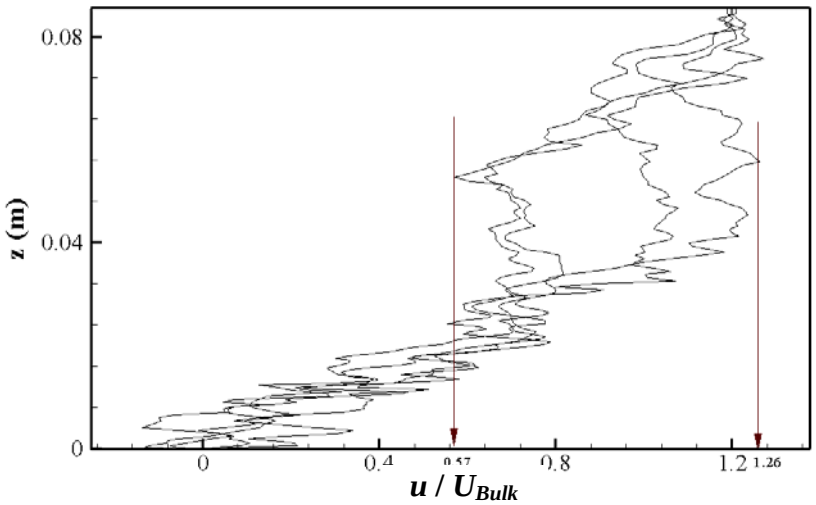

Figure 4.4 Instantaneous velocity profiles by LES at four locations in the middle of the groove (x =0.09m) along the spanwise direction $h_y/3$ apart for flow over rib roughness with 8.5 cm flow depth and 9 cm roughness wavelength (R05).

Figure 4.5 shows the distributions of the instantaneous streamwise velocity fluctuations u' and w' with the fluctuating velocity vectors (u'-w') in a selected x-z plane. The blue and red areas indicate fluid patches moving faster (red) or slower (blue) than the mean flow, while the overlaid vectors indicate the presence of vortical motions. It can be noted that the strongest vortical motions occur in the shear layer and in the recirculation zone downstream of the roughness element. Such plots allow to detect sweeps (red u' and blue w'), which push faster fluid towards the wall, and ejections (blue u' and red w'), which expel slower fluid away from the wall.

Analysis of the perturbation vectors and distribution of fluctuating velocity components provides valuable information for understanding how the flow is influenced by roughness. Turbulence intensity (or the level of turbulence) is defined as the root-mean-square of the instantaneous deviations from the value of the mean velocity (fluctuations), divided by the mean velocity. Turbulence intensities and their distribution in the flow domain vary from one flow situation to another. Analysis of turbulence intensities assists in identification of similarity parameters, and validation of scaling laws. Turbulence fluctuations play a critical role not only in sediment transport but also in the migration and life cycle of aquatic animals (Margalef, 1997). Figure 4.6 and Figure 4.7 illustrate perturbation vectors and turbulence intensities for flow over ribs with 8.5 cm depth and 9 cm wavelength. Results for other flow cases are presented and discussed in Chapter 5.

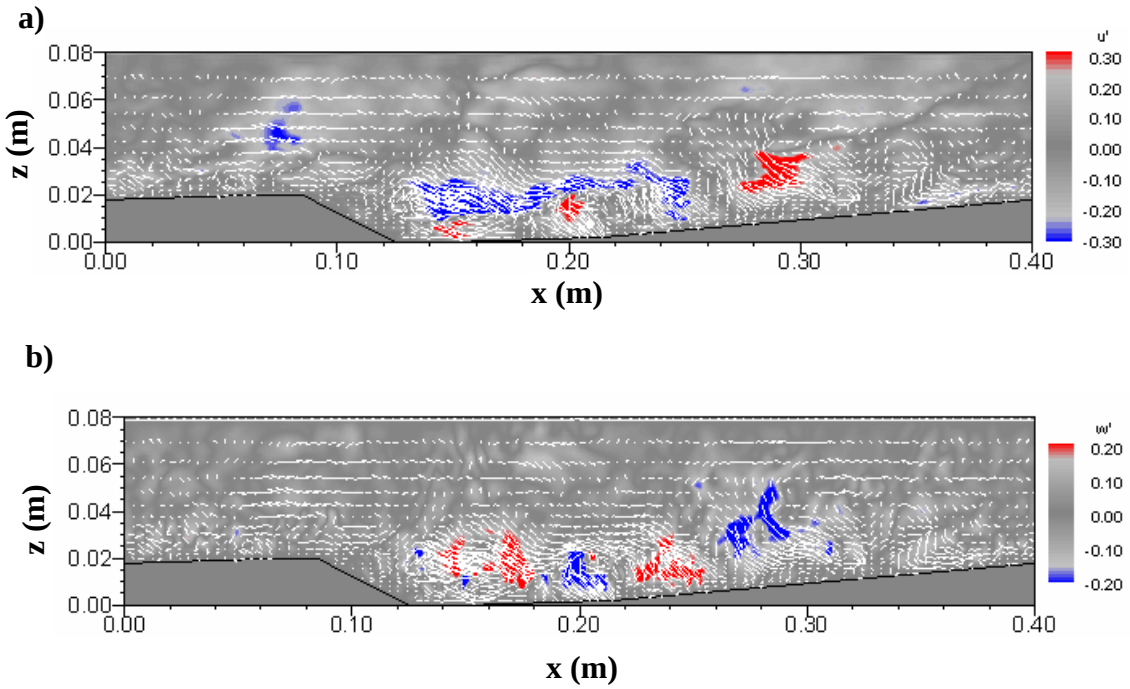

Figure 4.5 Perturbation vector in a selected longitudinal plane for flow over dunes with 8 cm flow depth (D02) with (a) streamwise (b) vertical turbulent fluctuations

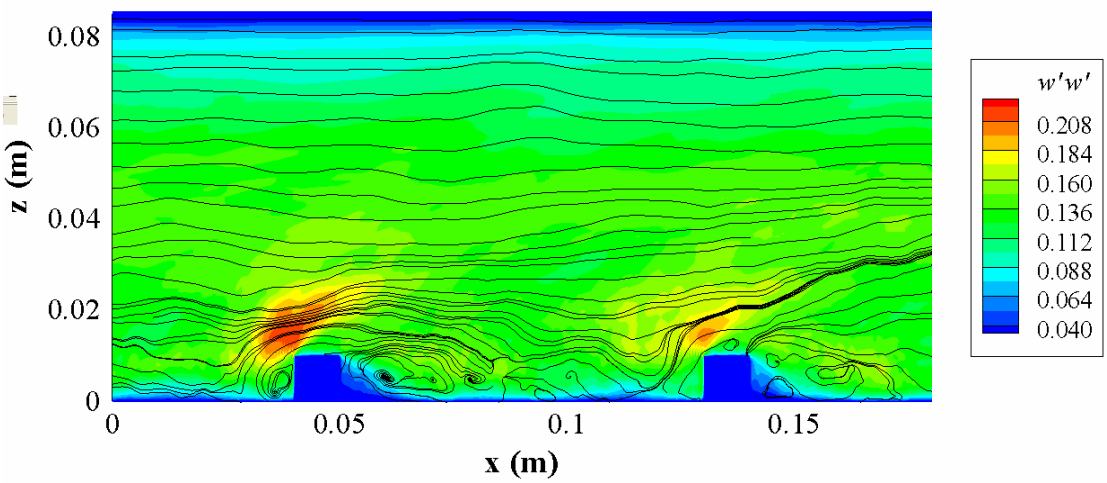

Figure 4.6 Streamtraces of perturbation vectors and contours of turbulence intensity, *w'w'*, in a selected longitudinal plane for flow over ribs with 8.5 cm flow depth and 9 cm roughness wavelength (R05).

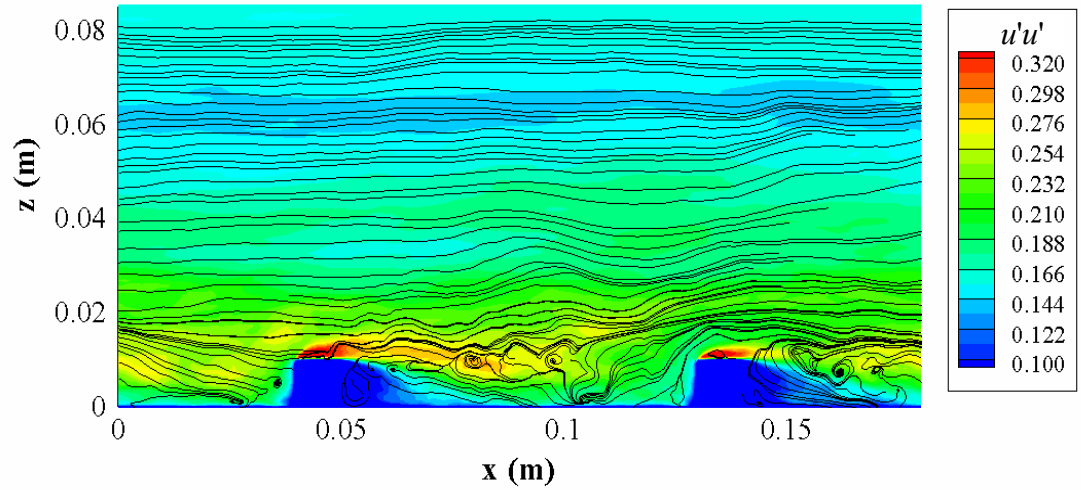

Figure 4.7 Streamtraces of perturbation vectors and contours of turbulence intensity, *u'u'*, in a selected longitudinal plane for flow over ribs with 8.5 cm flow depth and 9 cm roughness wavelength (R05).

4.2.1 Coherent Structures

Identification of coherent vortical motions is useful for understanding turbulent motions, momentum, mass and heat transfer, sediment transport, and aquatic life. For example, earlier studies of free-surface flows show that heat and mass transport rate across the interface is mainly controlled by large turbulent eddies generated in the main flow (Banerjee, 1992; Fulgosi *et al.* 2003).

Vorticity is a traditional measure of vortical structures, despite certain shortcomings of the method. Vorticity contours can be extremely complex, and the structures that are visible in plots of vorticity depend largely on the choice of a low level threshold (McIlwain & Pollard, 2002). Moreover, vorticity does not distinguish shear layers and vortical motions.

Figure 4.8 shows the contours of vorticity magnitude at an instant for cutoff values of 200 and 100. Most of the tube-like vortical structures in the figure are oriented in the streamwise direction. These large-scale structures are continuously produced in the roughness layer; they tilt upward, and travel downstream. Most of them are eventually dissipate before arriving at the free-surface.

Since the mixing layer that originates from the roughness and the wall layers near the bed produce very large spanwise vorticity (Figure 4.9), the λ_2-method suggested by Jeong & Hussain (1995) is employed as it is more appropriate in identifying vortical structures in these flows. Figure 4.10 shows snapshots of the large-scale vortical structures identified by isosurfaces of λ_2=-200. The effects of shear and mixing layers are absent in these structures, indicating the effectiveness of the λ_2-method in capturing vortical structures.

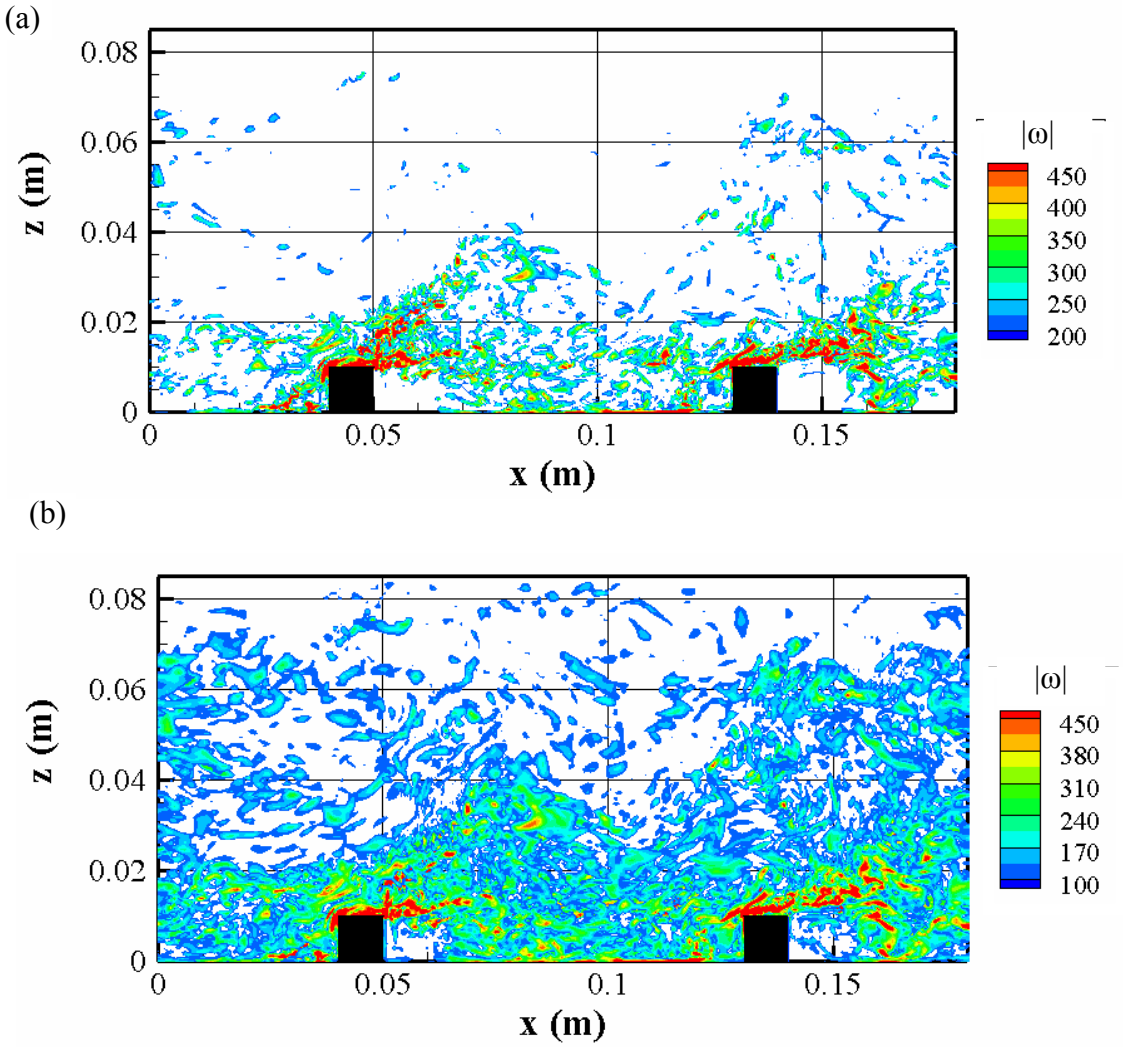

Figure 4.8 Contours of vorticity magnitude for flow over rib roughness with 8.5 cm flow depth and 9 cm roughness wavelength (R05) with lower cutoff value of (a) 200, and (b) 100.

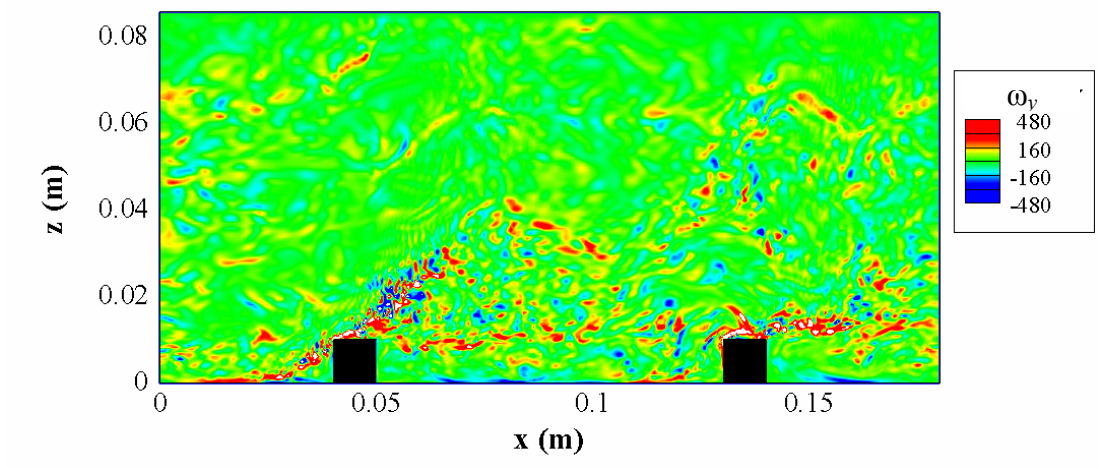

Figure 4.9 Contours of spanwise vorticity component (ω_y) for flow over ribs with 8.5 cm flow depth and 9 cm roughness wavelength (R05).

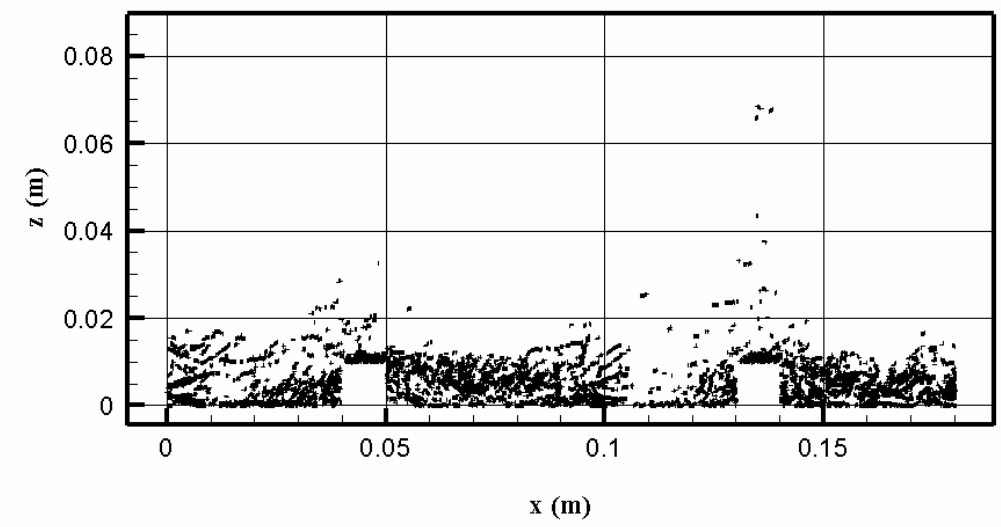

Figure 4.10 Isosurfaces of λ_2 = -200 for flow over ribs with 8.5 cm flow depth and 9 cm roughness wavelength (R05).

Figure 4.11 and Figure 4.12 visualize the coherent structures using pressure isosurfaces as suggested by Jackson (1976). Depending on the water depth to roughness height ratio these structures may protrude the entire flow depth and reach the surface where they produce so-called boils (Bennett & Best, 1996). For the sample case of D02 shown in the figures, these structures do not reach the surface at 0.085 m from the channel bottom, but dissipate approximately 0.06 m from the bed. It also can be observed that the flow separates at the dune crest and forms vortices which travel downstream in the upward direction. The upper parts of the structures reach faster flowing fluid (indicated by the red color) which stretches the vortex formation so that they break up into smaller structures until they finally dissipate. For smaller flow depths, some of these structures, however, reach to free-surface and create boil-like structures.

The vorticity field at the free-surface can be used to identify the boils when used in conjunction with the pressure and velocity distributions. The vorticity contours for the flow over a case with 8 cm flow depth (D02) shown in Figure 4.13 feature regions of strong vortical structures. Vertical sections through these regions given in Figure 4.14 and Figure 4.15 show that the vortical structures generated at the channel bed reach the free-surface. Figure 4.16 shows where the regions of high vorticity, marked with circles in Figure 4.13, correspond on the pressure distribution at the free surface. It is worth noting that, since a rigid-lid approximation was used in the simulations, the non-zero pressure at the free-surface represents a change in the water depth. As shown in Figure 4.17, detailed pressure contours at the free-surface show the upwellings and downdrafts of the free-surface. Consequently, by superimposing velocity vectors on to the pressure contours the boils at the free-surface are revealed.

4.2.2 Free-Surface Texture

Difficulties in the measurement and simulation of the waves and turbulence structures on the free-surface of the open-channel flows complicate the use of the information at this region for the identification of the underlying flow processes. There is lack of data for turbulent flows where the interface is disturbed. In the present study, the texture of the free-surface is analyzed through recordings of the experimental flows taken under various illumination conditions. As described in Chapter 2, it is found that different arrangement of the observation angle (camera orientation) and the illumination reveal a variety of structures of different scales at the free-surface. A sample image from the recordings of the free-surface for flow over a smooth bed with 6 cm flow depth (S06) is given in Figure 4.18.a.

In order to quantitatively characterize the waviness of the free-surface the following procedure was implemented: Free-surface texture was recorded using the illumination settings given in Figure 2.13. A sampling point was selected in the center of the image. Time series of the gray scale values were recorded at this location for all frames in the video clip. The series was analyzed for the power spectral density of the gray scale using Matlab routines. A sample output of the Fast Fourier Transform (FFT) analysis of the recordings is presented in Figure 4.18.b. It must be noted that this analysis is valid only when used in a relative manner, i.e., by comparing free-surface textures for different flow cases recorded under the same camera and illumination conditions. The improvement on the method to obtain a functional relationship between the changes in the gray scale time series recorded at the free-surface and the amplitude of the waves is proposed for subsequent studies using image correction methods.

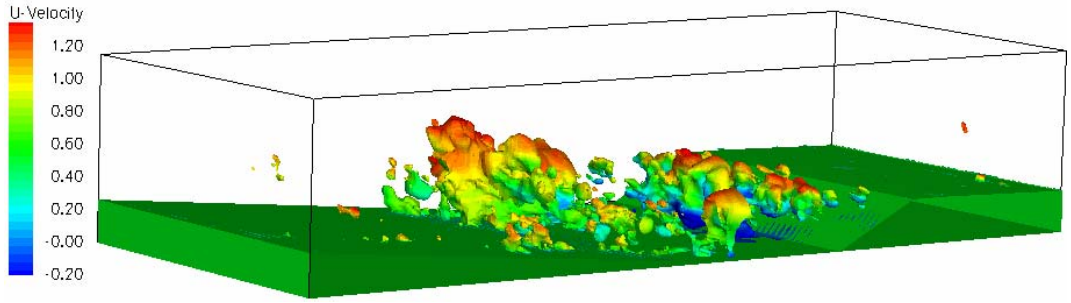

Figure 4.11 Isosurfaces of turbulent pressure fluctuations p' colored with the instantaneous streamwise velocity at an instant t=0 flow over dune with h = 8 cm (D02).

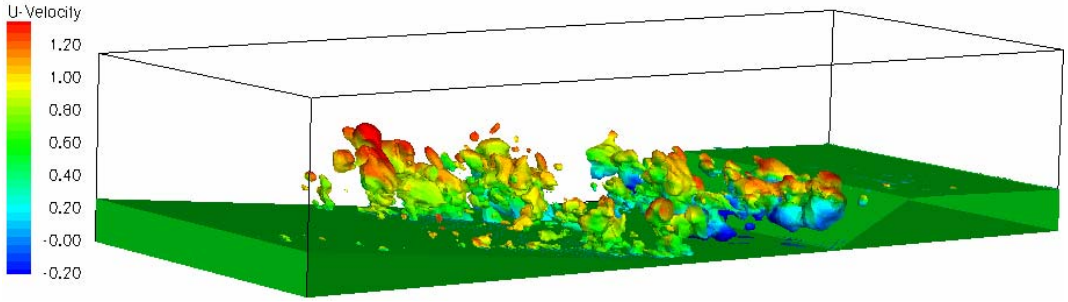

Figure 4.12 Isosurfaces of turbulent pressure fluctuations p' colored with the instantaneous streamwise velocity at an instant t=0+Δ t flow over dune with h = 8 cm (D02).

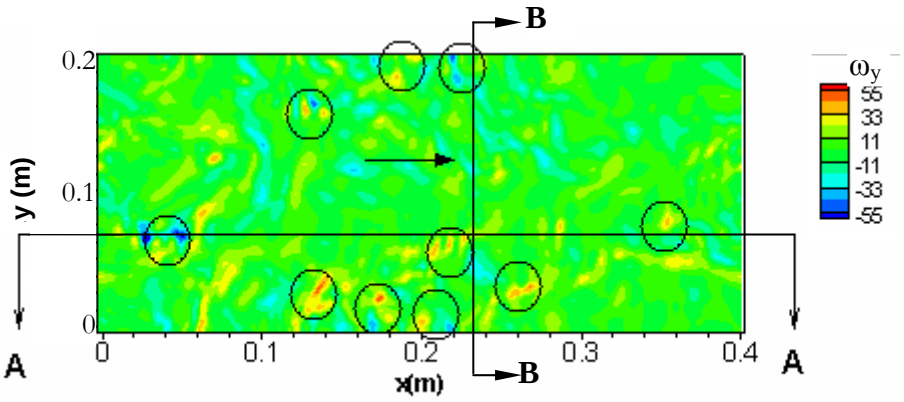

Figure 4.13 Instantaneous vorticity contours at the free surface for flow over dune with h = 8 cm (D02) (A-A at y = 0.075 m and B-B at x = 0.22 m).

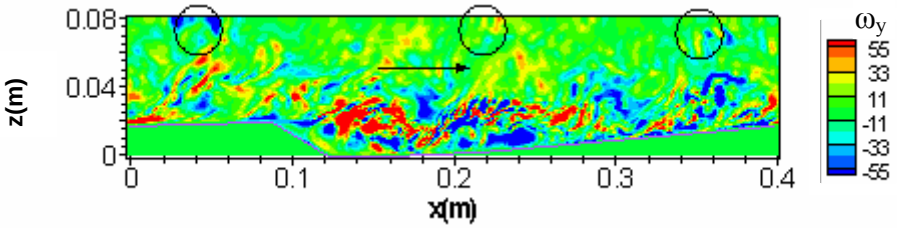

Figure 4.14 Instantaneous vorticity contours in vertical cross-section A-A of Figure 4.13 for flow case D02.

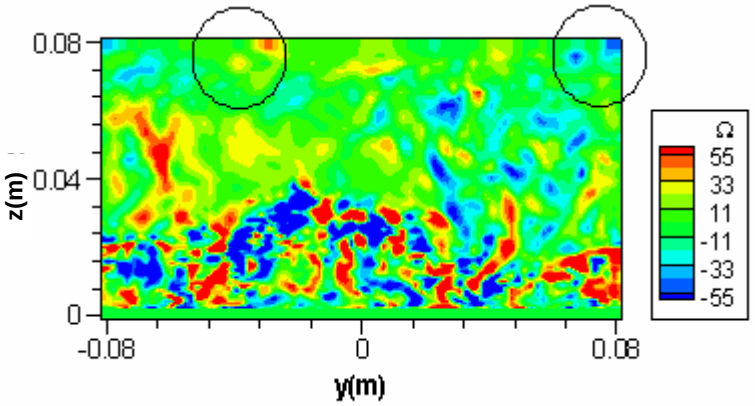

Figure 4.15 Vorticity contours of time averaged velocity field for flow case D02 in vertical cross-section B – B.

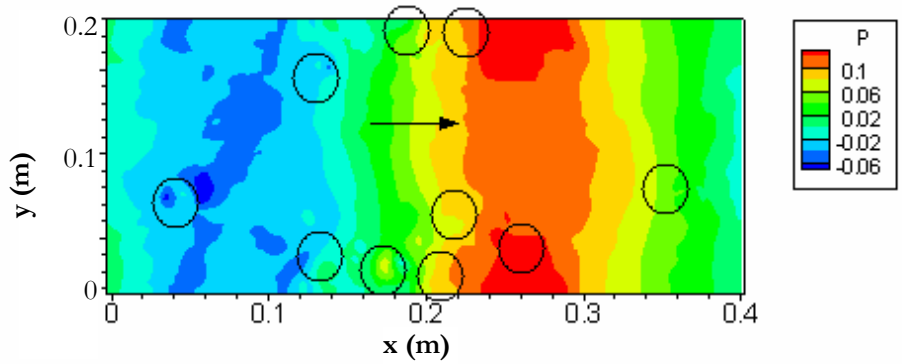

Figure 4.16 Instantaneous pressure contours for flow case D02 (circles are at the same locations with Figure 4.13).

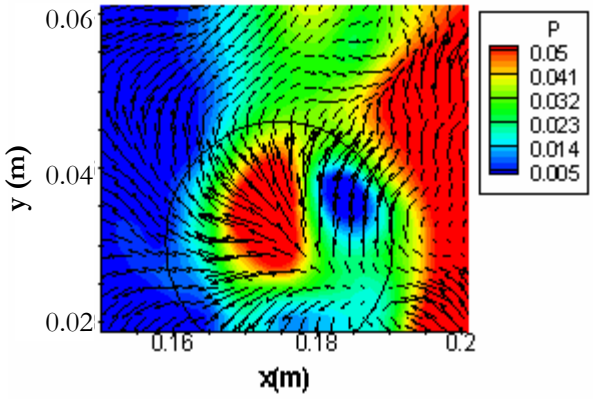

Figure 4.17 Detailed instantaneous pressure contours overlaid by ((u- U_{Bulk}) , v) vectors for flow case D02.

In order to quantitatively characterize the waviness of the free-surface the following procedure was implemented: Free-surface texture was recorded using the illumination settings given in Figure 2.13.

A sampling point was selected in the center of the image. Time series of the gray scale values were recorded at this location for all frames in the video clip. The series was analyzed for the power spectral density of the gray scale using Matlab routines.

A sample output of the Fast Fourier Transform (FFT) analysis of the recordings is presented in Figure 4.18.b. It must be noted that this analysis is valid only when used in a relative manner, i.e., by comparing free-surface textures for different flow cases recorded under the same camera and illumination conditions. The improvement on the method to obtain a functional relationship between the changes in the gray scale time series recorded at the free-surface and the amplitude of the waves is proposed for subsequent studies using image correction methods.

4.3 Time-Averaged Flow Field

Figure 4.19 shows streamlines of the time-averaged velocity field for sample rib roughness and dune flow. The time-averaged velocity fields reveal important features of the flow, such as the extent of the flow disturbance introduced by the roughness elements, reattachment length, and the mean flow patterns over the roughness.

Figure 4.20 compares the instantaneous and time-averaged velocity profiles over a vertical for flow case R05. The comparison of instantaneous and averaged velocity profiles reveals the effect of turbulence on the velocity distribution throughout the flow depth.

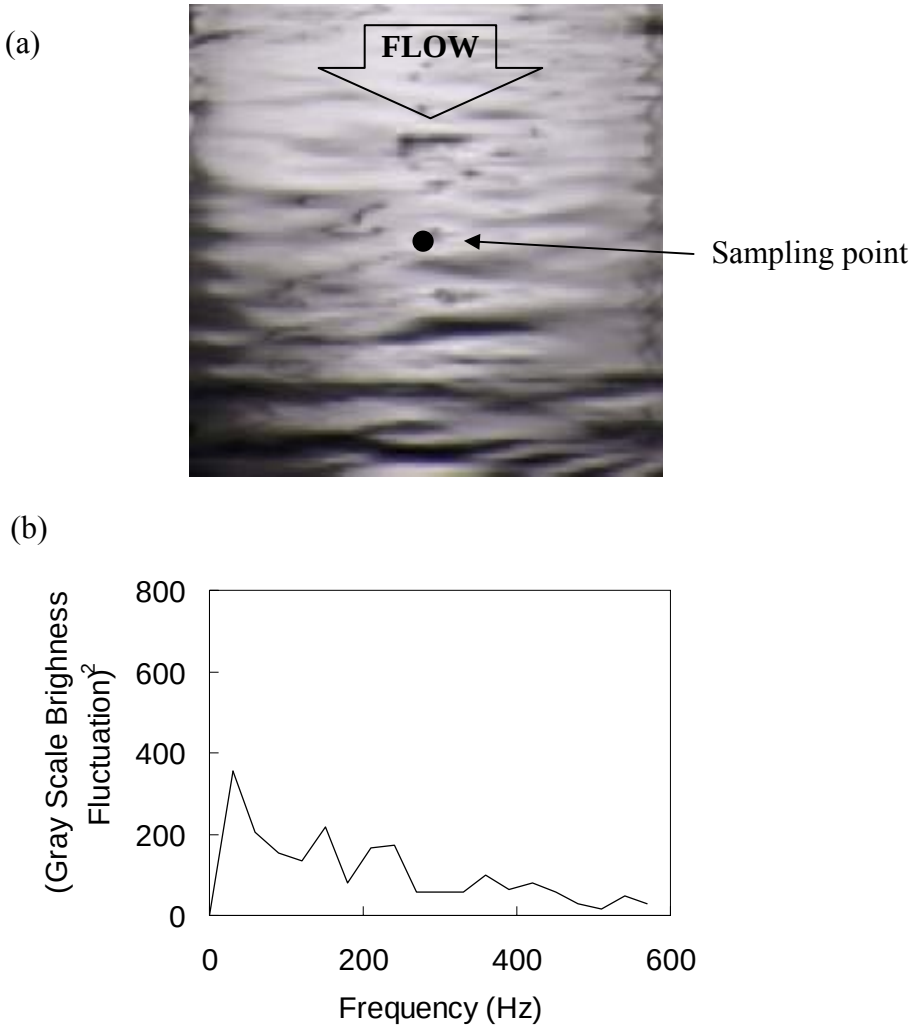

Figure 4.18 (a) Free surface texture and (b) power spectral density plots for the fluctuating gray scale brightness recorded in the center of the image for the flow over smooth bed with 6 cm flow depth (S06).

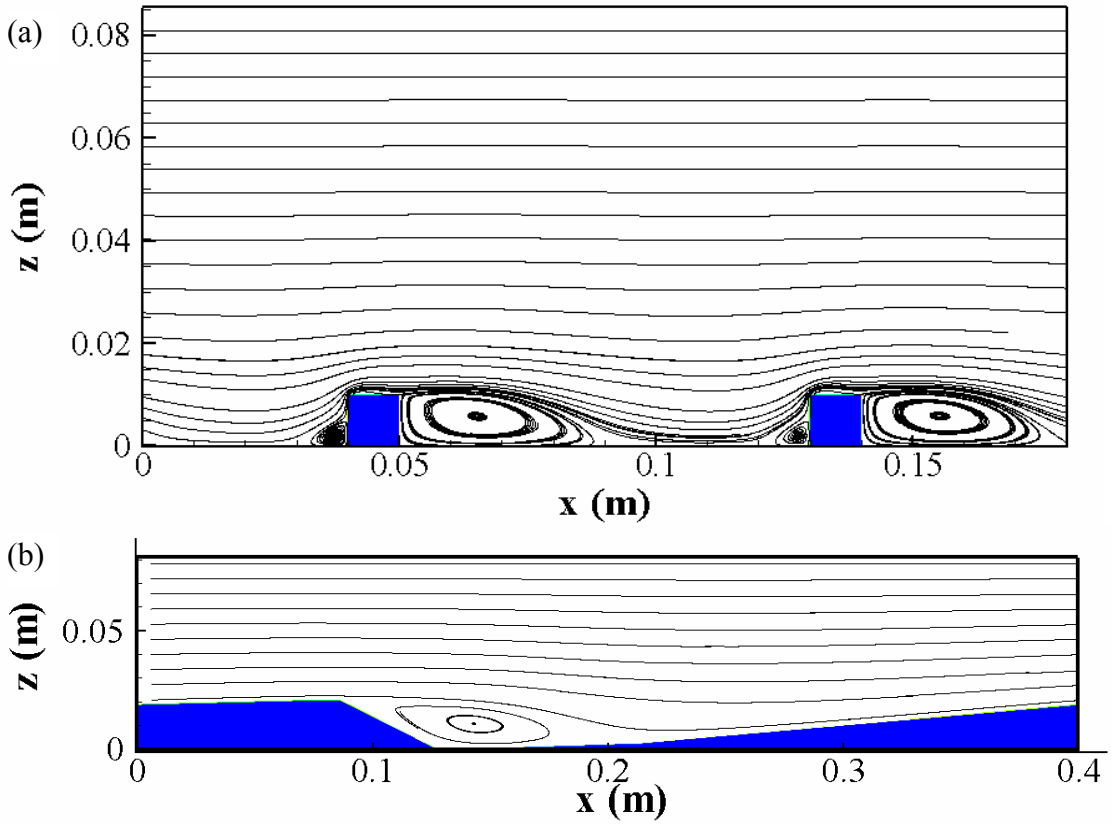

Figure 4.19 Streamlines for the time-averaged flow field over (a) R05 and (b)D02 cases.

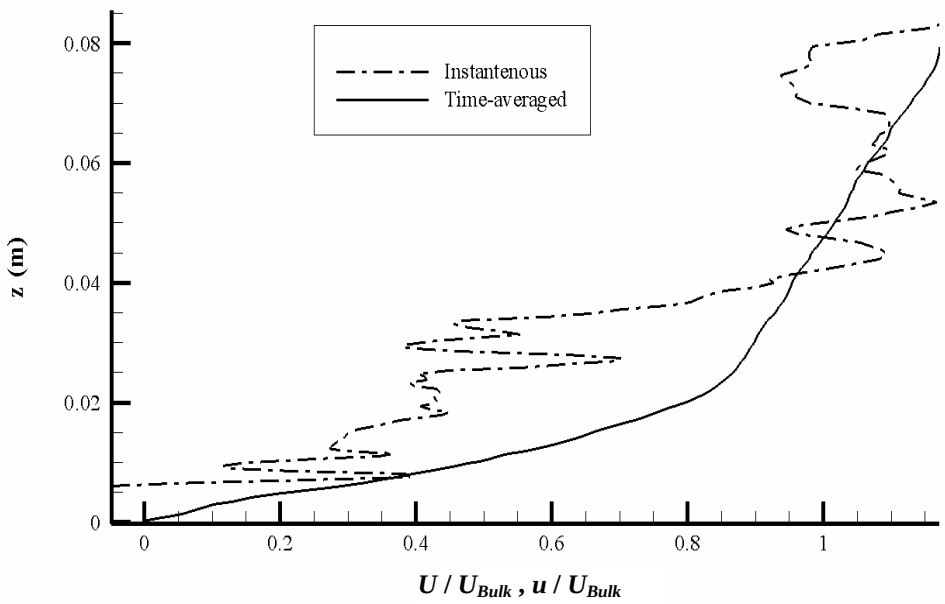

Figure 4.20 Instantaneous and time-averaged velocity profiles for R05 at location L2.

4.3.1 Quadrant Analysis

To quantify the differences in turbulent flow structure under various roughness conditions, quadrant analysis was performed. The method isolates the nature of the contributions to $u'w'$ from the sweeps, ejections, inward and outward interactions. As detailed in Chapter 1, quadrant analysis based on conditional sampling suggested by (Lu & Willmarth, 1973) is used to detect turbulent bursts in wall-bounded turbulence. Figure 4.21 and Figure 4.22 show results obtained from the quadrant analysis of the selected flow conditions.

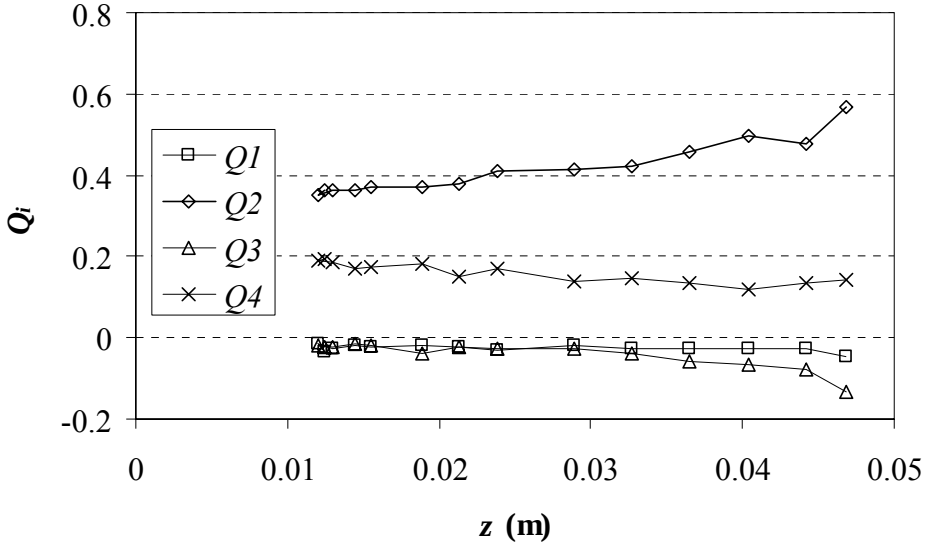

Figure 4.21 Distribution of quadrant events at a vertical location for flow over smooth bed with flow depth of 6 cm (S06).

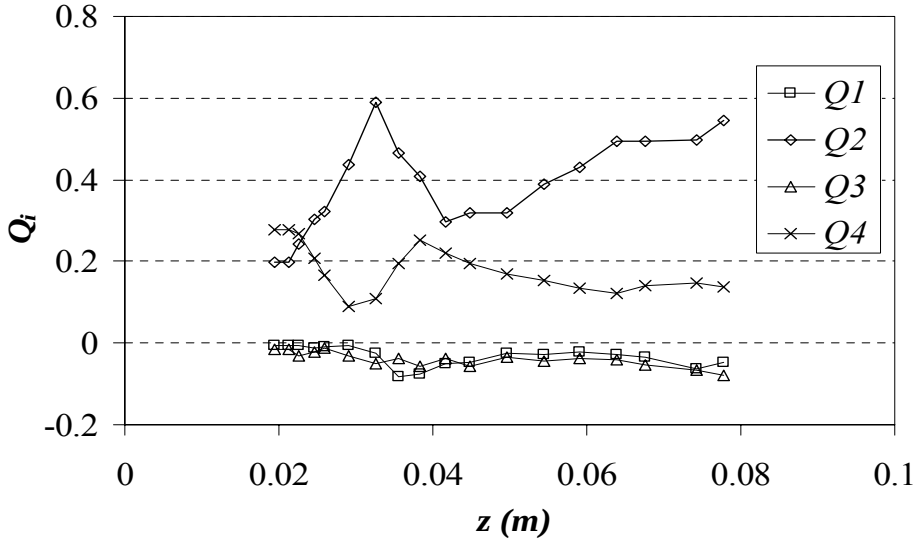

Figure 4.22 Distribution of quadrant events at vertical location L2 for flow over dunes with 8 cm flow depth (D01).

4.3.2 Free-Surface Velocity Distribution

In this study, free-surface velocity distribution was obtained both experimentally and numerically. Figure 4.23 and Figure 4.24 show the results for the sample case of flow over dunes with 8 cm flow depth (D02). Instantaneous velocity fields at the free-surface were averaged to obtain a representative surface velocity to be used in the velocity index calculation. As discussed later in Chapter 5, the analysis of the mean free-surface velocity distribution is influenced by the presence of the roughness elements on the channel bed.

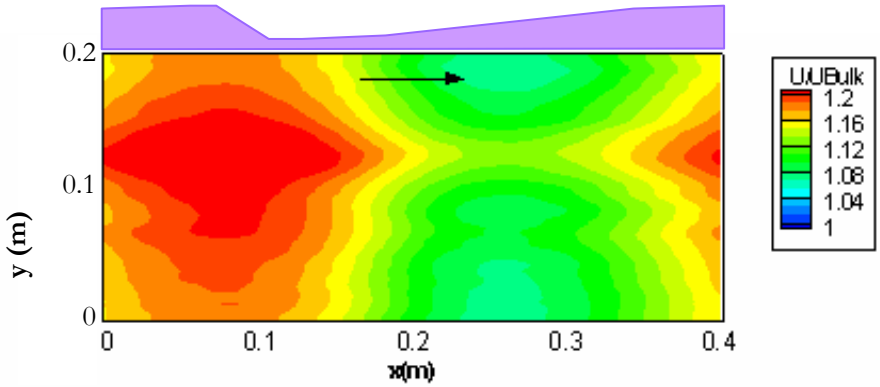

Figure 4.23 LES result of the normalized free-surface velocity U/U_{Bulk} for flow over dunes with 8 cm flow depth (D02).

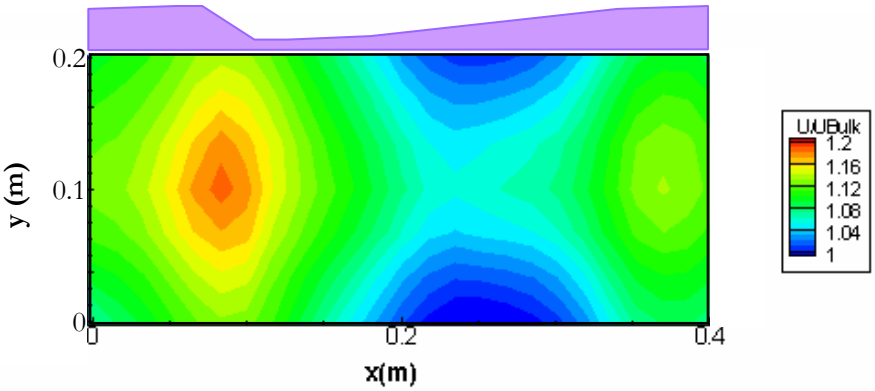

Figure 4.24 Experimental result of the normalized free-surface velocity U/U_{Bulk} flow over dunes with 8 cm flow depth (D02).

4.4 Spatially-Averaged Flow Field

4.4.1 Spatial Averaging

In order to obtain a general description of the flow over large roughness elements, the method of spatial averaging is introduced by Smith & McLean (1977). The method was applied to LES and experimental results by averaging the velocity profiles in the streamwise and spanwise directions over the roughness elements to produce a single, spatially-averaged profile (also called as double-averaged profile by Nikora *et al.,* 2001).

Figure 4.25 compares double-averaged velocity obtained by LES with experimental measurements at 6 locations. The figure points up that there are two distinct regions of velocity distribution. In the outer layer, local and spatially averaged profiles are similar, but they do not follow a general trend in the inner layer. Before McLean *et al.* (1999) raised concerns on its validity, it was believed that these two regions of the spatially averaged profile follow the log law, evaluated with different shear velocities. Nikora *et al.* (2004) reported the other possibilities for the velocity profile in the inner layer of the flow over large-scale roughness. The application of these models to the roughness conditions of the present study is discussed in Chapter 5.

4.4.2 Two-Layer Model of Velocity Profile

Given that the velocity profiles differ considerably in the vicinity of the roughness elements, it is reasonable to expect that the outer and inner layers (see Figure 4.26) of the flow can be described by two different functions. At the boundary of inner and outer layers, both functions must hold. The location of the extent of the inner layer, z_b, and the virtual origin, z_0, of the two-layer velocity profile will be discussed in the next sections.

4.4.3 Extent of the Inner Layer

The first step in characterization of the two-layer velocity profile is the identification of the location of the extent of the inner layer, z_b. A power law fit using Eq. (1.4) is applied to the experimental data above the elevation of z_b. This point is connected to the origin with inner layer profile to obtain the composite profile as illustrated in Figure 4.26.

At the extent of the inner layer z = z_b, the velocity, U_b, satisfies the velocity distribution functions from both inner and outer layers. This location is called the matching layer (Fedele & Garcia, 2000) or the inflection point (Nikora *et al.,* 2004). The position of this point over the channel bed, z_b, may be considered as a dynamic definition for the upper boundary of the roughness interfacial layer and, some studies assume it is roughly equal to roughness height (Raupach *et al.,* 1991; Finnigan, 2000). In the present study, the double-averaged velocity profiles are used to precisely define z_b.

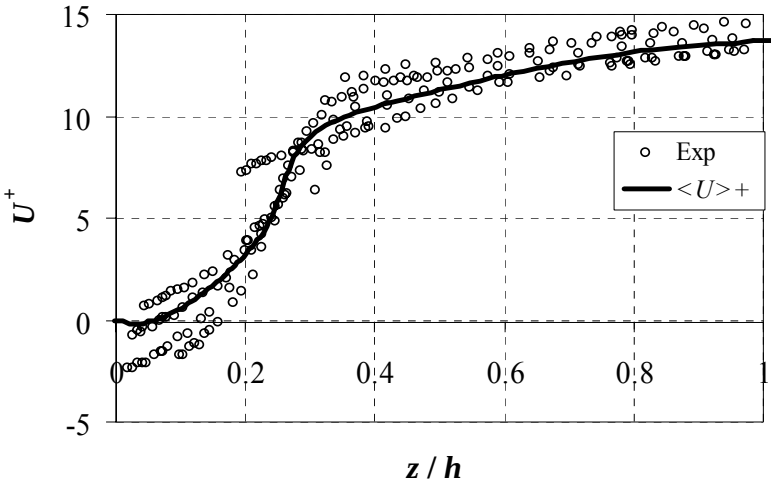

Figure 4.25 Spatially averaged velocity profile by LES and measured time-averaged velocity profiles for flow over dunes with 10 cm flow depth (D02).

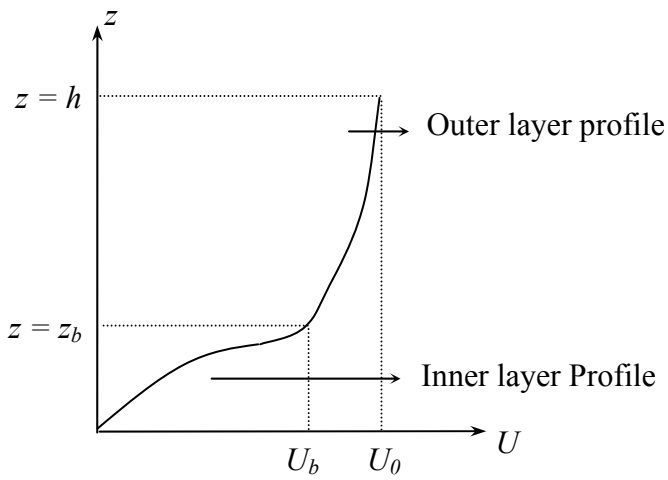

Figure 4.26 Schematic description of the two-layer velocity profile over large-scale roughness.

4.4.4 Virtual Origin Estimation

The location of the effective wall is not well defined for flows over roughness elements. The theoretical wall (or the location of the virtual origin) is defined as the location from which the z distances in the velocity profiles are measured. Several procedures were proposed to locate the virtual origin over the channel bed. Lyn (1993) and Hudson *et al.*(1996) suggested that the average roughness height can be used as the location of the theoretical wall over the bed. For rib roughness, the wave-averaged roughness height can be written as:

$$\langle k \rangle = \frac{1}{\lambda}\int_0^{\lambda} k(x)dx = \frac{kw}{\lambda} \tag{4.1}$$

where λ is the wavelength of the roughness, k is the rib height, and <.> represents averaging over the wavelength. For other roughness conditions, where the geometry is

well-defined with a function or in discrete form, Eq. 4.1 can be used to locate the virtual origin by this method.

The standard deviation of the roughness height also has been used to calculate the virtual origin (Aberle *et al.* 1999). For the rib roughness used in the study, the standard deviation of the roughness is defined as:

$$\sigma_k = \left(\frac{1}{\lambda} \int_0^{\lambda} \left(k(x) - \langle k \rangle \right)^2 dx \right)^{1/2} = \frac{k}{\lambda} \sqrt{w(\lambda - w)} \tag{4.2}$$

The $<k>$ and σ_k values for the rib roughness cases used in this study calculated with above equations are presented in Table 4.1.

Table 4.1 Mean and standard deviation of roughness height for test rib roughness.

	λ (cm)	$< k >$ (cm)	σ_k (cm)
RL045	4.5	0.222	0.416
RL090	9	0.111	0.314
RL180	18	0.056	0.229

Another approach locates the virtual origin by investigating the spatially averaged profiles for the vanishing streamwise velocity (Maddux, 2002; Cui *et al.*, 2000) as:

$$z_0 = z\big|_{<U>=0} \tag{4.3}$$

Lastly, as Nezu & Nakagawa (1993) suggested, virtual origin can also be located at the *z*-intersect of the line drawn from the linear part of the velocity profile in the semi-log plot (see Figure 4.28).

4.4.5 Shear Velocity Estimation

The large-scale variation of the channel bottom elevation causes spatial variations in the flow structure. Since the variations in the flow characteristics due to the bed roughness tend to diminish with increasing distance from the bed, it is expected that the flow characteristics collapse to a single profile sufficiently away from the wall. Based on this idea shear velocity, u_*, is calculated from the collapsing Reynolds stress profiles from all measurement locations (Figure 4.27). After finding the slope of Reynolds stress profile in outer layer, u_* can be calculated from (Nezu & Nakagawa, 1993):

$$-\overline{u'w'} = u_*^2\left(1-\frac{z}{h}\right) \tag{4.4}$$

which means that both slope and intercept of $-\overline{u'w'}$ vs. *z/h* plot give the square of shear velocity u_*. Shear velocities found from the slope of collapsing region of $-\overline{u'w'}$ vs. *z/h* plot for *k*-type rib roughness is given in Table 4.2. Nezu & Nakagawa (1993) also mention that shear velocity can be calculated from the slope of the energy line (or momentum balance) as

$$u_* = \sqrt{gRS_0} \tag{4.5}$$

where S_0 is the overall channel slope.

Table 4.2 Shear stresses calculated for case R05.

Code	u_***(m/s)**
R04	0.050
R05	0.055
R06	0.059

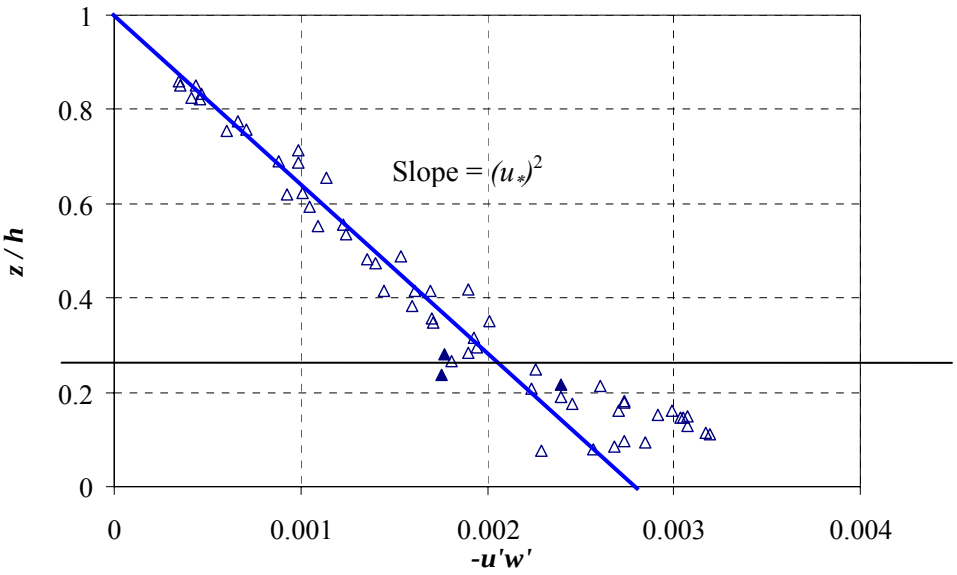

Figure 4.27 -$u'w'$ vs. z/h plot in the outer region for flow over ribs with h = 8.5 cm and λ = 9 cm (R05).

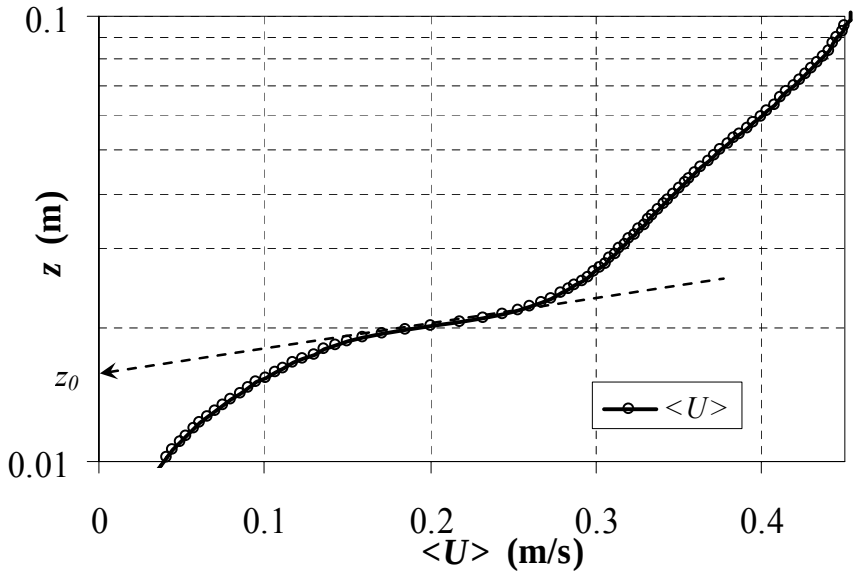

Figure 4.28 Location of the virtual origin as the z-intersect of the linear part or the velocity profile in semi-log plot for flow over dunes with 6 cm depth (D01).

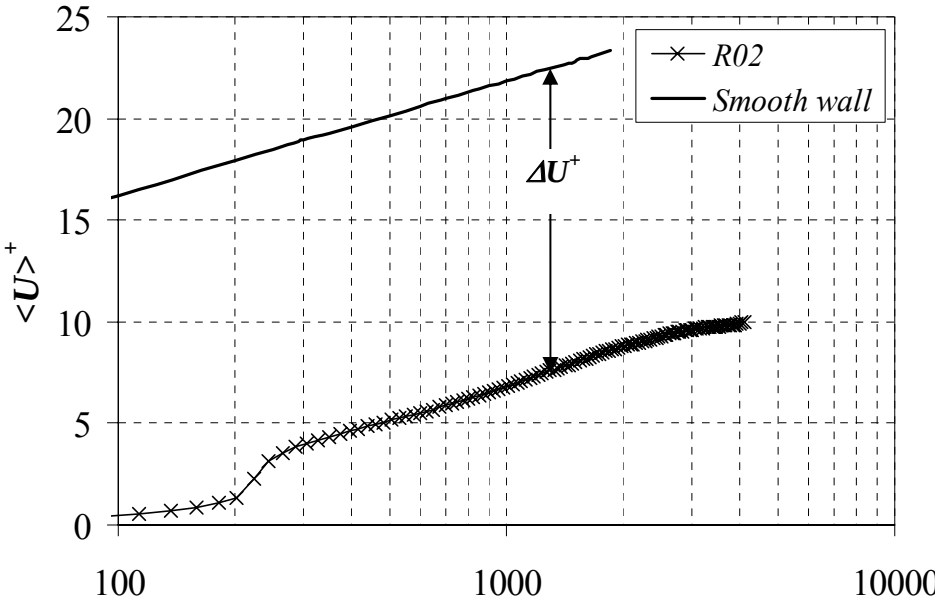

Figure 4.29 Downshift in double-averaged velocity profile for R02.

4.4.6 Roughness Function

For the flow cases described in Chapter 2, the double-averaged velocity profiles over the determined virtual origins are found and compared with smooth wall profile. For each flow, magnitude of ΔU^+ is found by plotting z^+ vs U^+ on semi-logarithmic scale, and then calculating the shift of the profile from the smooth wall velocity profile. The shift in the profile for the sample cases is shown in Figure 4.29. The roughness functions for the other flow cases are presented in Chapter 5.

4.5 Bulk Flow Properties

The bulk flow velocity is obtained by averaging the double-averaged velocity profile over the flow depth. Instantaneous velocity fields obtained by LES are averaged over the simulation period to obtain time-averaged flow field. Averaging this field further

along x- and *z*- directions yields spatially-averaged profiles. Bulk flow velocity is obtained by depth averaging these profiles. Free-surface velocities are related to the bulk velocities by velocity index. By taking free-surface velocity as the indexing velocity, velocity indices were found for each flow case by using the relationship given in Eq. (1.13).

CHAPTER 5
RESULTS AND DISCUSSIONS

5.1 Introduction

Chapters 2, 3 and 4 detailed the tools and data analysis methods used for the investigation of roughness effects on the open-channel flow characteristics with a special focus on the free-surface. This chapter discusses the results of the experimental and numerical investigations regarding the large-scale roughness effect on the free-surface flow in the order illustrated in Figure 4.2. The flow cases for which the numerical and experimental methods were used are listed in Table 5.1. The letters D, R, and S in the flow codes represents the flow over dunes, ribs, and smooth flat bed, respectively. “Sand” and “Wiremesh” represent the flow over dunes with superimposed sand particles, and wiremesh, respectively.

The effect of roughness and the flow depth on the free-surface texture is presented in Section 5.2. Results and discussion of the velocity distribution at the free-surface obtained by LSPIV are presented in Section 5.3. The remaining of the chapter deals with the practical issues of open-channel hydraulics relevant to implementation of non-contact discharge measurement methods: velocity distribution in the water column, roughness scaling issues, and discharge estimation. By relating the free-surface properties to the identified bulk properties of the flow in Section 5.5, the experimental and numerical results of the study are tied to the free-surface velocity indexing to facilitate remote discharge measurements.

Table 5.1 Flow cases studied experimentally and/or numerically.

Flow code	h (m)	λ (m)	Method
D01	0.08	0.4	Exp. & LES
D02	0.1	0.4	Exp. & LES
D03	0.12	0.4	Exp.
D04	0.06	0.4	LES
R01	0.065	0.045	Exp. & LES
R02	0.085	0.045	Exp. & LES
R03	0.105	0.045	Exp.
R04	0.065	0.09	Exp. & LES
R05	0.085	0.09	Exp. & LES
R06	0.105	0.09	Exp.
R07	0.065	0.18	Exp.
R08	0.085	0.18	Exp.
R09	0.105	0.18	Exp.
S01	0.025	-	Exp.
S02	0.025	-	Exp.
S03	0.025	-	Exp.
S04	0.025	-	Exp.
S06	0.06	-	Exp.
S08	0.08	-	Exp.
S10	0.1	-	Exp.
Sand	0.12	0.4	Exp.
WM	0.12	0.4	Exp.

5.2 Instantaneous Flow Field

This section discusses the numerical and experimental results for the instantaneous flow field, coherent structures, and the free-surface texture. Streamlines of the instantaneous flow field in a vertical plane for the flow over the dunes and ribs are shown in Figure 5.1 and Figure 5.2, respectively. They were obtained with LES and represent a snapshot of an instance. The plots for both cases reveal a recirculation region developing immediately downstream of the roughness crests. An important feature of the

instantaneous flow field over large-scale roughness is the reattachment point, which can be identified in these figures. Locating the reattachment point is important in identifying the free-surface structures, as kolk vortices are reported to be originated from the fluctuation of this point (Nezu & Nakagawa, 1993).

Figure 5.1 shows the effect of the flow depth on the instantaneous flow features for the same dune geometry. Starting with a parallel-to-surface formation at the free-surface, streamlines become irregular near the roughness surface.

As expected, decreasing flow depth intensifies the effect of roughness elements on the streamline patterns. For flow over dunes with 6 cm flow depth, the high curvatures in the streamlines are extended just below the free-surface, around z = 5 cm, which tells us that in the more than 80% of the flow depth, streamline pattern is deformed due to presence of the dune (Figure 5.1.a). For a higher flow depth case shown in Figure 5.1.b, the region of high-curvature streamlines is also observed to be confined below z = 5 cm, which corresponds to 60% of the flow depth. For the flow case with h = 10 cm, the major disturbance in the streamline pattern is limited below z = 0.4 m, which is 40 % of the flow depth (Figure 5.1.c). It must be added that the plots given in Figure 5.1 represents an arbitrary instant. The extent of the high-curvature-streamline region can be very different for other instants. The analysis of time-averaged streamlines will be given in Section 5.3.1.

For all three dune flows given in Figure 5.1 a reattachment point is observed. It is known that the location of the reattachment point from the dune crest, L_R, and size of the recirculation bulb fluctuate at time. For the given instants, L_R is observed to be around 4k to 6k.

For flow over ribs, the instantaneous streamline patterns shown in Figure 5.2 point up that the disturbed streamlines extent further for *k*-type configuration (Figure 5.2.b) than for transitional (Figure 5.2.a).

Figure 5.2.a and Figure 5.2.b allows to distinguish the fundamental difference between the *k*-type and transitional roughness: while in Figure 5.2.b a reattachment point is observed, this feature is not seen in Figure 5.2.a. Even though cross-sectional roughness geometry and the flow depth are identical, *k*-type roughness appears to disturb the main flow more than transitional (Figure 5.2.b). This observation is in agreement with conclusions of earlier research stating that the roughness wavelength decrease causes more uniform flow conditions in the outer layer of the flow below a threshold λ/k ratio. This threshold value recently was proposed to be 7, instead of previously excepted 9. A distinct reattachment point is not observed for flow over ribs with transitional roughness spacing.

To summarize, in the direction of the objectives of this research, Figure 5.1 and Figure 5.2 provide the information that for small submergence (h/k) more pronounced roughness effect on the free-surface is expected. The reattachment point is found to be $4k$ to $6k$ for dunes and *k*-type ribs. It is not observed for transitional rib roughness.

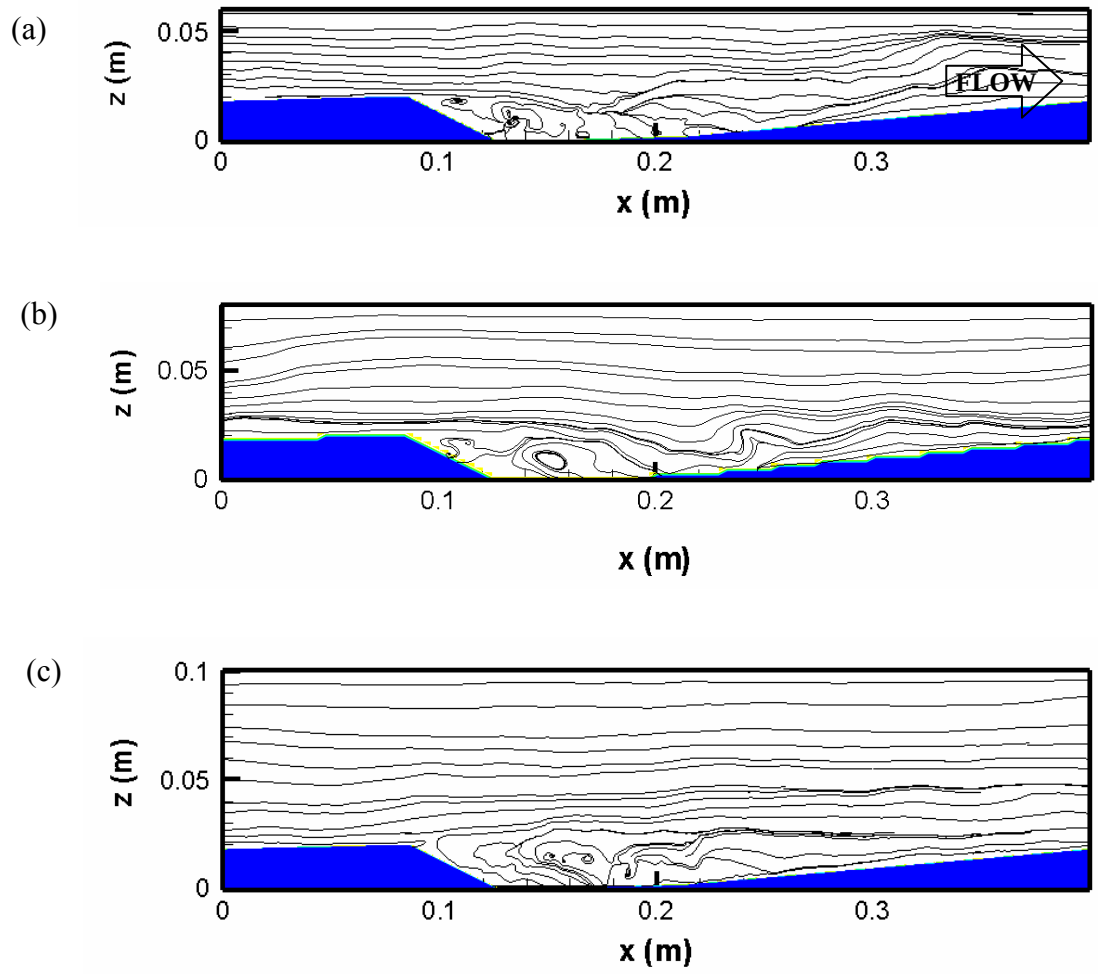

Figure 5.1 Streamlines of instantaneous vector field obtained by LES for flow over dunes with flow depth of (a) 6 cm, (b) 8 cm, and (c) 10 cm.

(a)

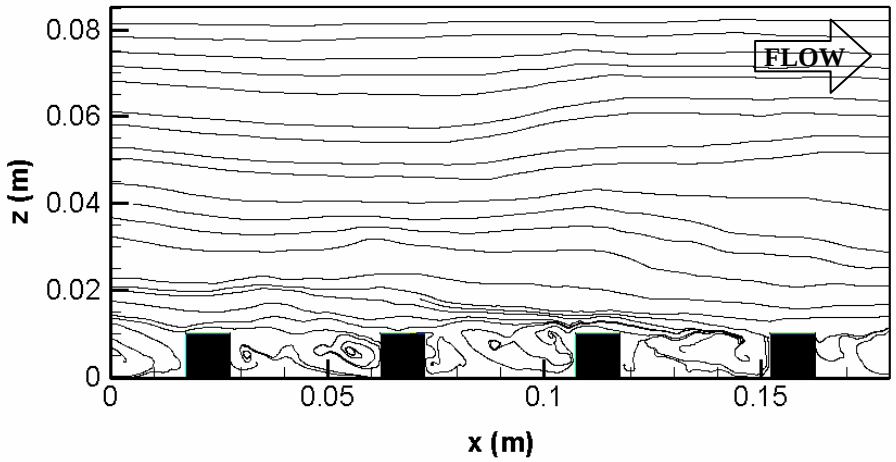

(b)

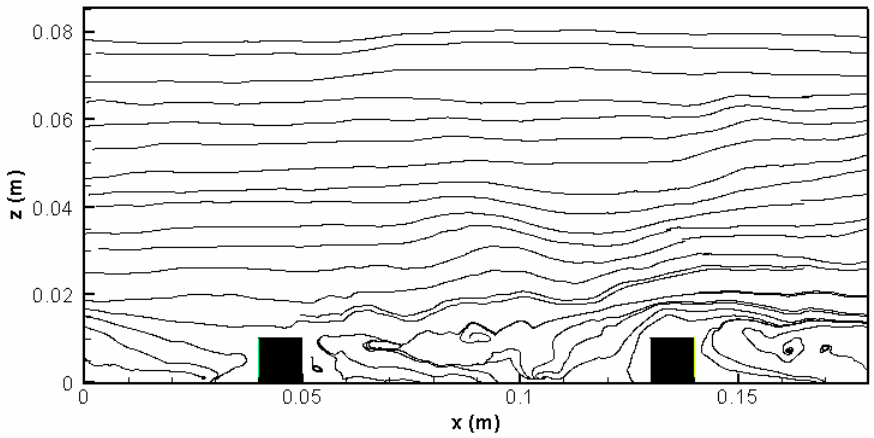

Figure 5.2 Streamlines of instantaneous vector field obtained by LES for flow over rib roughness with 8.5 cm flow depth and roughness wavelength of (a) 4.5 cm, and (b) 9 cm.

Contours of instantaneous streamwise velocity component, u, at the free-surface for flow over dunes and ribs are given in Figure 5.3 and Figure 5.4, respectively. The regions of highest velocity are observed to be above the roughness crest, which has a height of 2 cm for dunes and 1 cm for ribs. Distorted cross-sectional views of the roughness are shown at the top of the plots in each figure. The constraint for continuity inevitably causes higher velocities at the regions of smaller flow area. It is observed from Figure 5.3 that with decreasing relative submergence the variations in the instantaneous velocity become more marked.

Free-surface contours for flow over rib roughness given in Figure 5.4 show that for k type roughness the alternation of high and low velocity regions at the free-surface follow the bed roughness pattern. Even though the roughness cross-sectional geometry in Figure 5.4.a and Figure 5.4.b are identical, their reflections at the free-surface are very different. In Figure 5.4.b, the repeated regions of high and low velocity streets are located periodically with a wavelength similar to that of roughness. In the figure, two high velocity streets located around x = 0.09 m and x = 0.17 m can be explained with ribs located at x = 0.045 m and x = 0.135 m. This behavior can be explained by the combined effects of reduced flow area due to the changes in the bed elevation and existence of circulation region, where there is no net mass flux in streamwise direction. As the size of the circulation bulb fluctuates, the regions of higher/lower velocity at the free-surface also fluctuate.

The results shown in Figure 5.1 to Figure 5.4 demonstrate that the turbulence structures in flows over large-scale roughness are protruding to the free-surface and that the free-surface carries a “signature” of the bed forms that is echoing the geometry of the roughness elements. The signature of roughness on the free-surface is enhanced with decreasing relative submergence.

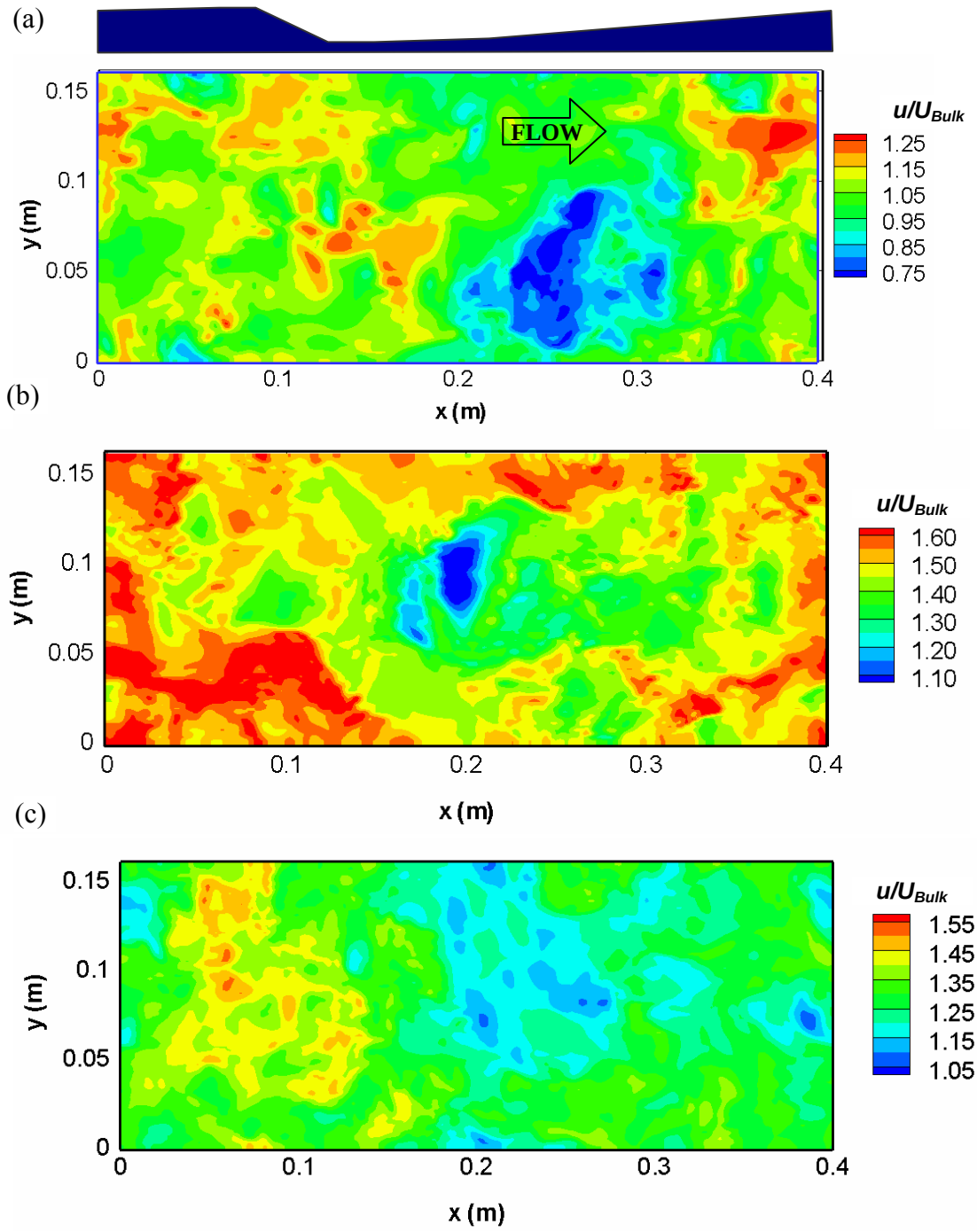

Figure 5.3 Normalized streamwise instantaneous velocity contours at the free-surface obtained by LES for flow over dunes with flow depth of (a) 6 cm, (b) 8 cm, and (c) 10 cm.

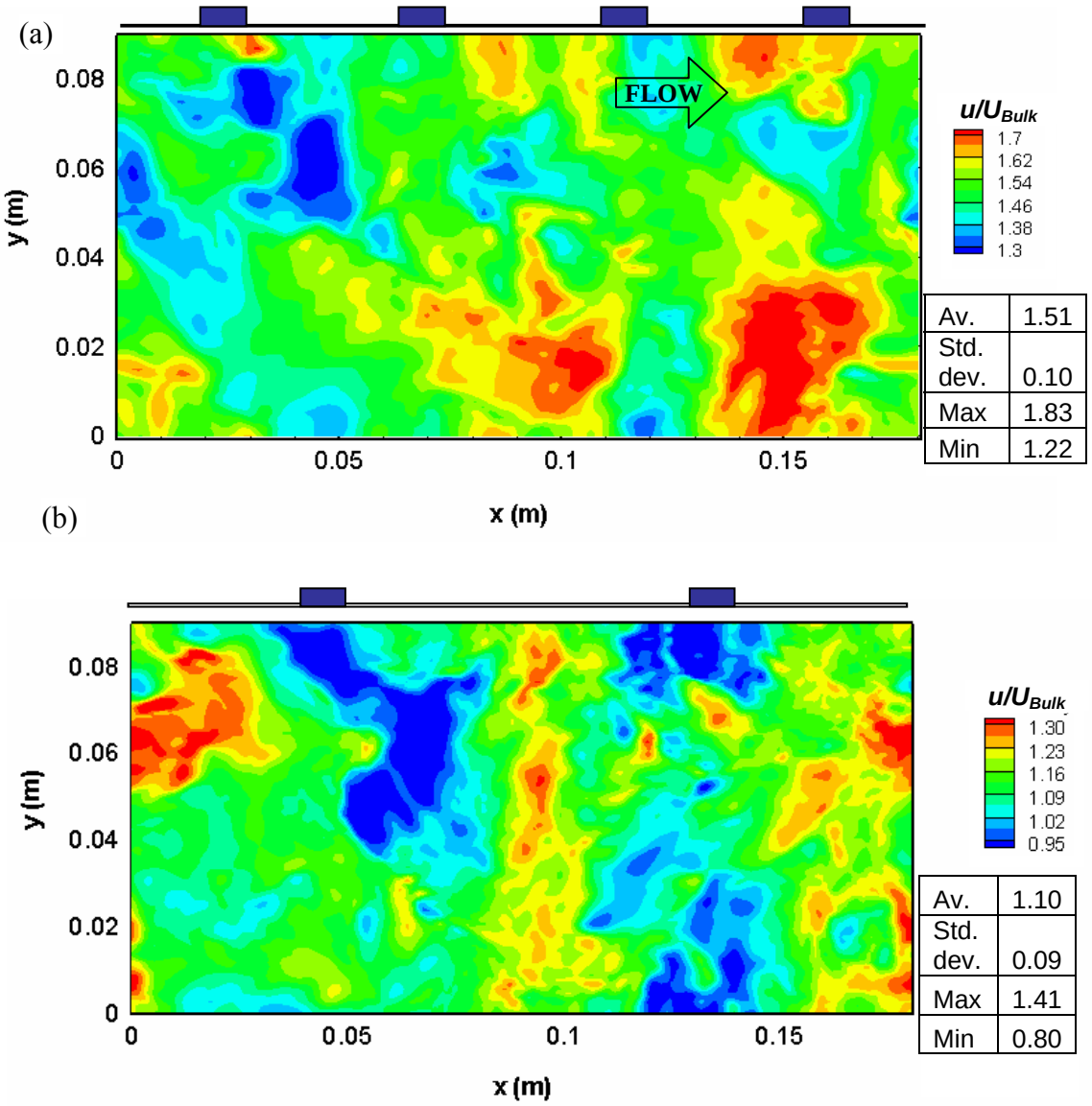

Figure 5.4 Normalized streamwise instantaneous velocity contours at the free-surface obtained by LES for flow over rib roughness with 8.5 cm flow depth and roughness wavelength of (a) 4.5 cm, and (b) 9 cm.

A similar dependence of free-surface properties on bed roughness change can be noticed by plotting the instantaneous pressure contours at the free-surface. The pressure contours illustrated in Figure 5.5 and Figure 5.6 also display the signature of the bed on the free-surface. Using the rigid-lid approximation for the free-surface, the differences from zero in surface pressure can be directly converted into the changes in free-surface elevations. The elevation head at the free-surface is the only source of non-zero pressure calculated at the free-surface.

The instantaneous pressure distribution for the flow over dunes shown in Figure 5.5 reveals that the water surface elevation features a depression over the dune crest. The changes in the water surface elevation intensify with increasing relative submergence of the dune. Unlike dunes, where clear effect of the changes in the bed elevation can be seen at the free-surface, transitional and *k*-type ribs seem to not to reveal their presence in instantaneous pressure plots. This difference can be explained by the higher submergence (h/k) ratio and the lack of persistent change in the channel bed variation in flow over ribs. For example, Figure 5.6 does not display a periodic pattern similar to that of Figure 5.5, hence illustrating that a combination of factors, i.e., roughness geometry, relative submergence, bulk flow velocity concurrently contribute to the signature of the roughness at the free-surface.

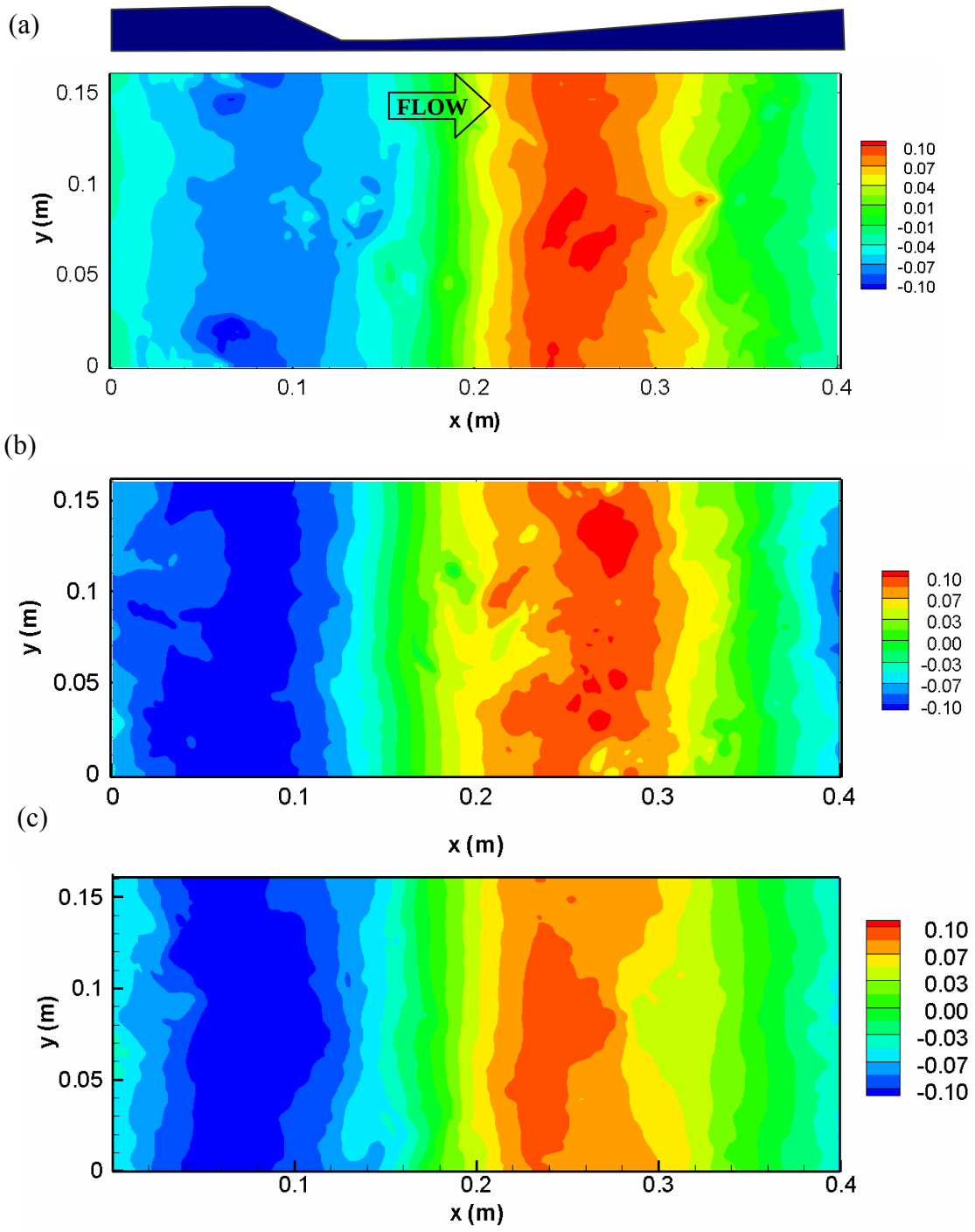

Figure 5.5 Instantaneous pressure contours at the free-surface obtained by LES for flow over dunes with flow depth of (a) 6 cm, (b) 8 cm, and (c) 10 cm.

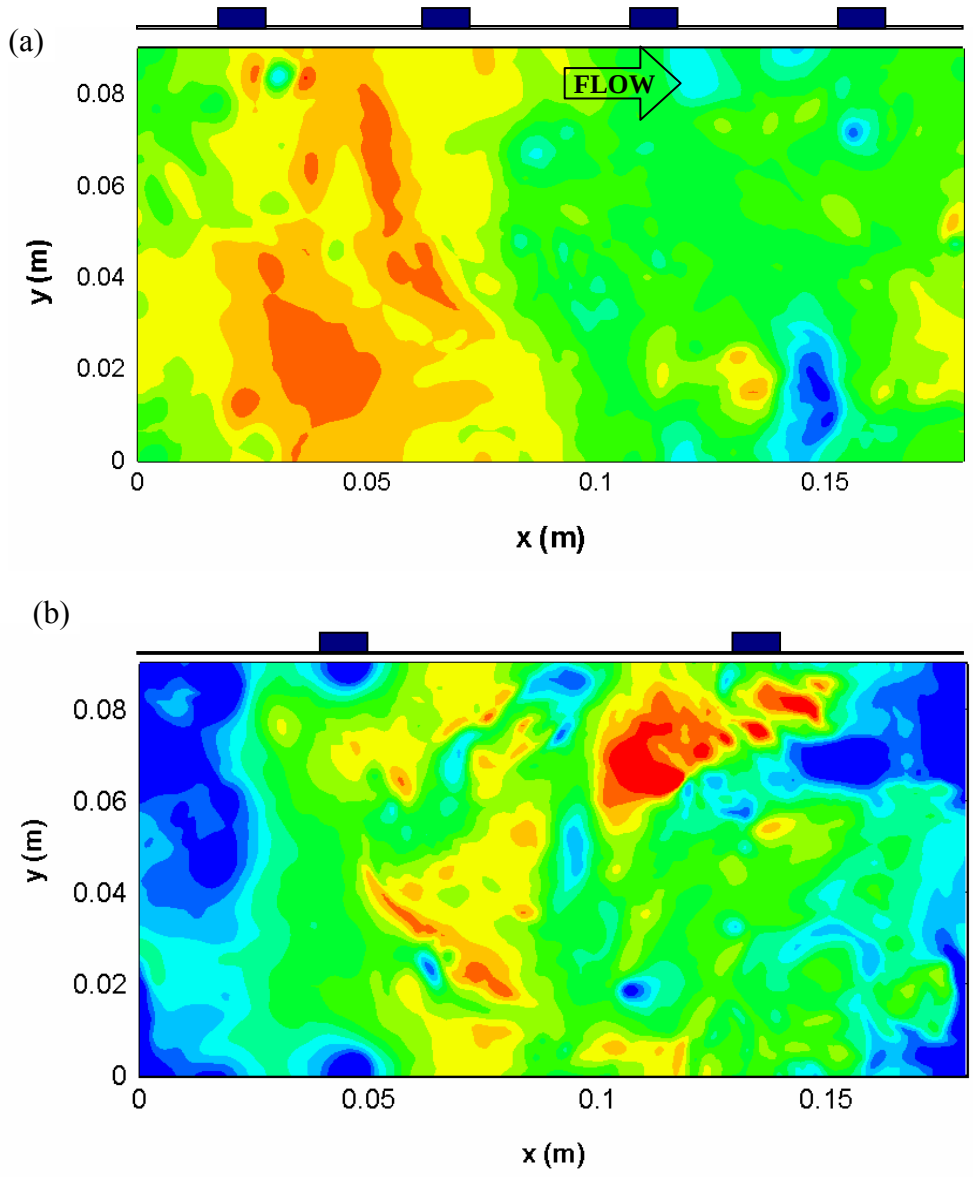

Figure 5.6 Instantaneous pressure contours at the free-surface obtained by LES for flow over rib roughness with 8.5 cm flow depth and roughness wavelength of (a) 4.5 cm, and (b) 9 cm.

Additional information regarding the free-surface structures and flow pattern can be obtained by plotting the vectors of (u-U_0, v) where U_0 is the time-averaged free-surface velocity. The streamtraces of (u-U_0, v) vectors are given in Figure 5.7 and Figure 5.8 for dune and rib flows, respectively. The regions where streamtraces converge and produce a swirling eddy are locations for the vortical structures at the free-surface.

The density of these eddies on the free-surface changes with flow depth. For dune flows shown in Figure 5.7, the maximum number of converging streamtraces is observed to be over 10 cm-flow depth. For lower flow depths, the density of occurrence of swirling eddies decreases.

For rib flows given in Figure 5.8, the number of eddies noticeably higher for *k*-type roughness. In compared to dunes, *k*-type rib roughness generate more eddies at the free-surface. A remarkable observation from Figure 5.7 and Figure 5.8 is that these structures tend to arrange in a line downstream of the separation point. It must be noted that the plots in the figures represent an arbitrary instant. The distribution of eddies at another instant could be dissimilar.

The vectors of these streamtraces overlaid on the contours of the instantaneous pressure, which is equivalent to the water surface elevation, can also help to locate the free-surface upwellings and downdrafts (Stoesser *et al.* 2005b). In addition to the water surface elevation at the free-surface, pressure contours and isosurfaces can be used to identify the coherent flow structures and vortex growth

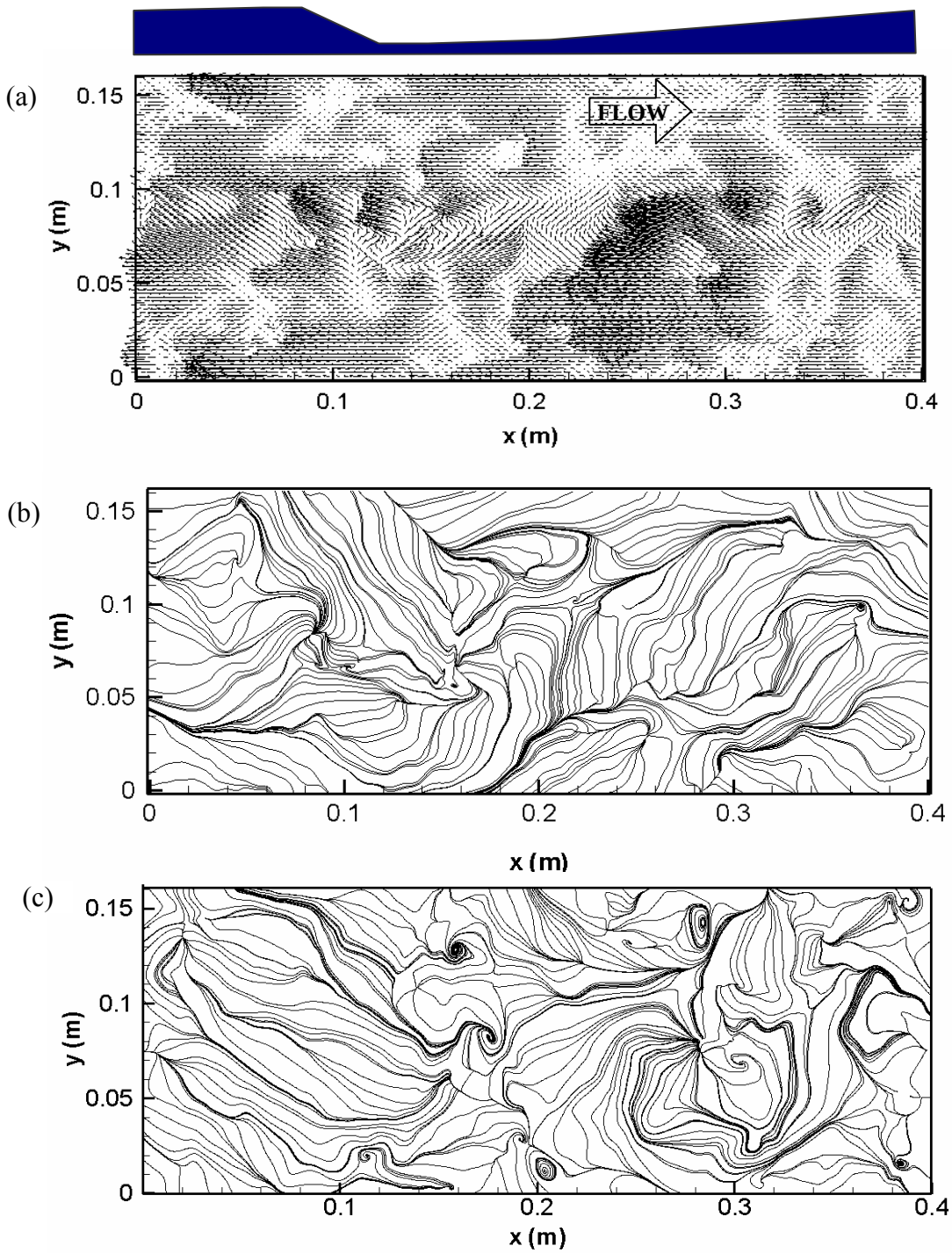

Figure 5.7 Streamtraces of $(u-U_0)/U_{Bulk}$ vs v/U_{Bulk} vectors on the free-surface obtained by LES for flow over dunes with flow depth of (a) 6 cm, (b) 8 cm, and (c) 10 cm.

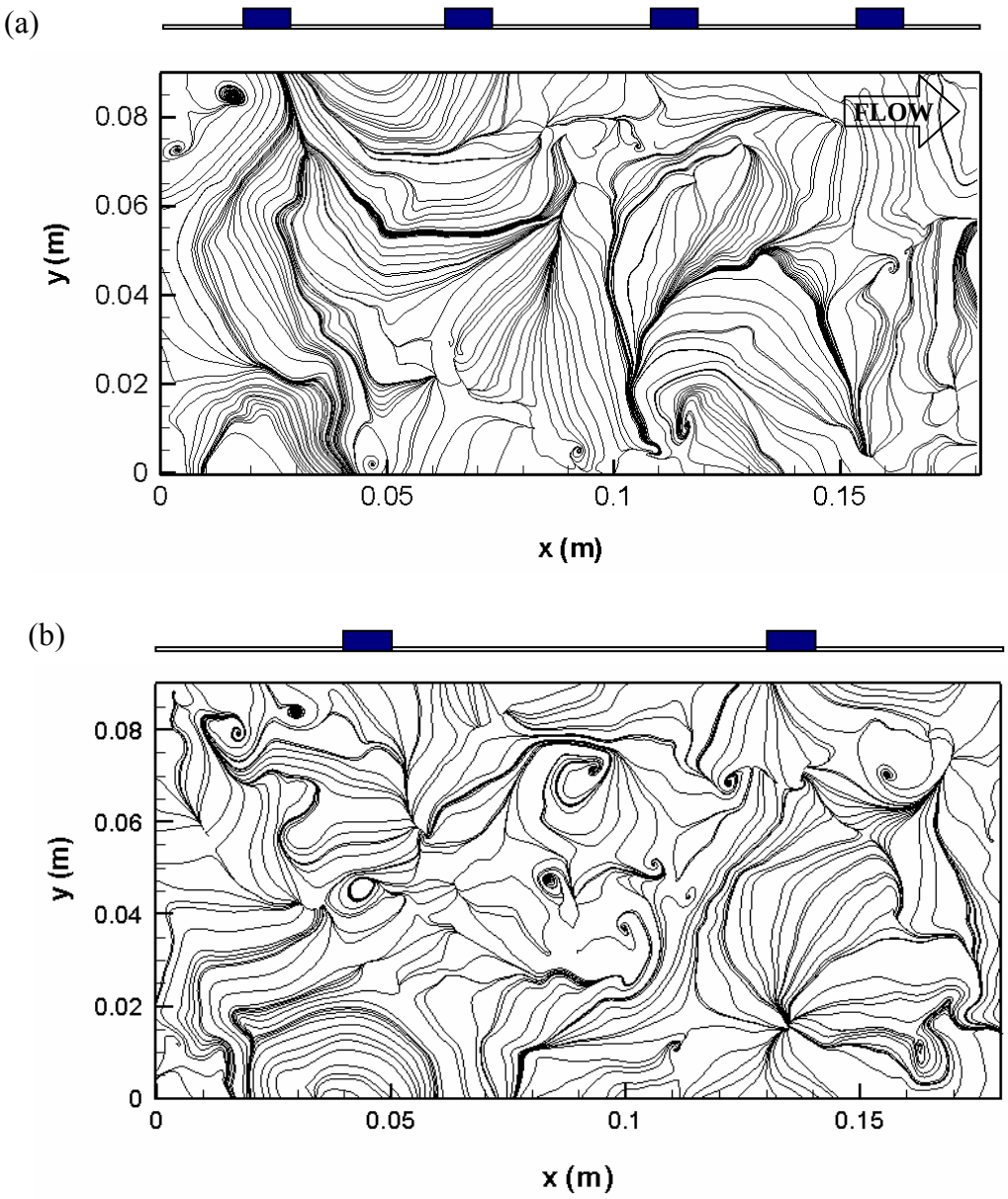

Figure 5.8 Streamtraces of $(u-U_0)/U_{Bulk}$ vs v/U_{Bulk} vectors on the free-surface obtained by LES for flow over rib roughness with 8.5 cm flow depth and roughness wavelength of (a) 4.5 cm, and (b) 9 cm.

Figure 5.9 and Figure 5.10 present the turbulence fluctuations at a given instant. Higher turbulence intensity areas are found in the shear layers originating at the crests of the roughness elements. The major contributions to the peak in the turbulence intensities are reported to be from large-scale organized structures that arise from flow separation at the crest (Maddux, 2002; Yue, 2003). Turbulent shear layers are observed to spread and dissipate with distance from the roughness crest.

Figure 5.9 shows that with increasing flow depth both the peak in the turbulence intensity and its streamwise extent increases. At the instant plotted in the figure, for flow depth of 6 cm, 8 cm and 10 cm, horizontal extent of this region is observed to be 7*k*, 10*k*, and 12*k*, respectively. Majority of the turbulent structures are generated in these regions, which further affect the location of the flow reattachment.

For flow over ribs shown in Figure 5.10, the turbulence intensities appear to have higher peaks than those of dunes. However, spread of high intensity contours is shorter than dunes. For transitional roughness shown in Figure 5.10.a, the contours of high turbulence intensity join to that of next roughness element. For *k*-type roughness, even though the contours reach almost to the next element, they do not overlap with each other.

The vertical spread of this region remarkably smaller for transitional roughness. Among the five flow cases presented in Figure 5.9 and Figure 5.10, *k*-type rib roughness has the largest vertical spread of turbulence intensities. The longest spread is observed to be in flow over dunes with the highest flow depth of 10 cm (Figure 5.9.c).

Time-averaged turbulent intensities for flow over dunes and ribs are presented in Section 5.3.4.

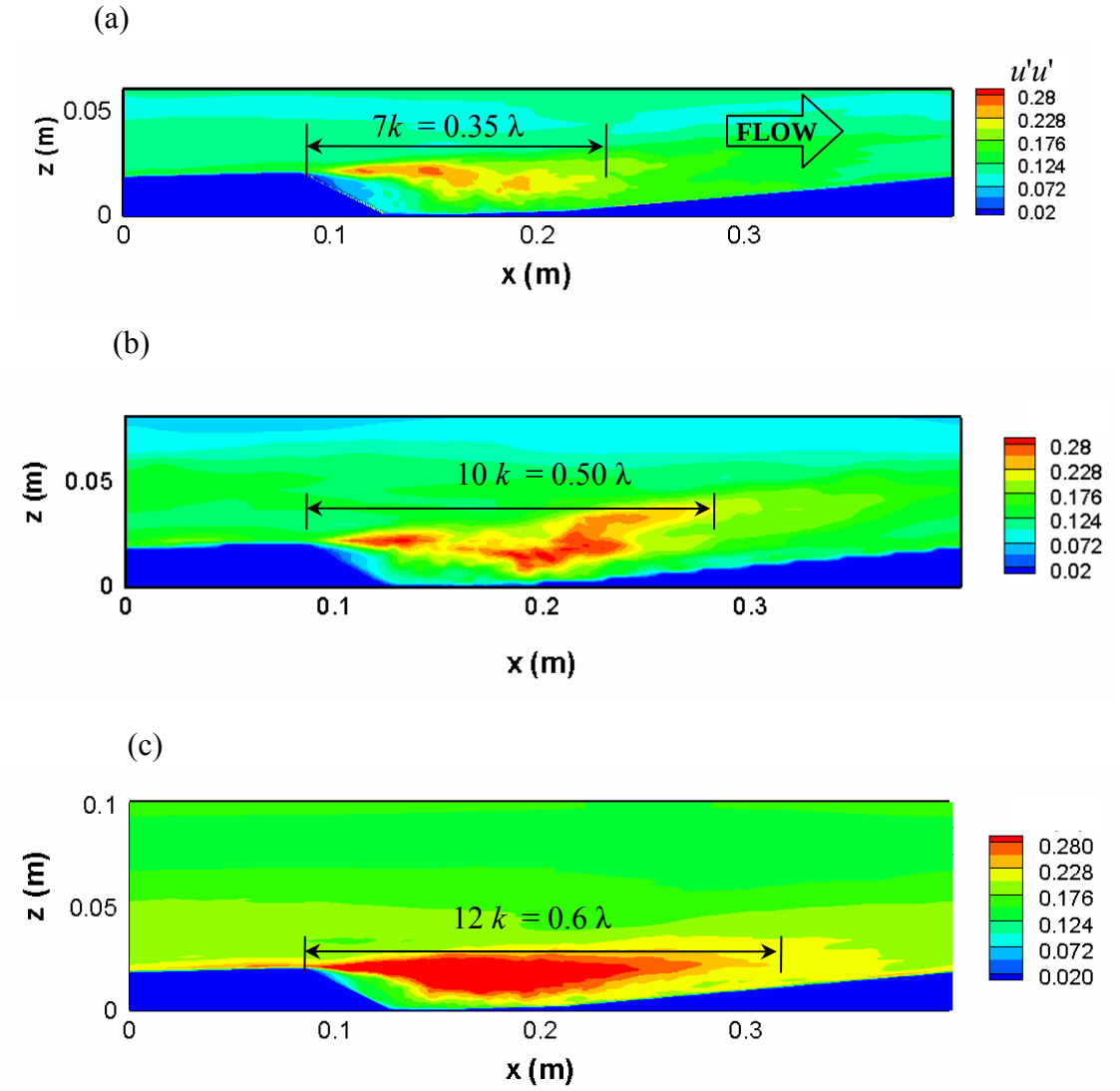

Figure 5.9 LES results for instantaneous streamwise turbulence fluctuations normalized by U_{Bulk} for flow over dunes with flow depth of (a) 6 cm, (b) 8 cm, and (c) 10 cm.

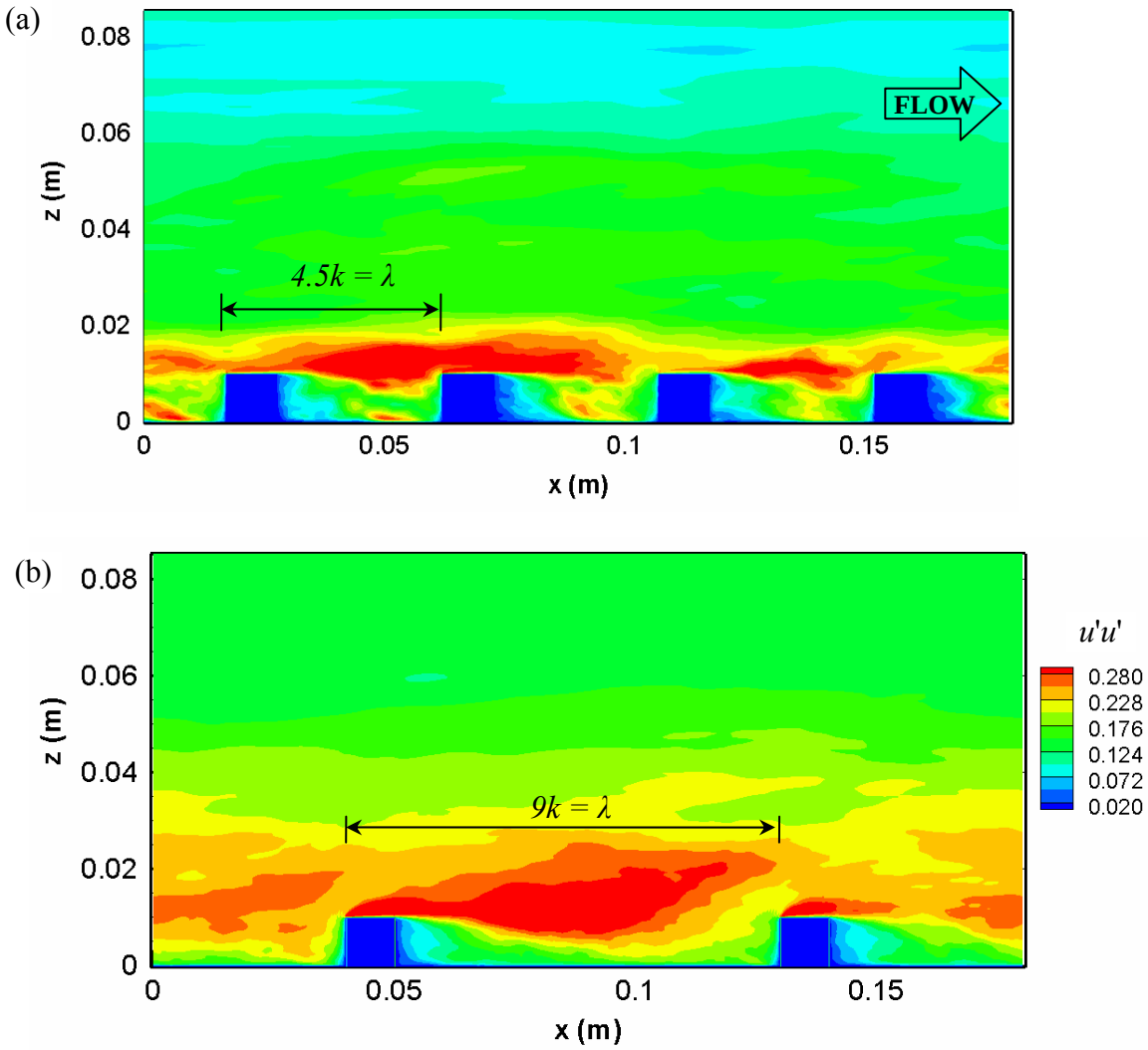

Figure 5.10 LES results for instantaneous streamwise turbulence fluctuations normalized by U_{Bulk} for flow over rib roughness with 8.5 cm flow depth and roughness wavelength of (a) 4.5 cm, and (b) 9 cm.

5.2.1 Coherent Structures

As mentioned in Chapter 4, identification of coherent vortical motions is an important part of this study, due to their involvement in free-surface texture. The isosurfaces of vorticity magnitude, $|\vec{\omega}|$, for flow over dunes and rib roughness are shown in Figure 5.11, Figure 5.12, and Figure 5.13. In all three figures, the high vorticity areas are observed to be aligned around the shear layer of Figure 5.9 and Figure 5.10.

Figure 5.11 shows the effect of flow depth on vortical motions for flow over dunes. Visual comparison of the plots in Figure 5.11 allows inferring that increase in the flow depth causes an increase in the vorticity across the flow depth. Increased relative submergence precludes protrusion of the vorticity created near the bed to the free-surface. Since the cases shown in the figure have the same bulk velocity, the increasing flow depth indicates increasing Reynolds number.

Vortical structures are observed to be generated at the separation zone, along the shear layer developing from the roughness crest and the reattachment point. While transported by the main flow, these structures align with an angle. This angle of inclination has previously been observed in boundary layers at zero pressure gradient conditions (Head & Bandyopadhyay, 1981; Krogstad & Kaspersen, 1991) to be close to 45^o. They explain this inclination by vortex stretching due to the mean shear that causes a tilting of the structure towards the wall.

The ellipses in Figure 5.11, Figure 5.12, and Figure 5.13 are rotated by 45^o. The vortical structures suspended in the main flow are observed to align with the same angle. They are transported downstream, and most of them dissipate before reaching to free-

surface. In compliance with the change in Reynolds number, with decreasing flow depth, more structures are observed in the roughness region. However, as dissipation rate also increases there is not substantial increase in the extent of the reach of these structures with flow depth.

For the rib roughness flows, it can be observed from Figure 5.12 and Figure 5.13 that *k* type roughness generates more vortical motion than the transitional roughness. However, higher vorticity regions are observed in the groove of the ribs for transitional roughness. Another important conclusion from the comparison of Figure 5.11, Figure 5.12 and Figure 5.13 is that, even with their higher submergence ratios, rib roughness causes more vortical motion, and thus mixing throughout the water column. As more vortex cores reach to the free-surface region, a stronger roughness – free-surface texture interaction is expected for flow over ribs than that for dunes.

As mentioned in Chapter 4, different cut-off values reveal different patterns. Even in the case that vortex core does not reach to the free-surface, higher vorticity regions can be observed at the free-surface in with detailed vorticity contour levels. Figure 5.12 and Figure 5.13 show the vorticity contours with two different cut off values of 100 and 200 for rib roughness of 4.5 cm and 9 cm wavelength.

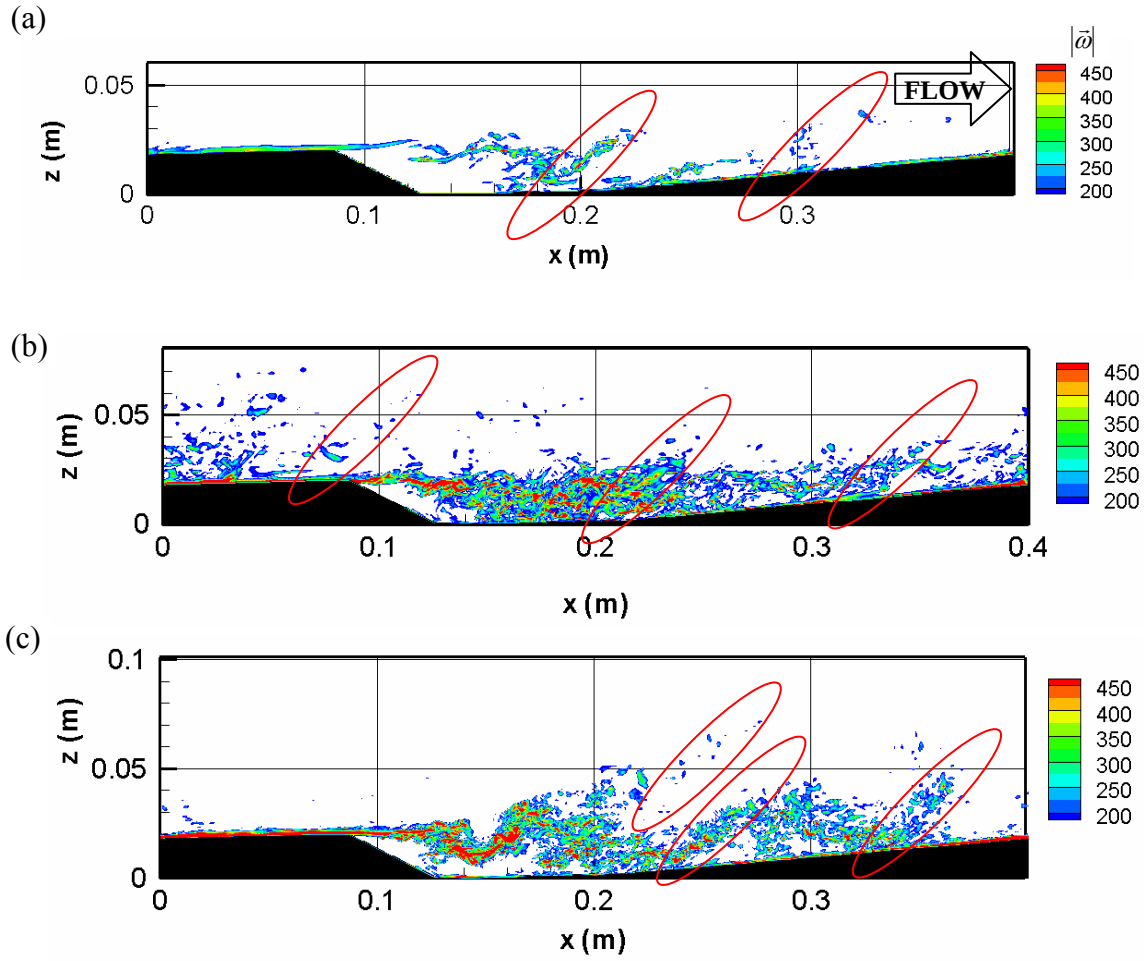

Figure 5.11 Contours of vorticity magnitude for flow cases obtained by LES for flow over dunes with flow depth of (a) 6 cm, (b) 8 cm, and (c) 10 cm.

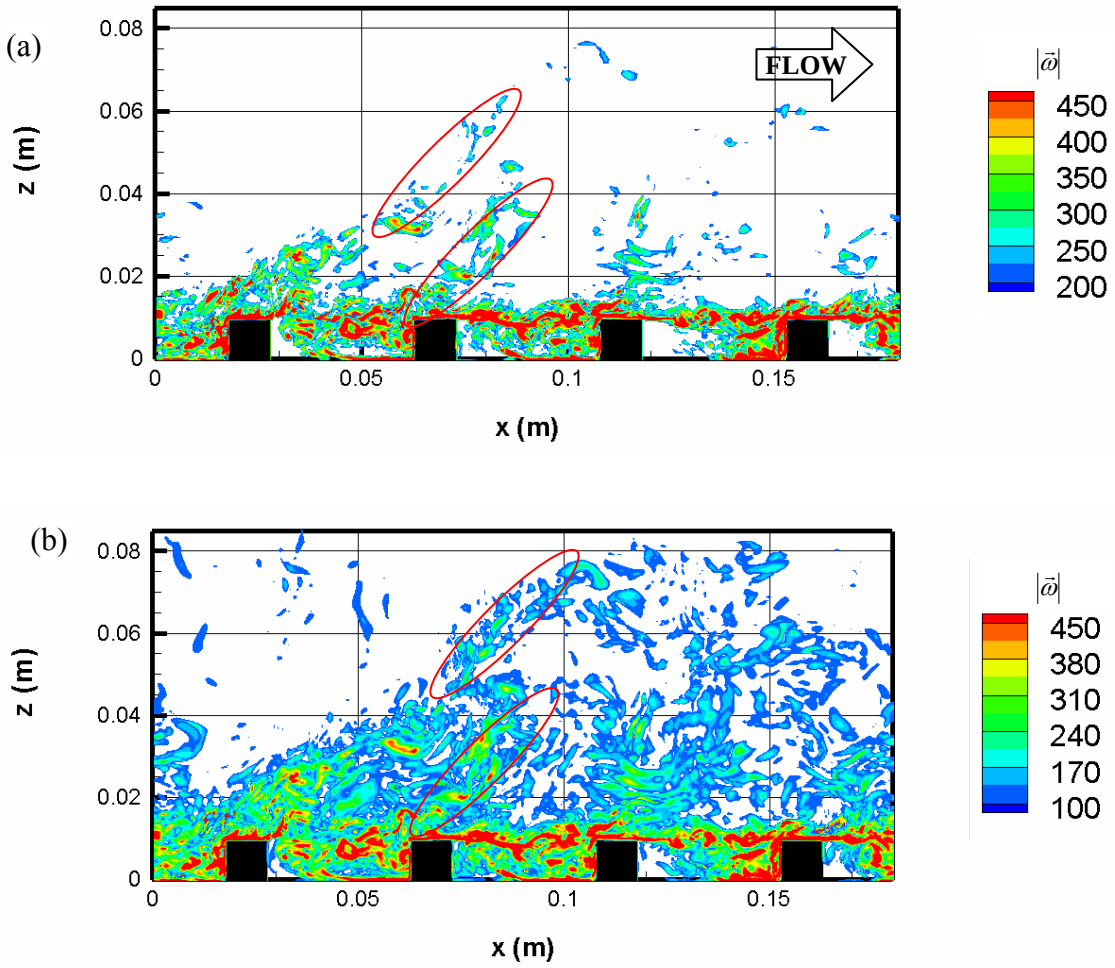

Figure 5.12 Contours of vorticity magnitude for flow over rib roughness with 8.5 cm flow depth and 4.5 cm roughness wavelength (R02) with cutoff value of (a) 200, and (b) 100.

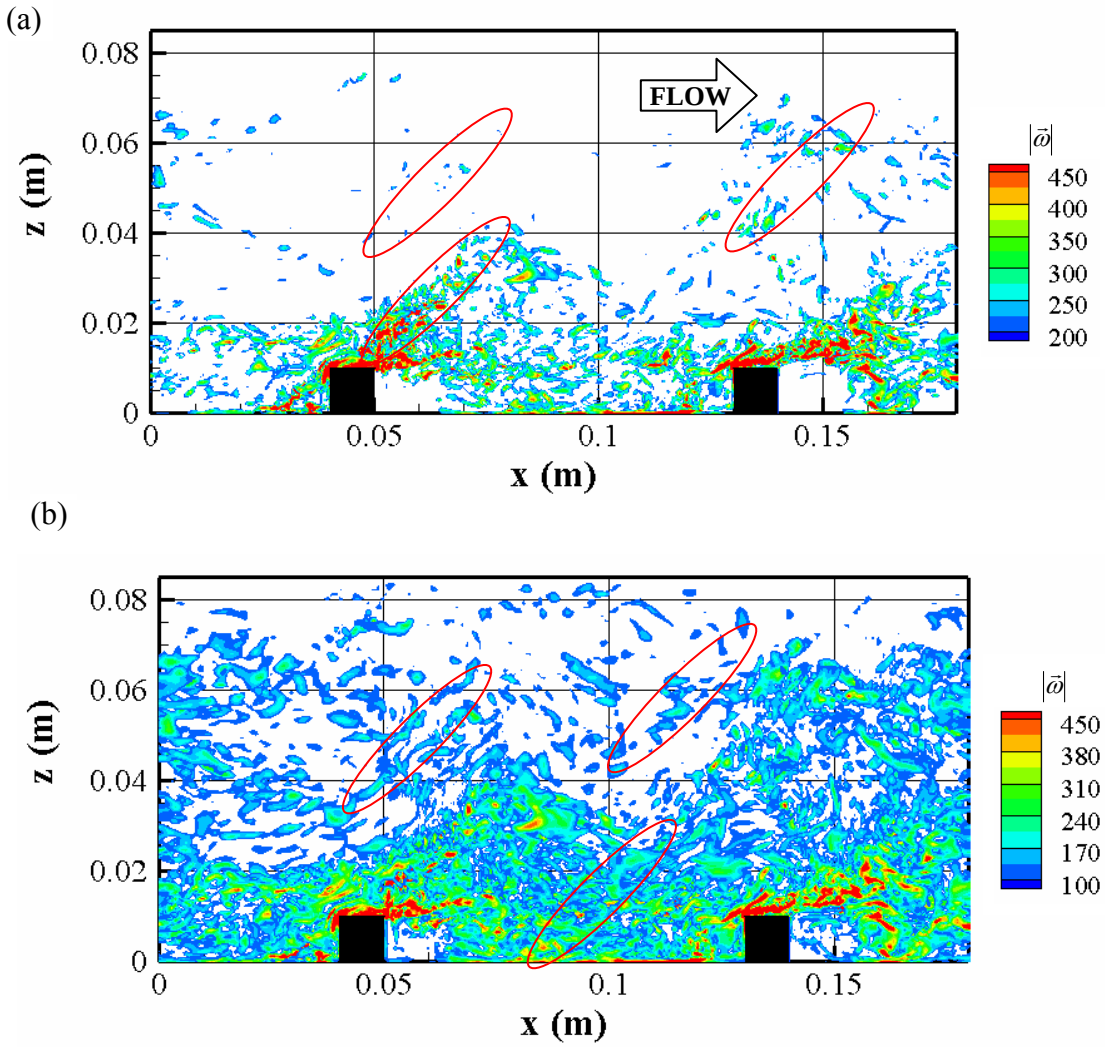

Figure 5.13 Contours of vorticity magnitude for flow over rib roughness with 8.5 cm flow depth and 9 cm roughness wavelength (R05) with lower cutoff value of (a) 200, and (b) 100.

5.2.2 Free-Surface Texture

As discussed in Chapter 4, images recorded at the free-surface were used to quantitatively and qualitatively analyze the free-surface texture. By changing the position of the lights and the camera with respect to free-surface different structures can be revealed. Smolentsev & Miraghaie (2005) state the three types of disturbance that always

present at the free-surface at the same time as gravity waves, capillary waves, and macroturbulence structures. However, not all of them are expected to be dominant for given flow conditions. Figure 5.14 through Figure 5.15 show sample images of the free-surface texture, for the smooth bed flow conditions listed in Table 2.1. The images in Figure 5.14 were obtained using the experimental arrangement given in Figure 2.9. An immediate observation is the existence of a spectrum of waves with various sizes. The size of the periodic largest structures in Figure 5.14 changes steadily with increasing flow depth. For shallow open-channel flow, the velocity of the surface waves is expected to linearly change with the square root of the flow depth ($c^2 = g\,h$). For a constant main flow velocity, the change in the wave speed is associated with the increase in the wavelength. For flow depth of 6 cm in Figure 5.14.a, the wavelength is observed to be 9.2 cm, which is increasing to 14.3 cm and 17.0 cm for flow depths of 8 cm and 10 cm, respectively. While the dimension of larger waves increases with increasing flow depth, it is difficult to draw conclusions about the smaller waves by just looking at the Figure 5.14.

Figure 5.15 shows the free-surface texture obtained by illuminating the free-surface from the sides of the channel through a 1-cm slit at the black masks covering the channel walls, as sketched in Figure 2.11. The camera zoomed on the central part of the channel. As can be seen from this figure, under these recording conditions, the large waves are masked and the smaller wavelength waves are enhanced. It can also be observed that an overall waviness presence is observed for larger depths.

For the quantitative analysis of the free-surface structures a different illumination arrangement was chosen as illustrated in Figure 2.13. The reason for choosing this arrangement is related to the fact that the conditions used for recording of the images

shown in Figure 2.9 and Figure 2.11 are not easily achievable under field conditions. The images shown in Figure 5.15 for smooth bed flows are very similar to the observations that we can make on the free-surface of a river with the naked eye from the riverside.

The free-surface velocity for all the flow cases discussed in this section was kept around a constant value. Experiments with various roughness types were subsequently made using the same flow depth. Consequently, the change in the surface texture can then be associated with the change in roughness.

Figure 5.17 compares images of free-surface for roughness conditions RL090 (rib roughness with λ =90 mm) and RL045 (rib roughness with λ = 45 mm) and the smooth bed. The visual inspection of the images allows us to observe that free-surface texture reacts to the changes in the bed roughness, and relative submergence. For all flow depths shown in Figure 5.17.a through Figure 5.17.c, free-surface over smooth bed is remarkably different than rib flows with either spacing. For the same flow depth and varying roughness condition, rib roughness with 4.5 cm wavelength features the highest free-surface wave amplitude. The effect of changing flow depth is not as obvious as that of roughness. However, a decrease in the wave amplitude with increasing flow depth can be observed with careful inspection. A qualitative analysis of the waves on the free-surface is needed to substantiate the effect of flow depth on free-surface texture. An analysis employing the power spectrum analysis is presented and discussed in Section 5.3.2.

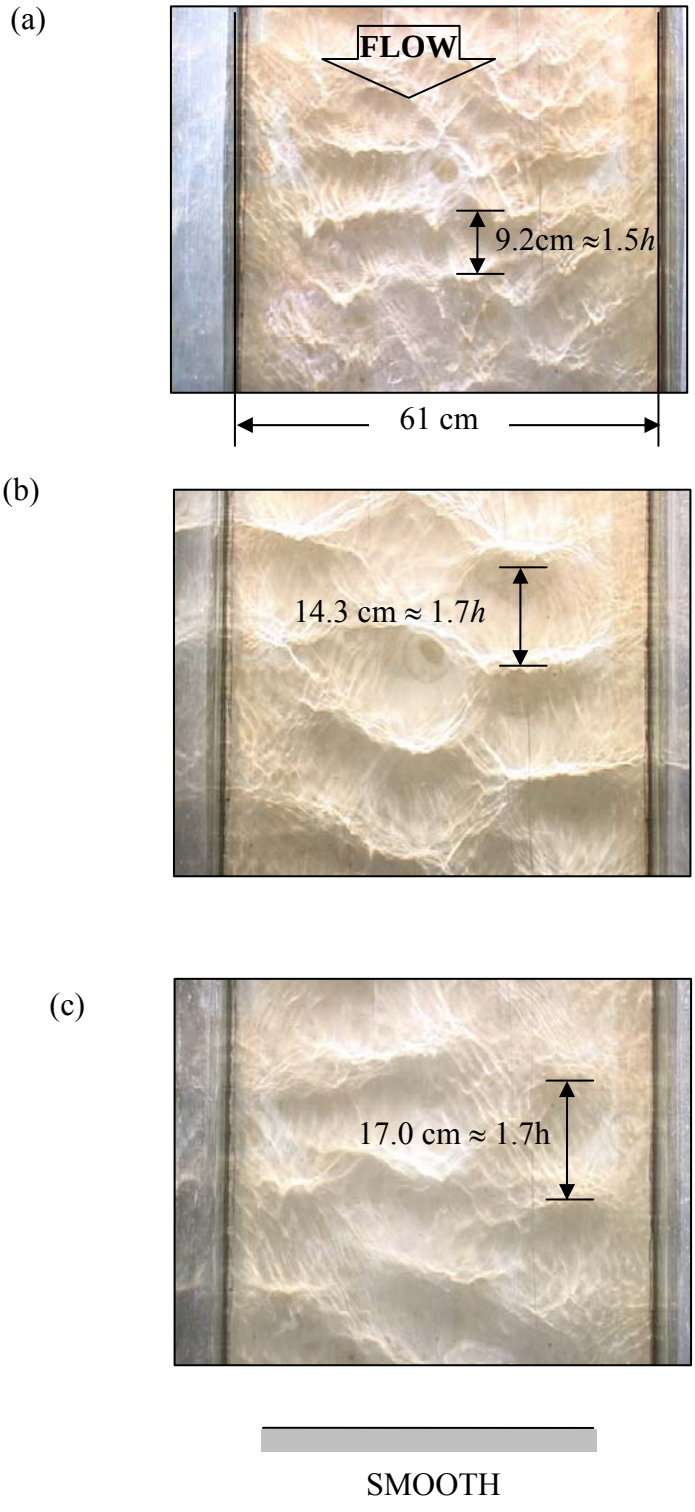

Figure 5.14 Free-surface textures for flow over smooth bed with flow depth of (a) 6 cm, (b) 8 cm, and (c) 10 cm. Illumination condition and camera orientation are given in Figure 2.9.

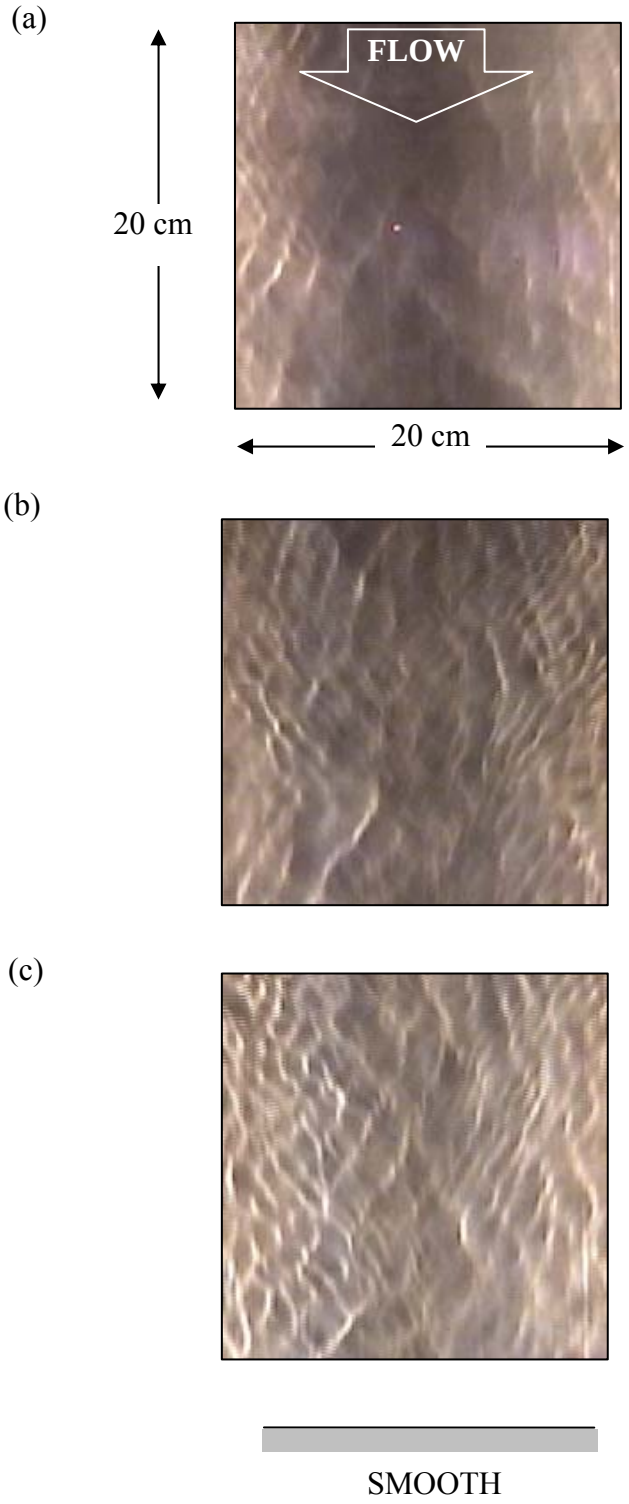

Figure 5.15 Free-surface textures for flow over smooth bed with flow depth of (a) 6 cm, (b) 8 cm, and (c) 10 cm. Illumination condition and camera orientation are given in Figure 2.11.

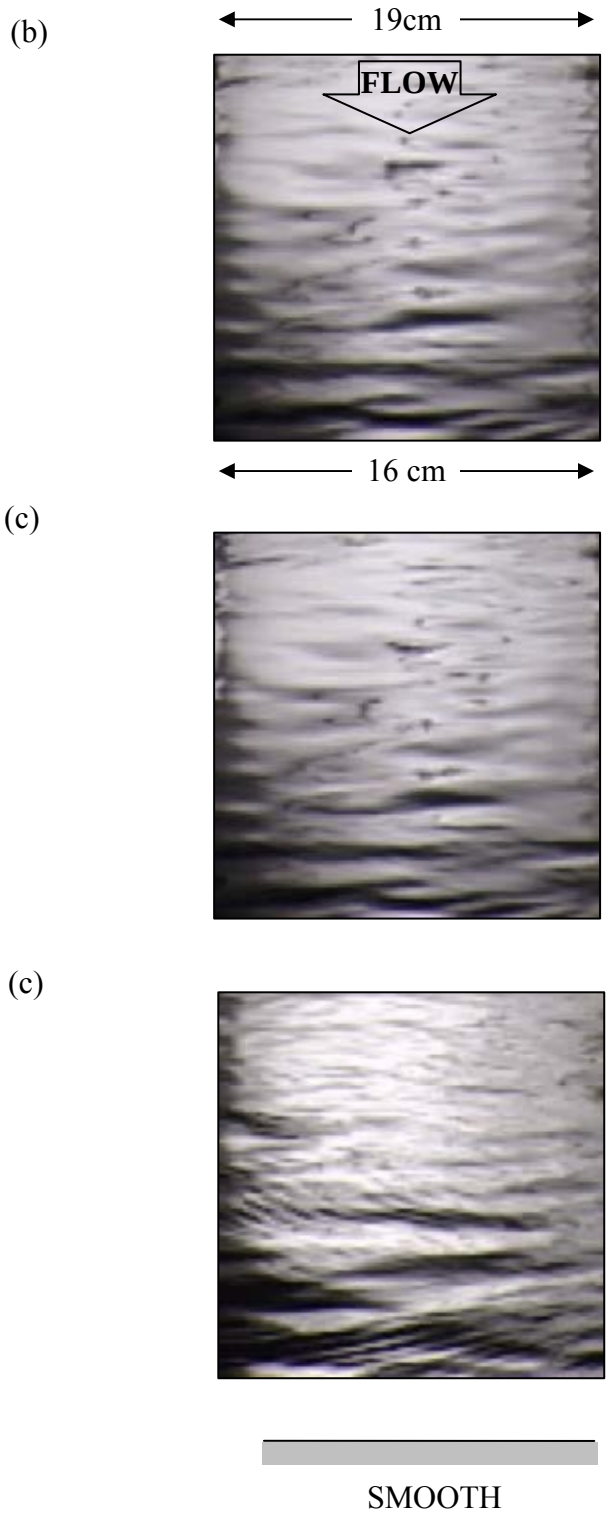

Figure 5.16 Free-surface textures for flow over smooth bed with flow depth of (a) 6 cm, (b) 8 cm, and (c) 10 cm. Illumination condition and camera orientation are given in Figure 2.13.

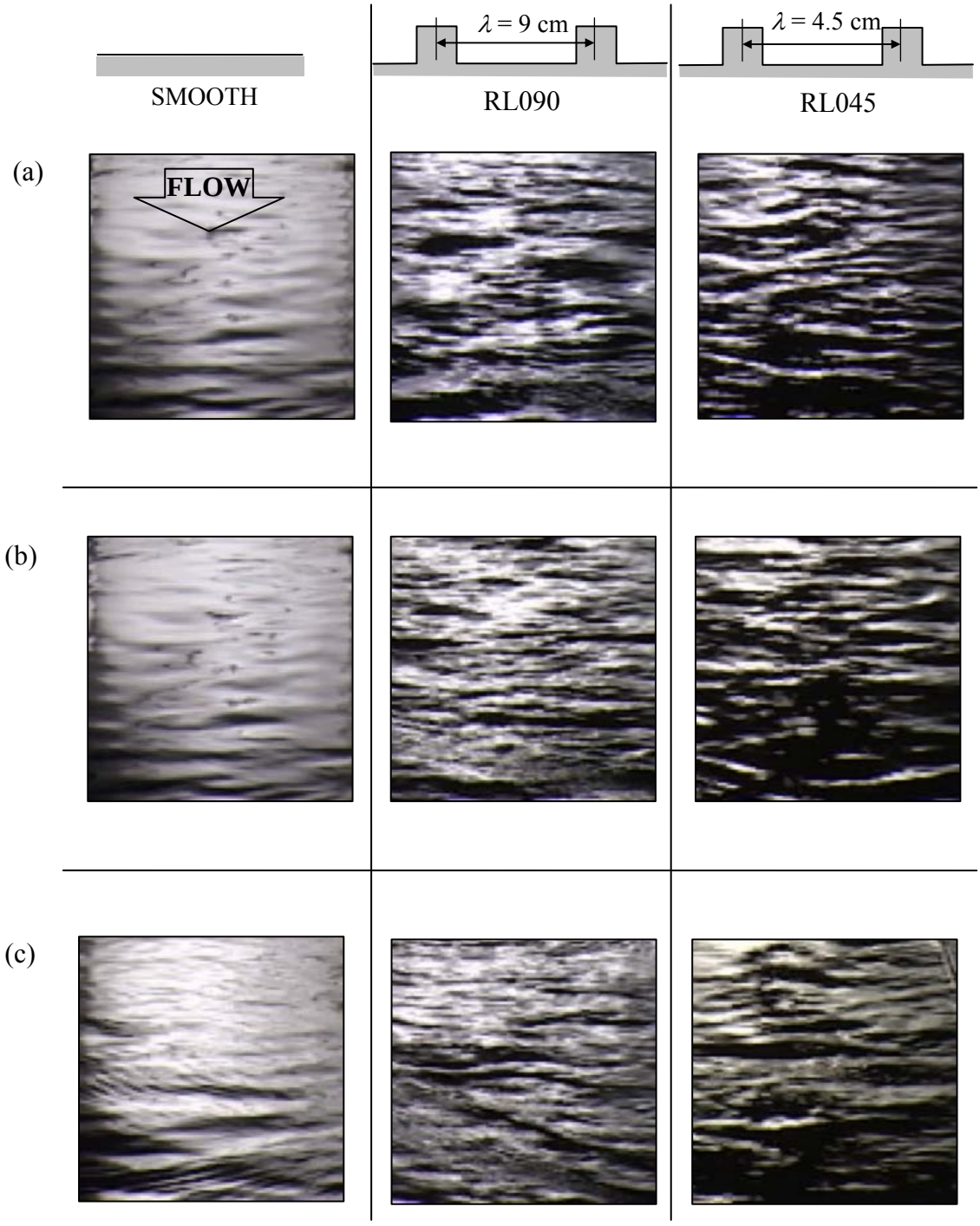

Figure 5.17 Comparison of free-surface textures for flow over smooth bed with flow over rib roughness for flow depth of (a) 6 cm, (b) 8 cm, and (c) 10 cm. Illumination condition and camera orientation are given in Figure 2.13.

Experimental and numerical results for instantaneous features of the flow field provide valuable resource in meeting the research objectives given in Chapter 1.

Instantaneous streamlines of Figure 5.1 and Figure 5.2 illustrate the features of the flow over large-scale roughness. They demonstrate the separation, and reattachment around the roughness elements, and how roughness effect protrudes to the main flow. Especially for dune flows, the changes in the channel geometry create substantial roughness effect on the free-surface. The analysis of turbulence intensities in Figure 5.9 and Figure 5.10 exhibit the differences between the effect of dunes and ribs on the flow. Ribs, despite their higher submergence ratio, cause stronger shear layer. Since the majority of the turbulence structures are generated in this layer, stronger vortical structures are expected for flow over ribs. Consistent with this conclusion, more significant turbulence-free-surface interaction is anticipated for rib flows.

The vortical structures presented in Figure 5.11, Figure 5.12, and Figure 5.13 provide additional support to earlier inferences. The effect of flow depth – Reynolds number – and roughness condition are detected in the plots. More vortex cores approach to the free-surface region for rib flows. For flow over dunes, increasing depth caused more structures. However, a noticeable difference in the number of structures reaching to free-surface is not observed.

Figure 5.14 through Figure 5.17 show the free-surface images captured under various illumination conditions. Figure 5.17 provided a strong evidence for the hypotheses for this study, illustrating a considerable variation in the free-surface texture with changing roughness condition.

5.3 Time-Averaged Flow Field

Streamlines derived from time-averaged streamwise velocities for the flows over dunes and ribs are shown in Figure 5.18 and Figure 5.19. The streamlines display similar patterns for all three flow cases in Figure 5.18. The influence of the bed roughness on the streamline pattern is extended towards the free-surface for smaller depth. Unlike the instantaneous flow field, the size of the recirculation area does not change with changing flow depth for time-averaged flow field.

Figure 5.19 shows the streamlines for both transitional and *k*-type roughness. The streamlines in the outer layer are uniform as in the flow over dunes. By changing the roughness wavelength, the streamline patterns in the vicinity of the roughness elements experiences a substantial difference. The recirculation area fills the cavity between two consecutive ribs for transitional roughness. For the *k*-type roughness, a small separation zone is seen at top of the rib. Flow reattaches on the top of the rib, and separates again from the corner of the rib. Next reattachment point occurs in the groove. Second recirculation area with a reverse circulation is generated upstream the next rib, bending the streamlines towards the top of the rib. A well defined recirculation area downstream the crest and a uniform streamline distribution in the outer layer is observed for flow over *k*-type rib roughness.

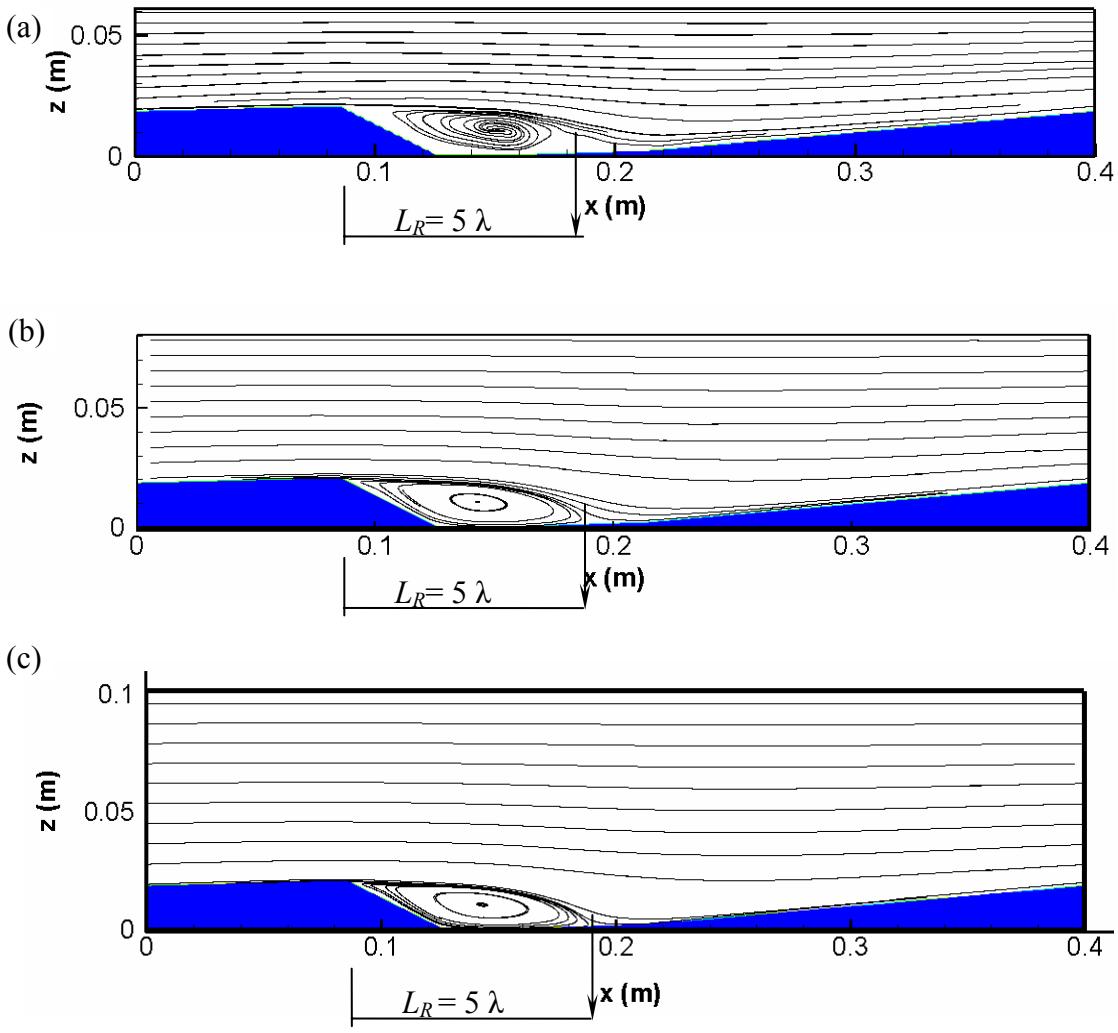

Figure 5.18 Streamlines of time-averaged vector field obtained by LES for flow over dunes with flow depth of (a) 6 cm, (b) 8 cm, and (c) 10 cm.

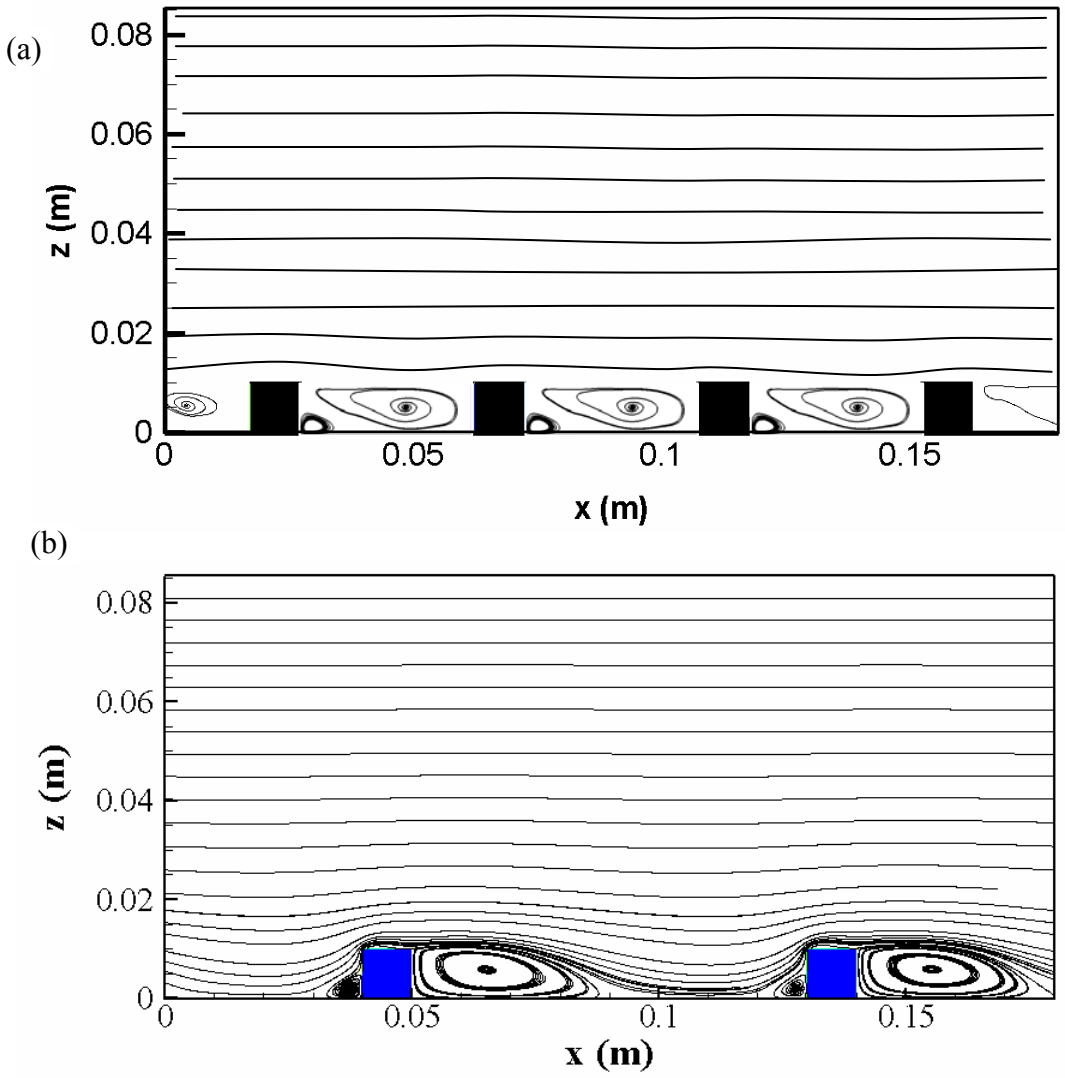

Figure 5.19 Streamlines of time-averaged vector field obtained by LES for flow over rib roughness with 8.5 cm flow depth and roughness wavelength of (a) 4.5 cm, and (b) 9 cm.

As mentioned earlier, the pressure distribution at the free-surface with numerical simulation is associated with the elevation head. Therefore, the contours of time-averaged pressure field illustrated in Figure 5.20 and Figure 5.21 can be interpreted as water surface elevations. Red zones represent the water elevations higher than the average elevation, while blue zones represent the lower elevations. The results for dune flow cases shown in Figure 5.20 reveal that the free-surface elevation displays larger variations from the average for lower flow depths. Both the lower and higher elevation areas expand with decreasing flow depth over dunes. This observation from the time-averaged flow field indicates that with decreasing flow depth the water surface elevation more strictly follows the channel bed elevation.

For ribs, the pressure distribution pattern is very different between the flow cases, as can be seen from Figure 5.21. Even with the very detailed contours of Figure 5.21.a, the signature of bed roughness pattern can not be observed at the free-surface of flow over transitional roughness. The streets of high and low pressure on the free-surface for *k*-type roughness flow illustrated in Figure 5.21.b are not seen for transitional roughness flow in Figure 5.21.a. With detailed pressure contours, a periodic pattern in the free-surface pressure distribution for *k* type roughness can be observed (Figure 5.21.b). This observation agrees with the results of the earlier studies reporting that as the roughness spacing approaches to the d-type, more flow over smooth wall properties are observed. Identical submergence ratios for ribs and dunes is suggested to be used in the subsequent studies to derive a decisive conclusion about the relative effects of ribs and dunes on the free-surface deformation and velocity distribution.

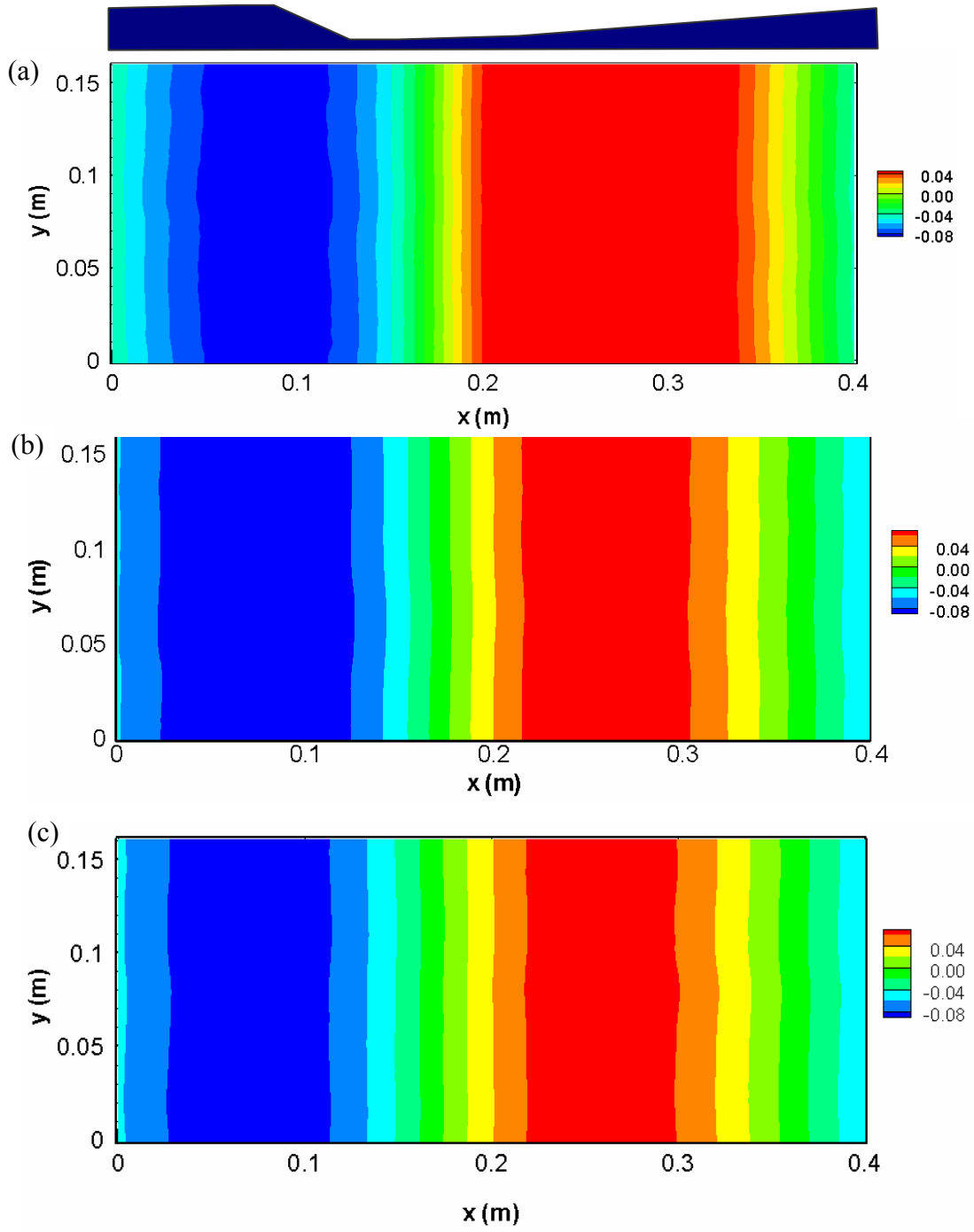

Figure 5.20 Contours of time-averaged pressure obtained by LES for flow over dunes with flow depth of (a) 6 cm, (b) 8 cm, and (c) 10 cm.

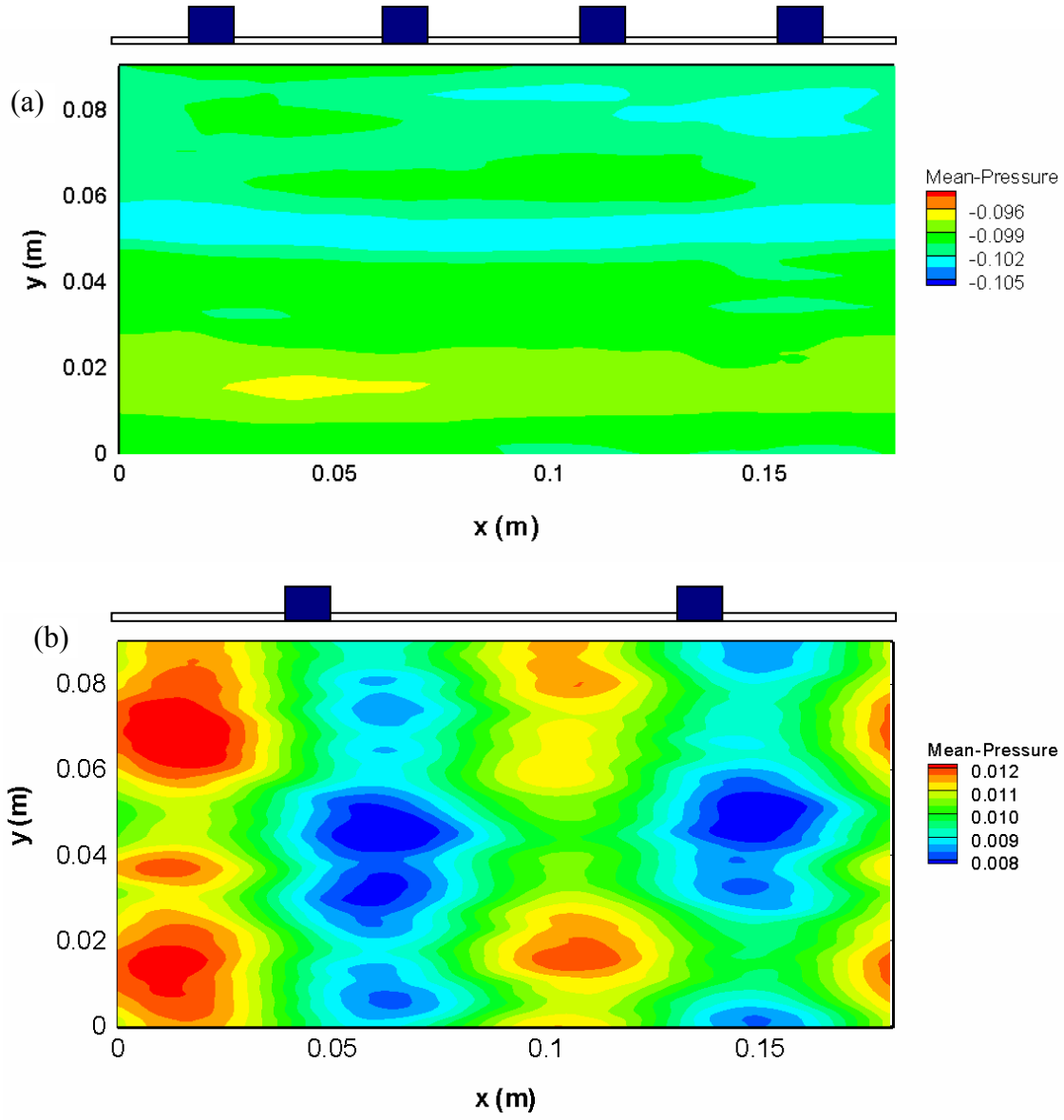

Figure 5.21 Contours of time-averaged pressure obtained by LES for flow over rib roughness with 8.5 cm flow depth and roughness wavelength of (a) 4.5 cm and, (b) 9 cm.

5.3.1 Analysis of Time-Averaged Free-Surface Texture

The analysis of the free-surface waviness using the power spectrum of the recordings is based on the assumption that the variations in the gray-scale brightness in the images are directly related to the wave amplitude at the free-surface. Larger surface disturbances are linked to larger brightness variation. Thus, the photos in Figure 5.22 and Figure 5.23 can be converted into power spectra of the wave amplitudes, through which the effect of depth and roughness condition changes on the free-surface texture can be quantified.

For smooth bed flows in Figure 5.22, Froude number is almost constant at 0.5, while Reynolds number increases with flow depth. For higher Reynolds number turbulence-interface interaction is expected to be more pronounced. The power spectral density plot of the recordings in Figure 5.22 show that, for flow over smooth flat bed, the peak moves towards larger frequency with increasing flow depth, indicating a more uniform texture at the free-surface.

The larger peak at Figure 5.23 for the rib cases for larger flow depth is an indicator of larger waves at the free-surface. As Smolentsev & Miraghaie (2005) reported, higher frequencies are also associated with the turbulence-interface interactions.

It is expected that with constant Froude number the spectra of the surface texture showing the contributions from the different frequency stays the same. This is substantiated by scrutinizing the power spectra given in Figure 5.23 for flow depths of 6 cm, 8 cm, and 10 cm. The flow conditions given in Figure 5.23.a, b, and c have similar

Froude numbers, but very different Reynolds numbers. Similar Froude numbers keep the power spectrum form similar, while increasing Reynolds number increases the peak.

An important conclusion from Figure 5.23 is that the dominant wavelength in the spectra is associated with rib wavelength, demonstrating free-surface texture reacts to the changes in the channel bottom. Both changes in the spectra and amplitude observed indicate more irregularities at the interface for rib roughness.

Analysis of Figure 5.22 and Figure 5.23 reveals that waviness we observe at the free-surface of an open-channel is a combination of effects of *Re*, *Fr*, and roughness. By comparing the power spectra for two different bed conditions, it is concluded that, for the *Fr* and *Re* range tested in the study, the dominant effect is observed to be from roughness.

As there is no substantial change in *Fr* of the experiments, it is hard to make a conclusion about *Fr* effect on the waves, but it is expected that with increasing *Fr*, more uniform spectra, and surface waviness are expected. The increase in *Re* moves the peak to higher frequencies and increases the magnitude of the peak. With increasing *Re*, more turbulence – free-surface interaction and more agitated waviness pattern is expected.

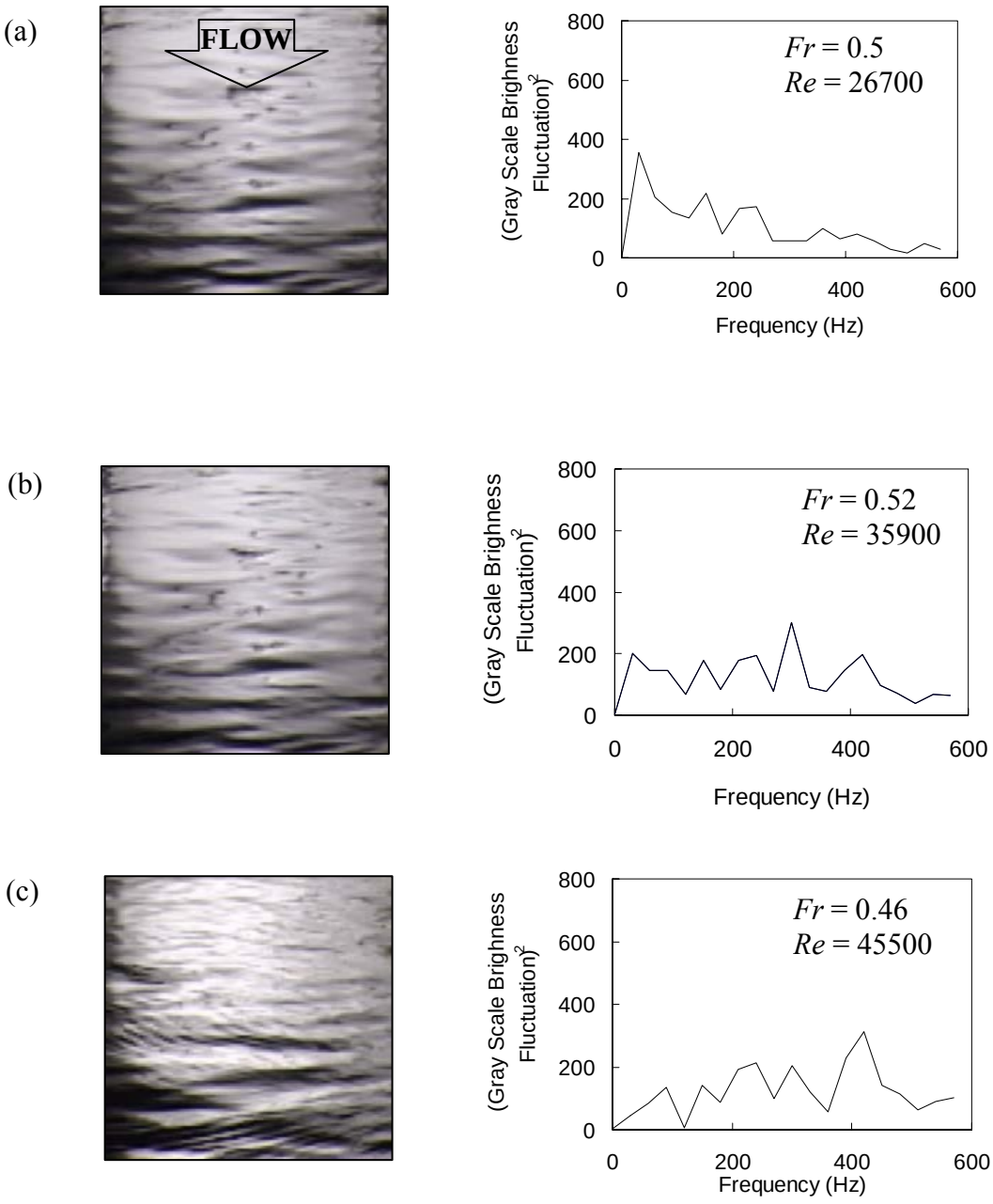

Figure 5.22 Power spectra for the free-surface texture recordings for flow over smooth bed with flow depth of (a) 6 cm, (b) 8 cm, and (c) 10 cm.

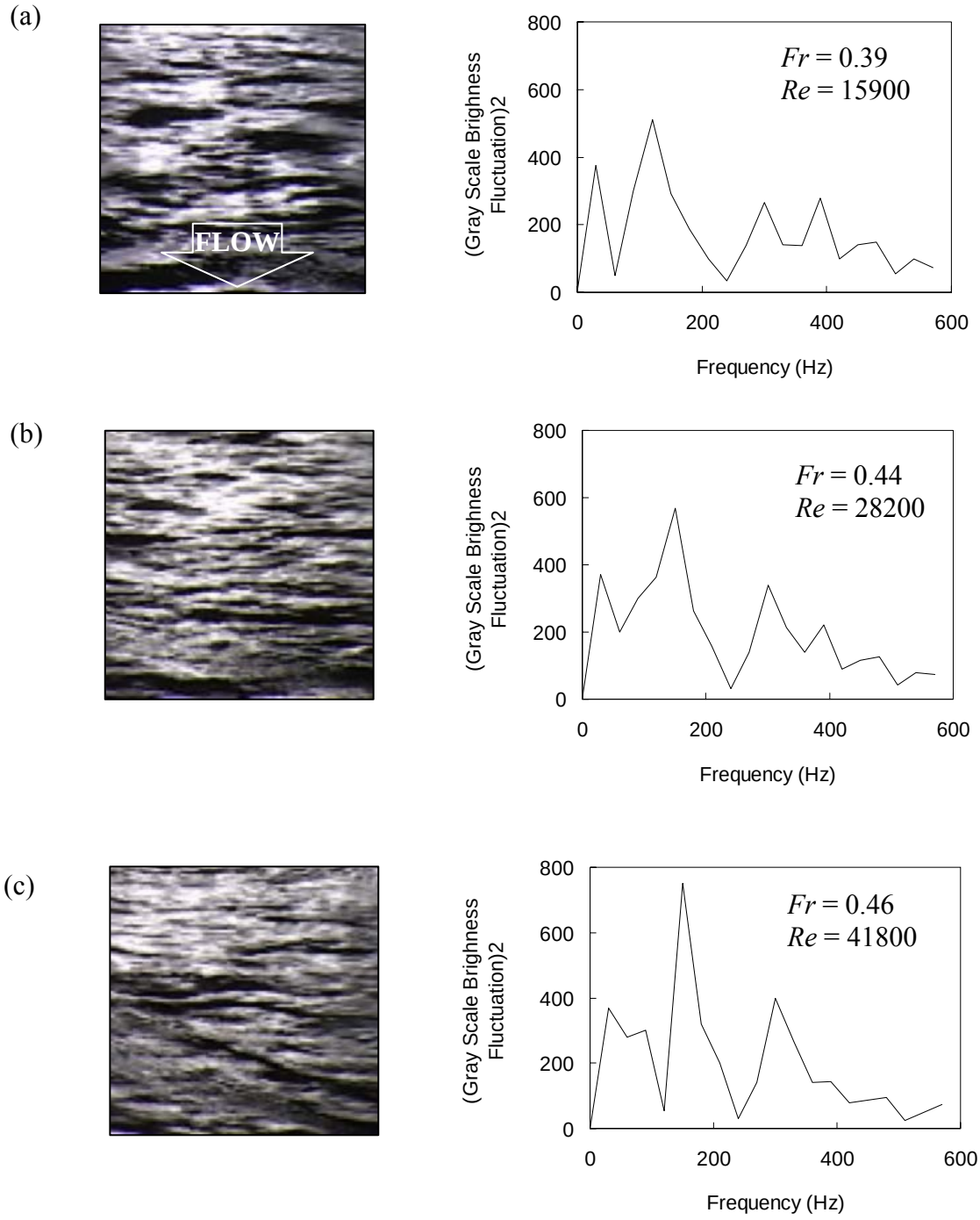

Figure 5.23 Power spectra for the free-surface texture recordings for flow over rib roughness with $\lambda = 9$ cm with flow depth of (a) 6 cm, (b) 8 cm, and (c) 10 cm (*Fr* and *Re* calculated over roughness crest, L1).

5.3.2 Free-Surface Velocity Distribution

The velocity distribution at the fee surface was obtained experimentally by LSPIV and numerically by LES. Figure 5.24 shows the LSPIV results for the flow over smooth bed. Surface velocities normalized with depth-averaged velocity (bulk velocity, U_{Bulk}) are plotted for a 50 cm x 50 cm area located in the center of the channel. The surface velocity is observed to be approximately 10% higher than U_{Bulk} for all three flow cases. The effect of side walls is increasingly noticed with the decrease of flow depth. Results feature a clear symmetry in the velocity distribution and a slight increase in the maximum U/ U_{Bulk} with the increase of the flow depth. Figure 5.24 (a) to Figure 5.24 (c) display that, in channel flows over smooth bed with aspect ratio of 6 – 10 a slight but consistent change in the velocity distribution in the spanwise direction occurs as the flow depth varies.

For the channel bed roughened with ribs, the free-surface velocity distribution for the same depths is changed. As can be seen in Figure 5.25, the ratio of the free-surface velocity, U_0, to bulk velocity, U_{Bulk}, decreases with addition of roughness elements. The average of the obtained U/U_{Bulk} ratio is 1.11 for case R01 (h= 6.5 cm and λ = 4.5 cm) and 1.13 for case R02 (h= 8.5 cm and λ = 4.5 cm). The normalized free-surface velocities shown in Figure 5.25 reveal that the velocity distribution experiences a higher variation for low flow depths than that of high flow depths, despite a lower average for normalized velocity magnitudes. The plots in Figure 5.25 display a clear difference from the uniform distribution of Figure 5.24 in the streamwise direction, which can be commented as the signature of the ribs on the free-surface.

Similarly, visual inspection of Figure 5.26, Figure 5.27, and Figure 5.28 confirms that there are substantial changes in the appearance of the free-surface when the flow depth and bed roughness characteristics are changed. Larger flow depths cause larger structures with

higher amplitudes. Both for rib and dune flows, the contours of high and low normalized free-surface velocities follow the roughness pattern in the channel bed. The maximum velocities occur at the centerline of the channel, away from the side walls. The velocities right above the roughness crest are consistently higher than those of other locations. The symmetry of the contours with respect to centerline is preserved for all flow cases.

A decrease in the flow depth leads to an increase in the variation in the free-surface velocities while causing a decrease in both the maximum and average normalized velocities. Roughness conditions RL090 (λ = 9 cm) and RL180 (λ = 18 cm) create same pattern in the statistics of the free-surface velocities reported in the figures. The average U/U_{Bulk} for these two cases is lower than that of RL045 (λ = 4.5 cm). This can be explained by the characteristics of the flow over *k*-type and transitional roughness. Transitional roughness causes a velocity distribution pattern in between smooth bed and *k*-type roughness flows. However, even for transitional roughness, the contours of U/U_{Bulk} follow the repetitive pattern of the roughness, with the roughness wavelength. Dunes, despite their smaller relative submergence ratios, do not create dramatic changes in U/U_{Bulk} statistics across the flow cases with different flow depth. However, the effect of local acceleration and decelerations caused by the dune geometry can also be seen at the free-surface.

Results of analysis of LSPIV data in Figure 5.24 to Figure 5.28 lead us to an important conclusion, which shapes the future direction of the current study, that is: local acceleration and decelerations of the flow over the roughness elements show their effect on the free-surface. This conclusion departs from the traditional approach of treating flow over dunes and gravel bed similar to the small-scale roughness flow. The results emphasize the need of considering channel bed roughness to accurately estimate discharge in open-channels with remote measurement techniques.

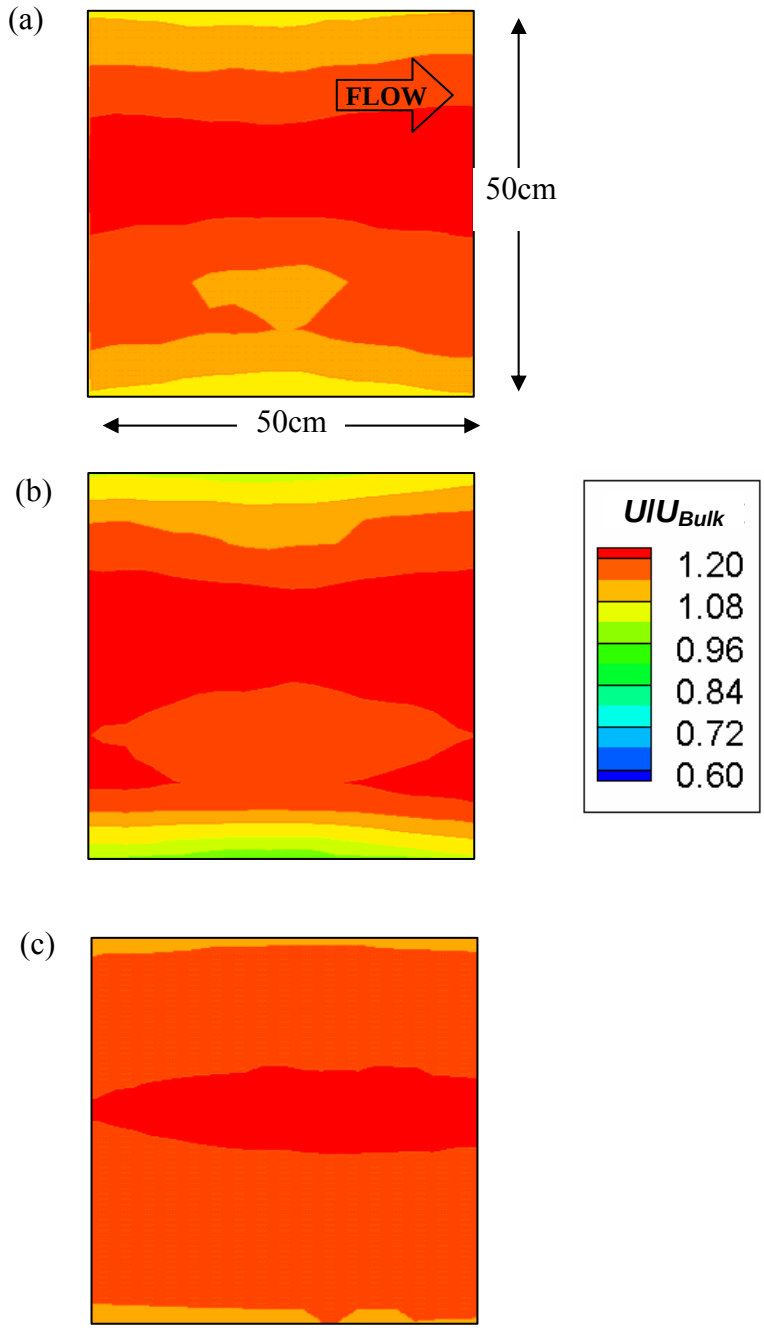

Figure 5.24 LSPIV results for normalized free-surface velocity distribution for flow over smooth bed for flow with flow depth of (a) 6 cm, (b) 8 cm, (c) 10 cm.

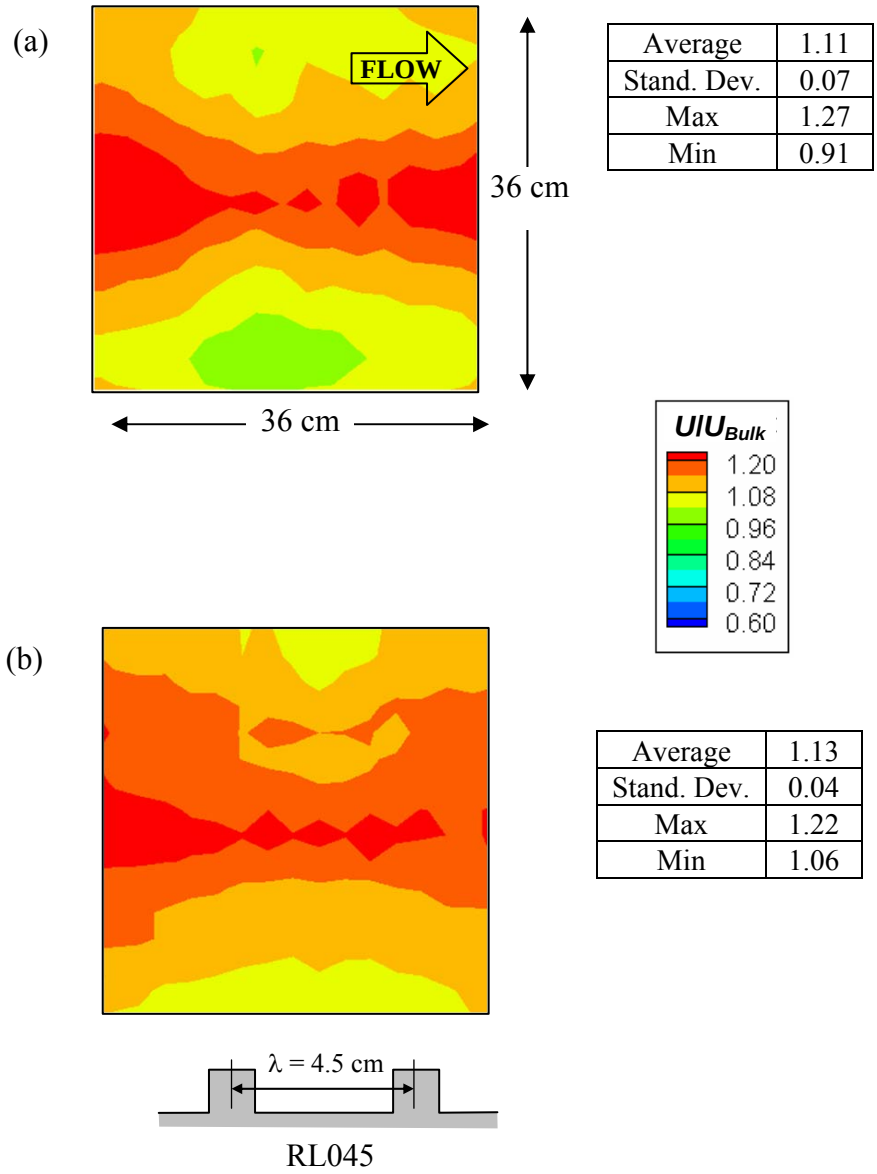

Figure 5.25 LSPIV results for normalized free-surface velocity distribution for flow over ribs with 4.5 cm wavelength and flow depth of (a) 6 cm (R01), and (b) 8 cm (R02).

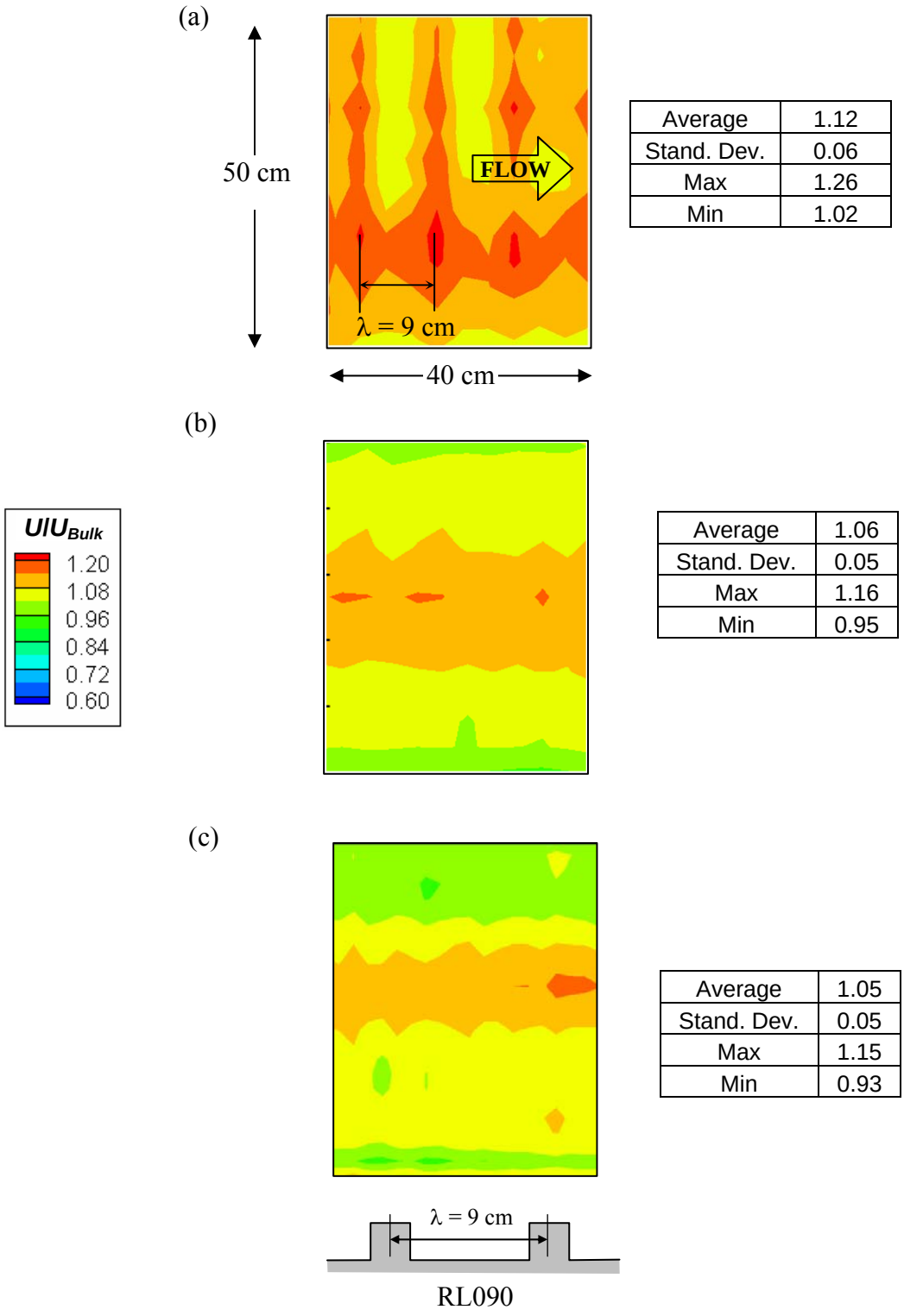

Figure 5.26 LSPIV results for normalized free-surface velocity distribution for flow over ribs with 9 cm wavelength and flow depth of (a) 6 cm (R04), (b) 8 cm (R05), and (c) 10 cm (R06).

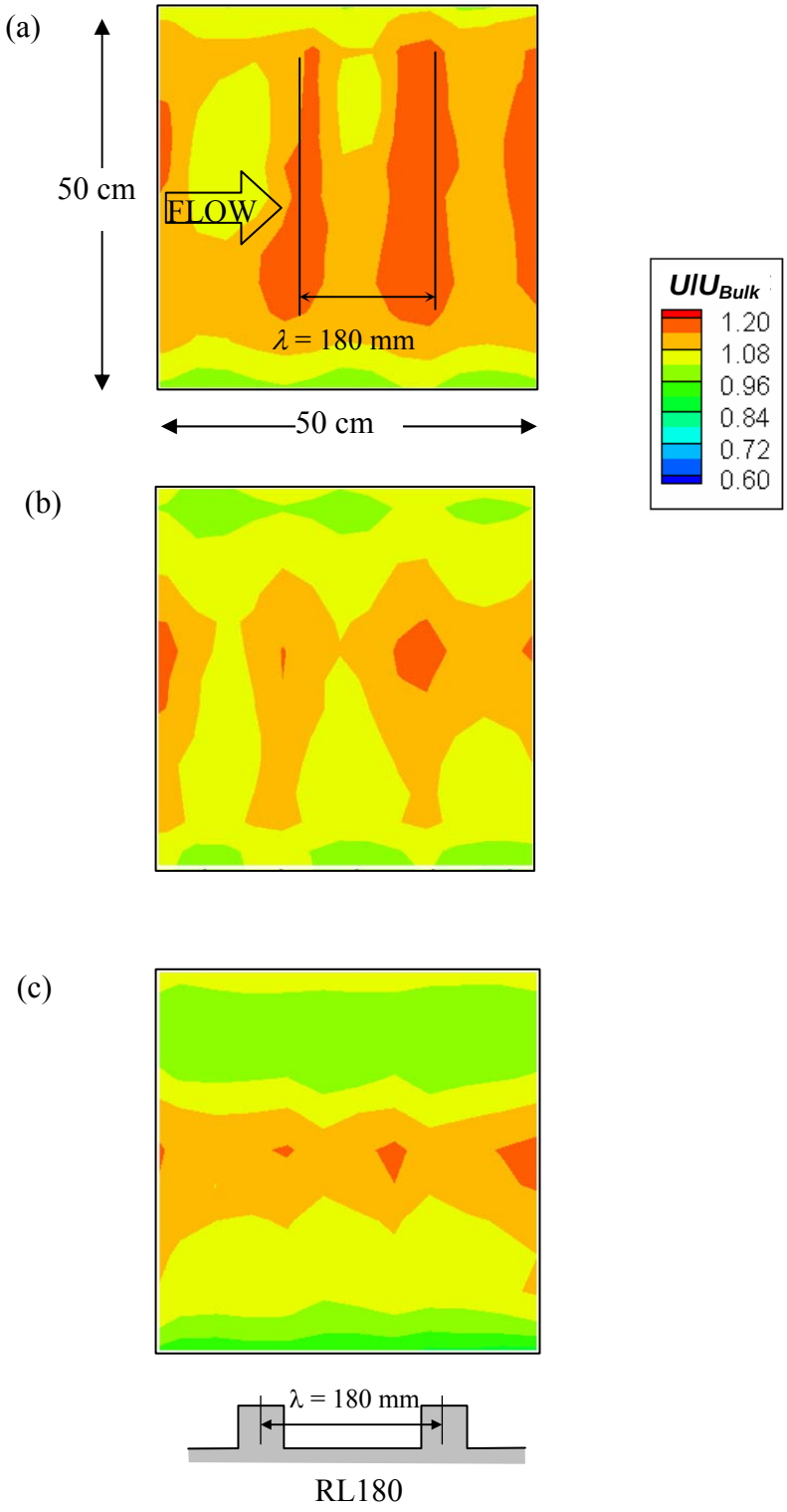

Figure 5.27 LSPIV results for normalized free-surface velocity distribution for flow over ribs with 18 cm wavelength and depth of (a) 6 cm (R07), (b) 8 cm (R08), (c) 10 cm (R09).

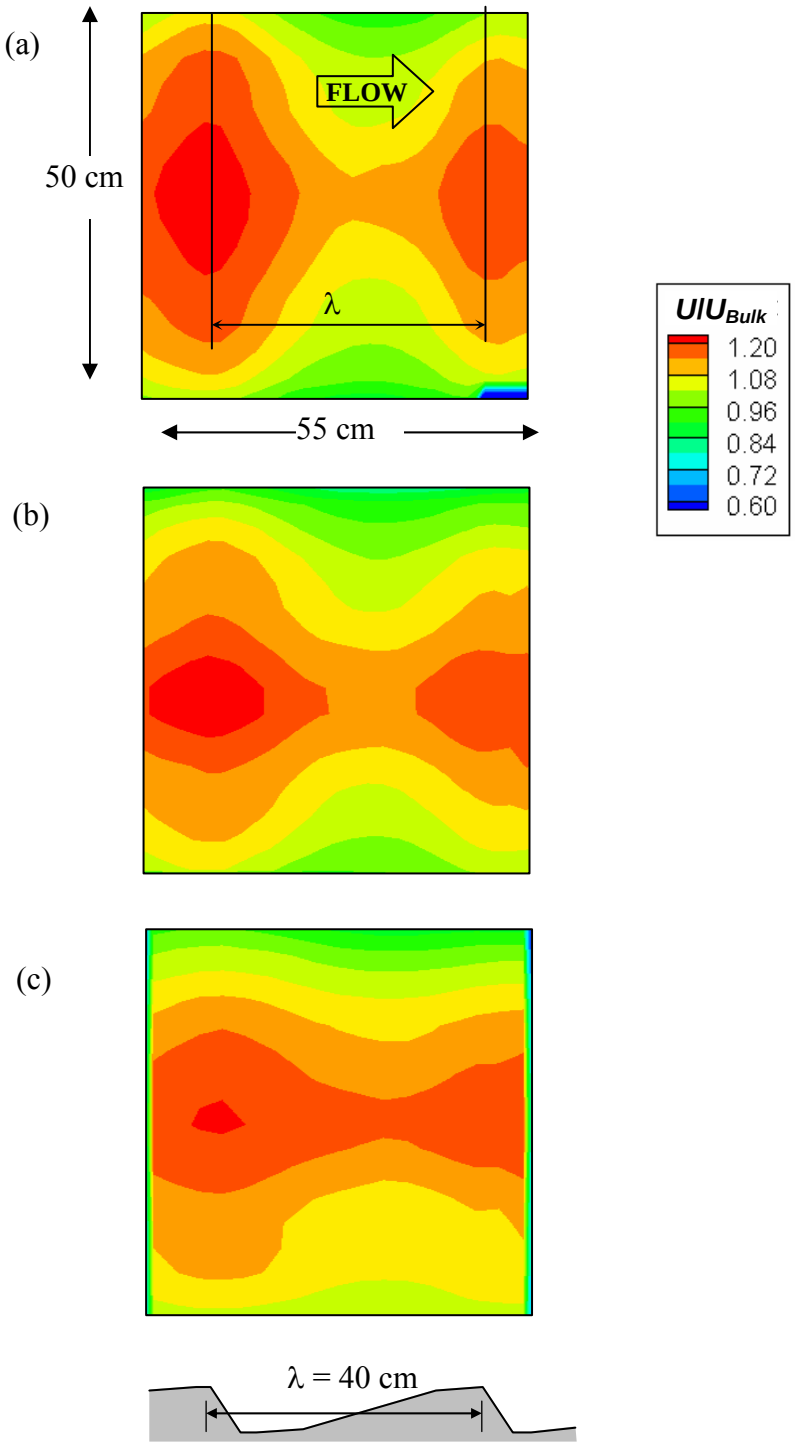

Figure 5.28 LSPIV results for normalized free-surface velocity distribution for flow over dunes with flow depth of (a) 6 cm, (b) 8 cm, (c) 10 cm.

A similar representation for the time-averaged velocity distribution of the free-surface was made from numerical experiments. LES results for time-averaged velocity profiles at the free-surface of dunes and ribs are given in Figure 5.29 and Figure 5.30, respectively. Overall the LES results display a more uniform distribution at the free-surface in comparison to the LSPIV measurements. Very detailed U/U_{Bulk} contours show the effect of the ribs on the free-surface velocity distribution as illustrated in Figure 5.29. Observed periodic pattern of the velocity distribution from LSPIV results for the flow over ribs can not be seen for the numerical results given in Figure 5.30.

This difference may be explained by the higher submergence ratios for ribs that dunes, and the existence of the free-surface waves that are not modeled by the rigid-lid approximation. The combined effects of rigid-lid assumption and the high submergence ratio (h/k = 8.5) wash away the rib effect on the free-surface of the numerical results. As Hodges (1997) explained, the loss of the dynamic and kinematic boundary conditions makes shear-free rigid-lid approximation unsuitable for studying the small scale viscous realm in the free-surface region.

The main difference between experimental and numerical results for rib roughness flows is caused by the fact that the floating particles at the free-surface moves with the waves that are not modeled by rigid-lid approximation. The captured movements of seeding particles by LSPIV enhance the repetitive pattern of high/low velocity regions with a wavelength of roughness. The effect of seeding on LSPIV measurements is discussed in Appendix B.

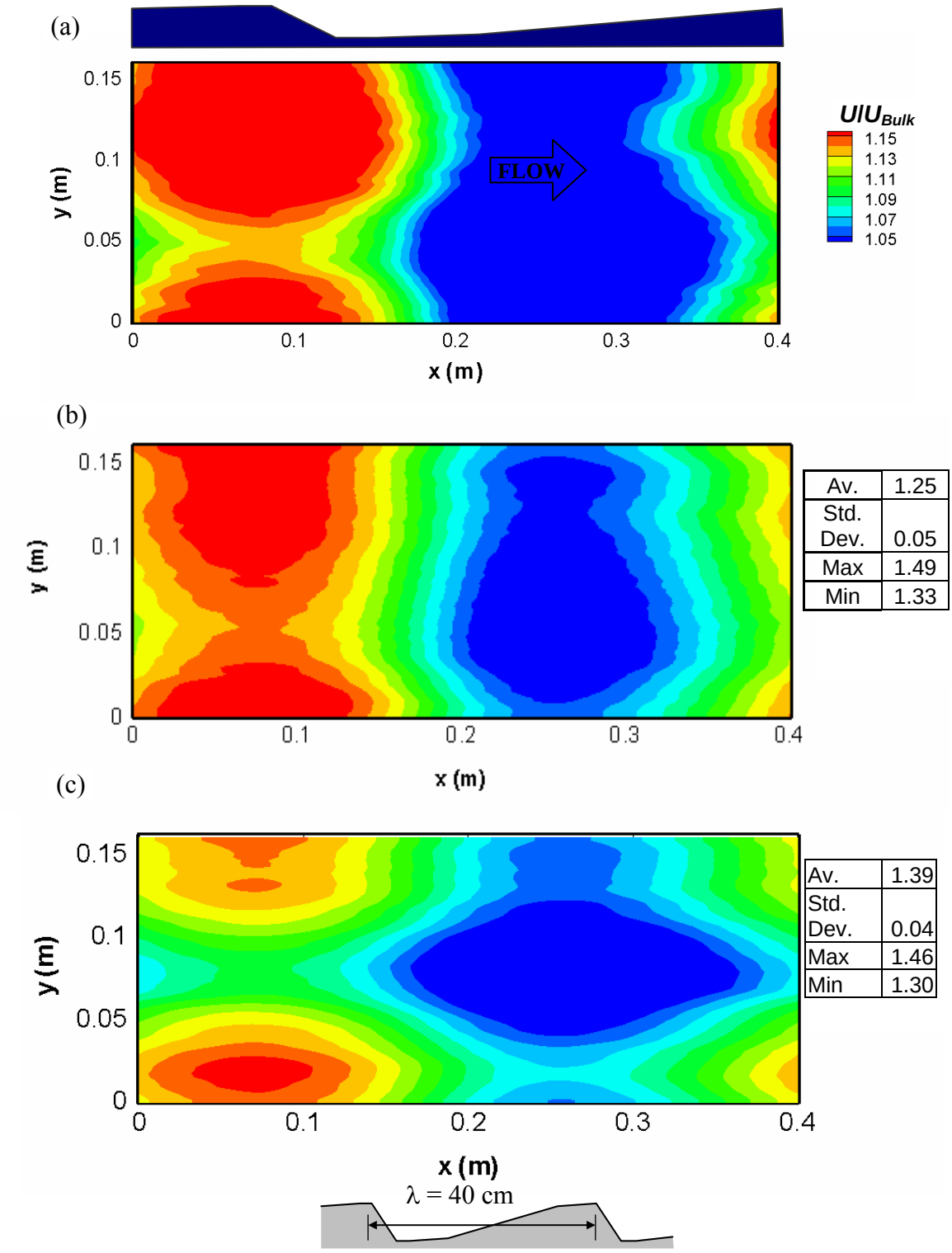

Figure 5.29 LES results for normalized free-surface velocity distribution for flow over dunes with flow depth of (a) 6 cm, (b) 8 cm, (c) 10 cm.

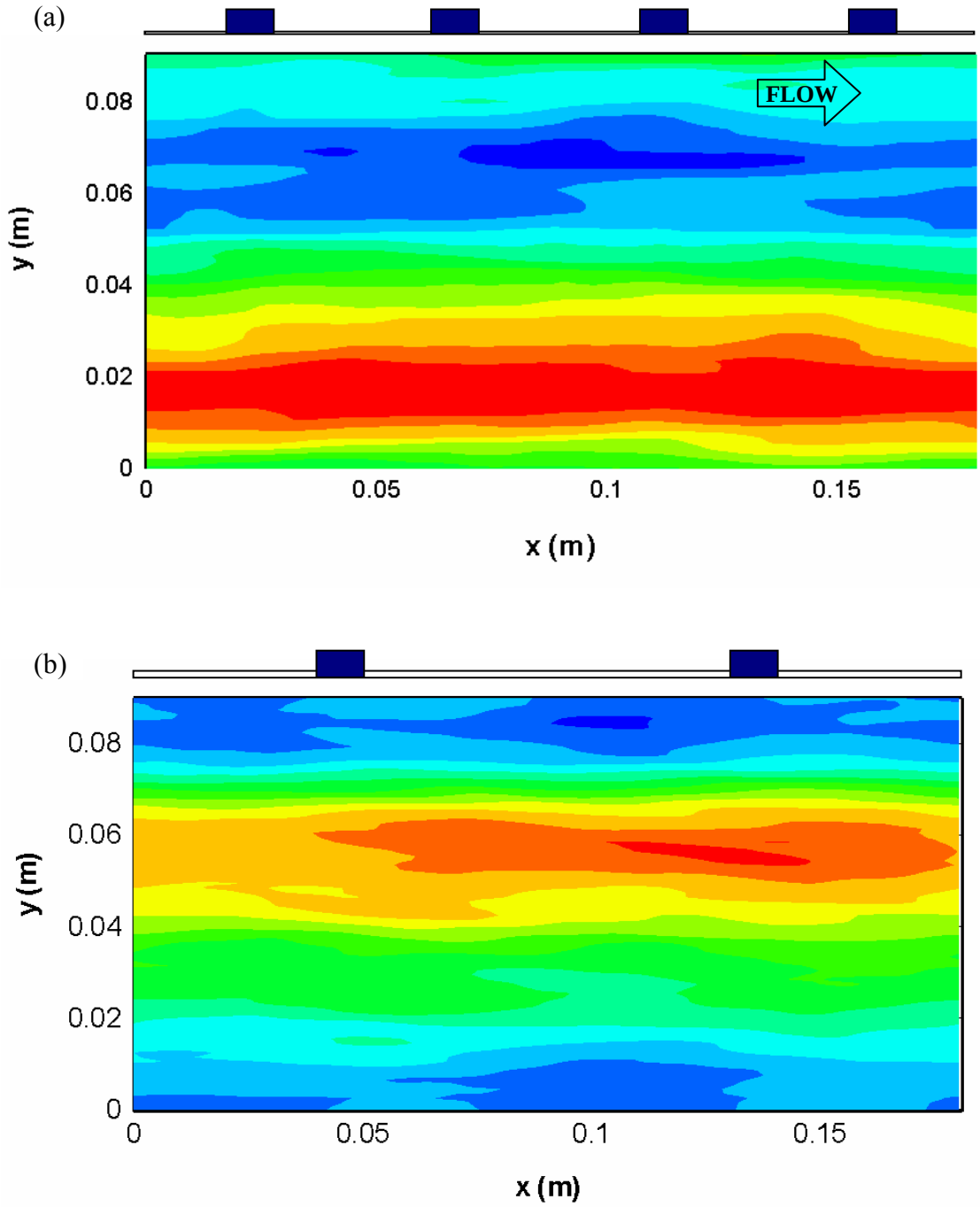

Figure 5.30 LES results for normalized free-surface velocity distribution for flow over rib roughness with 8.5 cm flow depth and roughness wavelength of (a) 4.5 cm, and (b) 9 cm.

5.3.3 Mean Velocity Profiles over the Roughness Elements

Several features of flow over roughness can be observed from time-averaged velocity profiles. Figure 5.31 and Figure 5.32 profiles of time-averaged streamwise velocity component. In the figures it is observed that distribution of velocity in vertical strongly depends on the streamwise location. Overall, flow experiences mild acceleration, deceleration, separation, reattachment and finally acceleration as it moves downstream.

Mild slope towards the dune crest causes a favorable pressure gradient, which accelerates the flow towards the crest. The negative pressure gradient counteracts the retarding effect of the shear stress. At the roughness crest (point S in the figures), sudden change in the flow area, and the pressure gradient bring the wall shear stress to zero and flow detaches from the channel bed. From this point on (separation point), the shear stress becomes negative and flow reverses with a recirculation region. Flow no longer follows the channel bed surfaces.

Shear layer originating at the dune crest bounds the recirculation region, and creates a turbulent wake which spreads and dissipates with distance. As this layer lies between the high-velocity flow in the outer wake zone and the low-velocity flow within the recirculation zone, very large Reynolds stresses and gradient of streamwise velocity is expected (Smith & Ettema, 1995). Velocity gradients in the region dissipate in flow direction, with the changes in thickness and horizontal spread of the shear layer.

Downstream of crest, pressure gradient becomes favorable (negative) due to change in bed geometry (positive slope). This condition terminates the recirculation region, and flow reattaches creating a recirculation bubble. From the discussion given in Section 5.3, the size of this region is found to be 5λ for the test flow and roughness

conditions. The reattachment points observed in Figure 5.18 are marked by letter R in the figures. The observation of same reattachment length, L_R, for all dune cases supports the findings of earlier research stating L_R to be a strong function of dune geometry.

At the reattachment point, an internal boundary layer begins to form. While velocity profiles develop towards the roughness crest, due to mild slope at the roughness crest, they gradually approach to typical profile of flow over distributed roughness. Before a fully developed profile achieved, flow separates at the crest of the next dune crest.

Streamwise velocity profiles over *k*-type ribs given in Figure 5.32.b present a similar flow field as of dunes. Abrupt changes in the roughness geometry and smaller horizontal roughness size are the main difference from dunes. Geometrical changes in the bed geometry impose abrupt changes in the pressure gradient, causing recirculation regions at the downstream and upstream of the roughness elements. Similar to dune flows, flow reattaches before the next element and an internal boundary layer begins to develop. The shear layer encompassing the recirculation region extents up to next roughness element.

Velocity field over transitional ribs lack many of the features common to dunes and *k*-type roughness. A reattachment point is not observed in the velocity profiles given in Figure 5.32.a. Another noticeable difference is the similarities in the velocity profiles at different locations along streamwise directions. In contrary to *k*-type roughness, velocity profiles are observed to have a very similar form except a region in roughness proximity.

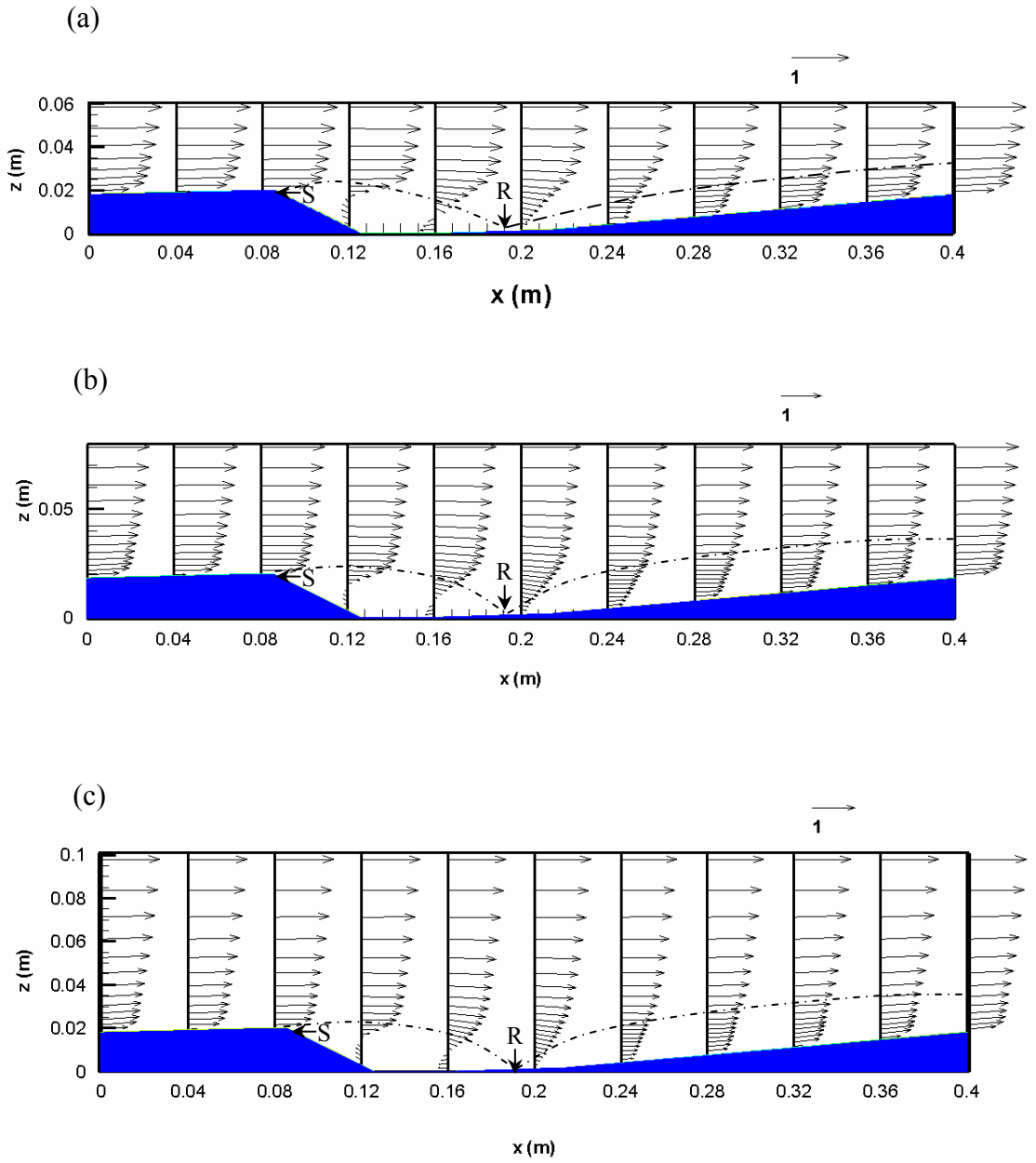

Figure 5.31 Velocity profiles normalized by U_{Bulk} and obtained by LES for flow over dunes with flow depth of (a) 6 cm, (b) 8 cm, and (c) 10 cm.

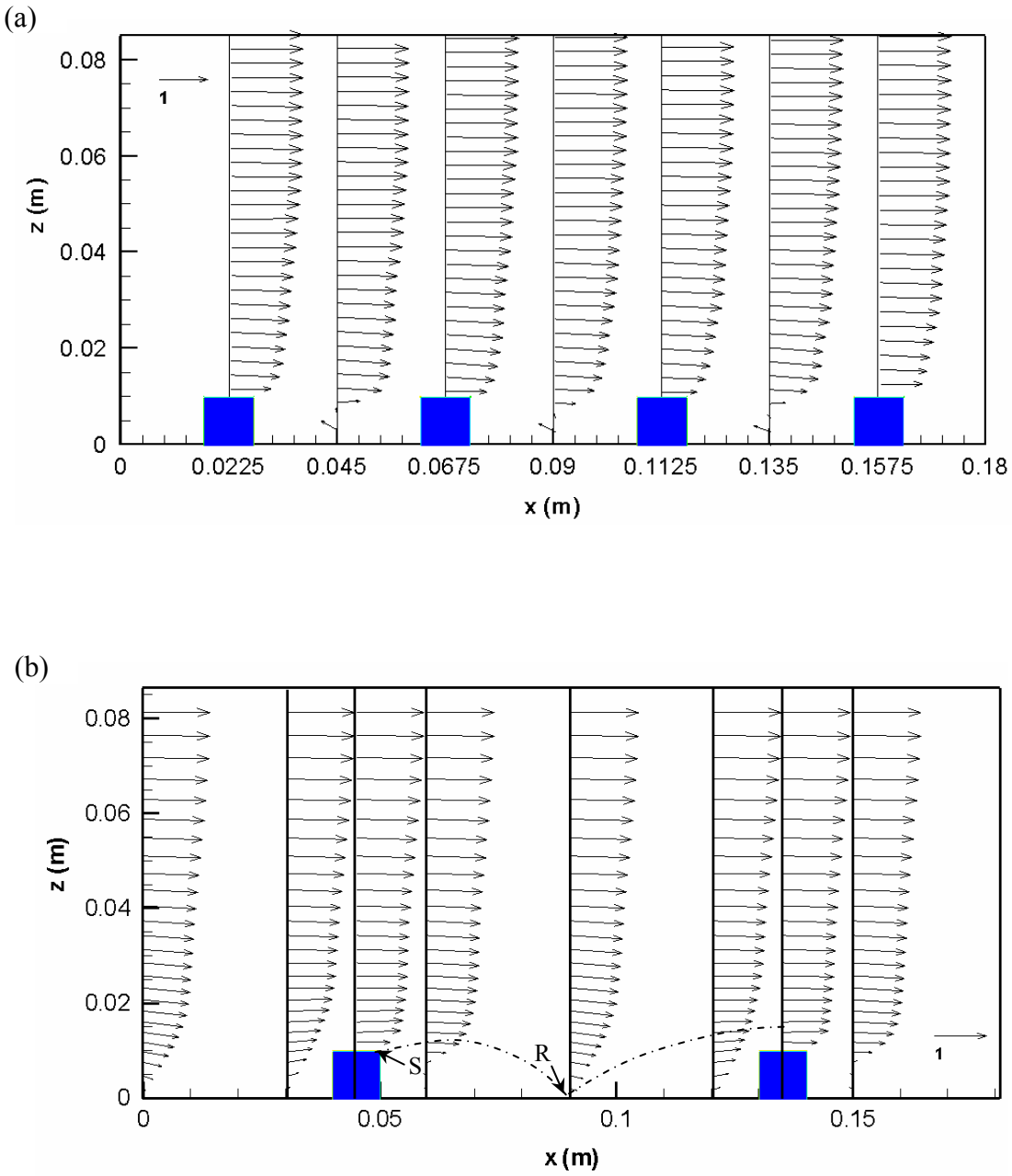

Figure 5.32 Velocity profiles normalized by U_{Bulk} obtained by LES for flow over rib roughness with 8.5 cm flow depth and roughness wavelength of (a) 4.5 cm, and (b) 9 cm.

5.3.4 Turbulence Characteristics over the Roughness Elements

Figure 5.33 and Figure 5.34 show the time-averaged streamwise turbulence intensity plotted over a dune wavelength and over several ribs. It was shown in Section 5.2 that higher turbulence intensities are found in the shear layer. Time-averaged field of turbulence intensities reveal that the peak intensities are located at the boundary of recirculation region and developing boundary layer. Superimposing the lines representing the recirculation region and internal boundary layer found in Figure 5.31 with turbulence intensity contours, the peak values of intensities located along these lines in Figure 5.33.

As for the extent of the instantaneous intensity contours, time-averaged turbulent shear layers are observed to spread and dissipate with distance from the roughness crest. Determination of the extent of the shear layer depends on the cut-off intensity value. Selecting the same cut-off value for all flow cases, comparison across the cases is made possible. The horizontal extent of the layer is observed to increase steadily with increasing flow depth, and attain 6.5k, 9k, and 13k for flow depths of 6 cm, 8 cm and 10 cm, respectively.

Turbulence intensity contours for flow over ribs of Figure 5.34 represent more complicated distribution than dunes. Flow separates at every abrupt change in the flow geometry. Including the small region at the roughness crest, three recirculation regions occur in rib flows. Higher turbulence intensity peaks and vertical extent are observed for k-type roughness than dunes. Strong shear layer downstream of the roughness element, originate more turbulence structures and mixing.

The shear layer over the transitional ribs reaches the next element before dissipating. This continuous layer is thinner than that of k-type, and has smaller peak.

The analysis of time-averaged flow field over large-scale roughness presented in this section provides us with a useful framework in reaching the research objectives of this study.

The flow over large-scale roughness is characterized by flow reattachment, recirculation zones, and internal boundary layer (Figure 5.18 and Figure 5.19). For flow conditions where roughness height is in the same order with flow depth, as in the present study, the distinct differences from smooth wall advises caution in using empirical or semi-empirical equations derived for flow over smooth bed.

For macro roughness elements where the geometry of the roughness imposes pressure gradients, such as dune, water surface elevation is expected to strongly react to the roughness geometry. For this roughness type, a robust roughness identification technique can be developed by jointly using free-surface elevation and velocity distribution. Considering some of the coherent structures generated due to shear layer and fluctuating attachment point, back tracking surface structures can assist in roughness identification.

The analysis of free-surface texture presented in Section 5.3.1 provides a useful tool in the direction of current research objectives. The power spectra given in Figure 5.22 and Figure 5.23 provide a quantitative support for the qualitative observations of Section 5.2.2.

Instantaneous and time-averaged flow field analysis show how free-surface texture and velocity distribution affected by the flow regime and bed roughness conditions. At the rest of the chapter, the relation between roughness, free-surface and bulk flow properties are presented.

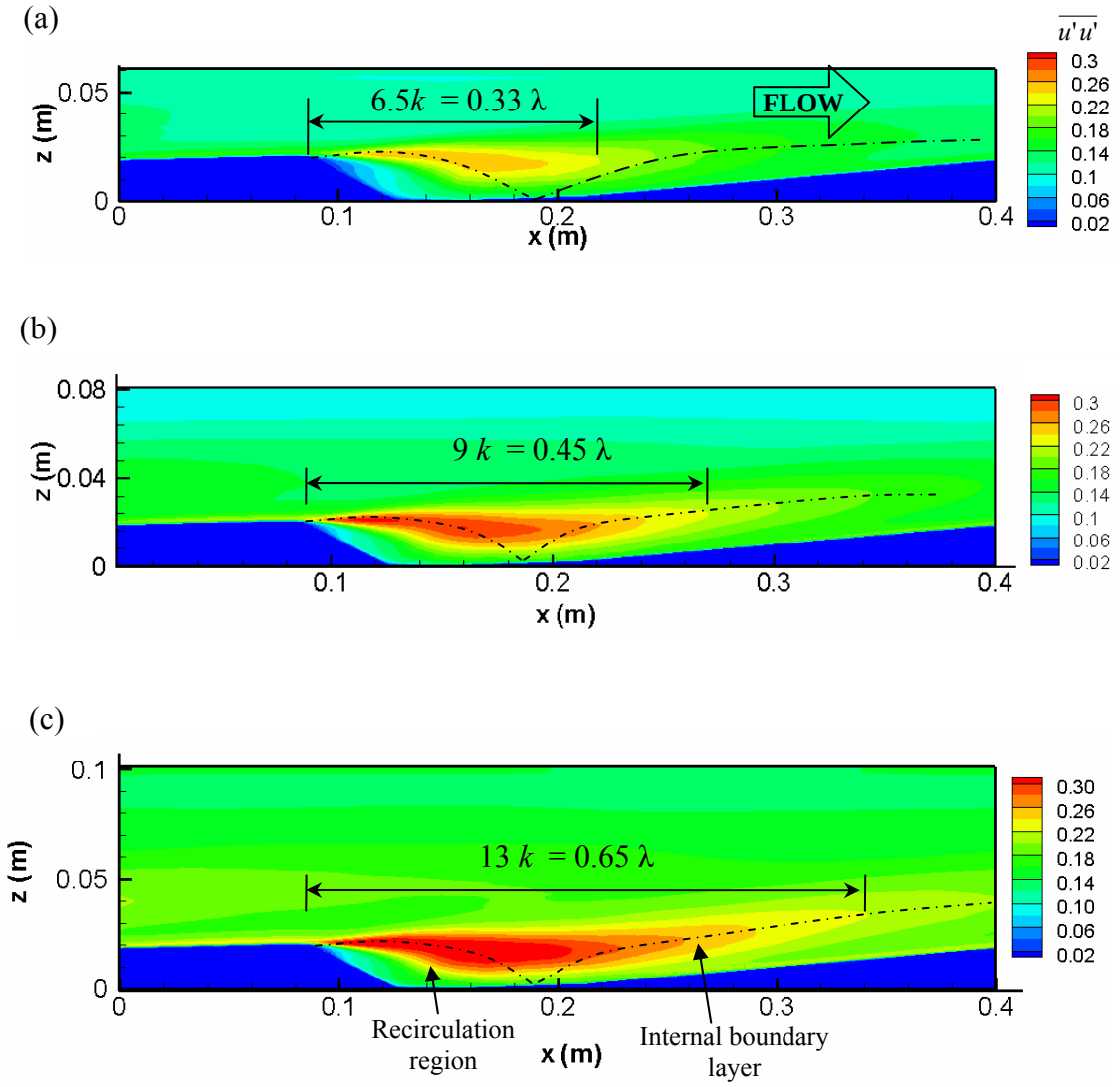

Figure 5.33 LES results for time-averaged streamwise turbulence intensities normalized by U_{Bulk} for flow over dunes with flow depth of (a) 6 cm, (b) 8 cm, (c) 10cm.

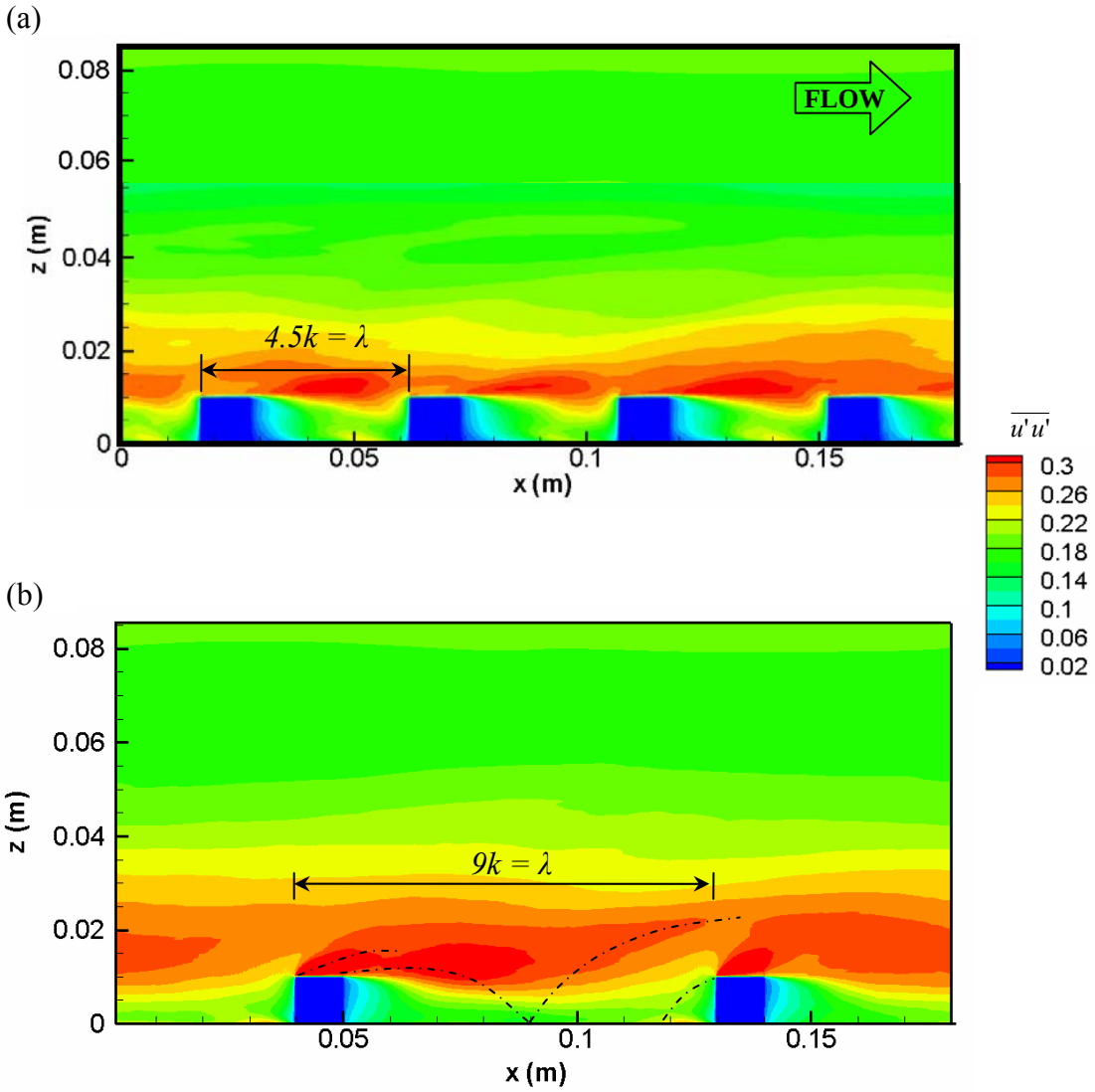

Figure 5.34 LES results for time-averaged streamwise turbulence intensities obtained by LES for flow over rib roughness with flow depth of 8.5 cm and roughness wavelength of (a) 4.5 cm, and (b) 9 cm.

5.4 Spatially-averaged Flow Field

5.4.1 Spatial Averaging

Spatially-averaged streamwise velocity profiles have been extensively investigated in turbulent open-channel flow studies, particularly for flows over large-scale roughness (Smith & McLean, 1977; Fedele & Garcia, 2000; Nikora *et al.*, 2001; Maddux *et al.*, 2003). This analysis is applied herein to LES results by averaging the velocity profiles in the streamwise and spanwise directions to produce a single, spatially-averaged profile over the wavelength of the roughness elements.

Figure 5.35 through 5.40 present how the double-averaged velocity profile compares with the local velocity profiles over the dunes and ribs. The figures contain the spatially-averaged profile obtained from numerical simulations and the individual velocity profiles measured by LDV at locations shown in Figure 2.2. It is seen that the velocity profile spatially-averaged over the roughness wavelength provides a representative profile for the outer layer of flow over ribs, where the submergence ratio is high in compared to that of dunes. However, such a description of the representative velocity profile is inherently imperfect for flow with low-submergence ratios (h/k).

For flows over large-scale roughness where roughness height is of the same order of the flow depth, the constraint of conservation of mass and energy lead to significant local variations in the water surface elevation and velocity profiles. As shown in Figure 5.35 and Figure 5.36, due to low relative submergence, dune flows of this study do not exhibit an outer layer with collapsing velocity profiles. For this kind of flow conditions, spatially averaged velocity profile is the only choice for velocity profile representation.

For all six cases represented in the figures spatially-averaged velocity profiles display two regions separated by a high velocity gradient. In the outer layer, away from the channel bed, velocity profiles follow a similar pattern. The high gradients in the velocity profile are located along the shear layer generated from the roughness crest. In the inner layer, local velocity profiles vary considerably. Very close to the channel bed, spatially averaged profile exhibits a small region with negative velocity due to the recirculation regions downstream of the roughness elements. This two-layer profile of velocity over large-scale roughness has also been reported by Fedele & Garcia (2000), Maddux (2002), Cui *et al.* (2003) and will be discussed in the next section in detail.

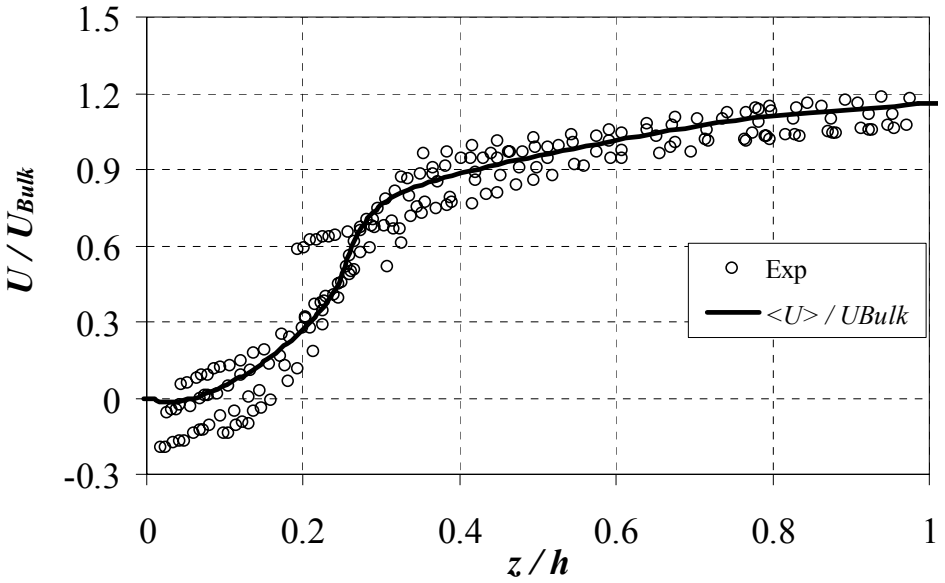

Figure 5.35 Spatially-averaged velocity profile by LES vs. LDV measurements for flow over dunes with 8 cm flow depth (D01).

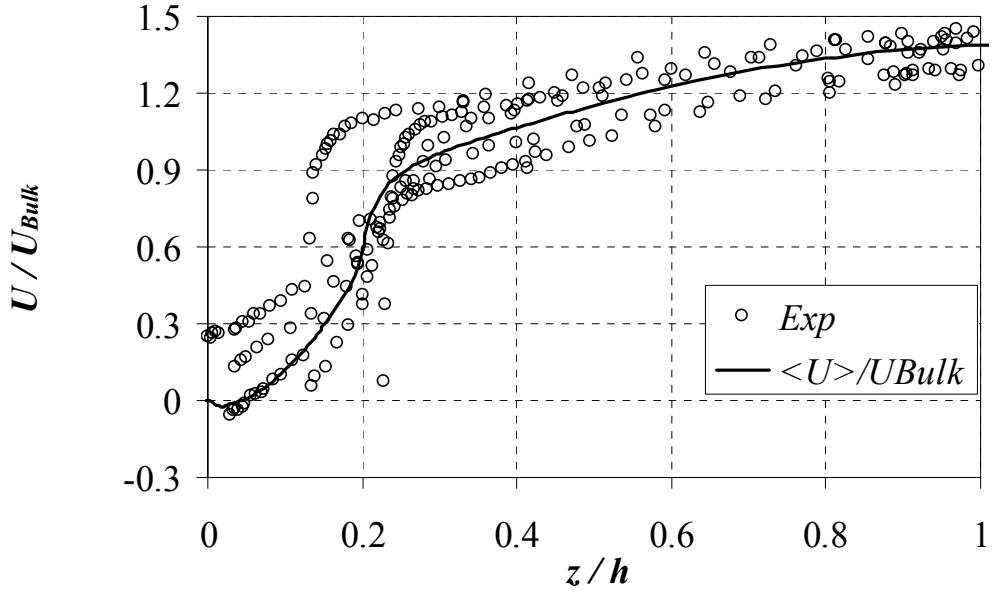

Figure 5.36 Spatially-averaged velocity profile by LES vs. LDV measurements for flow over dunes with 10 cm flow depth (D02).

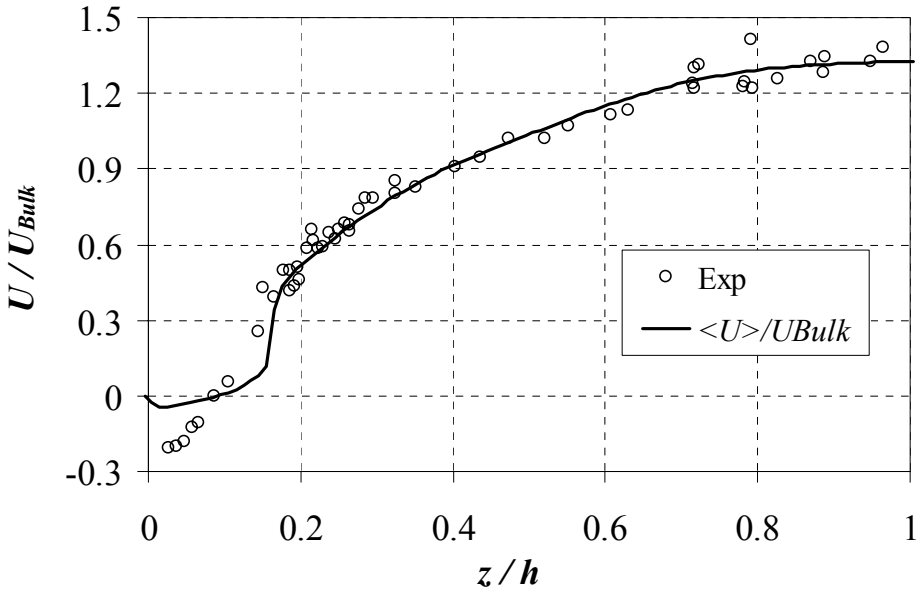

Figure 5.37 Spatially-averaged velocity profile by LES vs. LDV measurements for flow over ribs with λ = 4.5 cm, and h = 6.5cm (R01).

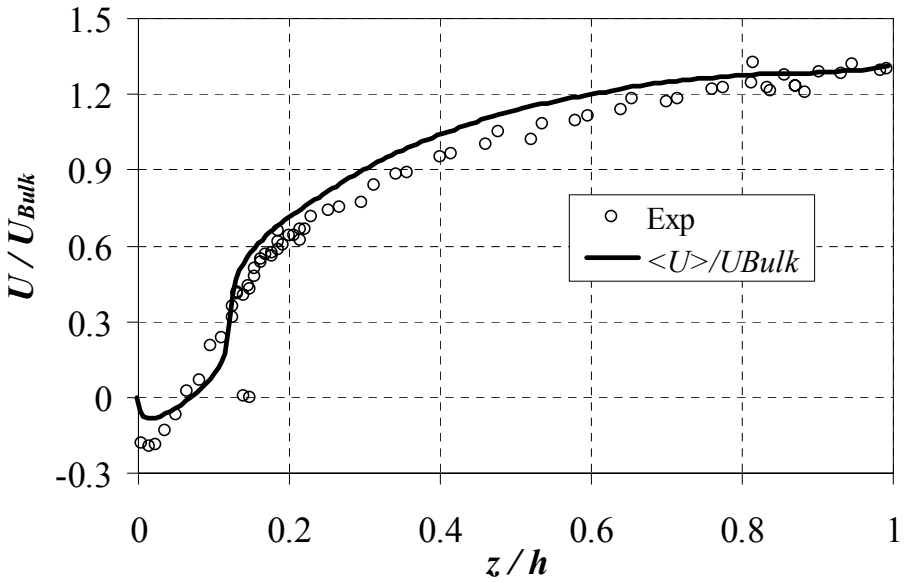

Figure 5.38 Spatially-averaged velocity profile by LES vs. LDV measurements for flow over ribs with λ = 4.5 cm, and h = 8.5 cm (R02).

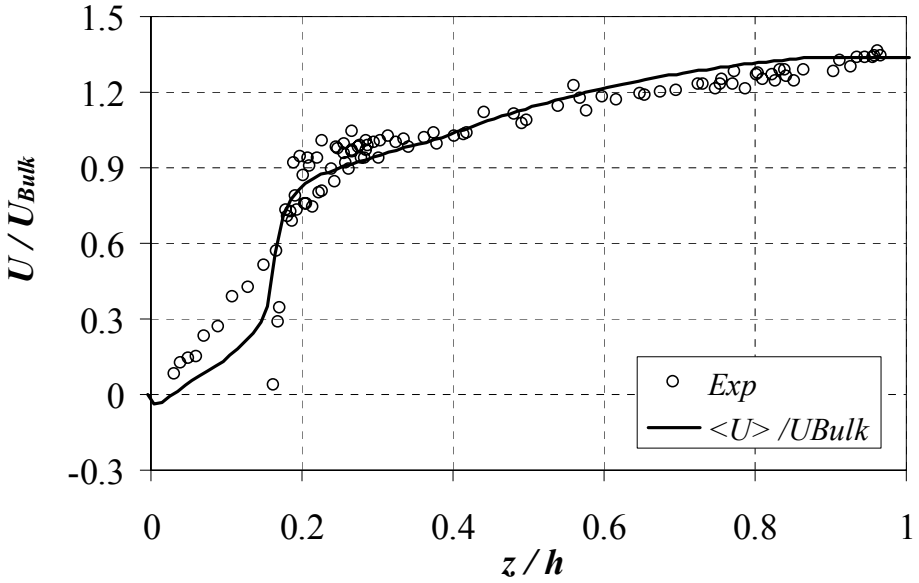

Figure 5.39 Spatially-averaged velocity profile by LES vs. LDV measurements for flow over ribs with $\lambda = 9$ cm, and $h = 6.5$ cm (R04).

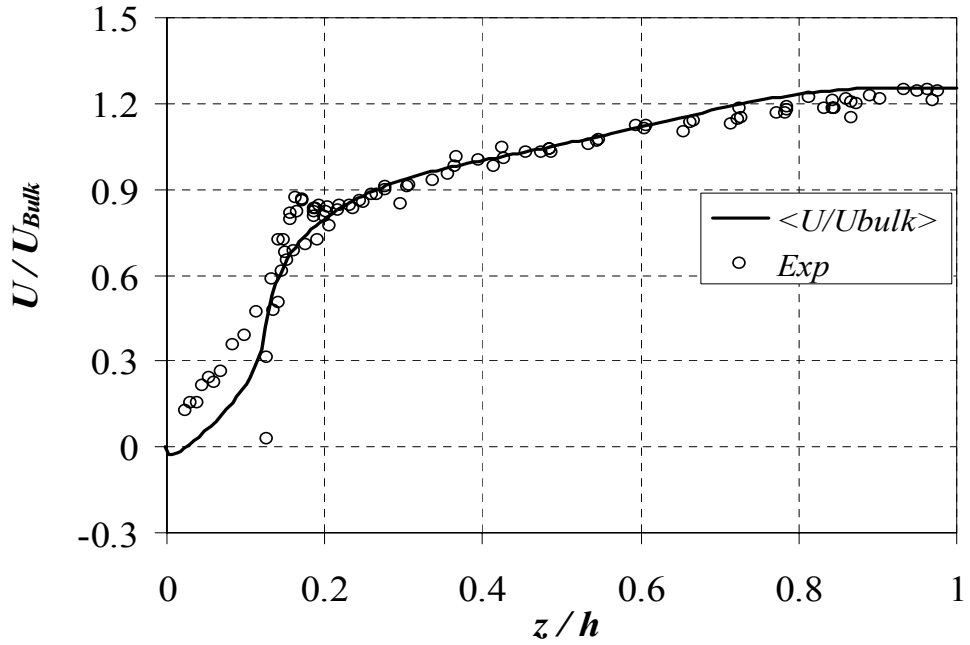

Figure 5.40 Spatially-averaged velocity profile by LES vs. LDV measurements for flow over ribs with $\lambda = 9$ cm, and $h = 8.5$ cm (R05).

5.4.2 Two-Layer Velocity Profile

Given the differences in the velocity profiles, it is reasonable to assume that the outer and inner layers are described by different functions. In compliance with the flow physics, length and velocity scales of these two layers are also different. In the inner layer, flow depends mainly on roughness geometry, and on flow depth in the outer layer. The investigation of local velocity profiles of Section 5.4.3 indicates that the extent of the inner layer lies between 0.2 h to 0.4 h depending on the submergence ratio. Given the substantial differences in the velocity profiles, and length and velocity scales, an accurate positioning of the boundary location between inner and outer layer is crucial.

In the outer layer, local profiles and spatially-averaged profiles are similar, while they do not follow a general trend below the crest elevation. Before McLean *et al.* (1999) raised concerns on its validity, it was believed that these two regions of the spatially-averaged profile follow the log-law, evaluated with different shear velocities. A functional description of the inner layer profile is not currently available. Earlier research of Nikora *et al.* (2001b) showed that for flow over two-dimensional dunes the spatially-averaged mean velocity displayed a logarithmic region in the outer layer of the flow, and a linear profile in the region below the roughness crests.

Although it is not commonly used for flow over dunes, a power-law function can also be used as the mean velocity distribution function. As discussed in Chapter 1, power-law description of the velocity profile depends on length scales from inner and/or outer layers (Barenblatt, 1993). Moreover, the complete similarity assumption of the log-law

does not hold for flow over large-scale roughness. Due to these reasons, a power-law description of the velocity profile in the inner layer is recommended in this study.

The choice of log or power-law for the velocity profile in the outer layer is not important, since both can be used to express the velocity profile in this layer (see Appendix A for details). However, in this study, for the sake of consistency of the profiles from the layers of the velocity field, power-law model is used for both inner and outer layers of the flow over large-scale roughness. Power-law fit to the obtained spatially averaged profiles is presented in Section 5.4.6.

The structural properties of spatially-averaged velocity profiles, e.g. the boundary location between inner and outer layers and the virtual origin, are presented in Sections 5.4.3 and 5.4.4, respectively. The discussion of models describing the velocity profiles from these two layers is presented in Section 5.4.6.

5.4.3 Extent of the Inner Layer, z_b

Accurate description of two-layer velocity profile requires specification of additional parameters, namely, the virtual origin, or the shift in the z-origin (z_0), and the extent of the inner layer (z_b). At the extent of the inner layer $z = z_b$, the velocity, U_b, satisfies the velocity distribution functions from both inner and outer layers. This location is called the matching layer (Fedele & Garcia, 2000) or the inflection point (Nikora *et al.,* 2004). The position of this point over the channel bed, z_b, may be considered as a definition for the upper boundary of the roughness interfacial layer and, some studies assume it is roughly equal to roughness height (Raupach *et al.,* 1991; Finnigan, 2000). In the present study, the double-averaged velocity profiles are used to precisely define z_b.

The most direct method to obtain z_b is to find the inflection point in the double-averaged velocity profile. Figure 5.41.a shows the variation in the z derivative of $\langle U \rangle$ for flow case D01, which has a peak value around $z/h = 0.253$. Values for z_b obtained with this method for other flow cases are listed in Table 5.2.

Another approach for determining location of z_b is to associate it with the maximum streamwise turbulence intensity $\langle u'u' \rangle$. Illustration of this approach for flow case D01 is plotted in Figure 5.41.b, where $\langle u'u' \rangle$ is shown in the axis on the right.

The z_b values for the other flow cases obtained in similar way are listed in Table 5.2, which demonstrate that these two methods of locating z_b yield very similar results. For practical purposes, roughness height can be taken as the boundary location. However, for more refined investigation of the velocity profiles, the method of highest turbulence intensity is recommended for flow over large-scale roughness.

Table 5.2 Extent of the inner region (z_b).

	$z(\text{Max}(\partial\langle U \rangle/\partial z))$			$z(\text{Max}(\langle u'u' \rangle))$		
	z (m)	z/k	z^+	z (m)	z/k	z^+
D01	0.020	1.0	628	0.022	1.1	675
D02	0.020	1.0	652	0.021	1.1	678
R01	0.010	1.0	523	0.011	1.1	591
R02	0.098	1.0	497	0.011	1.1	579
R04	0.010	1.0	443	0.012	1.2	458
R05	0.010	1.0	408	0.012	1.2	472

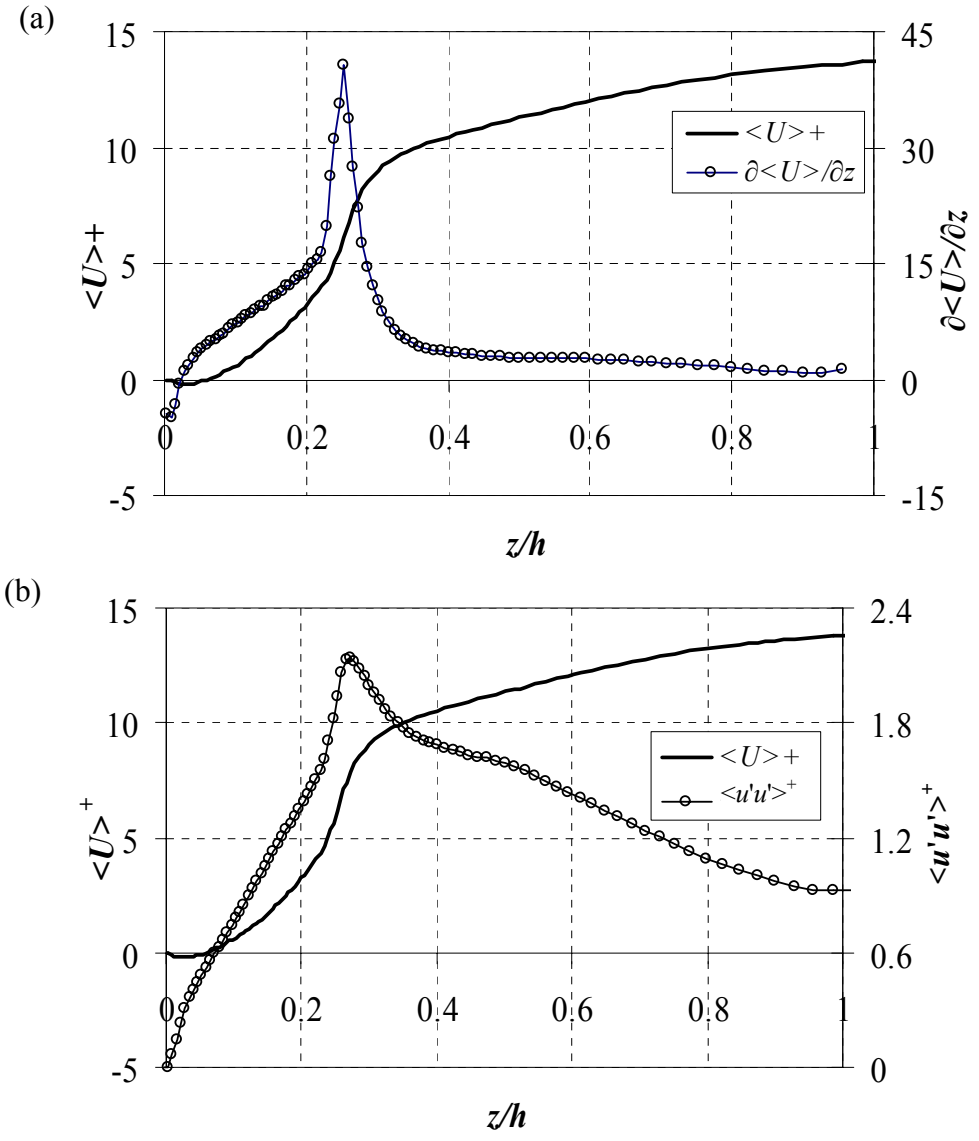

Figure 5.41 Double-averaged profile with (a) $\partial\langle U\rangle^{+}/\partial z$, and (b) $\langle u'u'\rangle^{+}$ profile for flow over dunes with 8 cm flow depth (D01).

5.4.4 Location of the Virtual Origin, z_0

As mentioned in Chapters 1 and 4, flow over large-scale roughness responds to an effective surface as the virtual origin of the distribution functions. Depending on the relative submergence and geometry of the roughness, virtual origin can be located anywhere between the channel bed and roughness crest elevations.

Figure 5.42 shows how virtual origin is located by extending the linear part of the velocity profile for flow over dunes. Table 5.3 gives the location of virtual origin over the channel bed, obtained by this method, and also by finding the location of zero spatially-averaged streamwise velocity. It is seen from the table that the method of locating virtual origin from z-intercept does not yield accurate results. For both k-type and transitional rib roughness, the virtual origin is found to be at the roughness crest by this method, which is not the case for k-type roughness. Thus, this study recommends the zero spatially-averaged velocity criteria for locating virtual origin over the large-scale roughness.

Table 5.3 Location of virtual origin over the channel bed (z_0).

	From z intercept		At $<U>$ = 0	
	z (m)	z/k	z (m)	z/k
D01	0.015	0.75	0.005	0.25
D02	0.016	0.8	0.004	0.2
R01	0.01	1	0.006	0.6
R02	0.01	1	0.006	0.6
R04	0.01	1	0.002	0.2
R05	0.01	1	0.002	0.2

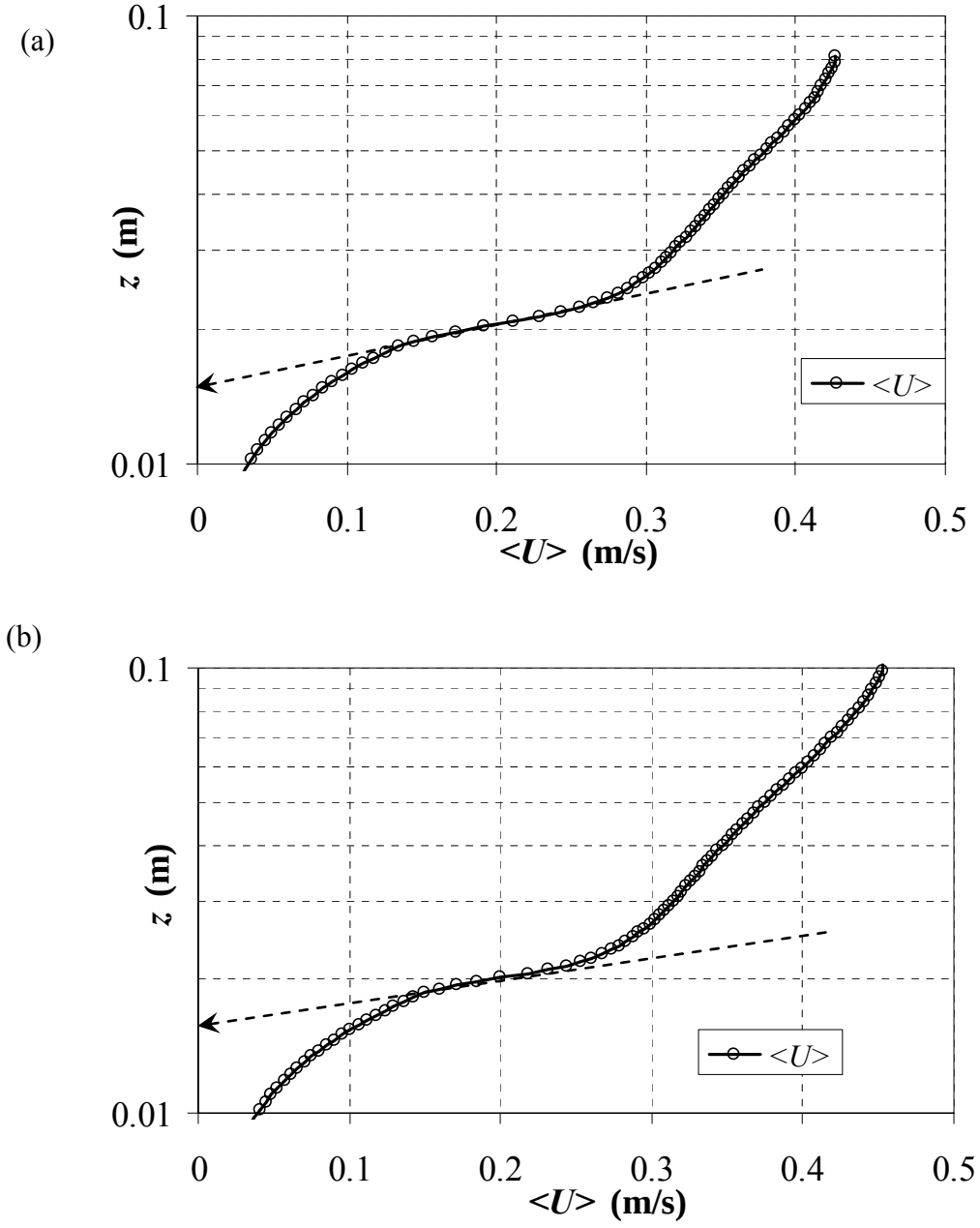

Figure 5.42 Location of virtual origin from the z-intercept of the linear part of the velocity profile for flow over dunes with (a) 8 cm , and (b) 10 cm flow depth.

Obtained values in Table 5.3 indicate that z_0 has a weaker dependence on the flow depth than the roughness type. As expected, it is located at a higher elevation for transitional roughness than for *k*-type roughness. For dunes and *k*-type ribs, the virtual origin is located roughly at $z/k = 0.2$.

5.4.5 Roughness Function

The double-averaged velocity profiles above the virtual origins determined according to the procedure described in Section 4.4.1 are plotted in Figure 5.43. As expected, the increase in bed roughness produces a downshift in the velocity profiles relative to the smooth wall profile. Even though log-law can not be applied for a large region of the velocity profile, the concept of roughness function can be used to assess the resistance generated by the roughness elements on the channel bed. The magnitude of the roughness function, ΔU^+, for the test flow cases are listed in Table 5.4.

From the table it is first noticed that dunes, despite their lower submergence ratios, cause less shift than ribs. There is a small difference between the roughness functions obtained for transitional and *k*-type ribs. Decreasing roughness wavelength has a reducing effect on ΔU^+.

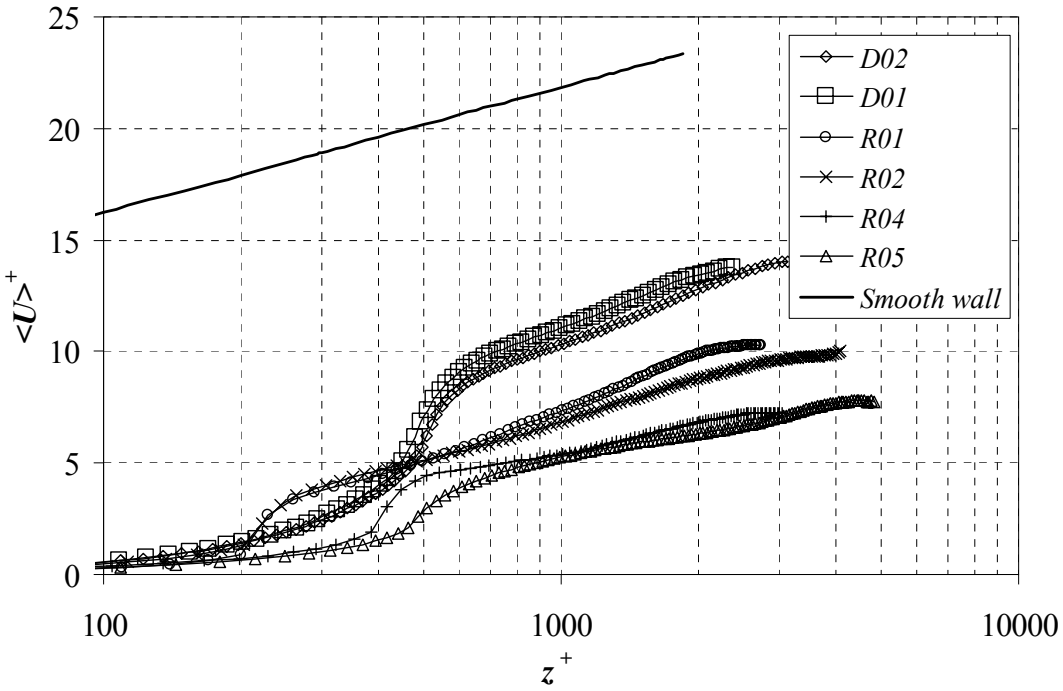

Figure 5.43 Double-averaged profiles for six flow cases obtained by LES.

Table 5.4 Roughness function.

Flow case	ΔU^+
D01	10.8
D02	11.6
R01	14.8
R02	15.8
R02	16.4
R05	16.5

5.4.6 Power-Law Fit for the Two-Layer Velocity Profile

Proper roughness length scales should be used for a generalized description of the flow over rough surfaces. Finding the proper scaling parameters is important not only for describing universal flow trends, but also to understand and classify the way the flow responds to the roughness.

In this study a two-layer velocity profile, where the profiles from inner and outer layer are approximated with different power-law functions. is suggested for flow over large-scale roughness. The procedure to obtain the power-law fit for the two layer velocity profile is as follows:

1) The extent of the inner layer and the location of the virtual origin are obtained. Not locating the virtual origin accurately causes a rotation in the semi-logarithmic velocity profile from the smooth wall.
2) Power-law fit coefficients for the outer layer are obtained by least squares fitting.
3) A power-law fit is obtained for the inner layer using the z-intercept of this profile and slope as the fitting parameters to satisfy the continuity along the vertical cross-section.

It is observed from Figure 5.44 to Figure 5.49 that, as it is well-documented by earlier studies, the power-law does not approximate the free-surface region well. Regions of high velocity gradient in Figure 5.41 can not be presented well with either inner or outer layer functions. (Both log- and power-law are based on the assumption of mild gradient, and no inflection point in the velocity profile). This is indicative of a strong alteration of the turbulence production, dissipation and transfer in the vicinity of the shear layer generated by the roughness elements.

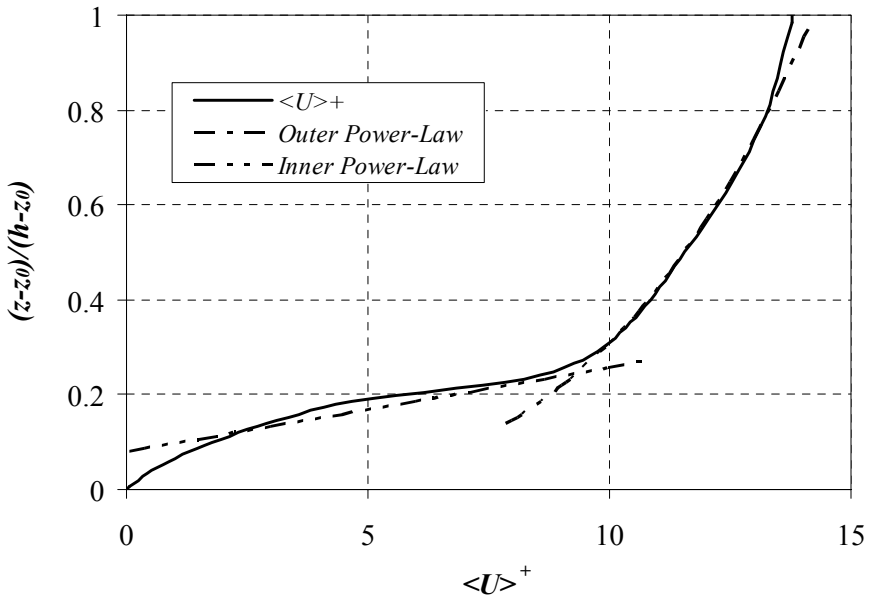

Figure 5.44 Two-layer power-law fit for spatially-averaged velocity profile by LES for flow over dunes with 8 cm flow depth (D01).

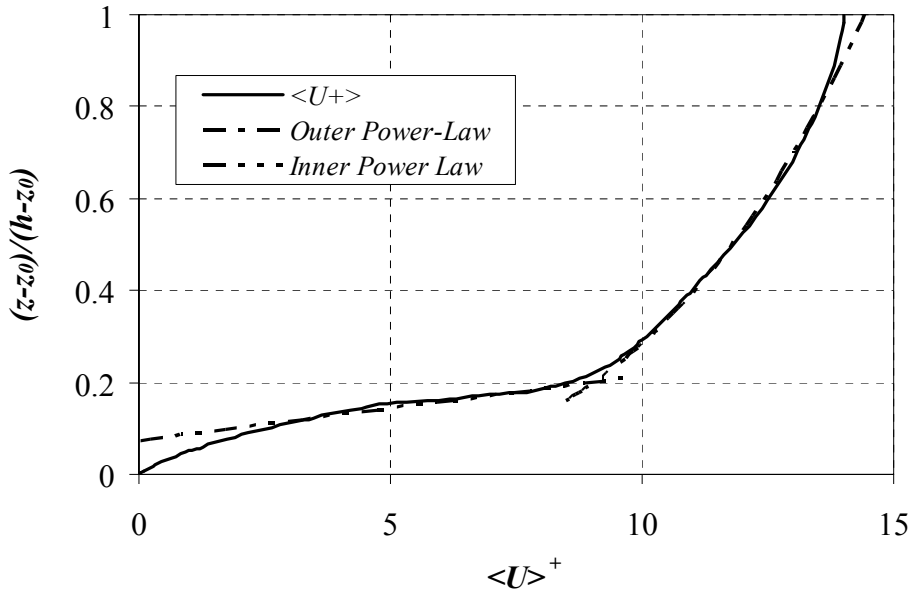

Figure 5.45 Two-layer power-law fit for spatially-averaged velocity profile by LES for flow over dunes with 10 cm flow depth (D02).

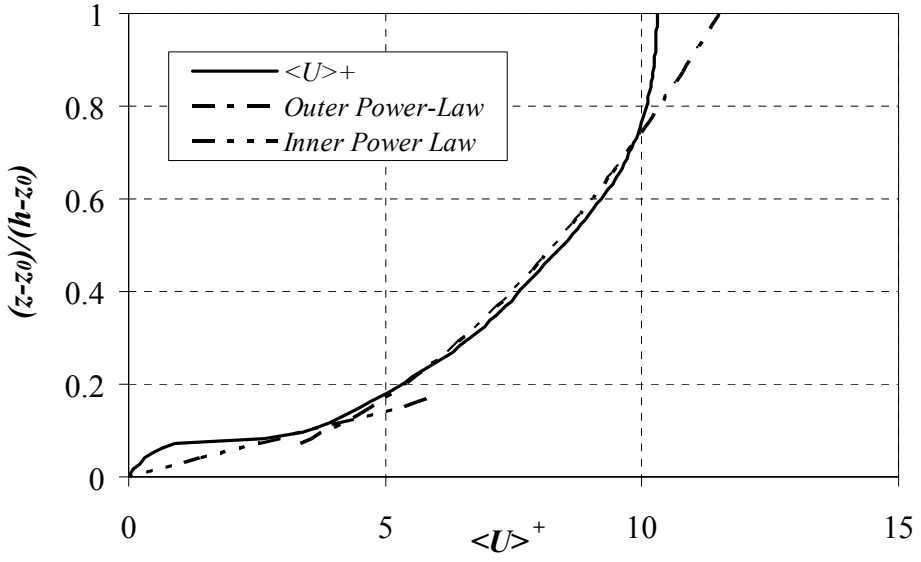

Figure 5.46 Two-layer power-law fit for spatially-averaged velocity profile by LES for flow over ribs with λ = 4.5 cm, and h = 6.5 cm (R01).

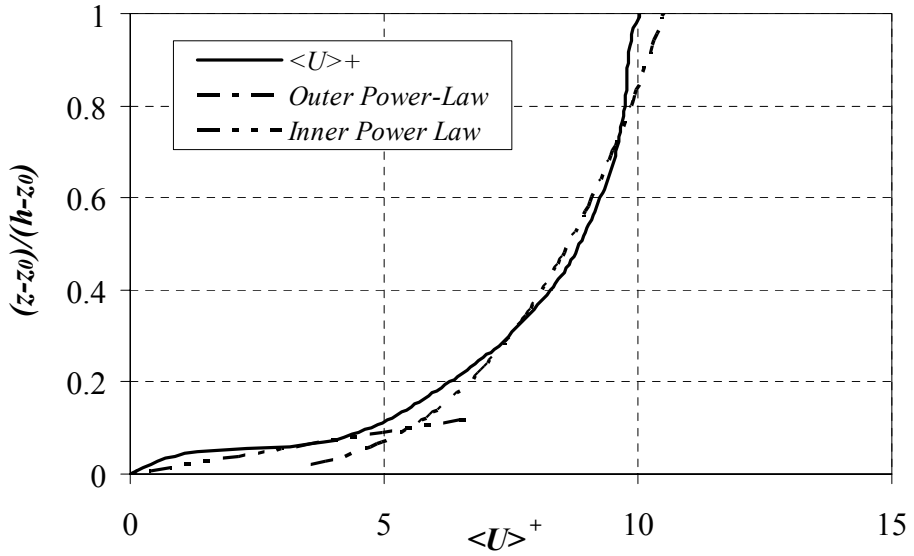

Figure 5.47 Two-layer power-law fit for spatially-averaged velocity profile by LES for flow over ribs with λ = 4.5 cm, and h = 8.5 cm (R02).

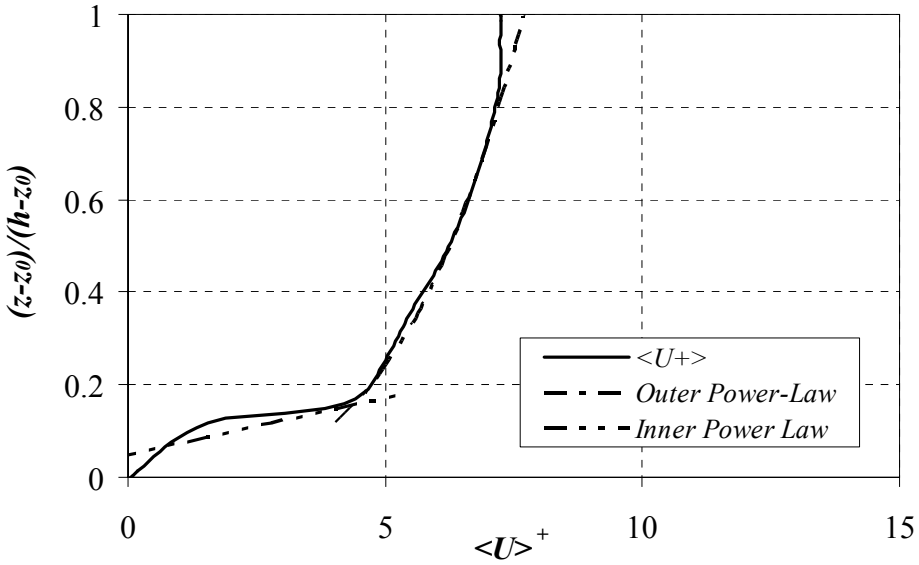

Figure 5.48 Two-layer power-law fit for spatially-averaged velocity profile by LES for flow over ribs with $\lambda = 9$ cm, and $h = 6.5$ cm (R04).

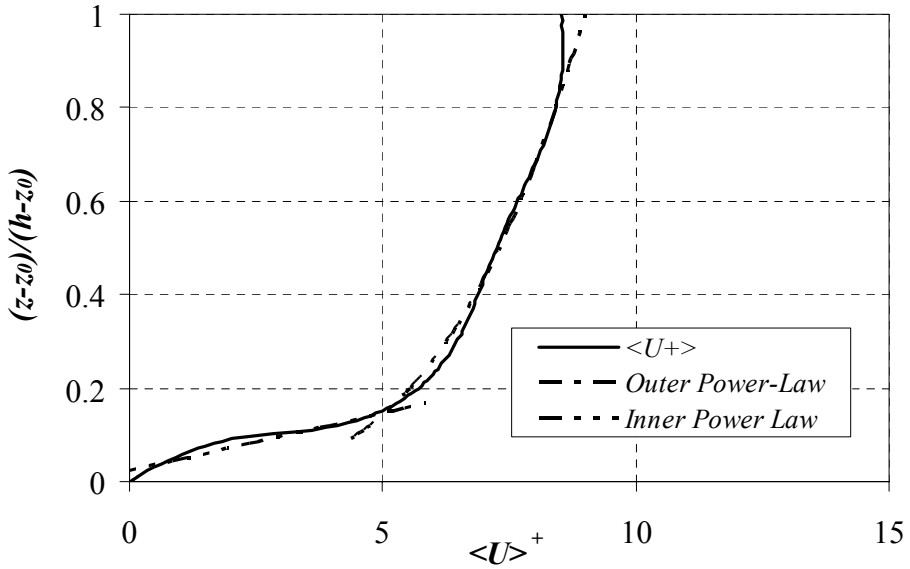

Figure 5.49 Two-layer power-law fit for spatially-averaged velocity profile by LES for flow over ribs with $\lambda = 9$ cm, and $h = 8.5$ cm (R05).

5.5 Bulk Properties

The motivation for this research was to facilitate remote discharge measurement techniques. A functional relationship relating free-surface velocity measurement to the depth-averaged velocity is needed to remotely estimate the discharge. For this purpose, velocity indices are calculated by depth-averaging the experimentally obtained velocity profiles of channel flows over various bed roughness and flow conditions (e.g. Froude number and aspect ratio). The velocity indices, α, relating the free-surface velocities to bulk flow velocity, are calculated using Eq. 1.4, and presented in Figure 5.50 and in Table 5.5. They are found to vary in the range 0.659 to 0.910 for the flow cases investigated herein.

Table 5.5 Velocity indices by LSPIV.

	Code	***α***
Smooth Bed	S01	0.659
	S02	0.773
	S03	0.824
	S04	0.862
	S06	0.890
	S08	0.898
	S10	0.910
RL045	R01	0.872
	R02	0.880
	R03	0.908
RL090	R04	0.850
	R05	0.874
	R06	0.898
RL180	R07	0.878
	R08	0.878
	R09	0.887
2D dunes	D01	0.900
	D02	0.895
	D03	0.895

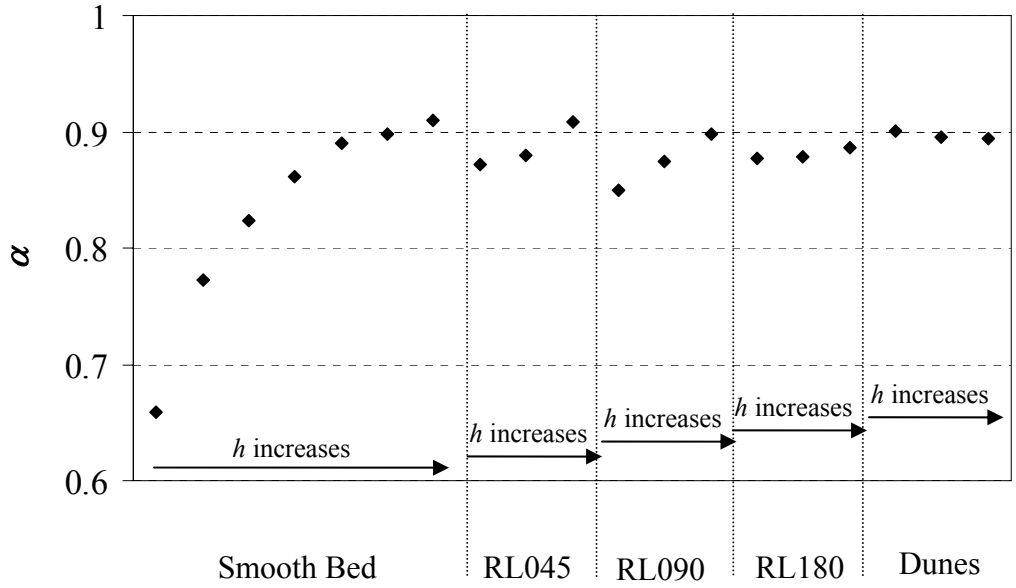

Figure 5.50 Velocity indices obtained by LSPIV.

Figure 5.50 demonstrates the consistency in the obtained trends of velocity indices with the flow depth supports the concept of using free-surface velocity as the indexing velocity. The *k*-type rib roughness with the lowest flow depth (R01) has the smallest velocity index among tested bed roughness configurations. Figure 5.50 also shows that variation of α with depth follows a pattern: higher velocity indices are observed for higher depth flows. As the resistance to flow decreases, velocity indices over the dunes get closer to the smooth bed values. The wide range of the indices found in the present investigation shows the importance of roughness consideration in velocity indexing.

It is generally accepted for flow over flat, smooth bed that the free-surface velocity is related to the depth-averaged velocity with a velocity index of 0.85 in rivers. The results of this study demonstrate that ratio of free surface velocity to depth-averaged

velocity depends on the channel bed roughness. For the given flow conditions, even though aspect ratios are smaller than the values seen in natural rivers, the surface velocity reacts to spatial changes in channel bottom. Thus, it is recommended to consider the channel bed roughness while estimating discharge by indexing.

It is demonstrated in this study that the state of the free surface in open channel flows has a unique relationship with the velocity distribution and other flow conditions. Identifying this relationship makes it possible to directly estimate the discharge by only one velocity measurement at the free surface.

Free surface velocity, as indexing velocity, has advantages in the aspects of convenience in finding location and magnitude of the free surface velocity and appropriateness to non-contact measurements. As noted in review by Costa *et al.* (2002), recently developed methods such as radar and image velocimetry make it possible to measure free surface velocity, and subsequently determine the discharge. The present results provide evidence that discharge can be appropriately estimated by free surface velocity indexing for a given roughness condition.

CHAPTER 6
SUMMARY AND CONCLUSIONS

The overall objective of the study is to identify the effect of large-scale roughness on the free-surface and bulk flow properties of open-channel flows. This chapter synthesizes the findings of the study, discusses the new insights provided by the results, and highlights the overall contribution of the study toward the implementation of remote velocity and discharge measurements in open-channel flows. To synthesize the findings of the research the questions posed in Section 1.3 are answered using the results presented in Chapter 5.

6.1 Flow – Roughness Interaction

Can dunes and ribs be treated by classical roughness theories?

The analysis of the instantaneous flow field over ribs and dunes reveals that the flow over large-scale roughness elements is characterized by spatial non-uniformities that are not present in flow over uniformly distributed small-scale roughness, such as sand and gravel. The flow over dunes and ribs displays regions of separation behind the roughness elements, fluctuating reattachment points downstream of the roughness crests, and a distinct inner layer where the flow is strongly affected by the protrusion of the roughness elements.

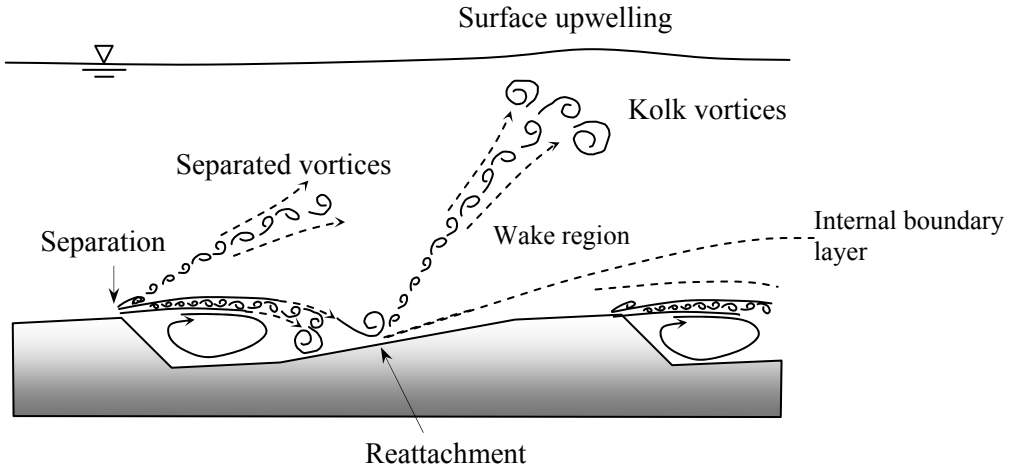

Figure 6.1 Schematic of flow over dunes.

The time-averaged flow field also provides important evidence for distinct roughness-flow interaction. The streamline pattern is affected by the presence of the roughness over a significant part of the flow field. The size of the recirculation areas and distribution of turbulence intensities substantiates the observation of significant roughness effect.

From the analysis of the instantaneous flow field, distinct features of flow over large-scale roughness are identified. Schematic depictions of the findings from the experimental and numerical results of the instantaneous flow field for dunes and ribs are given in Figures 6.1 and 6.2, respectively. The streamlines of the instantaneous velocity field of Figures 5.1 and 5.2 suggest that the irregularities in the streamline pattern persist up to some distance from the channel bed, and show existence of the flow features over large-scale roughness shown in Figures 6.1 and 6.2. Analysis of turbulence intensities in Figures 5.9 and 5.10 exhibit the distinct effect of dunes and ribs on the flow: a shear layer

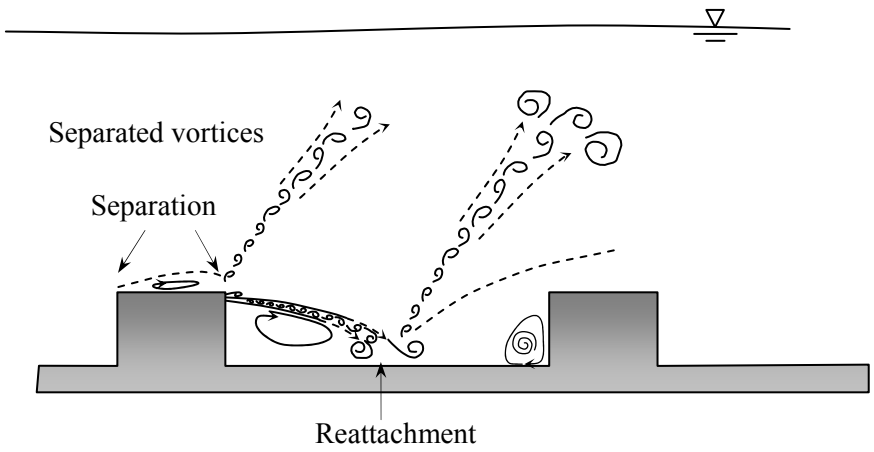

Figure 6.2 Schematic of flow over ribs.

developing from the roughness crest, which spreads and dissipates with distance. The majority of the turbulent structures is generated in this layer, thus stronger vortical structures is expected for flow over large-scale roughness. Since classical methods of analyzing flow over roughness do not account for the irregularities in the streamline pattern and existence of strong shear layers, these methods can not be directly applied to large-scale roughness.

How the macro turbulence structures caused by dunes and ribs affect the velocity distribution and free-surface appearance?

Results of the experimental and numerical analysis indicate the effect of roughness geometry on the main flow and the free-surface. It is shown in Chapter 5 that *k*-type rib roughness disturbs the flow the most among the tested roughness geometries. More vortices are generated by this roughness, hence stronger free-surface – roughness interaction is observed for this type of roughness. Dunes, with their more streamlined

geometries, do not impose as much resistance to flow, and do not generate as much mixing as ribs. However, they have stronger influence on the time-averaged water surface elevation and free-surface velocity distribution, while ribs are found to have stronger effect on the instantaneous flow field.

The coherent structures generated in the roughness region modify the instantaneous velocity field. Turbulent structures are generated mainly in the shear layer, and at the reattachment point, which are important features of the velocity field. It is found from the analysis of spatially-averaged flow field that the shear layer and the inflection point in the velocity profile overlap, indicating the relationship between the generation of separated vortices and the velocity profile properties.

The power spectra of the free-surface recordings are considered as a time-averaged feature of free-surface texture. This tool was employed to investigate the free-surface texture. This method, with improvements in data collection and analysis, is expected to assist in remote characterization of roughness and velocity indexing by free-surface velocity.

How available velocity distribution functions can be applied to large-scale roughness flows?

Spatial averaging of the flow field is the most appropriate method to obtain representative velocity and turbulence intensity profiles over large-scale roughness. Unlike flow over small roughness, spatially-averaged velocity field over large-scale roughness features a two-layer velocity profile. Structural properties of this profile, e.g. extent of the inner layer, and virtual origin, can only be seen in large-scale roughness flows. Roughness function from the outer layer profile can also be obtained for large

roughness, which provides comparison of flow resistance caused by roughness elements of different geometry.

Two-layer model of the spatially-averaged field indicates that unlike the outer layer, inner layer of the flow field needs special treatment. Both power- and log-laws are applicable to the outer layer. However, power-law function is favored for the inner layer velocity profile.

How can roughness characteristic lengths and scaling parameters be defined for large-scale roughness?

Extent of the inner layer and the location of virtual origin are found to depend on roughness height. However, comparison of results for dunes and ribs revealed that roughness characterization based solely on roughness height is not sufficient for large-scale roughness. The wavelength and cross-sectional geometry of the roughness also play significant role in main flow – roughness interaction for large-scale roughness. Bulk flow characteristics of the flow are also found to depend on the roughness geometry and the relative submergence (flow depth). Considering the strong relationship between the roughness, and turbulence structures and the free-surface, this study reiterates the importance of proper roughness characterization. Comparing the velocity fields over dunes and ribs, another roughness parameter considering the shape effect is suggested to be taken in to account. The structural properties of the spatially-averaged velocity profiles, i.e., virtual origin and extent of the inner layer, have also significance in characterizing roughness effect for known velocity profiles. As mentioned in Chapters 4 and 5, the extent of the inner layer, z_b, and virtual origin, z_0, carry the information about the main flow – roughness interaction.

6.2 Indexing by Free-Surface Velocity

Can we use water surface velocity as an index-velocity?

Time-averaged free-surface velocity distributions obtained by LSPIV and LES confirm the relationship between the free-surface, main flow, and roughness. The results of the data analysis illustrate a consistent change in α with free-surface velocity, suggesting that the relationship between free-surface and depth-averaged velocity can be indexed by free-surface velocity. Application of this method under field conditions, such as with wind effect on the surface and under natural illumination, are studied by Muste *et al.* (2004), and Kim (2006).

What is the relation between surface velocity and depth averaged mean velocity?

Ratio of free-surface velocity to depth-averaged velocity, α, depends on the channel bed roughness characteristics and their relative submergence. From variation of α given in Figure 5.50 and comparison of obtained profiles in Figure 5.43, it is concluded that a slight by evident decrease in α is observed with increasing flow resistance.

For the tested flow conditions, even though aspect ratios are smaller than the values seen in natural rivers, the surface velocity is observed to react to spatial changes in channel bed. By following the sequence of time and space averaging summarized in Figure 6.3, bulk flow velocities are obtained. A systematic change in α is observed with changing flow depth and roughness type. The velocity indices presented in Figure 5.44 and Table 5.4 also demonstrate the need for modifying the generally accepted value of α = 0.85 for large-scale roughness flows.

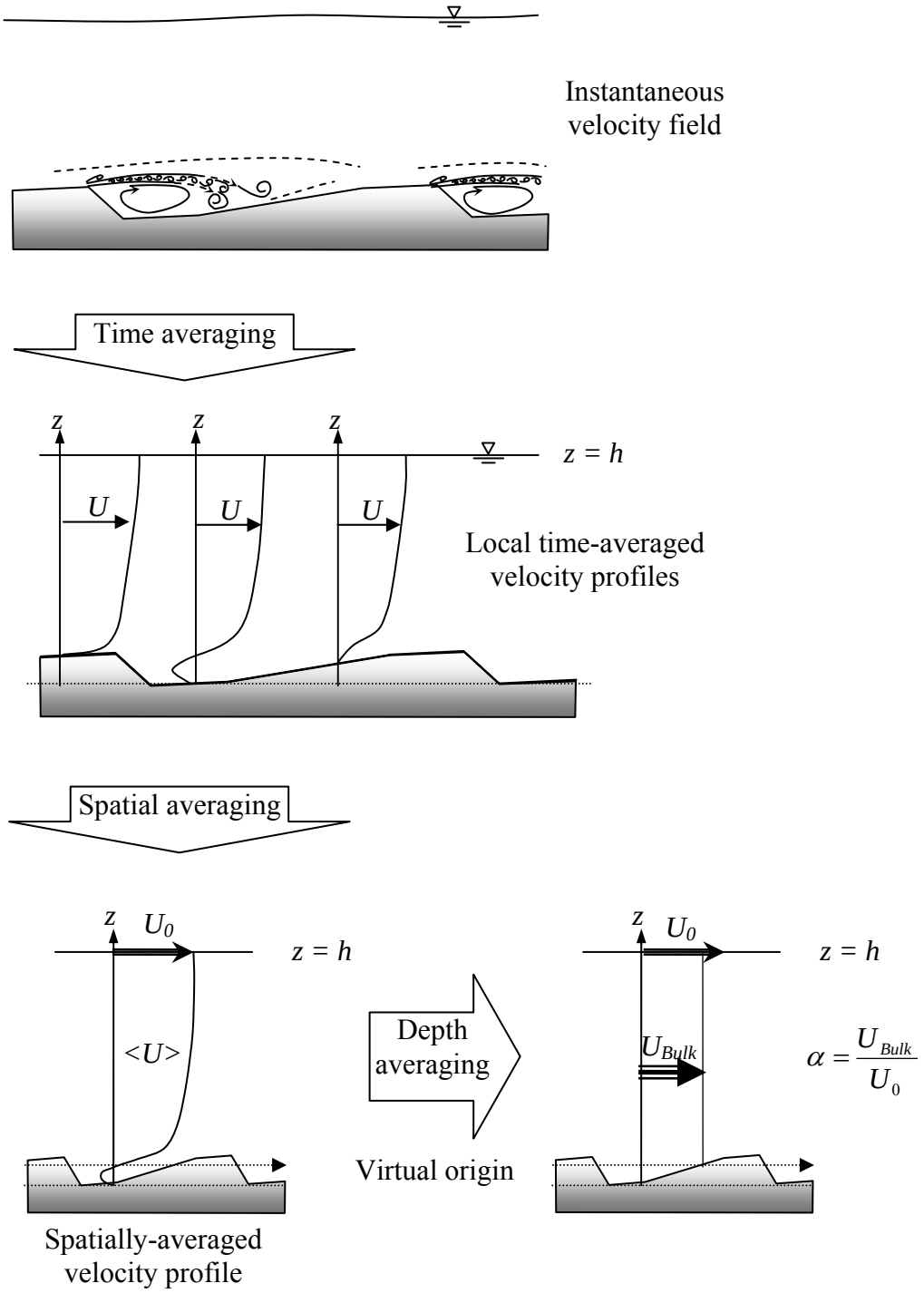

Figure 6.3 Sequence of time/space averaging employed to obtain bulk flow characteristics.

6.3 Free-Surface Deformations

How the bed roughness, Reynolds number, secondary flows and aspect ratio affect the surface deformations?

Images from the free-surface of flow with various roughness geometry and flow depth in Figure 5.17 illustrate the significant effect of roughness. The roughness effect on the free-surface texture can be qualitatively identified with naked eye. The quantitative analysis of affect of aspect ratio and roughness on the texture is obtained through the power spectrum of the texture recordings.

As the ratio of water level to roughness height decreases, more coherent structures break through the outer region and disturb the surface in burst events. Macro turbulence is a property of instantaneous flow field, and is not observed in averaged flow fields. However, statistical analysis can be applied to the instantaneous flow field to understand the time and space dependent characteristics of macro turbulence (coherent) structures. In Chapter 5, boils are identified by the help of changes in water surface elevation and velocity field.

The vortical structures presented in Figures 5.11, 5.12, and 5.13 provide additional support to earlier inferences. The effect of flow depth – Reynolds number – and roughness condition is detected in the plots. More vortex cores are observed to approach the free-surface region for rib flows. For flow over dunes, increasing depth caused more structures. However, a noticeable difference in the number of structures reaching to free-surface is not observed.

For flow over dunes, water surface elevation is observed to react to the changes in the bed roughness elevation. This feature is not seen in the numerical simulation of rib

flows, where roughness has higher submergence, and roughness width, k_x, is small with respect to roughness wavelength.

Can we remotely capture these deformations?

In the present study a digital camera is used to remotely capture the free-surface texture, and velocity distribution. This method can be applied to the field conditions with modifications. Other acoustic- and radar-based techniques can also be used in the field for this purpose. Figures 5.14 through 5.17 show the free-surface images captured under various illumination conditions. Figure 5.17 provided a strong evidence for the hypotheses of this study, illustrating a considerable variation in the free-surface texture with changing roughness condition.

Can quantify them?

The power spectra of the free-surface recordings are used for the quantitative analysis of the free-surface deformations. As given in Figures 5.22 and 5.23, the dependence of free-surface texture on the flow depth and roughness can be quantified by power spectrum analysis. This method, with improvements in data post processing, can be applied to the field conditions.

How these deformations are related to surface velocity?

Power spectra of the free-surface with various free-surface velocities are given in Figures 5.22 and 5.23. The peak of the spectrum is observed to move towards higher frequencies for increasing flow depth. Further investigation of free-surface texture recordings considering the distortion of the images is needed to derive a functional relationship between surface deformations and the free surface velocity.

6.4 Conclusions

This study originated as a result of the increasing interest in instrumentation for remote measurement of stream discharges under field conditions. The difficulty associated with this type of measurement is that velocity at the free-surface needs to be obtained, which is subsequently used to calculate the discharge. The free-surface velocity has to be related to the velocity distribution in the water column or to the depth-averaged velocity taking into account the main relevant flow parameters: bed roughness, aspect ratio or relative submergence, and flow regime.

The coupled laboratory and numerical experiments performed here provided a detailed description of open-channel flows over large-scale roughness elements. The results led to important insights on the flow structure, its signature at the free surface, and parameters that uniquely describe the mean bulk flow.

Most of the reported quantities were obtained experimentally as well as from numerical simulations. Some characteristics could be investigated using only one of the approaches because of the limitations of the technique (e.g. instantaneous pressure field is obtained only numerically). Time-averaged velocity and turbulence profiles were used to validate the numerical simulations so that the numerical results for the parameters and flow cases that could not be measured could be considered with confidence.

Numerical and experimental analysis of open-channel flows over large scale roughness showed a substantial interdependence between the bed roughness, bulk flow characteristics, and velocity and appearance of the free-surface. The analysis provided valuable information about the flow and roughness characteristics of the free-surface.

Spatially-averaged profiles are used in an attempt to account for local effects of the topography in one representative velocity distribution function similar to that of

turbulent flow over bed with uniform roughness. Spatially-averaged velocity profiles are presented, and various approaches for defining important structural flow properties, such as the virtual origin and the extent of the inner region, are discussed. It is found that the flows display a two-layered structure, and the roughness geometry and relative submergence directly affect the location of the virtual origin and the extent of the inner layer. A conceptual velocity distribution model for these flows is suggested, whereby the power law for smooth wall is adjusted using characteristics of the bed roughness.

The experiments demonstrate that the ratio of free-surface velocity to depth-averaged velocity, α, depends on the bed roughness characteristics and their relative submergence. For the given flow conditions, even though aspect ratios are smaller than the values seen in natural rivers, the surface velocity reacts to spatial changes in channel bottom. Thus, it is recommended to consider channel bed roughness and relative submergence while estimating discharge by index-velocity method.

The findings of the research are expected to facilitate remote discharge measurements through investigation of the factors affecting the free-surface appearance and velocity. The relationship between the free-surface and vertical velocity profile obtained here is expected to assist the use of non-contact discharge measurement methods currently being developed by various instrument manufacturers and water-resources management agencies.

The present work is a beginning of the development of an approach where, based on knowledge of the roughness characteristics and relative submergence in the natural scale flows, users can attribute velocity distribution laws for flow over large-scale roughness.

6.5 Recommendations

This research is a significant step forward in remote discharge estimation, and roughness characterization. However, it is recognized that it is preliminary in many respects, and much more additional research remains before we develop a functional relationship between free-surface, and roughness and flow conditions. Improved understanding of the roughness effect on the free-surface is necessary to further our understanding of the physical processes that occur in free-surface flows.

Based on the experience gained in this study, the following improvements are recommended for the future studies investigating the relationship between free-surface, bulk flow properties and large-scale roughness.

1. Even though the rigid-lid approximation of the free-surface in LES modeling has been reported to influence small region in the free-surface proximity, a better free-surface model is needed for accurate simulation of the free-surface texture. Yue *et al.* (2003) have summarized the previous work on this subject, and suggest the use of level-set method for simulating free-surface of large-scale roughness flows.
2. A wider range of flow and roughness conditions needs to be considered to develop functional relationships between the free-surface and the bulk flow properties.
3. Other factors affecting the free-surface texture and velocity needs to be considered. The effect of wind on the LSPIV measurements is studied by Muste *et al.* (2004). Kim (2006) presents the uncertainties involved in free-surface measurements by LSPIV under various flow and illumination conditions.

4. In most river flows, captured free-surface images inherently distorted due to the oblique recording angle. In the present study, since the camera and illumination conditions were kept constant, in comparison of free-surface texture across a range of flow and roughness conditions the effect of distortion is not seen. To obtain the power spectrum of the free-surface waviness that does not depend on the camera angle this distortion needs to be corrected.
5. Thorough understanding of the dynamics of the large-scale flow structures propagating from the time they originate at the bed to the point of their appearance at the free-surface will support the identification of roughness-free-surface interaction.

APPENDIX A
LOG-LAW VS. POWER-LAW FOR FLOW OVER ROUGHNESS

Velocity profile estimation for rough boundary flows is a very controversial issue. While there is no theoretical function presents, models based on dimensional analysis and functional relationships, which are divided in to main two groups as power-law (Eq. A.1) and log-law (Eq. A.2), are widely used.

$$U^+ = a\left(z^+\right)^m \tag{A.1}$$

$$U^+ = \frac{1}{\kappa}\left(z^+\right) + B \tag{A.2}$$

For complete similarity, the velocity gradient in overlap region is independent of both the inner and outer length scale, and the scaling of the velocity profile can be shown to be logarithmic (Tennekes & Lumley, 1972). For incomplete similarity, the velocity gradient depends on one or both length scales, and the scaling of the velocity profile has been shown to be a power-law using a number of different arguments (Barenblatt, 1993; Barenblatt & Prostokishin, 1993).

Besides the discussion of which law describes the overlap layer, it should be kept in mind that existence of this region is case dependent. Overlap region occurs only at high *Re* flows, and as White (1991) states, in certain flow conditions such as separation or high adverse pressure it may not be seen at all. Experimental and numerical results of this study showed that in large-scale roughness flows with low submergence ratio (h/k) this region will not occur. As seen demonstrated in Chapter 5, the velocity distribution

curve has an inflection point around $z/h \sim 0.2$, which undermines the necessity of looking for an overlap region, and a log-law description of this region, as the arguments of log-law are based on the scaling of this region.

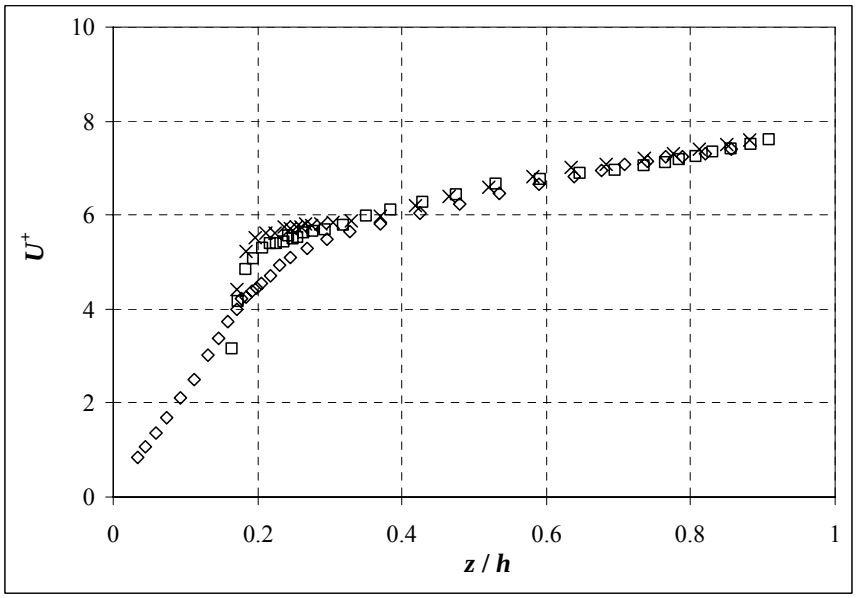

Figure A.1 Time-averaged velocity distribution (□: at location A, ◇: at location B, ×: at location C) for R04.

To investigate the existence of log-law region, experimental data should be plotted on semi-logarithmic plot. Regions where U^+ vs. log $z+$ relationship is linear can be described by log-law. And, to investigate the existence of a power-law the following diagnostic function is used (Osterlund *et al.*, 2000).

$$\Gamma = \frac{z^+}{U^+}\frac{dU^+}{dz^+} \tag{A.3}$$

Power-law is applicable in regions of constant Γ. This parameter is obtained by taking the derivative of Eq. A.1 as:

$$dU^+ = ma\left(z^+\right)^{m-1} dz^+ \tag{A.4}$$

and then inserting the given definition of U^+ again, it is obtained that

$$\frac{dU^+}{dz^+}\frac{z^+}{U^+} = m \tag{A.5}$$

This means that the diagnostic parameter, Γ, described earlier is noting but the power coefficient of the power-law fit. Similarly, taking the *z* derivative of the log-law given in Eq. (A.2) we will obtain;

$$\frac{dU^+}{dz^+}\frac{z^+}{U^+} = \frac{1}{\kappa U^+} \tag{A.6}$$

From the comparison of Eq. (A.5) and Eq. (A.6), it can be concluded that within the regions of constant $\left(\kappa u^+\right)$, the discussion of power-law or log-law is trivial, since an identical power-law fit can be found for each log-law formulation.

$$m = \frac{1}{\kappa U^+} = Const. \tag{A.7}$$

The parameter κU^+ is approximately a constant only in the core region of fully turbulent flows, where *z*-derivative of the time-averaged velocity is very small. This is in accordance with the assumption of log-law that *Re* is very large, since a uniform velocity distribution is expected in the core region of high-Reynolds number flows.

This also brings the justification to an important affair that for regions where the relationship given by Eqn. (A.7) does not hold, a choice between power-law and log-law must be done since the other cannot describe what one can describe.

A similar analysis to check for existence of log-law can also be done. Another diagnostic function, Ψ can be defined as the deviation of the mean velocity from the log function as;

$$\Psi = U^+ - \frac{1}{\kappa}\ln(z^+) \tag{A.8}$$

which can be used to investigate the additive constant, *B*, at Eq. (A.2).

These functions, Γ and Ψ, are calculated for R04 and R06 cases, and presented in Figure A.2 and Figure A.3. As seen from the figures, both of these functions are not constant, especially in the inner layer. To decide on which function describes the outer layer better, their mean values and standard deviations around means are calculated and presented in Figure A.2 and Figure A.3. Comparing the scattering of data for power and log-law diagnostic functions, power-law is selected as the fitting velocity distribution function for the outer layer.

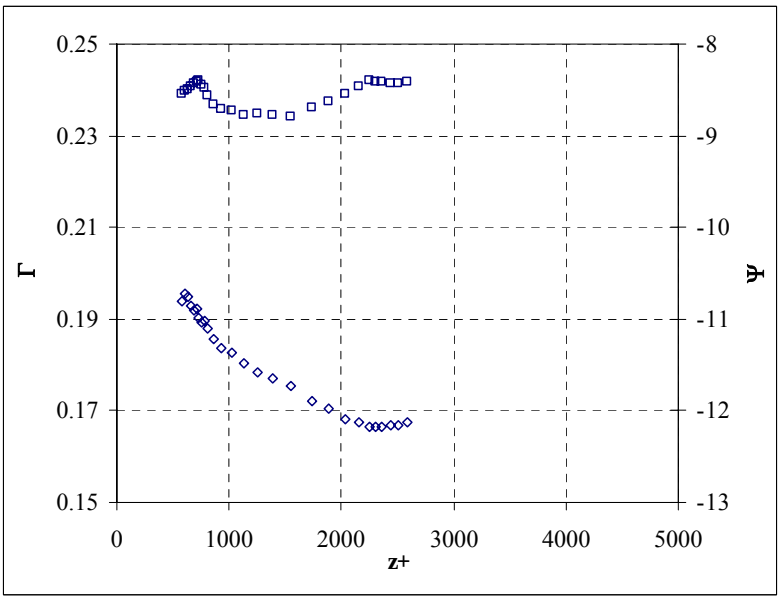

Figure A.2 Variation of Γ (□) and Ψ (◇) in the outer layer for case R04.

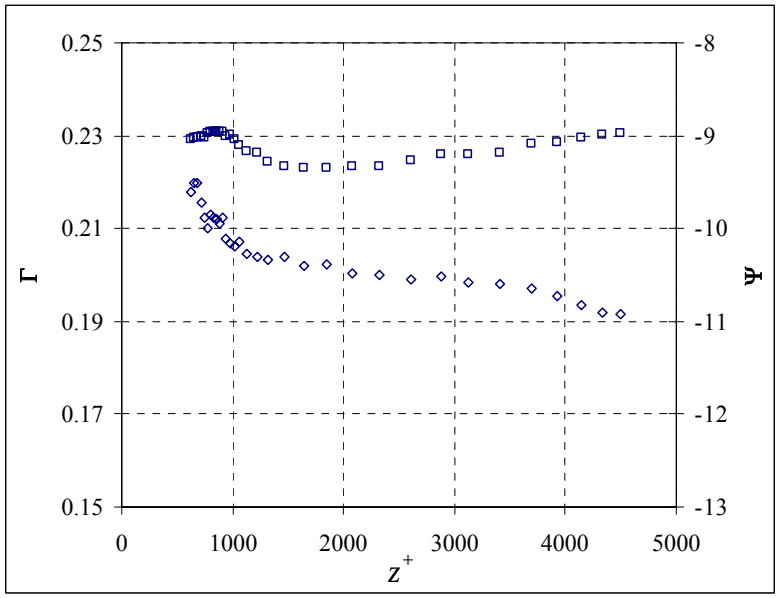

Figure A.3 Variation of Γ (□) and Ψ (◇) in the outer layer of case R06.

Table A.1 Mean values and standard deviations of Γ and Ψ in outer layer for R04 and R06.

	R04		**R06**	
	Γ	**Ψ**	**Γ**	**Ψ**
Standard deviation, σ_s	0.0029	0.5202	0.2278	-10.2808
Mean	0.2391	-11.5599	0.0028	0.3650
σ_s /Mean x100	1.2054	-4.5000	1.2294	-3.5505

While power-law gives a better fit at the outer layer, it is not possible to obtain a function that can describe the inner layer velocity distribution. Due to the local differences in the geometry and flow structure a self-similar, universal behavior may not

exist in this layer. Still, a spatially averaged velocity profile can be used to describe the average velocities in inner layer. Disturbances caused by roughness elements and separation regions force us to look for dimensional reasoning instead of diagnostic parameters (Γ and Ψ) to investigate the velocity distribution function in the inner layer.

The argument of Barenblatt (1993) for the pipe flow about the appropriateness of Power-law in inner layer is also valid for the open-channel flows. Especially for flow over large-scale roughness, inner layer has stronger Reynolds number dependence, which refutes the existence of a log region in the inner layer. Besides above reasoning, log-law description can accommodate only one characteristic length scale for roughness. As mentioned in Chapters 1 and 5, an accurate characterization for the large-scale roughness needs more than one roughness length scale (especially for *k*-type roughness). These lead us to the conclusion that selecting a power-law scaling is more appropriate than log-law for the inner layer, as for the outer layer.

Even though power-law is chosen for both inner and outer law, different power-law parameters are required for these layers. Thus, in this study a composite profile consists of two power-law functions is suggested to describe the velocity distribution for open channel flow over large-scale roughness.

APPENDIX B
SEEDING AFFECT ON LSPIV MEASUREMENTS

Free-surface measurement is the key point of this research. However, surface velocity obtained by LSPIV reflects the effect of some other factors along with the actual time-averaged free-surface velocity, U_0. Superimposed to the actual free-surface velocity, there are two main error sources affecting the velocity measurement by LSPIV; one caused by the fact that the assumption of seeding particles are perfectly following the flow is biased by the drag and inter-particle forces, and the other is bias and precision errors introduced during data collection and reduction. Thus, the measured LSPIV velocity, U_{LSPIV}, can be formulated as

$$\left\{\begin{array}{c}\text{Measured velocity} \\ (U_{LSPIV})\end{array}\right\} = \left\{\begin{array}{c}\text{Actual free-surface velocity, } U_0\end{array}\right\} + \left\{\begin{array}{c}\text{Effect of other forces on seeding particles, } \varepsilon_F\end{array}\right\} + \left\{\begin{array}{c}\text{Measurement and data reduction errors, } \varepsilon_M\end{array}\right\}$$

$$U_{LSPIV} = U_0 + \varepsilon_F + \varepsilon_M \qquad \text{(2.1-Repeated)}$$

To estimate the effect of seeding material on LSPIV measurements, three types of seeding material was tested under the same flow conditions, namely, white Styropor® expandable polystyrene beads, paper confetti, and black polypropylene beads. Physical properties of the seeds are given in Figure B.1. White beads with density of 12.5 g/m^3 and diameter of 2 to 3 mm were used in the experiments presented in the study. Black beads with same diameter and density of 900 g/m^3 were selected as the other test seeding material, since they are almost neutrally buoyant. Paper confetti, which has a very small

thickness, and a density of 750 g/m^3, was selected since it was expected to have the minimum air resistance with their negligible cross-sectional area.

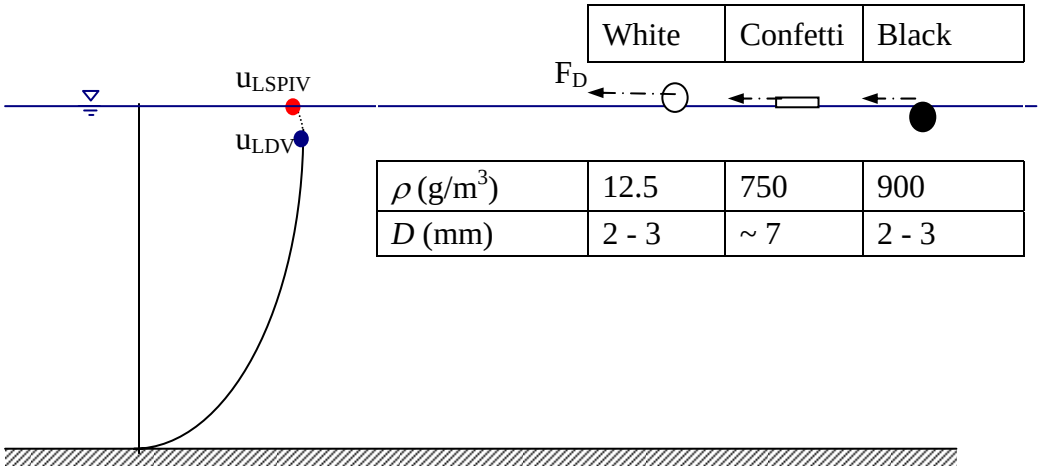

Figure B.1 Properties of three different seeding materials.

There are two forces acting on the particles on the free-surface, (1) Drag force, (2) Interpartical attraction. The drag force, F_D, on an object in a fluid flow is given by general form of Newton's resistance equation as

$$F_D = 1/2\ C_D\ \rho\ A\ U^2 \qquad \text{(B.1)}$$

where C_D is the drag coefficient, A is the area that drag force applies, and U is the relative velocity between the fluid and the particle. Eq. B.1 suggest that drag force is proportional to the velocity square. While U_0 increases, viscous drag force by water and air both increase. Since the area of application for the air-drag force is bigger for white bead, it is expected that while the U_0 increases, net drag force on the particle will increase and cause ε_F to increase.

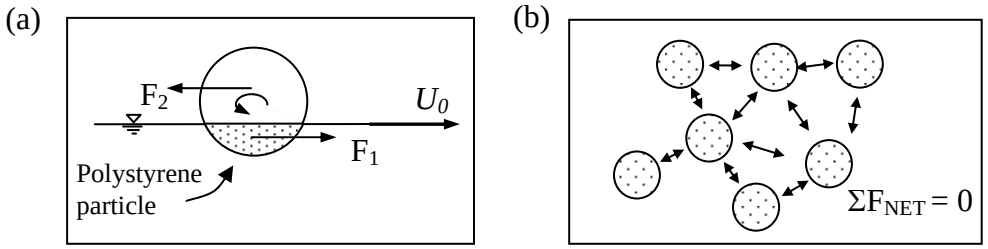

Figure B.2 Forces applied on seeding particles: (a) Drag forces exerted by water and air, and (b) interfacial forces.

Since the seeding particles are floating at the free-surface, air will also exert a resistance force, F_2, that can be calculated by Eq. B.1. Paper confetti, having the minimum air resistance, is assumed to yield the most accurate free-surface measurement.

Seeding material used in the experiments is very light (ρ=12.5 kg/m^3), so the attraction force between the particles has an effect in scattering of particles. The seeding particles floating in the air-water interface tend to clump together.

As a basic physics principle, interfacial tension and buoyancy forces cause capillary actions between the floating particles (Figure B.2.b). For individually scattered particles, random distribution makes it reasonable to assume that the resultant force by interfacial tension and buoyancy acting on the particles is zero at equilibrium condition.

During the experiments, sufficiently large distance was maintained between the seeding and testing locations to let the particles to clump together before entering the test region. As it is desired, the LSPIV method calculates not the velocity of the single particle but that of patch of clumped particles. The assumption of zero attraction force is still valid due to random distribution of seeding clusters (Figure B.2).

To compare the relative effects of the seeding materials, LDV measurements at the closest possible point to the surface is used. Results of the experiments are seen in the figure below. As it was expected, LSPIV results for the paper confetti is closer to the LDV measurement, as the drag on the particles is minimum. Average values for percent differences for these three types of materials are found to be 13.5, 11.3, and 12.1 for white beads, paper confetti, and black beads, respectively. Thus, LSPIV results with white beads were corrected by a percentage of (%13.5 – %11.3 =) 2.2 due to the drag force on the particles.

REFERENCES

Aberle J., Dittrich A. & Nestmann F. 1999. Description of steep stream roughness with the standard deviations. *Proceedings of the 28th Congress of the IAHR*, Graz, 1999.

Bandyopadhyay, P. R. 1987. Rough-wall turbulent boundary layers in the transition regime. *J. Fluid Mechanics* **180**, 231-266.

Banerjee, S. 1992. Turbulence structures. *Chemical Engineering Science* **47**(8), 1793.

Barenblatt, G. I. & Prostokishin, V. M. 1993. Scaling laws for fully developed turbulent shear flows. II - Processing of experimental data. *J. Fluid Mechanics* **248**, 521-529.

Barenblatt, G. I. 1993. Scaling laws for fully developed shear flows. II. Basic hypotheses and analysis. *J. Fluid Mechanics* **248**, 513-520.

Barenblatt, G. I., Chorin, A. J. & Prostokishin, V. M. 1997. Scaling laws for fully developed turbulent flows in pipes. *Applied Mechanics Reviews* **50** (7), 413-429.

Becker, S., Stoots, C. M., Condie, K. G., Durst, F. & McEligot, D. M. 2002. LDA-measurements of transitional flows induced by a square rib. ASME *J. Fluids Engineering* **124**, 108-117.

Bennett, J. P. 1995. Algorithm for resistance to flow and transport in sand-bed channels, *J. Hydraulic Engineering*, **121**(8), 578-590.

Bennett, J. P. 1997. Resistance, sediment transport, and bedform geometry relationships in sand-bed channels. *Proceedings of the of the USGS Sediment Workshop*, February 4-7, 1997

Bennett, S. J. & Best, J. L. 1995. Mean flow and turbulence structure over fixed, two-dimensional dunes: implications for sediment transport and bedform stability. *Sedimentology* **42** (3), 491**.**

Bennett, S. J. & Best, J. L. 1996. Mean flow and turbulence structure over fixed ripples and the ripple dune transition, In: *Coherent Flow Structures in Open Channels*. Wiley & Sons, 281-304.

Best, J. L. 2005a. The fluid dynamics of river dunes: a review and some future research directions, *J. Geophysical Research*, **110**, pp.1.

Best, J. L. 2005b. The Kinematics, topology and significance of dune-related macroturbulence: some observations from the laboratory and field. *Spec. Publs. Int. Ass. Sediment.* **35**, 41–60.

Best, J.L. & Kostaschuk, R.A. 2002. An experimental study of turbulent flow over a low-angle dune. *J. Geophys. Research* [Oceans] **107** (C9), 3135.

Bjerklie, D. M., Dingman, S. L., Vorosmarty, C.J., Bcolster, C.H. & Congalton, R.G. 2002. An approach to estimating river discharge from space. Hydraulic Measurements and Experimental Methods 2002, *Proceedings of the Specialty Conference*, July 28-August 1, 2002, Estes Park, Colorado.

Buffin-Bélanger, T., Roy, A. G. & Kirkbride, A. 2000. On large-scale flow structures in a gravel-bed river. *Geomorphology* **32**, 417-435

Chen, Y.-C. & Chiu, C.-L. 2002. An efficient method of discharge measurement in tidal streams. *J. Hydrology*, **265** (1), 212-224.

Cheng, R. T., Costa, J. E., Haeni, F. P., Melcher, N. B. & Thurman, E. M. 2001. In search of technologies for monitoring river discharge. *Advances in Water Monitoring Research*, T. Younos, Ed., Water Resources Publications, 203-219.

Cheng, R. T., Gartner, J. W., Mason, R. R., Costa, J. E., Plant, W. J., Spicer, K. R., Haeni, F. P., Melcher, N.B., Keller, W. C. & Hayes, K. 2004. Evaluating a radar-based, non contact streamflow measurement system in the San Joaquin River at Vernalis, *California. U.S. Geological Survey open file report*, OF 2004-1015, Menlo Park, California.

Cheng, R.T., Costa, J. E., Mason, R. R., Plant, W. J., Gartner, J. W., Spicer, K. R., Haeni, F. P. & Melcher, N. B. 2004. Continuous non-contact river discharge measurements. *Proceedings of the 9-th Inter. Symposium on River Sedimentation*, October 2004, Yichang, China, p. 2535-2542.

Chiu, C. L. & Tung, N. C. 2002. Maximum velocity and regularities in open-channel flow. *J. Hydraulic Engineering* **128** (4), 390-398.

Chow, F. K. 2004. *Subfilter-scale modeling for large-eddy simulations of the atmospheric boundary layer over complex terrain.* Ph.D. Dissertation, Stanford University.

Chow, V. C. 1959. *Open-Channel Hydraulics*. McGraw-Hill Book Co., New York, USA.

Church, P. E., Granato, G.E. & Owens, D. W. 1999. *Basic requirements for collecting, documenting, and reporting precipitation and stormwater-flow measurements*. Report # 99-255. U.S. Geological Survey.

Costa, J. E., Cheng, R. T., Haeni, F. P., Melcher, N.B., Spicer, K. R., Plant, W. J., Keller, W. C. & Hayes, K. 2002. Looking to the future: Non-contact methods for measuring, Hydraulic Measurements and Experimental Methods 2002, *Proceedings of the Specialty Conference*, July 28-August 1, 2002, Estes Park, Colorado.

Costa, J. E., K. R. Spicer, R. T. Cheng, F. P. Haeni, N. B. Melcher & Thurman, E. M. 2000. Measuring stream discharge by non-contact methods: A proof-of-concept experiment. *Geophysical Research Letters*, **27** (4), 553-556.

Cui, J. 2000. *Large-eddy simulation of turbulent flow over rough surfaces*. Ph.D. thesis, The University of Iowa.

Cui, J., Lin, C.-L. & Patel, V.C. 2003. Use of large-eddy simulation to characterize roughness effect of turbulent flow over a wavy wall. *J. Fluids Engineering* **125**, 1075.

Cui, J., Patel, V. C. & Lin, C.-L. 2000. *Large-eddy simulation of turbulent flow over rough surfaces*. IIHR Technical Report No. 413. Iowa City, Iowa.

Cui, J., Patel, V. C. & Lin, C.-L. 2003. Large-eddy simulation of turbulent flow in a channel with rib roughness. *Int. J. Heat and Fluid Flow* **24**, 372-388.

Dankwerts, P.V. 1951. Significance of liquid-film coefficients in gas absorption. *Industrial and Engineering Chemistry* **43**, 1460-1467.

Djenidi, L., Elavarasan, R. & Antonia, R. A. 1999. The Turbulent Boundary Layer Over Transverse Square Cavities, *J. Fluid Mechanics* **395**, 271-294.

Dypvik, K. & Lohrmann, A. 2003. Online discharge measurements in large rivers. *Proceedings of the XXX IAHR Congres*, Thessaloniki, Greece, 24-29 August 2003.

Engel, P. 1981. Length of flow separation over dunes. *J. Hydraulic. Div. ASCE* **107** (10), 1133-1143.

Fedele, J. J. & Garcia, M. H. 2000. Alluvial resistance and sediment transport for flows over dunes. *Proceedings of the ASCE Hydraulics Division Conference*, August 2000, Minneapolis, Minnesota.

Finnigan, J. 2000. Turbulence in plant canopies. *Annu. Rev. Fluid Mechanics* **32**, 519-571.

Froehlich, J., Mellen, C. P., Rodi, W., Temmerman, L. & Leschziner, M. A. 2005. Highly resolved large-eddy simulation of separated flow in a channel with streamwise periodic constrictions, *J. Fluid Mechanics*, **526**, 19 – 66.

Fujita, I., Muste, M. and Kruger, A. 1998. Large-scale particle image velocimetry for flow analysis in hydraulic applications. *J. Hydraulic Research* **36** (3), 397-414.

Fulgosi, M., Lakehal, D., Banerjee, S. & De Angelis, V. 2003. Direct numerical simulation of turbulence in a sheared air–water flow with a deformable interface. *J. Fluid Mechanics* **482**, 319-345.

Germano M., Piomelli U., Moin P. & Cabot W.H. 1991. A dynamic subgrid-scale eddy viscosity model. *Physics Fluids* **3** (7), 1760-1765.

Grass, A. J., Stuart, R. J. & Mansour, M. 1991. Vortical structures and coherent motion in turbulent flow over smooth and rough boundaries. *Philosophical Transactions: Physical Sciences and Engineering* **336,** 1640. Turbulent Flow Structure near Walls. Part I, pp. 35-65.

Gui, L., Merzkirch., W. & Fei, R. 2000. A digital mask technique for reducing the bias error of the correlation-based PIV interrogation algorithm. *Fluids* **29**:30–35.

Gunther, A. & von Rohr, P. R. 2003. Large-scale structures in a developed flow over a wavy wall, *J. Fluid Mechanics* **478**, 257-285.

Haeni, FP, Buursink, Marc L., Costa, John L., Melcher, Nick B., Cheng, Ralph T. & Plant, William J. 2000. Ground-Penetrating RADAR Methods Used in Surface-Water Discharge Measurements. *in* Noon, David A., Stickley, Glen F., and Longstaff, Dennis, ed., *GPR 2000 – Proceedings of the Eighth International Conference on Ground Penetrating Radar,* University of Queensland, Queensland, Australia, p.494-500.

Head, M. R. & Bandyopadhyay, P. 1981. New aspects of turbulent boundary-layer structure. *J. Fluid Mechanics* **107**, 297–338.

Hodges, B. R. 1997. *Numerical simulation of nonlinear free-surface waves on a turbulent open-channel flow.* Ph.D. Dissertation. Dept of Civil Engineering, Stanford University, 235 pp.

Hyun, B.S., Balachandar, R., Yu, K. & Patel, V. C. 2003a. Assessment of PIV to measure mean velocity and turbulence in water flow. *Experiments in Fluids* **35**, 262-267.

Hyun, B.S., Balachandar, R., Yu, K. & Patel, V. C. 2003b. PIV/LDV measurements of mean velocity and turbulence in a complex open channel flow. *IIHR Technical Report No. 424,* IIHR-Hydroscience and Engineering, Iowa City, Iowa.

Islam, M. S., Haga, K., Kaminaga, M., Hino, R. & Monde, M. 2002. Experimental analysis of turbulent flow structure in a fully developed rib-roughened rectangular channel with PIV, *Experiments in Fluids* 33, 296-306.

Jackson, R.G. 1976. Sedimentological and fluid dynamic implications of the turbulence bursting phenomenon in geophysical flows. *J. Fluid Mechanics* **77**, 531–560.

Jeong, J. & Hussain, F. 1995. On the identification of a vortex. *J. Fluid Mechanics* 285, 69–94.

Jimenez, J. 2004. Turbulent flows over rough walls. *Annu. Rev. Fluid Mechanics* **36**, 173–96.

Kim, Y. 2006. *Uncertainty analysis for non-intrusive measurement of river discharge using image velocimetry.* PhD Dissertation, The University of Iowa.

Kiya, M. & Sasaki, K. 1985. Structure of large-scale vortices and unsteady reverse flow in the reattaching zone of a turbulent separation bubble. *J. Fluid Mechanics* 154, 463-491.

Komori, S., Murakami, Y. & Ueda, H. 1989. The relationship between surface renewal and bursting Motions in an Open-Channel flow. *J. Fluid Mechanics* **203**, 103.

Kotey, N. A., Bergstrom, D. J. & Tachie, M. F. 2003. Power laws for rough wall turbulent boundary layers, P*hysics of Fluids* **15** (6), 1396-1404.

Krogstad P.-A. & Kaspersen, J. H. 2002. Structure inclination angle in a turbulent adverse pressure gradient boundary layer. *J. Fluids Engineering* **124** (4), 1025-1033.

Krogstad P.-A. 1991. Modification of the van Driest damping function to include the effects of surface roughness, *AIAA J.* **29** (6), 888-894.

Krogstad, P.-A. & Antonia, R. A. 1999. Surface roughness effects in turbulent boundary layers. *Exp. in Fluids* **27**, 450-460.

Kurose, R. & Komori, S. 2001. Turbulence structure over a particle roughness. *International J. Multiphase Flow* **27** (4), 673-683.

Lam, K. & Banerjee, S. 1992. On the condition of streaks formation in a bounded turbulent flow. *Physics of Fluids* **4**, p. 306.

Liou, T. –M., Chang, Y. & Hwang, D. –W. 1990. Experimental and computational study of turbulent flows in a channel with two pairs of turbulence promoters in tandem, *ASME J. Fluids Engineering* **112**, 302-310.

Liou, T.-M. & Kao, C.-F. 1988. Symmetric and asymmetric turbulent flows in a rectangular duct with a pair of ribs. *J. Fluids Engineering* **110**, 373-379.

Liou, T.-M., Wu, Y.-Y. & Chang, Y. 1993. LDV measurements of periodic fully developed main and secondary flows in a channel with rib-disturbed walls. *J. Fluids Engineering* **115** (1), 109.

Lu, S. S. & Willmarth, W. W. 1973. Measurements of the structure of the reynolds stress in a turbulent boundary layer. *J. Fluid Mechanics* **60**, 481–511.

Lyn, D.A. 1993. Turbulence measurements in open-channel flows over artificial bed forms. *J. Hydraulic Engineering* **119** (3), 306–326.

Macdonald, R.W. 2000. Modeling the mean velocity profile in the urban canopy layer. *Bound. Layer Meteorol.* **97** (1), 25–45

Maddux, T. B. 2002. Turbulent open channel flow over fixed three-dimensional dune shapes. *Ph.D. dissertation*, Univ. of California, Santa Barbara.

Maddux, T.B., Nelson, J. M. & McLean, S.R. 2003a. Turbulent flow over 3D dunes. I: Free surface and flow response, *J. Geophys. Research*, **108** (F1).

Maddux, T.B., McLean, S.R. & Nelson, J.M. 2003b. Turbulent flow over 3D dunes. II: Fluid and bed stresses, *J. Geophys. Research*, **108** (F1).

Manhart, M. ,Tremblay, F. & Friedrich, R. 2001. MGLET: a parallel code for efficient DNS and LES of complex geometries. In *Parallel Computational Fluid Dynamics 2000*, Edited by C. B. Jenssen, T. Kvamsdal, H. I. Andersson, B. Pettersen, A. Ecer, J. Periaux, N. Satofuka, and P. Fox. (Elsevier Science, Amsterdam, 2001).

Margalef, R. 1997. Turbulence and marine life. *Scientia Marina* (Barcelona) **61** (1).

McIlwain, S. & Pollard, A. 2002. Large eddy simulation of the effects of mild swirl on the near field of a round free jet. *Physics of Fluids* **14** (2), 653-661.

McLean, S. R., Nelson, J. M. & Shreve, R. L. 1996. Flow-sediment interactions in separating flows over bedforms. In P.J. Ashworth et al. (Eds.), *Coherent Flow Structures in Open Channels*, pp. 733, John Wiley, Hoboken, N. J.

McLean, S. R., Nelson, J. M. & Wolfe, S. R. 1994. Turbulence structure over two-dimensional bed forms: Implications for sediment transport. *J. Geophys. Research*, **99**(C6), 12729–12747.

McLean, S. R., Wolfe, S. R. & Nelson, J.M. 1999. Spatially averaged flow over a wavy boundary revisited. *J. Geophys. Research* **104** (C7), 15743– 15753.

Melcher, N.B., Costa, J.E., Cheng, R.T., Thurman, E.M. & Haeni, P.F. 2000. Use of radar for making noncontact river-discharge measurements. *in* Arizona Hydrological Society 13th Annual Symposium, Phoenix, Arizona, September 20-23, 2000, p. 63-64.

Mochizuki, S., Izawa, A. & Osaka, H. 1996. Turbulent drag reduction in a d-type rough wall boundary layer with longitudinal thin ribs places within traverse grooves. *JSME International Journal*, Series B, **39** (3), 461-474.

Moog, D. B. & Jirka, G. H. 2002. Air-water gas transfer in uniform flows with large gravel-bed roughness. Geophysical Monograph- American Geophysical Union **127**, 371-376.

Morvan, H. P. 2005. Channel shape and turbulence issues in flood flow hydraulics. *J. Hydraulic Engineering* **131** (10), 862-865.

Mueller, A. 1987. An experimental investigation of the mixing layer behind dunes with combined flow visualization and velocity measurement. In: *Turbulence Measurements and Flow Modeling.* Hemisphere Publishing, Washington. 229-238.

Muller, A. & Gyr, A. 1986. On the vortex formation in the mixing layer behind dunes. *J. Hydraulic Research* **24** (5), 359-375

Muste, M., Bradley, A., Kruger, A. & Cheng, R. T. 2001. *Complementary Investigation for Implementation of Remote, Non-Contact Measurements of Streamflow in Riverine Environment*, USGS / National Institutes for Water Resources, Proposal, IIHR- Hydroscience & Engineering, Iowa City, IA.

Muste, M., Xiong, Z., Schone, J. & Li, Z. 2004. Validation and extension of image velocimetry capabilities for flow diagnostics in hydraulic modeling, *J. Hydraulic Engineering* **130** (3): 175-185.

Nagaosa, R. & Handler, R. A. 2003. Statistical analysis of coherent vortices near a free surface in a fully developed turbulence. *Physics of Fluids* **15** (10), 375.

Nakagawa, H., Nezu, I. & Ueda, H. 1975. Turbulence of open channel flow over smooth and rough beds. *Proceedings of the JSCE* **241,** 155-168.

Nakagawa, S. & Hanratty, T. J. 2001. Particle image velocimetry measurements of flow over a wavy wall. *Physics of Fluids* **13** (11), 3504 – 3507.

Nakagawa, S. & Hanratty, T. J. 2003. Influence of a wavy boundary on turbulence. II. Intermediate roughened and hydraulically smooth surfaces. *Experiments in Fluids* **35,** 437-447.

Nakagawa, S., Na, Y. & Hanratty T. J. 2003. Influence of a wavy boundary on turbulence. I. Highly rough surface, *Experiments in Fluids* **35**, 422-436.

Nakayama, A. & Yokojima, S. 2001. Direct numerical simulation of the fully developed open-channel flow at subcritical Froude numbers. *DNS/LES Progress and Challenges,*Third AFOSR Int' Conference Arlington, Texas 2001, 569-576.

Nakayama, T. 2000. *Turbulence and coherent structures across air-water interface and relationship with gas transfer*, PhD Dissertation, Kyoto University, Japan.

Nelson, J. M., McLean, S.R. & Wolfe, S.R. 1993. Mean flow and turbulence fields over two-dimensional bed forms. *Water Resources Research* **29** (12), 3935-3953.

Nezu, I. & Nakagawa, H. 1993. *Turbulence in Open- Channel Flows*, IAHR Monograph Series, A.A. Balkema, Rotterdam, 281 p.

Nezu, I. & Rodi, W. 1986. Open-channel flow measurements with a Laser-Doppler Anemometer. *J. Hydraulic Engineering* **112** (5), 335-355.

Nikora, V. I., Goring, D. G., McEwan, I. & Griffiths, G. 2001. Spatially averaged open-channel flow over rough bed. *J. Hydrauic Engineering* **127** (2), 123– 133.

Nikora, V., Koll, K., McEwan, I., McLean, S. & Dittrich, A. 2004. Velocity distribution in the roughness layer of rough-bed flows. *J. Hydraulic Engineering* **130** (10), 1-7.

Nordin, Jr., C. F. & Algert, J. A. 1965. Geometrical properties of sand waves. Discussion. *J. Hydraulic. Div.* **91**, No. HY5.

Okamoto, S., Seo, S., Nakaso, K. & Kawai, I. 1993. Turbulent shear flow and heat transfer over the repeated two-dimensional square ribs on ground plane, *J. Fluids Engineering* **115**, 631-637.

Paduan, J. D. & Garber, H. C. 1997. Introduction to high-frequency radar: reality and myth, *Oceanography* **10**, 36-39.

Pan, Y. & Banerjee, S. 1995. A numerical study of free surface turbulence in channel flow. *Physics of Fluids* **7**, 1649–1664.

Patel, V. C. & Lin, C. L. 2004. Turbulence modeling in flow over a dune with special reference to free surface and bed roughness effects. *Proceedings of the 6th Int. Conf. on Hydroscience and Engineering (ICHE-2004)*, May 30-June 3, 2004, Brisbane, Australia.

Patel, V. C. 1998. Perspective: flow at high Reynolds number and over rough surfaces-Achilles heel of CFD, *ASME J. Fluids Eng* **120**, 434-444.

Perry, A. E., Schofield, W. H. & Joubert, P. N. 1969 Rough wall turbulent boundary layers. *J. Fluid Mechanics* **37**, 2, 383-413.

Polatel, C., Stoesser, T. & Muste, M. 2005. Velocity profile characteristics in open channel flow over two–dimensional dunes with small relative submergence, *Proceedings of the EWRI Congress, Anchorage, Alaska, 2005.*

Pope, S. B. 2000. *Turbulent flows*. Cambridge, UK. Cambridge University Press.

Raffel M., Willert, C. E. & Kompenhans, J. 1998. *Particle image velocitimetry, a practical guide.* Springer, Berlin, Heidelberg, New York.

Rantz, S. E. & others 1982a. Measurement and computation of streamflow, Vol. 1, Measurement of Stage and Discharge, *U.S. Geological Survey Water Supply Paper 2175*, U.S. Geological Survey.

Rantz, S.E. & others 1982b. Measurement and computation of streamflow, Vol. 2: Computation of Discharge, *U.S. Geological Survey Water Supply Paper 2175*, U.S. Geological Survey.

Rashidi, M. 1997. Burst-interface interactions in free surface turbulent flows. *Physics of Fluids* **9**, 3485.

Raudkivi, A. J. 1966. Bed forms in alluvial channels. *J. Fluid Mechanics* **26** (3), 507-514.

Raupach, M. R. 1981. Conditional Statistics of Reynolds Stress in Rough-wall and Smooth-wall Turbulent Boundary Layers, *J. Fluid Mechanics* **108,** 363-382.

Raupach, M. R., Antonia, R. A. & Rajagopalan, S. 1991. Rough wall turbulent boundary layers. *Applied Mechanics Review* **44** (1), 1-25.

Rhodes, D. G. & Senior, A. K. 2000. Numerical study of resistance with rib roughness of various scales, *J. Hydraulic Engineering* **126** (6), 541-545.

Rifai, M.F. & Smith, K.V.H. 1971. Flow over triangular elements simulating dunes. *J. Hydraulic Engineering* **97** (7), 963-976.

Rodi, W. 1980. Turbulence models and their application in hydraulics. IAHR, Section on Fundamentals of Division II: Exp. and Math. Fluid Dynamics, Delft.

Shen, H. W., Fehlman, H. M. & Mendoza, C. 1990. Bed form resistance in open channel flows. *J. Hydraulic Engineering* **116** (6), 799–815.

Shi, J., Thomas, T.G. & Williams, J.J.R. 2000. Fee-surface effects in open channel flow at moderate Froude and Reynold's numbers. *J. Hydraulic Research*, **38** (6), 465-474.

Simpson, M. R. & Bland, R. 2000. Methods for accurate estimation of net discharge in a tidal channel. *IEEE J. Oceanic Engineering* 25 (4), 437-445.

Smagorinsky, J. 1963. General circulation experiments with the primitive equations. *Monthly Weather Review* **91**, 99-152.

Smalley, R. J., Leonardi, S., Antonia, R. A., Djenidi, L. & Orlandi, P. 2002. Reynolds Stress Anisotropy of Turbulent Rough Wall Layers, *Experiments in Fluids* **33**, 31-37.

Smart, G. M., Duncan, M. J. & Walsh, J. M. 2002. Relatively rough flow resistance equations. *J. Hydraulic Engineering* **128** (6), 568-578.

Smith, B. T. & Ettema, R. 1995. *Ice-cover influence on flow and bedload transport in dune-bed channels.* Report No. 374. Iowa Institute of Hydraulic Research, Iowa City, IA.

Smith, B. T. & Ettema, R. 1997a. Flow resistance in ice-covered alluvial channels. *J. Hydraulic Engineering* **123** (7), 592-599.

Smith, B. T. & Ettema, R. 1997b. Ice-cover influence on flow structure over dunes. *J. Hydraulic Research*, IAHR 35 (5), 707-719.

Smith, J. D. & McLean, S.R. 1977. Spatially averaged flow over a wavy surface. *J. Geophys. Research* **82**, 1735-1746.

Song, S. & Eaton, J. K. 2002. The effects of wall roughness on the separated flow over a smoothly contoured ramp. *Experiments in Fluids* **33**, 38-46.

Spicer, K. R., J. E. Costa& G. Placzek 1997. Measuring flood discharge in unstable stream channels using ground-penetrating radar, *Geology* **25** (5): 423-426.

Stoesser, T., Rodi, W. & Froehlich, J. 2005. Large eddy simulation of open-channel flow over a layer of spheres. *Proceedings of the XXXI IAHR Congress, Seoul, 2005.*

Stoesser, T., Rodi, W., Polatel, C., Patel, V. C. & Muste, M. 2005. Large eddy simulations of flow over two dimensional dunes, *Proceedings of the XXXI IAHR Congress, Seoul, 2005*.

Stone, H.L. 1968. Iterative Solution of Implicit Approximation of Multi-dimensional Partial Differential Equations. *SIAM J. Numerical Analysis*. No. 3.

Tamburrino, A. & Gulliver, J. S. 1999. Large flow structures in a turbulent open channel flow. *IAHR J. Hydraulic Research* **37**(3), 363-380.

Temmerman, L., Leschziner, M.A., Mellen, C.P. & Fröhlich, J. 2003. Investigation of wall function approximations and subgrid-scale models in Large Eddy Simulations of separated flow in a channel with streamwise periodic constrictions. *J. Heat Fluid Flow* **24**, 157-180.

Tennekes, H. & Lumley, J. L. 1992. *A First Course in Turbulence*, MIT Press, NJ.

Tremblay, F. & Friedrich, R. 2001. An algorithm to treat flows bounded by arbitrarily shaped surfaces with cartesian meshes. *In: Notes on Numerical Fluid Mechanics*, Vol. 77, Springer.

Van Mierlo, M. C. L. M. & Ruiter, J.C.C. 1988. Turbulence measurements above artificial dunes, Report on Measurements, *Delft Hydraulics, Report Q798*, Vol. I., Delft, The Netherlands.

White, F. M. 1991. *Viscous fluid flow*, 2nd Edition, McGraw-Hill, Inc, New York.

Wood, D. H. & Antonia, R. A. 1975. Measurements in a turbulent boundary layer over a d-type surface roughness, *J. Applied Mechanics*, September, 591-597.

Yalin, M.S. 1992. *River mechanics*. Pergamon Press Ltd, Oxford, G. Britain, 219 p.

Yoon, J.Y. & Patel. V.C. 1999. Numerical model of turbulent flow over sand dune. *J. Hydraulic Engineering* **122**, 10-18.

Yue, W., Lin, C.-L. & Patel, V.C. 2003. Numerical simulation of turbulent free surface flows using level set method and large eddy simulation. *IIHR Technical Report No. 435,* IIHR-Hydroscience and Engineering, Iowa City, Iowa.

Yue, W., Lin, C. -L. & Patel, V. C. 2005a. Coherent structures in open-channel flows over a fixed dune. *J. Fluids Engineering* **127**, 858-864.

Yue, W., Lin, C. -L. & Patel, V. C. 2005b. Large eddy simulation of turbulent open-channel flow with free surface simulated by level set method. Phys. Fluids **17**. 025108.